Photodegradation of Hair Proteins: Mechanistic Insights and the Role of Transition Metals

Philip Richard Groves

Doctor of Philosophy

University of York

Chemistry

August 2017

Abstract

The main aim of this project was to study the effects of redox active transition metals present in hair fibres upon the photodegradation of hair proteins. Tyrosine based keratin model systems were developed to enable this photochemically critical amino acid to be studied in isolation from other photo-active hair components.

The photochemical activity of tyrosine was found to be strongly dependent on molecular environment. In free solution, tyrosyl radicals were very short-lived, whereas radicals in solid systems persisted for many hours.

PEG-Tyr block copolymers provide accurate models of tyrosine in a protein polypeptide, in the form of micelles and stable hydrogels. Tyrosine molecular environment in micelles is comparable to α-helical structures of proteins, as analysed by nitroxide spin labelling experiments. Despite significantly different bulk properties, the molecular environment and reactivity of tyrosine in micelles and gels is remarkably similar, although diffusion of reactive oxygen species (ROS) and Fe(III) becomes a limiting factor in gels. Spin labelling provided a method to monitor the gelation process in real-time.

Both Fe(III) and Cu(II) influenced tyrosine photodegradation in PEG-Tyr systems: 100 ppm Fe(III) increased degradation by around 2.2 times, whereas Cu(II) slowed photodegradation due to Cu-Tyr complexation. The effect of Fe(III) was attributed to increased ROS production leading to autoxidation, direct redox chemistry between metal and tyrosine, and sensitisation of tyrosine by metal complexes. Partitioning of Fe(III) within micelles resulted in a significant enhancement in activity, indicating that Fe(III) can catalytically influence tyrosine photooxidation at concentrations relevant to hair fibres.

In a separate study, the effect of humidity upon the formation and decay of protein-based radicals in UV exposed human hair samples was investigated. Increased water content increases radical reactivity, explaining greater protein degradation at higher humidity. Antioxidant studies suggest autoxidation is less significant within hair proteins compared to model systems.

Contents

List of Figures

List of Schemes

Acknowledgements

I am indebted to Dr Victor Chechik, my supervisor, who guided and supported me throughout my research and writing. His kind, friendly and encouraging nature helped me to build confidence in my work and persevere throughout the project.

I am also very thankful for the regular discussions, helpful advice and contributions from Dr Jennifer Marsh throughout my time in York and afterwards. My heartfelt thanks also to Prof. Dave Adams and members of his group, who provided PEG-Tyr polymer samples and advice on gel formation.

Further thanks to other members of the Chechik group: Andrew Grantham, Chris Unsworth and Sindhu Suravaram for their advice, support and company. Also, I am grateful to Dr Brendan Garrett for helpful advice with hair experiments, and to Dr Yury Gorbanev for ensuring there was never a dull day in the office. Thanks to the technical staff who assisted with many experiments, particularly Dr Emma Dux for ICP-MS and general assistance.

Thanks to The Procter and Gamble Company for funding this research.

I am immensely grateful for all the support I have received from colleagues, friends and family during the writing of this report. Staff at Leyton Sixth Form College have provided huge encouragement. Mum and dad, for all their support, and a quiet place to work with a plentiful supply of tea. And lastly to Sarah, for her patience as I worked through evenings and weekends, and putting up with my grumpiness when work took longer than expected. Without her unending support, I could never have achieved my goals.

Declaration

I declare that this thesis is a presentation of original work and that I am the sole author. This work has not previously been presented for an award at this, or any other, university. All sources are acknowledged as References.

1. Photodegradation of hair proteins: The role of transition metals

The damaging effect of sunlight upon hair and wool has long been of interest to both the cosmetics and textile industries. The earliest investigations into the photochemistry of these natural fibres was driven by the wool industry, to explain and prevent the discolouration "photo-yellowing" of white wool.[1] This colour change upon UV exposure was attributed to the breakdown and oxidation of tyrosine and tryptophan residues within keratin fibres.[2]

Wool and hair are structurally similar, and prolonged exposure of human hair to sunlight can also lead to undesired effects. These include loss or change of colour (bleaching), changed texture and a loss in mechanical strength.[3] The extent of damage can be mitigated or exacerbated by other factors, such as air pollution, cosmetic treatments, grooming and cleansing.

Consequently, understanding the mechanisms behind light-induced damage to hair is of considerable interest to the cosmetics industry. The global haircare market was worth an estimated $50.2 billion in 2012,[4] and the development of products which help protect hair from sunlight is important.

Hair contains trace transition metal ions, which are known to influence photochemical processes,[5] particularly the production and reactions of reactive oxygen species (hydroxyl, alkoxyl and peroxyl radicals). These species can interact with a wide range of targets, including proteins, lipids and pigments. Trace metals may therefore play a critical role in the photooxidation of hair, however few investigations have tested this theory. This project aims to explore the role of transition metals in hair photooxidation.

1.1 The Structure of Human Hair

Hair is a complex biological cellular structure made primarily of proteins and lipids. Scalp and beard hair fibres are typically 40-100 μm thick, and grow approximately 0.33 mm per day.[6] Hair is one of the fastest growing body tissues. Hair fibres are formed in follicles up to 3 mm deep within the skin: living cells produce keratin proteins and lose their cytoplasm and cellular structure as they are pushed up through the skin.[7] There are two main types of hair cell: flat, thin *cuticle* cells; and long, spindle shaped *cortex* cells. Cuticle cells are arranged around the cortex cells, overlapping like scales. Cortex cells make up the bulk (80%) of the hair, and are fibrillar, arranging parallel to the hair axis. Thicker hairs may contain a *medulla*, a central column of vacuole containing cells, although this is not present in all hairs. Figure 1-1 shows the cross section of a typical human hair.

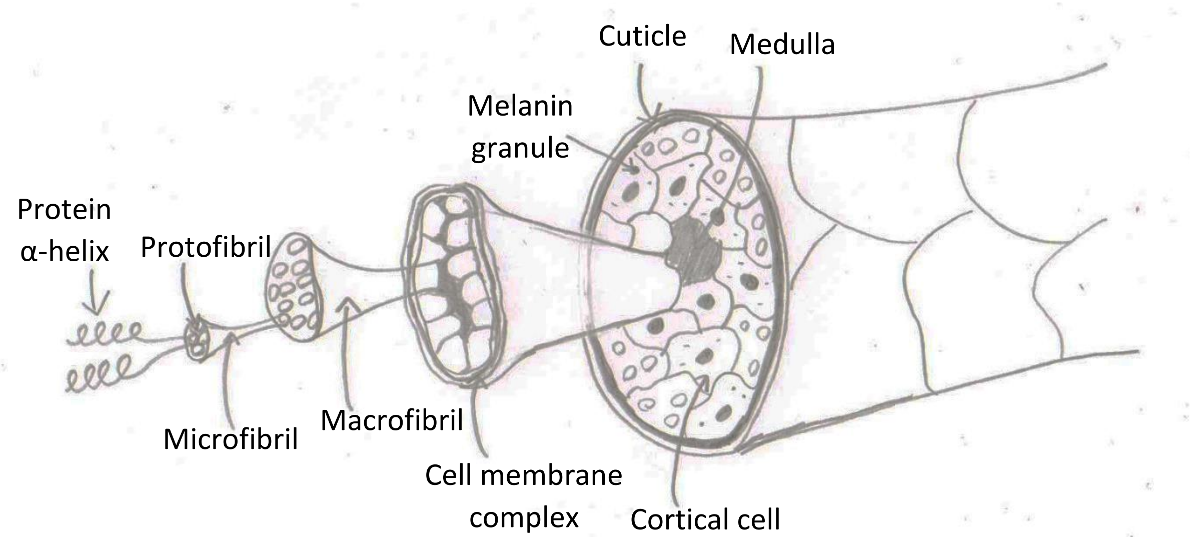

Figure 1-1: Cross-sectional structure of a typical human hair. Figure adapted from [7].

Cortex cells are categorised as *ortho*- or *para*-, depending on their cysteine content and solubility.[8] The arrangement of different cortex cells determines whether hair is curly or straight.[9] Cells are joined together by an *intercellular cement* which is made up of smaller proteins and the lipids which form part of the *cell membrane complex*. This gives the fibre strength and provides cohesion. Melanin pigment, when present, exists as granules within cortex cells.

Hair is subjected to various weathering processes. Damage can occur from light and heat exposure, and friction caused by day-to-day activity. Understandably therefore the structure of hair varies from root to tip, as older hair at the tip will have been subjected to more weathering. On a macroscopic level, hair damage can be observed in split ends, detached cuticle scales, greater surface friction, increased porosity and decreased elasticity. On a molecular level, damage to proteins, lipids and other molecules gives rise to these observed changes.

The approximate chemical composition of hair (by weight), at 20 °C and 65% relative humidity, is:[10]

- 80% proteins
- 14% water
- 5% lipids
- <1 % pigments, metals and other trace elements

The amount of melanin pigment present in hair varies significantly depending on hair colour, typically ranging from 28 ± 1 ng/mg in albino hair[11] to 7200 ng/mg in black hair.[12] These figures are the total melanin content (sum of the two types, eumelanin and pheomelanin). In albino and very light hair, eumelanin is often absent.[11]

Calcium is the most abundant metal in hair fibres (uptake from washing as well as endogenous sources), however both copper and iron are found in concentrations of up to 200 ppm.[13] The origin of the metals in hair is uncertain, and is likely a combination of endogenous processes such as enzyme decomposition in the follicles, and exogenous sources such as water supply, hair treatment products and air pollution.[14]

1.1.1 Structure of keratin in hair

Keratin proteins form the main structural component of hair, the macrofibrils (see Figure 1-1). Macrofibrils are made up of microfibrils, which in turn consist of protofilaments, made up of keratin protein dimers, as outlined in Figure 1-2. Fibrils are arranged parallel to one another creating a fibrous structure.

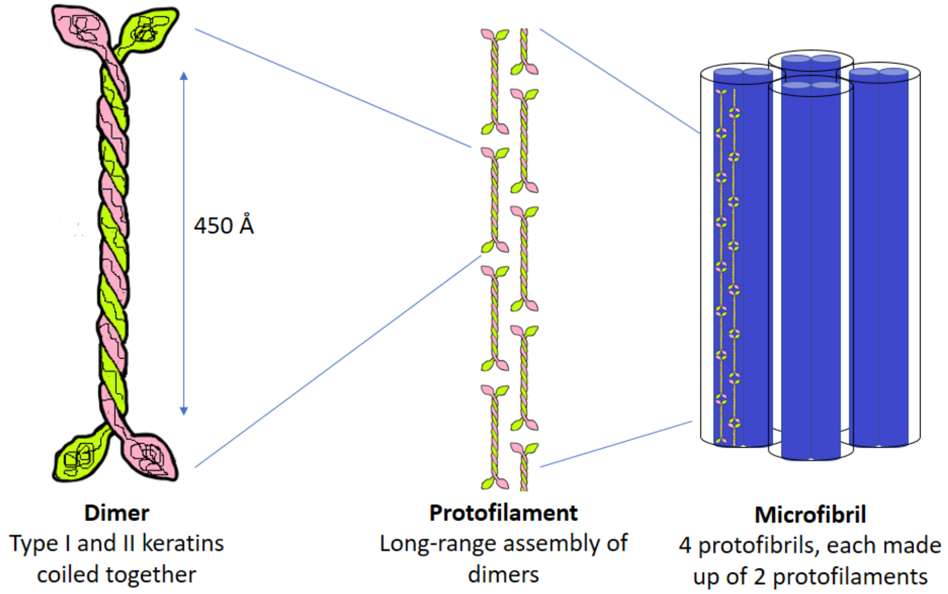

Figure 1-2: The arrangement of keratin within hair fibres. Figure adapted from [34].

The main type of keratin in mammal hair is α-keratin, so called because it exhibits an α-helical structure. The spacing of the helix is slightly smaller than other proteins (5.1 Å instead of 5.4 Å). This is a result of type I (acidic) and type II (basic) α-helical proteins twisting around one another in a left-handed coil, giving rise to a “coiled coil” dimer.[15] This is observed in crystal structures of human intermediate filament and epidermis keratin proteins.[16-17]

α-Keratin is rich in cysteine (Cys) amino acid residues compared to other proteins. Cys residues can form disulfide bonds with other sulfur-containing amino acids, thereby cross-linking adjacent polypeptide chains. This gives the protein structural rigidity. Keratin proteins are classed as “hard” or “soft”, depending on their Cys content and number of disulfide bonds. “Hard” keratins have many cross-links, and are typically found in hair, horn and nails. “Soft” keratins have fewer disulfide bonds and are typically found in the skin.[18]

1.1.2 Amino acid composition of keratins in hair

Hair fibres contain many distinct “keratin associated proteins” (KAPs) which make up the overall keratin content of fibres, as well as other protein structures. Those which are most highly expressed in hair fibres are summarised in a review by Rogers et al.[19] Different proteins are expressed in the cortex and cuticle.

The amino acid sequence of KAPs and other proteins in hair varies. Particular residues relevant to a photochemical study are those with aromatic side chains (see section 1.2). The structures of these amino acids are shown in Figure 1-3. Table 1-1 summarises the amino acid composition of some of the most highly expressed proteins in the hair cuticle and cortex.

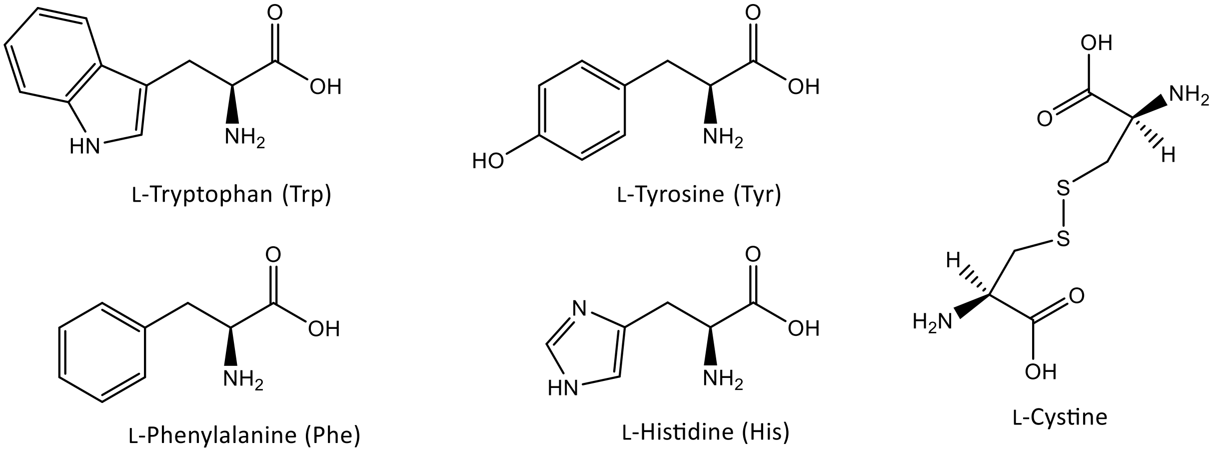
L-Tryptophan (Trp)
L-Tyrosine (Tyr)
L-Cystine
L-Phenylalanine (Phe)
L-Histidine (His)

Figure 1-3: Structures of amino acids with aromatic side chains and disulfide cystine, capable of absorbing UVB/UVA radiation. Uncharged forms shown.

Table 1-1:Percentage amino acid composition of selected highly expressed proteins present in hair fibres. Data from [19] and from amino acid sequences on the UniProt database [20].

Protein	**Expressed in**	**Mole percentage of amino acid in whole protein**				
		Cystine	**Trp**	**Tyr**	**Phe**	**His**
KAP 5s	Cuticle	29.0-35.7	0.0	0.0	0.0	0.0
KAP 10.1	Cuticle	24.8	0.3	1.4	0.3	0.3
KAP 19.6	Cuticle	10.3	0.0	22.4	5.2	0.0
KAP 19.4	Cuticle	7.1	0.0	16.7	5.9	0.0
S100A3	Endocuticle	9.9	1.0	5.9	5.0	1.0
KAP 1.1	Cortex	21.6	0.6	2.3	2.8	1.1
KAP 7.1	Cortex	6.0	1.2	11.9	8.0	0.0
KAP 19.1	Cortex	7.8	0.0	20.0	7.8	1.1
KAP 19.2	Cortex	23.0	0.0	15.4	5.8	1.9
KAP 8	Cortex	6.6	3.3	18.0	8.2	0.0

Levels of cystine disulfide in keratin proteins vary significantly: whilst some (KAP5s, KAP10.1, KAP1.1, KAP19.2) are highly crosslinked, others are much softer. This reflects different structural functions of proteins within the fibre.

The percentage of aromatic amino acids (Trp, Tyr, Phe and His) in keratin proteins also varies. In general, Trp, Phe and His are less abundant in cuticle keratin, with virtually no tryptophan present in the cuticle. Tyrosine shows by far the highest abundance in both cortex and cuticle proteins, with some proteins containing over 20% tyrosine (KAP19.1, KAP19.6). However, a dominant group of cuticle proteins, KAP5s, contain no aromatic amino acids.

Intermediate filament proteins (not shown in Table 1-1) are keratins which have not fully formed fibres as shown in Figure 1-2. They are present in both the cortex and cuticle and typically show lower sulfur content, but similar aromatic content to the KAPs.[21] The overall concentration of aromatic amino acids and cysteine in hair is summarised in Table 1-2, derived from protein hydrolysis experiments on hair fibres.[21-22] The ranges reported are based on values for different samples reported in literature.

Table 1-2: Concentrations of selected amino acids in dry hair fibres. Data calculated from values reported in [22-23].

Amino Acid	**Amount in hair µ mol / g**	**Mass percent equivalent**
Cysteine	1380 – 1512	16.7 – 18.3 %
Tryptophan	20 – 64	0.4 – 1.3 %
Tyrosine	177 – 195	3.2 – 3.5 %
Phenylalanine	132 – 149	2.2 – 2.5 %
Histidine	40 – 86	0.6 – 1.3 %

Disulfide bonds within keratin proteins play a crucial structural role in hair fibres, with cysteine making up around 17.5% of the fibre by mass. Tyrosine is the most abundant of the aromatic amino acids. The photochemistry of the aromatic amino acids, particularly tyrosine, and disulfides will reflect overall keratin photochemistry, and is discussed in section 1.2.

1.1.3 Lipids

There are two main sources of lipids present in hair. External lipids derive from sebaceous glands on the scalp, and coat hair fibres externally. Integral lipids in hair fibres are primarily present as part of cell membrane complexes. Most lipids in hair fibres are fatty acid residues, although sterols are also present. In cuticle cells, fatty acids typically form a monolayer bound to the epicuticle (outermost layer of cuticle cells) by thioester linkages, see Figure 1-4.[24]

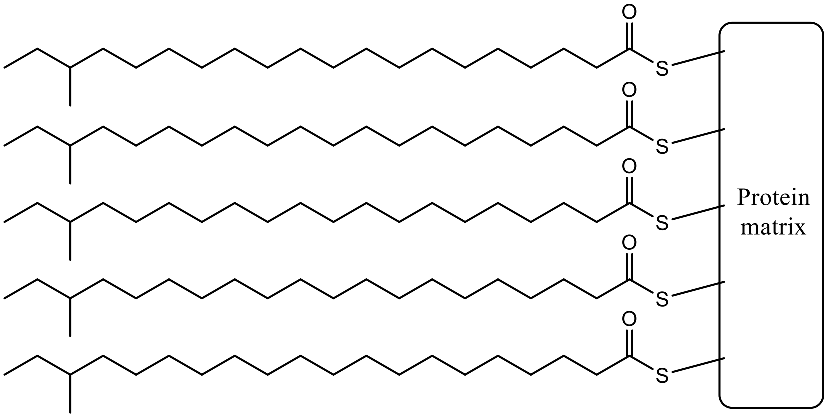

Figure 1-4: The structure of 18-MEA bound to the outermost layer of proteins in cuticle cells

Within the cortex, fatty acids typically form bilayers and interact with cell membrane proteins by polar interactions.[25] Photochemically relevant fatty acids include 18-methyl eicosanoic acid (18-MEA) as well as other monoene unsaturated fatty acids such as palmitoleic acid and oleic acid. Cholesterol and cholesterol sulfate are also subject to photochemical degradation. 18-MEA is primarily found bound to cuticle cells, whereas lipids in the cortex are typically other fatty acids and cholesterol or cholesterol sulfate.[25] Free fatty acids are also present around bound 18-MEA in the cuticle.

1.1.4 Melanin

As shown in Figure 1-1, melanin is present in some hair fibres as granules within cortex cells. There are two types of melanin: eumelanin and pheomelanin. The two differ in chemical structure and colour: eumelanin is black/brown whereas pheomelanin is red/pink.[26] The ratio of different melanins determines hair colour.

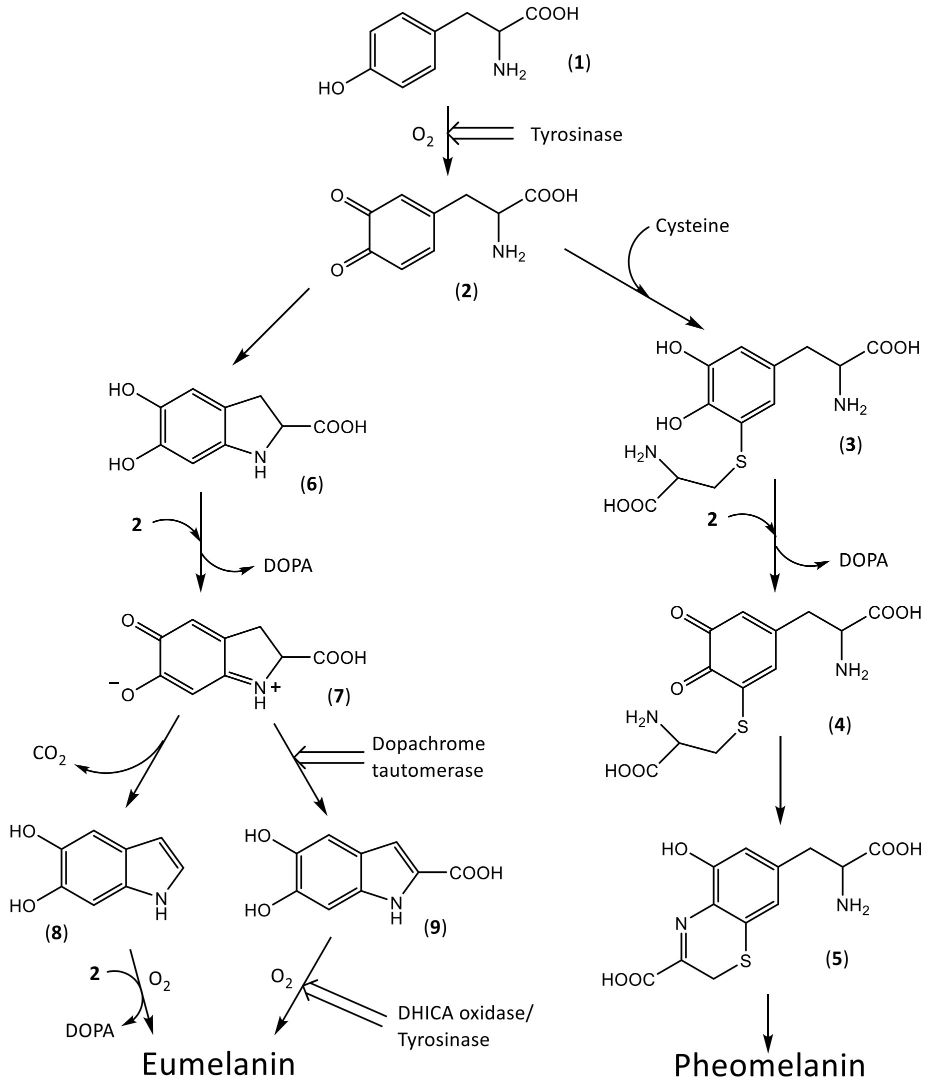

Scheme 1-1: Biosynthetic pathways for eumelanin and pheomelanin production

Melanin is a biopolymer, and the exact chemical structure varies for different melanin types, colours and location. Eumelanin consists of 5,6-dihydroxyindole (DHI) (**8**) and 5,6-dihydroxyindole-2-carboxylic acid (DHICA) (**9**) monomeric units (the ratio determines colour). In contrast, pheomelanin is constructed from 1,4-benzothiazine (**5**), outlined in Scheme 1-1.

Melanin is produced via a multi-step biosynthetic pathway, initiated with the oxidation of tyrosine (**1**) to dopaquinone (**2**) by the tyrosinase enzyme (Scheme 1-1). In eumelanin production, intramolecular addition of the amine group in dopaquinone leads to the formation of cyclodopa (**6**). This then undergoes a redox exchange process with dopaquinone, forming dopachrome (**7**), which rearranges to 5,6-dihydroxyindole (**8**) and 5,6-dihydroxyindole-2-carboxylic acid (**9**), the monomeric units of the eumelanin polymer.

Pheomelanin is produced through the addition of cysteine to dopaquinone, and the subsequent oxidation of the resulting cysteinyldopa (CD) (**3**) to a quinone (**4**). This cyclises to form a benzothiazine (**5**). Pheomelanin production is preferential when cysteine concentration in melanosomes is higher than 0.13 μM.[27] Because of this, melanin granules often contain a core of pheomelanin, surrounded by eumelanin.[28]

1.2 The Photochemistry of Amino Acids

Most amino acid residues do not show significant absorption of UV light at wavelengths >250 nm.[29] The atmosphere effectively absorbs harmful UVC radiation below 280 nm and the majority of UVB radiation (280-315 nm),[30] although evidence shows an increase in UVB reaching the surface due to depletion of the ozone layer.[31-32] This may change: recently reported evidence suggests a gradual healing of the Antarctic ozone layer in recent years.[33] However, small amounts of harmful UVB from sunlight has the potential to cause damage to proteins with prolonged and repeated exposure. Hair proteins are likely to be particularly susceptible due to their exposed location.

The only amino acids capable of direct photoexcitation by sunlight are those with significant absorption above 280 nm. This is limited to those with aromatic side chains (see Figure 1-3): tryptophan, tyrosine, phenylalanine and histidine (although phenylalanine and histidine do not absorb significantly at 280 nm).[29] Disulfides show negligible absorbance above 280 nm in most circumstances (see section 1.2.3). The absorption spectra of Phe, Tyr and Trp are shown in Figure 1-5.

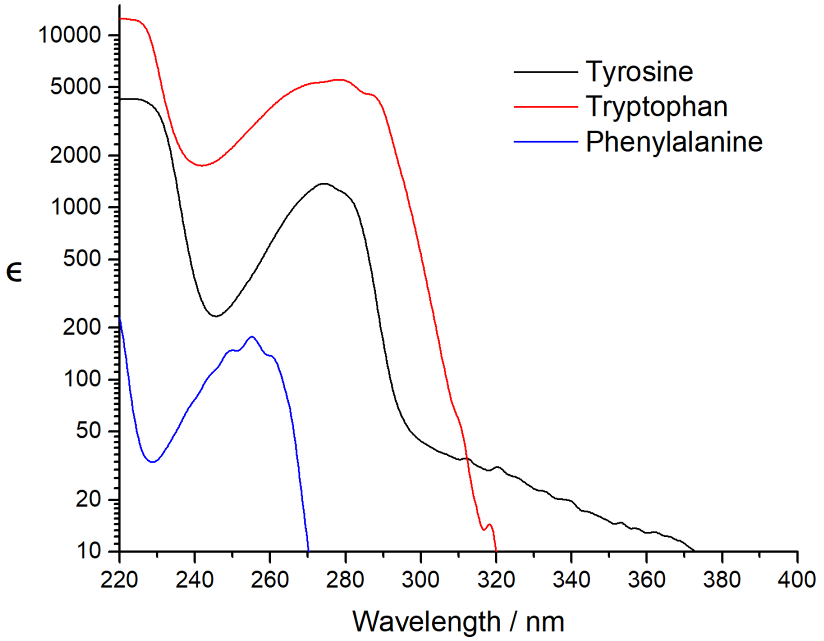

Figure 1-5: UV absorbance spectra of aromatic amino acid residues: Trp, Tyr and Phe. Data Source: [115]

Tryptophan is the most effective absorber UVB chromophore of the aromatic amino acids, based on the solution phase spectra in Figure 1-5. However, given that tyrosine has far greater abundance than tryptophan in many keratin proteins (see Table 1-1) and hair overall (see Table 1-2), it is likely that tyrosine photochemistry is relevant to the overall photochemistry of hair proteins. In addition to the aromatic amino acids, cystine photochemistry is also significant, particularly as disulfide bonds are a critical structural component of keratin proteins.

The photochemistry of chromophoric amino acids can be divided into two main categories: direct reactions through the absorption of UV light by the aromatic side chain; and secondary reactions through photochemically generated reactive oxygen species. This section focuses on direct processes, secondary reactions are discussed in section 1.5.

1.2.1 Tyrosine Photochemistry

In aqueous solution at neutral pH, tyrosine exhibits two absorption bands at wavelengths of around 220 nm and 275 nm. These are assigned to π-π* transitions.[35] Absorption bands are particularly sensitive to the ionisation state and interactions of the phenolic hydroxyl group: the phenolate ion shows a bathochromic shift in absorption bands to 240 nm and 290 nm. Intermolecular hydrogen bond interactions of the phenolic group within proteins result in a smaller (but significant) shift in the lower energy band to around 279 nm.[36] The ionisation state of the amine or carboxylate groups of the amino acid has little impact upon absorption bands.[37]

Upon absorption of a photon of sufficient energy for a π-π* transition on the aromatic side chain of tyrosine, the amino acid is excited to the first singlet excited state. This state is highly unstable, and can fluoresce, with λ_{em} = 303 nm in aqueous buffer,[38] or undergo intersystem crossing to a triplet state, with a longer lifetime of several microseconds.[39] Singlet oxygen can form from energy transfer between ground state oxygen and singlet excited tyrosine, although the quantum yield of this process is low.[45-46]

From both singlet and triplet excited states, energy transfer processes occur readily to tryptophan, with up to 69% efficiency, leading to the formation of the corresponding Trp excited states.[40-41] Perhaps because of this efficient energy transfer to tryptophan, the photochemistry of tyrosine itself is less well studied than tryptophan. However, many keratin proteins contain little or no tryptophan, making other reaction pathways of excited state tyrosine highly significant. These are summarised in Scheme 1-2.

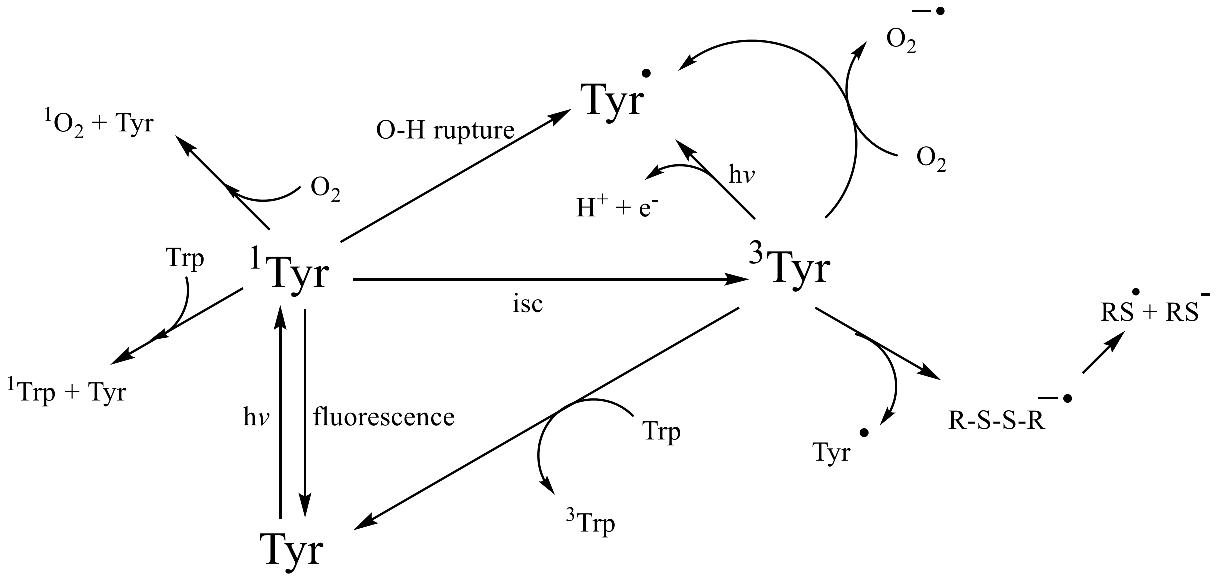

Scheme 1-2: Summary of the main reaction pathways of tyrosine upon photoexcitation

It should be noted for both Trp and Tyr photochemistry that the electron transfer is only effective at short distances. Singlet-singlet energy transfers in biopolymers typically show half-efficiency at distances of 20-30 Å, although values can be higher.[52] In contrast, triplet-triplet energy transfers can occur only over distances of 11-15 Å, with efficiency decreasing an order of magnitude for every 1.3 Å increase in distance.[53] This is likely to limit the transfer of excited state from tyrosine to tryptophan in keratin proteins, increasing the relative significance of tyrosine photochemistry compared to tryptophan.

Triplet state tyrosine can be quenched by electron transfer processes. Interaction with a disulfide can lead to the formation of a disulfide radical anion $RSSR^{\bullet -}$ (see Scheme 1-2).[42] This leads to the rupture of the disulfide and the formation of a sulfur-centred radical.[43]

A major species formed upon Tyr photoexcitation is the tyrosyl radical, $Tyr^{\bullet}$. This is most likely formed from the triplet state through the absorption of a second photon,[42] although some studies suggest the radical may also form from a singlet excited state via O-H bond rupture, driven by vibrational excitation.[44] In aerobic environments, ^3Tyr can also interact with oxygen, leading to tyrosyl radical and superoxide ($O_2^{-\bullet}$) formation. The production of reactive oxygen species greatly increases potential oxidative damage, this is discussed further in section 1.5. In the presence of oxygen, the rate of tyrosyl radical formation increases significantly, with ~2.2 times higher radical concentration observed by kinetic absorption spectrophotometry 1 µs after a 15 ns laser pulse compared to after 15 µs in an oxygen free sample.[42]

1.2.1.1 Reactions of tyrosyl radicals

Once formed, tyrosyl radicals can undergo a wide variety of reactions. Two radicals can combine through either C-C linkage or C-O linkage to form dityrosine, outlined in Scheme 1-3.[47] As tyrosyl radicals can form without oxygen, and dimerization does not require oxygen, dityrosine can form in anaerobic systems upon irradiation.

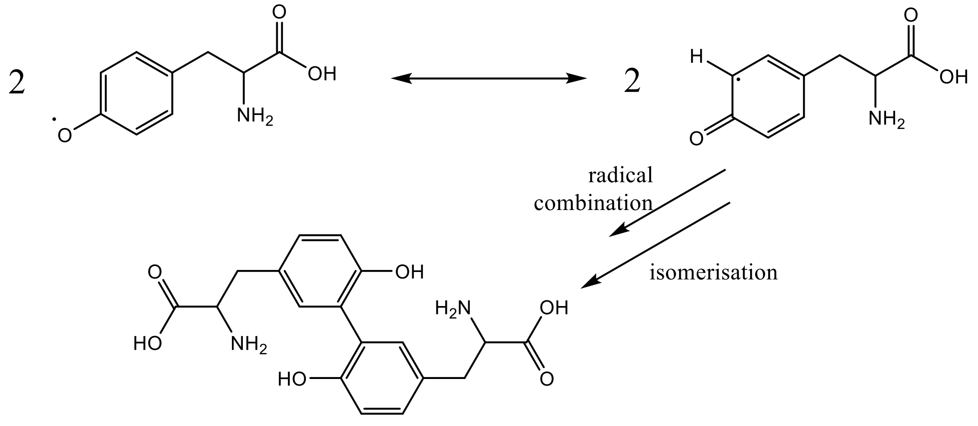

Scheme 1-3: Formation of dityrosine by combination of two tyrosyl radicals

In the presence of oxygen, the phenoxyl ring can be oxidised, yielding 3,4-dihydroxyphenylalanine (DOPA).[35] This can go on to form cyclodopa, a precursor to melanin formation (see Scheme 1-1). Prolonged irradiation of free tyrosine in solution leads to the formation of melanin.[48] Tyrosyl radicals can also abstract hydrogen from other molecules, transferring the radical centre and regenerating tyrosine. This transfer may occur with other tyrosine units, lipids such as linoleic acid as well as small organic molecules present in low concentrations in hair such as urate.[49,112] Photogenerated tyrosyl radical species therefore have a potential to cause far-reaching damage to proteins and lipids within hair fibres.

1.2.2 Tryptophan Photochemistry

The molar absorptivity of the indole side chain of tryptophan is significantly higher than tyrosine in the UVB region (see Figure 1-5). Despite this, a much lower abundance in hair proteins means that the overall significance of Trp photochemistry may be overshadowed by Tyr.

The photochemistry of tryptophan may be considered broadly similar to that of tyrosine outlined in Scheme 1-2. Upon direct absorption of UV energy, singlet excited Trp is formed, which can fluoresce (λ_{em} = 350 nm),[54] interact with oxygen to form singlet oxygen (although the process is inefficient),[45] and photoionize directly, yielding a radical cation which rapidly deprotonates to a neutral indolyl radical.[55] Unlike the opposite process, energy transfer from the excited states of Trp to Tyr does not readily occur except at extreme pH, due to the unfavourable energy levels of the excited states.[35] Trp triplet quenching by Tyr can occur through charge transfer via exciplex formation.[50] This requires a specific orientation of indole and phenol side chains, which limits applicability in restrictive proteins.

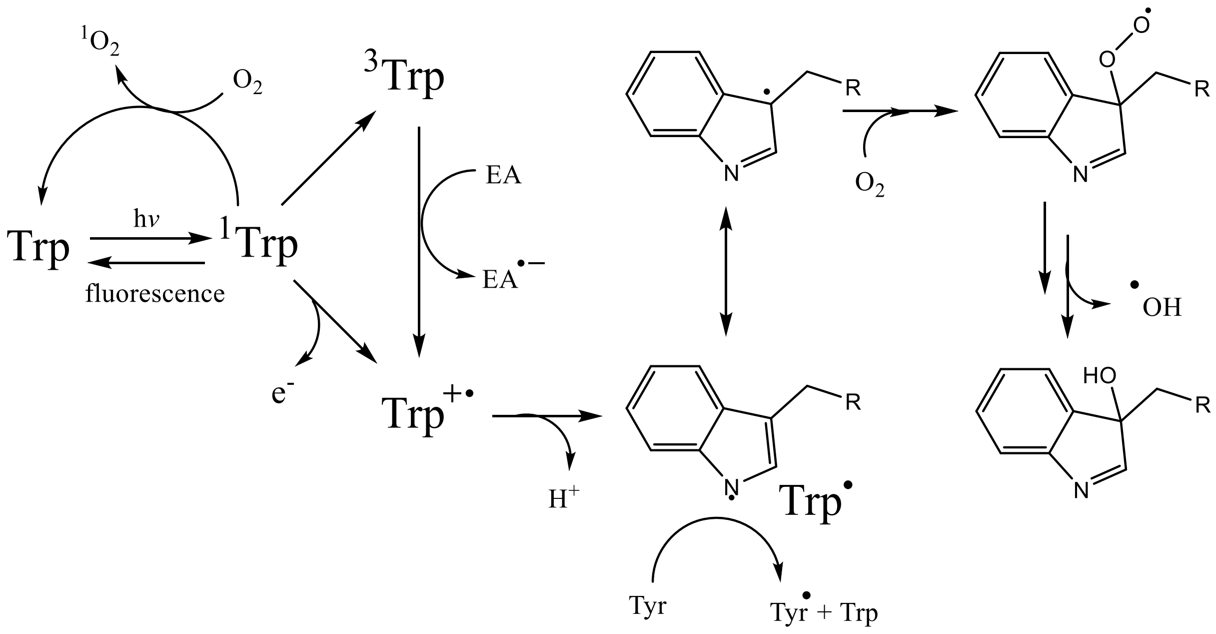

Scheme 1-4: Summary of the main reaction pathways of tryptophan upon photoexcitation. EA = general electron acceptor.

Triplet state Trp can interact with a wide range of electron accepting groups, including disulfides, leading to the production of a disulfide radical anion as observed with Tyr, and a Trp radical cation, which rapidly deprotonates to a neutral indolyl radical. Free amino acids also interact with singlet and triplet excited states of Trp via excited state electron transfer or excited state proton transfer, leading to tryptophan based radical formation.[51]

Tryptophan indolyl radicals can undergo electron transfer reactions with a range of substrates.[56] They can also abstract hydrogen from tyrosine, leading to the formation of tyrosyl radicals.[57] Oxygen can add to tryptophan based radicals, leading to the formation of a peroxyl radical (see Scheme 1-4).[58] This can abstract hydrogen, forming a hydroperoxide, which can break up by light or Fenton chemistry, ultimately producing hydroxyl radicals and hydroxy-tryptophan. The formation of reactive oxygen species such as hydroxyl radicals, singlet oxygen and superoxide opens a wide range of other reaction pathways, discussed in section 1.5.

1.2.3 The photochemistry of disulfides

Compared to Tyr and Trp, the disulfide cystine does not exhibit significant absorbance above 240 nm. The molar absorptivity of Tyr and Trp at 290 nm is 100 M^{-1} cm^{-1} and 2500 M^{-1} cm^{-1} respectively, compared to 40 M^{-1} cm^{-1} for cystine.[59] These figures are strongly dependent upon the polypeptide structure: disulfide bonds between nearby amino acids in a chain creates ring structures which can significantly red-shift absorption bands.[60] As outlined in Table 1-1, keratin proteins exhibit very high levels of cysteine (and consequently cystine). Direct photolysis of disulfides may therefore be a significant degradation pathway in keratin. This is in addition to energy transfer processes from excited state Tyr/Trp (see sections 1.2.1-1.2.2) and interactions with reactive oxygen species (see section 1.5).

Direct photoexcitation of cystine leads to a singlet state which undergoes homolytic cleavage. The identity of the primary products of this reaction is the subject of some controversy, with uncertainty over whether S-S (Scheme 1-5) or R-S (Scheme 1-6) cleavage dominates.[58-59] There is evidence for both processes occurring, as well as further reactions such as the addition of $RS^{\bullet}$ to another cystine moiety, giving $[RS - (SR) - SR]^{\bullet}$.[61] These reactions also occur upon energy transfer from excited Tyr/Trp.

$$R - S - S - R \xrightarrow{h\nu} RS^{\cdot} + {}^{\cdot}\mathrm{SR} \qquad \text{(Scheme 1-5)}$$

$$R - S - S - R \xrightarrow{h\nu} R^{\cdot} + {}^{\cdot}\mathrm{SSR} \qquad \text{(Scheme 1-6)}$$

The radical pairs formed by homolytic cleavage are likely to rapidly recombine, especially in a restricted protein environment which limits diffusion and the potential to interact with other species. However, the photochemistry can be more complex: studies with model peptides show a complex rearrangement resulting in thioether and H_2S formation.[62] In addition to this, thiyl radicals ($RS^{\bullet}$) can interact readily with oxygen, leading to peroxyl radical formation. Both peroxyl radicals and thiyl radicals can abstract hydrogen from neighbouring amino acids, particularly alanine and glycine, in a reversible reaction which leads to the formation of a carbon-centred radical (see Scheme 1-7).[63]

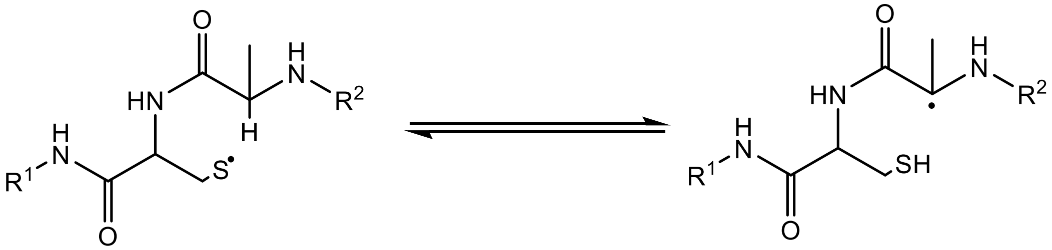

Scheme 1-7: Hydrogen abstraction by cysteine thiyl radical, creating a carbon centred radical on neighbouring alanine residue.

This reaction is of particular relevance to keratin proteins as they contain a large number of Cys-Ala/Gly pairs.[20] The creation of a carbon centred radical on the α-carbon of Gly/Ala can lead to polypeptide cleavage upon interaction with oxygen (see Scheme 1-17).[64]

1.3 Lipid Photochemistry

The photochemistry of lipids present within hair fibres can be split into two main areas: damage to the thioester linkages which bind lipids to cells (see Figure 1-4); and peroxidation of unsaturated fatty acid chains.

Upon irradiation, thioesters undergo homolytic cleavage, resulting in the formation of thiyl and acyl radical species.[65] These readily form peroxyl radicals upon interaction with oxygen, which further react, eventually leading to the formation of sulfonic acid on membrane surfaces and the loss of fatty acids from the cell membrane complex (Scheme 1-8). The wavelength of light required to cleave 18-MEA thioester linkages is unclear. Literature reports show activity in the UVA region, at 365nm,[65] however the study uses model thioesters with aromatic substituents, which may affect photochemical properties. Studies upon hair fibres have shown significant loss (36% over 30 cm length) in MEA from root to tip as hair ages,[66] as well as an increase in sulfonic acid in older hair further from the root.[67]

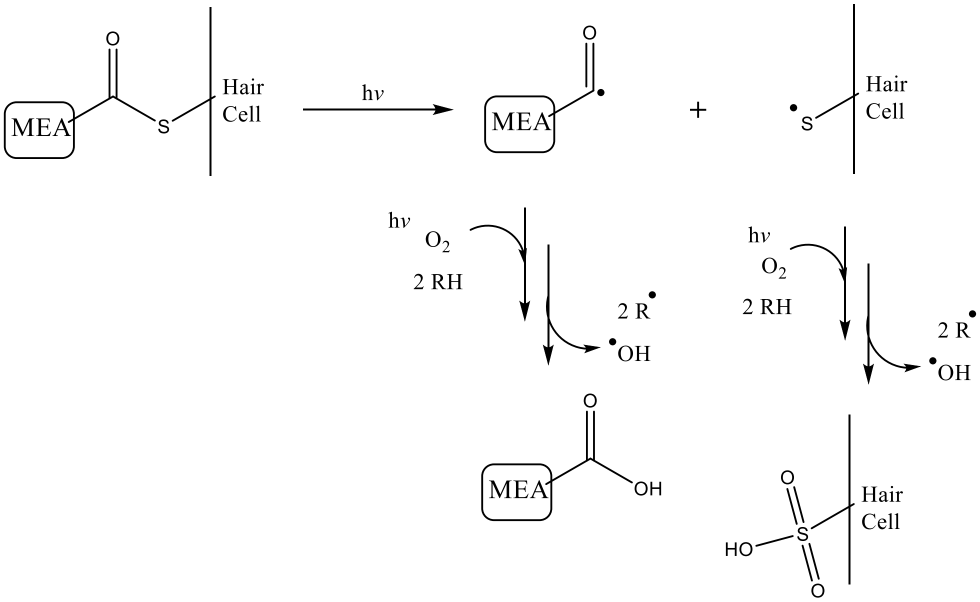

Scheme 1-8: Photochemical cleavage of thioester bonds in cell membrane complex, leading to the loss of covalently bound lipids

Non-covalently bound lipids in hair fibres, such as free unsaturated fatty acids and cholesterol, are also degraded upon exposure to sunlight. Levels of cholesterol and fatty acids drop by 59%

and 47% respectively in blonde hair upon extended (1000 hours) exposure to simulated sunlight.[68] The decrease in darker coloured hair is less significant, due to the photoprotective influence of melanin. A corresponding increase in lipid peroxide degradation products present within hair is also observed.[69]

Lipid peroxidation can occur either via a radical mechanism or through interaction with singlet oxygen. Both require an additional photosensitiser, such as tyrosine or tryptophan in proteins. Singlet oxygen can be produced from photoexcited Tyr/Trp (see Schemes 1-2/1-4), and stable lipid-centred radicals ($L^\bullet$) can be formed on polyunsaturated fatty acids via radical transfer from protein-based radicals.[70] This process is less efficient for monounsaturated fatty acids, which make up most free lipids in hair fibres. The singlet oxygen pathway is therefore more relevant to hair lipids. Both the radical mechanism and singlet oxygen lead to the formation of lipid hydroperoxides, outlined in Scheme 1-9. This initiates an autoxidative cycle, eventually leading to the production of reactive aldehydes and other degradation products.[71]

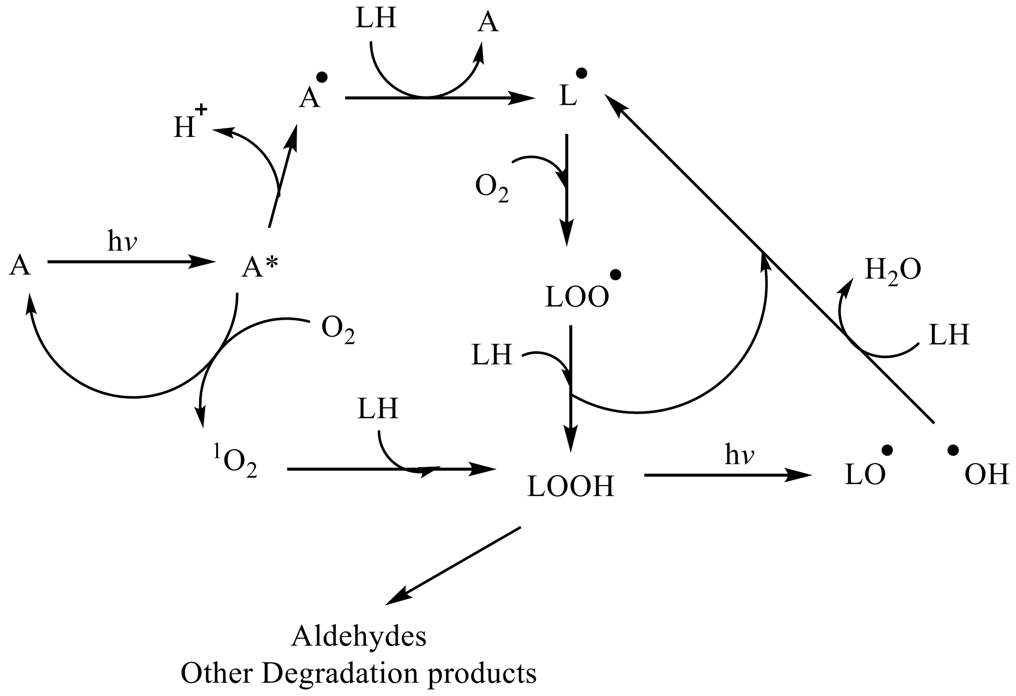

Scheme 1-9: Lipid peroxidation reactions, where L refers to a general lipid, and A is a sensitiser (such as Tyr or Trp on a nearby keratin protein)

1.4 Melanin Photochemistry

Melanin pigments exhibit broadband absorbance over the entire UV and visible spectral range.[72] This property is ascribed to the different HOMO-LUMO energy gaps of the DHI, DHICA and CD units which make up eumelanin and pheomelanin polymers,[73] which cause overlapping absorption from a wide range of different oligomeric molecules. Excitation of these oligomers leads to intramolecular proton transfer. Decay of the excited state is more rapid in DHICA rich oligomers, which are consequently more effective at dissipating UV energy as heat.[74]

The photoprotective effect of melanin is evident from a wealth of evidence showing lower damage in highly pigmented skin and hair.[75] The large polymer structure and aggregation of melanin into granules helps prevent photoionisation and the formation of reactive oxygen species.[76-77] As such, eumelanin dissipates the majority of UV-vis radiation, less than 0.05% of absorbed light is emitted radiatively.[78]

Both eumelanin and pheomelanin contain intrinsic, stable radical species. In the case of eumelanin, this is attributed to semiquinone radicals in a redox equilibrium with non-radical quinone/hydroquinone species (Scheme 1-10).[80] Pheomelanin based radicals likely arise from benzothiole radicals (Figure 1-6).[79]

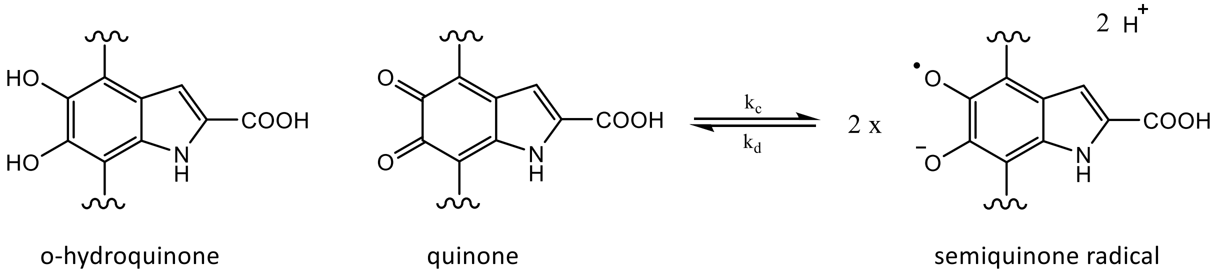

Scheme 1-10: Redox equilibrium between hydroquinone/quinone and semiquinone radical forms within eumelanin

Upon UV exposure, the concentrations of radical species in melanin increase significantly by EPR analysis. Arnaud et al attribute this increase in solid eumelanin samples to the formation of several distinct radical components: neutral and deprotonated forms of the semiquinone radical, and indolyl radicals, shown in (Figure 1-6). Indolyl radicals can form directly by excitation of the indole. In addition to this, short-lived species produced by electron hole pair formation in the semi-organised melanin structure were identified.[81]

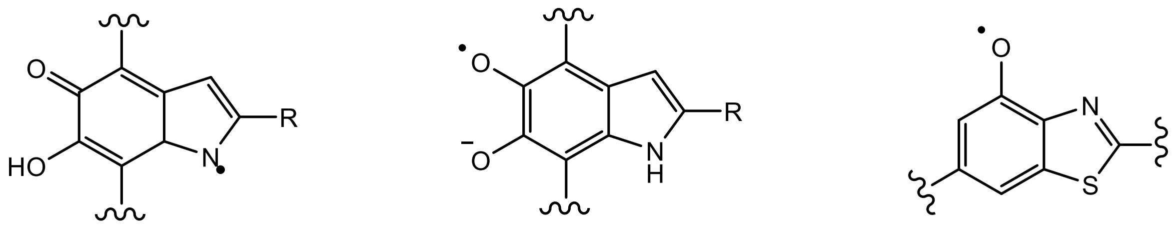

indolyl radical semiquinone radical benzothiazole radical

Figure 1-6: Deprotonated forms of indolyl and semiquinone radicals within eumelanin pigments, and benzothiazole radicals in pheomelanin. R = H (DHI) or COOH (DHICA).

Both semiquinone and indolyl radicals can relatively easily undergo disproportionation reactions (reverse reaction in Scheme 1-10 for semiquinone radicals, Scheme 1-11 for indolyl radicals), leading to the formation of non-radical hydroquinone/quinone species. Degradation of semiquinone radicals is relatively slow in a solid matrix: the neutral form has a half-life of around 6 hours, whilst the anionic form is more stable.[81]

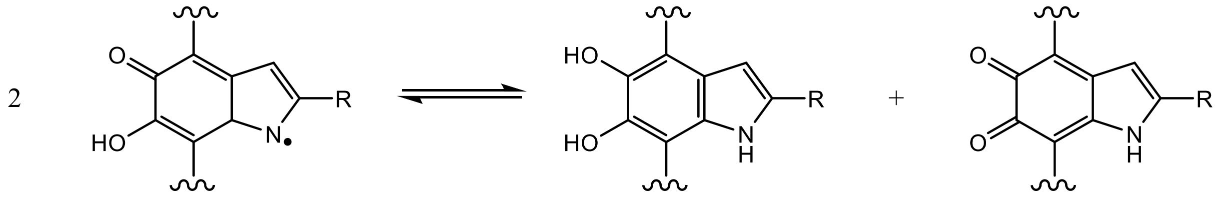

indolyl radical

DHI (R=H)
DHICA (R=COOH)

indolequinone

Scheme 1-11: Disproportionation equilibrium for indolyl radical species

The ability of melanin to regulate excited states caused by UV through intramolecular disproportionation mechanisms is a key feature in its photoprotective activity. However, radicals within melanin can also decay via other pathways, such as interaction with oxygen leading to the formation of superoxide and other reactive oxygen species.[72]

Pheomelanin is much less effective at dissipating excitation within the macromolecular structure: the heterocyclic benzothiazine and benzothiazole structures do not enable semiquinone formation.[72] This prevents the disproportionation mechanism possible in eumelanin. Radicals in pheomelanin are therefore more prone to degrade through interaction with oxygen, leading to superoxide production. When irradiated with sunlight, pheomelanin produces 100 times more superoxide than eumelanin.[79] Whilst eumelanin is considered to have a photoprotective effect (particularly when high in DHICA), pheomelanin is pro-oxidative.[82]

The pheomelanin core/eumelanin shell structure of melanin granules (see section 1.1.4), along with the DHICA/DHI ratio in the eumelanin shell therefore determine the overall influence of melanin upon oxidative stress in hair. Initially, the eumelanin shell of granules would offer a photoprotective effect,[83] however upon prolonged exposure, eumelanin is degraded through decarboxylation of DHICA to DHI, and the pro-oxidative influence of the pheomelanin core becomes more dominant.[84] Hair of different colours will therefore respond differently to sunlight: red hair (with high pheomelanin content) will be more susceptible to pro-oxidative melanin sensitised photodamage than hair with high eumelanin/low pheomelanin levels.

1.5 Reactive Oxygen Species

So far, the direct photochemistry of the key components of hair has been discussed. It is clear in reviewing literature that these direct interactions form only part of the story. Direct photochemistry in proteins, lipids and melanin leads to the production of reactive oxygen species (ROS) which are capable of further, far-reaching oxidative damage. The main ROS relevant to hair photochemistry are singlet oxygen ($^1O_2$), superoxide radical anion ($O_2^{-\bullet}$) and hydroxyl radicals ($^\bullet OH$). Autoxidative processes are outlined for lipid chemistry in Scheme 1-9. This section will focus upon reactions between ROS and amino acids and proteins.

1.5.1 Damage to amino acid side chains

1.5.1.1 Hydroxyl radicals

Different reactive oxygen species interact differently with amino acid side chains. The most common reaction of hydroxyl radicals is to abstract hydrogen from a side chain (Scheme 1-12), leading to the formation of an amino acid centred radical.[85] Hydroxyl radical attack shows selectivity towards certain amino acid residues, notably aromatic and sulfur containing residues.[86] Attack on sulfur containing side chains can lead to the formation of sulfoxides and new disulfide bonds, critically changing the tertiary structure of the protein. Biological systems often contain reductase enzymes capable of reversing these changes: the only known example of a reversible oxidative protein modification.[64] However, these enzymes are not active in hair fibres.

$$RH + {}^{\cdot}\mathrm{OH} \rightarrow {}^{\cdot}\mathrm{R} + H_2O \qquad \text{(Scheme 1-12)}$$

1.5.1.2 Superoxide

In contrast to singlet oxygen and hydroxyl radicals, superoxide is relatively unreactive towards amino acid side chains.[87] However, superoxide can act both as a reducing and oxidising agent, and two superoxide molecules dismute readily to form hydrogen peroxide (Scheme 1-13).[88] This can then be split photochemically (Scheme 1-14) or via Fenton Chemistry (see section 1.6), yielding hydroxyl radicals.

$$2\,O_2^{-\cdot} + 2\,H^+ \rightarrow \mathrm{HOOH} + O_2 \qquad \text{(Scheme 1-13)}$$

$$HOOH \overset{h\nu}{\rightarrow} 2\,{}^{\cdot}\mathrm{OH} \qquad \text{(Scheme 1-14)}$$

1.5.1.3 Singlet oxygen

Singlet oxygen is a highly reactive species generated by photosensitisers in proteins and other molecules interacting with ground state oxygen. Due to a limited lifetime and diffusion capability (<70 nm in biological systems),[89] singlet oxygen generated within proteins is likely to target amino acid residues near where it is formed.

Amino acid side chains can either react chemically or physically quench singlet oxygen. Physical quenching involves energy transfer and dissipation of excited state energy. Within protein structures, only tryptophan and histidine side chains show a significant rate of quenching compared to chemical reaction.[90]

Certain side chains show higher selectivity for singlet oxygen, with only His, Tyr, Trp, Met and Cys reacting rapidly at neutral pH.[91] As cysteine residues are typically involved in forming disulfide bonds, the effect of singlet oxygen upon Cys is discussed with reference to damage to protein structure in section 1.5.2.

Tyrosine and tryptophan side chains readily interact with singlet oxygen, leading to the formation of endoperoxides and hydroperoxides. In the case of tyrosine, this can eventually lead to cyclised products through nucleophilic addition of the deprotonated amine group, (Scheme 1-15). In polypeptides and proteins this is less likely, as substituted amines are much less efficient nucleophiles for the ring closing reaction.[92] However, other nucleophiles (such as neighbouring nucleophilic amino acids Lys, Arg, Cys) may attack, leading to cross-linking within the protein structure.[58]

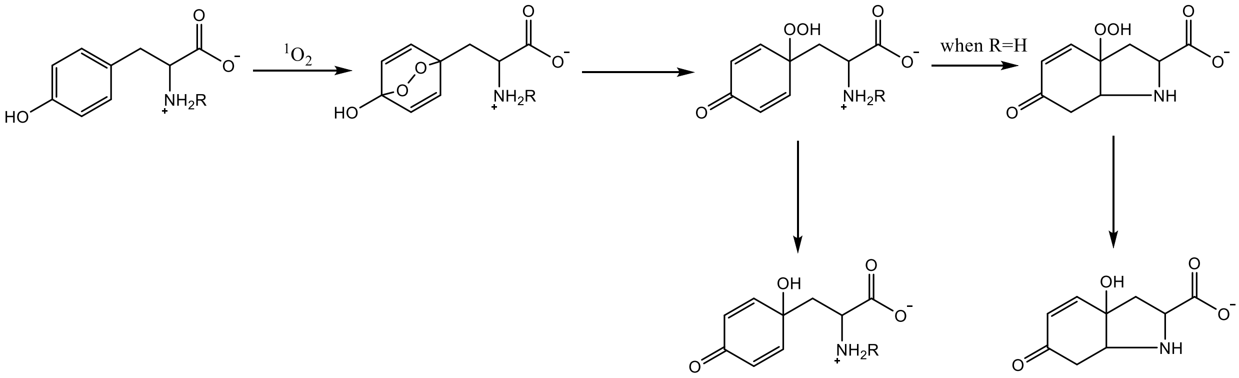

Scheme 1-15: The reaction of singlet oxygen with tyrosine side chain

Tryptophan reacts with singlet oxygen in a similar manner as tyrosine, leading to the formation of a dioxetane intermediate which decomposes to N-formylkynurenine, with further hydrolysis yielding kynurenine (Scheme 1-16).[93] Kynurenine is a characteristic biomarker for tryptophan oxidation in proteins. It is also a stronger chromophore and sensitizer for singlet oxygen production compared to tryptophan, meaning that tryptophan oxidation with singlet oxygen can accelerate oxidative damage.[94]

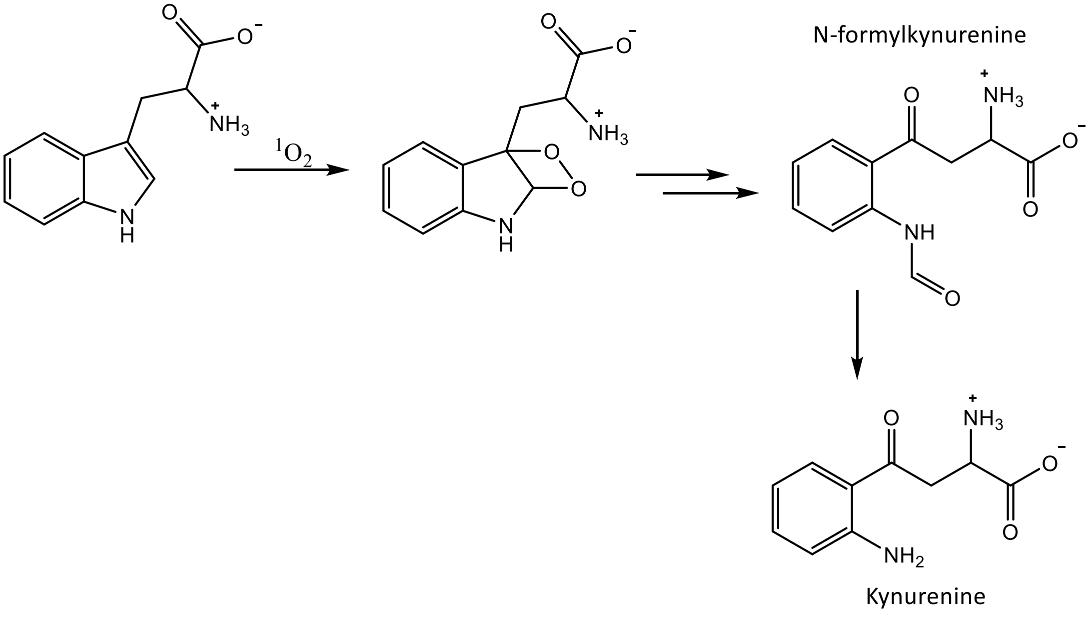

Scheme 1-16: Simplified reaction scheme showing the formation of kynurenine from tryptophan upon reaction with singlet oxygen.

1.5.2 Damage to protein structure

In addition to causing damage to amino acid residues within a protein, reactive oxygen species can damage overall protein structure through the breaking of polypeptide and disulfide bonds.

Oxidative cleavage of peptide bonds (Scheme 1-17) is one of the most damaging reactions mediated by hydroxyl radicals, as it leads to a permanent structural change in the protein. The first step involves hydrogen abstraction by a hydroxyl radical from the α-carbon, creating a carbon centred radical. In the absence of oxygen, this can interact with another carbon centred radical, forming a cross-link between two polypeptide chains.[64]

The carbon-centred radical can then interact with oxygen, resulting in peroxyl radical formation. This initiates an autoxidative cycle similar to lipids (see Scheme 1-9), whereby the peroxyl radical can abstract hydrogen from other α-carbons, propagating the reaction along a peptide chain. Peroxyl radicals can undergo an elimination reaction, yielding an imine which can then hydrolyse, breaking the peptide (see Scheme 1-17).[113] Hydroperoxyl radicals are reduced to alkoxyl radicals by superoxide, and then break down to yield a carbonyl radical.[64,95] Fragmentation of the peptide can also occur via carbon-centred radical formation on glutamic acid, aspartic acid and proline side chains.[95]

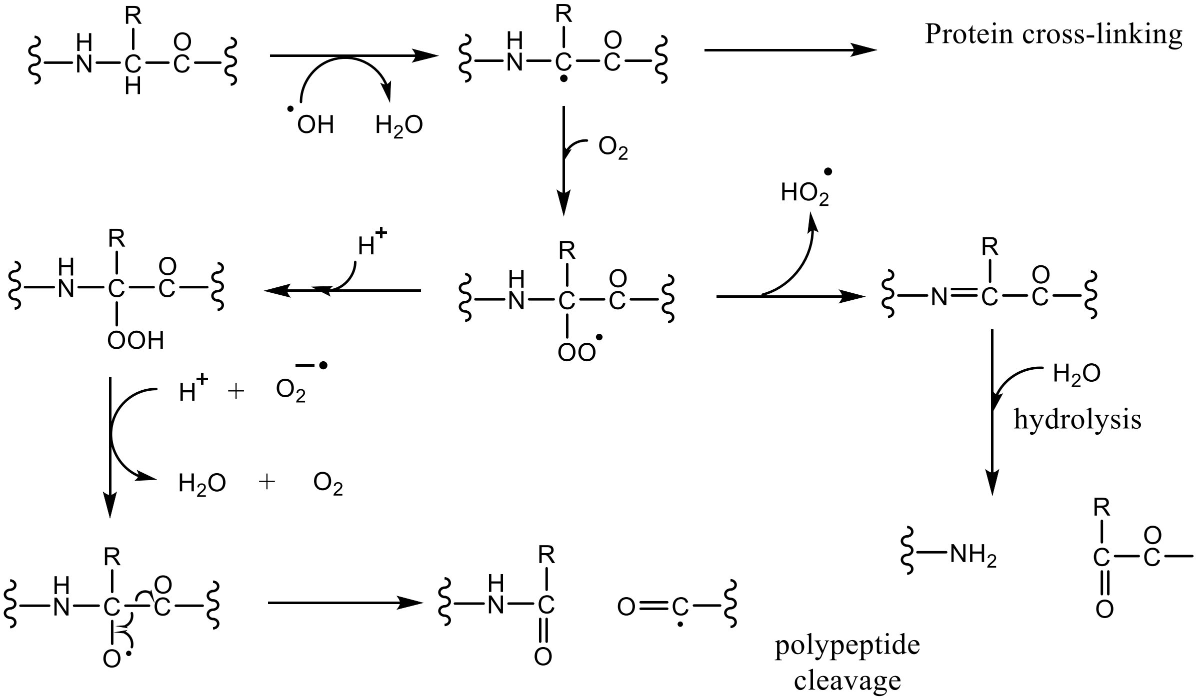

Scheme 1-17: Oxidative cleavage of protein backbone through interaction with hydroxyl radicals and superoxide

Disulfide bonds, critical to the structure of keratin proteins, are susceptible to attack from a wide range of oxidising agents, including hydrogen peroxide, superoxide and singlet oxygen. Mechanisms for ROS attack on disulfides are not well understood. However, several radical intermediates have been detected: disulfide radical cations,[96] disulfide radical anions,[97] perthiyl (R-SS$^\bullet$), thiylperoxyl (R-S-OO$^\bullet$), sulfinyl (R-S$^\bullet$=O), sulfonyl (R-S$^\bullet$O$_2$) and thiyl (R-S$^\bullet$) radicals.[98] Highly reactive sulfenium (R-S$^+$) and thiosulfenium (R-SS$^+$) cations are also formed.[99] End oxidation products are generally sulfonic acids or Bunte salts.[67] The reactions of hydroxyl radicals and superoxide upon disulfides are summarised in Scheme 1-18.

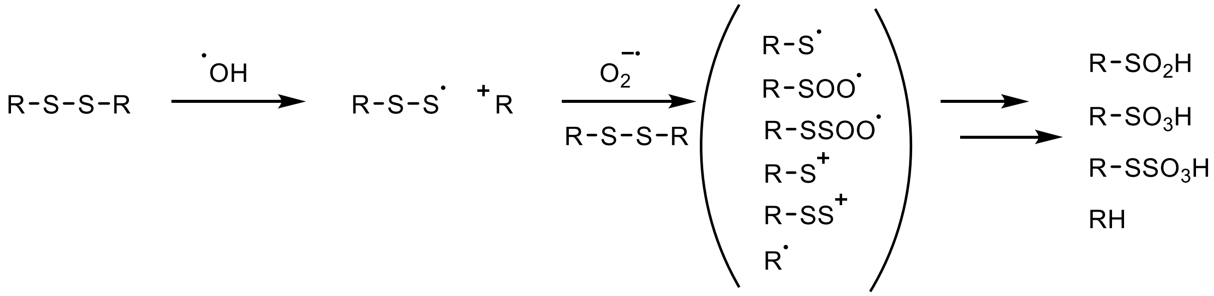

Scheme 1-18: Simplified reaction scheme showing possible intermediates and products upon disulfide interaction with hydroxyl and superoxide radicals

Singlet oxygen can also interact with disulfides. Initially, this leads to the formation of disulfide monoxide and dioxide species, as outlined in Scheme 1-19, which then decay through interaction with superoxide to sulfinic and sulfonic acids.[100]

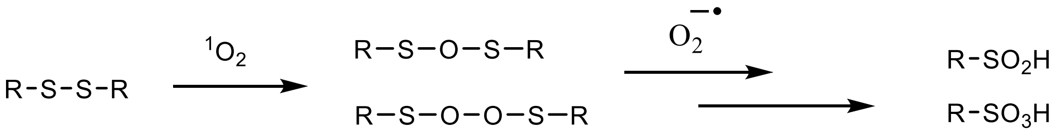

Scheme 1-19: Simplified reaction scheme showing intermediates and products upon disulfide interaction with singlet oxygen and superoxide radicals

The wide range of oxidative reactions possible with disulfides means that it is likely different reactions occur in different areas of a protein, depending on oxygen availability, nearby ROS sensitisers, and mobility. However, all degradation pathways ultimately lead to the breakdown of disulfide bonds and the formation of sulfonic acids, which will significantly change protein structure and chemical properties.

1.6 Transition Metals

Metals are present in hair fibres from both endogenous and exogenous sources. These include alkali and alkaline earth metals such as calcium and magnesium, transition metals (iron, copper and zinc) and low levels of heavy metals such as lead.[101] Exogenous sources include water supply used for washing, as well as air pollutants. Levels of exogenous metals therefore vary significantly depending on environment. Endogenous metals typically derive from enzyme decomposition within the follicles.

Of particular interest are transition metals capable of participating in redox chemistry, Fe and Cu. Synchrotron XRF images of hair fibres indicate that Fe is primarily present in outer cuticle regions of hair fibres (although some is detected deeper within the fibre), suggestive of exogenous build-up.[101] In contrast, Cu is more uniformly spread throughout the fibre, indicative of an endogenous source. The overall levels of iron in hair fibres are typically around 30-60 ppm, whilst copper levels can be as high as 200 ppm.[13,105]

Both Cu(II) and Fe(III) are known to bind to hydroxyl and amine groups in melanin,[114] however the complexation of these metals within hair proteins is uncertain. Fe(II), Fe(III) and Cu(I), Cu(II) ions may bind through metal-sulfur interaction with cysteine and methionine, interaction with alcohols and amine groups or the carboxylate groups of aspartic and glutamic acid.[102-103] EPR studies have indicated that Cu(II) binds to oxygen and nitrogen in hair proteins in a square planar or tetragonal arrangement,[104] however no comparable information is available for iron.

1.6.1 Transition metal catalysed ROS production

Fe(II) and Fe(III) can break down peroxides by Fenton chemistry, yielding radical species and similarly reactive hypervalent iron intermediates.[106] Hydrogen peroxide can be formed from superoxide (Scheme 1-13), and other organic peroxides and hydroperoxides are readily formed in the photochemical reactions described in this chapter. Iron within proteins could therefore accelerate hydroxyl radical production through Fenton chemistry, as outlined in Scheme 1-20. Copper can also catalyse ROS production with a Fenton-like mechanism.[107]

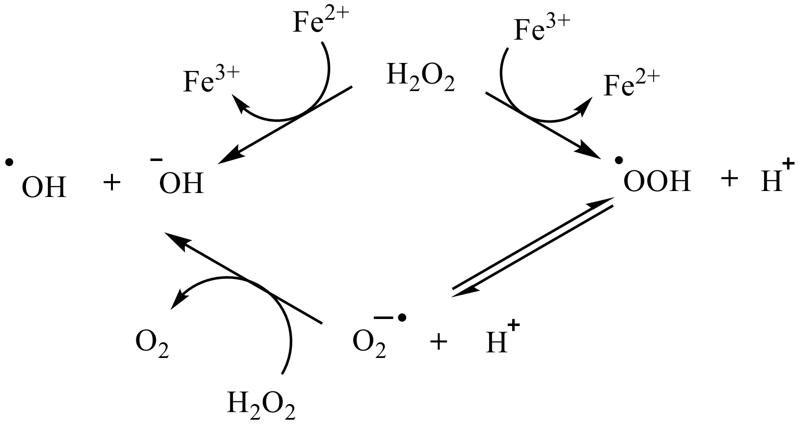

Scheme 1-20: Fenton chemistry mechanism: iron catalysed breakdown of hydrogen peroxide, generating superoxide and hydroxyl radical species

1.6.2 Possible involvement of transition metals in photochemical processes

In addition to facilitating the production of reactive oxygen species, redox active transition metals may directly influence photochemical processes. As described in section 1.6.1, metals can cause the breakdown of hydroperoxides such as those formed on Tyr, Trp (see Scheme 1-15), lipids (Scheme 1-9) and the polypeptide backbone (Scheme 1-17). This will yield an alkoxyl radical and hydroxide ion, as shown in Scheme 1-21.

$$\mathrm{ROOH} + \mathrm{Fe}^{2+} \longrightarrow {}^{\cdot}\mathrm{OR} + {}^{-}\mathrm{OH} + \mathrm{Fe}^{3+} \qquad \text{(Scheme 1-21)}$$

Metal complexes may act as photosensitisers for protein photochemistry: direct absorption by tyrosine and tryptophan requires high energy UVB light, however iron(III) complexes may absorb more abundant visible light and then transfer excitation energy to amino acids or oxygen (leading to ROS production).[108-109]

Iron complexes bound at a specific location within a polypeptide or protein can induce site-specific oxidative cleavage of the peptide chain, on the same or a neighbouring polypeptide within 17 Å of the metal binding site.[110] This is thought to be due to metal catalysed hydroxyl radical production leading to oxidative cleavage (Scheme 1-17), and consequently shows selectivity for cleavage at certain amino acid residues (where the metal preferentially binds).

Transition metals can also have a photoprotective effect, through the quenching of excited states. Iron(III) and Cu(II) both quench tyrosine fluorescence, through either a dynamic mechanism (collisional energy transfer) or static quenching (changing photo-physical properties of the amino acid through complex formation).[111] Fe and Cu can also undergo redox chemistry with radical species, leading to radical quenching. An increase in quenching rate will decrease excited state lifetime, and consequently the quantum yields of radical species and oxidation products.

Project Outline and Aims

The photochemistry of hair fibres reviewed in this chapter is very complex, with many components interacting with sunlight, leading to the formation of a range of products through many intermediates and reactive species. Generally, mechanisms are reasonably well understood, allowing theoretical prediction of how transition metals might influence reactions. However, given the complexity of the system: the range of different reactions, and different pathways available depending on specific conditions within the protein environment, the impact of transition metals is unlikely to be straightforward.

This project aims to probe the effects of the common transition metals (iron and copper) present in hair fibre upon the photochemistry of keratin proteins, the key structural component of hair. A quantitative assessment of how the metals influence degradation processes is needed, as well as improved mechanistic understanding.

To achieve this, it will be necessary to develop a simplified model system to study individual photo-active components of hair proteins. Chapter 2 discusses the development of a model system for the investigation of tyrosine photochemistry. Important considerations are the ability to monitor photodegradation within the system, as well as the ability to control metal and other additives.

Many chemical and photochemical reactions are highly dependent upon the chemical and physical environment. In developing a model system, a reasonable mimic of the environment expected within hair proteins is needed, although this is difficult to quantify. Some understanding of how model systems compare to real proteins is needed. Chapter 3 focusses on characterising model systems by physical and chemical environment, making use of EPR spin labelling techniques, and drawing comparisons to protein environments. This includes a separate study on how physical micellar and gel environments affect the photochemical reactivity of tyrosine, possible due to the unique properties of the model system.

As well as modelling the environment of amino acids within proteins, the chemical environment of transition metals tested must be considered. As the exact nature of metals in hair is unclear, this presents a challenge. Chapter 4 examines a variety of different iron (III) and copper (II) complexes at different concentrations. In addition to quantitative data on how metals influence degradation, the chapter probes different possible mechanisms of action by looking at the impact of antioxidants, localised metal centres and wavelength filters. The chapter aims to determine if metals can significantly influence protein degradation at realistic concentrations.

Chapter 5 aims to relate the findings from model systems to a real hair environment, by examining radical formation and destruction within keratin proteins. Environmental conditions are also considered, by investigating the impact of humidity upon reaction rates, and the role of oxygen is also probed.

2. Development of simplified model system

Many components within hair fibres can undergo chemical changes upon exposure to sunlight. The photochemical processes in proteins, lipids and pigments make the overall photochemistry of hair fibres complex. Manipulating hair proteins, for example adding metal ions to investigate the effect upon photochemical processes, is not straightforward without potentially damaging the protein. Studying keratin photochemistry *in situ* is therefore not straightforward.

To enable a thorough investigation into the role of transition metal ions in keratin photochemical processes, a simplified model system is needed. Only two amino acids, tyrosine and tryptophan, significantly absorb the highest energy UVB wavelengths of sunlight, with maxima at 276 nm and 280 nm respectively (see Figure 1-5).[116] Tyrosine has much higher abundance in keratin proteins (up to 22%) compared to tryptophan (< 1%) (see Table 1-1).[117] Model systems will study the photochemistry of tyrosine, as this is likely to be a reasonable reflection of the overall photochemistry of keratin.

A model system needs to allow for the controlled addition of transition metals and antioxidants. As well as being simple and easy to manipulate, the system needs to maintain a degree of realism in the context of tyrosine in hair proteins. The environment of tyrosine in the model system must be characterised and be a close mimic to tyrosine in hair proteins, as far as possible.

The aims of this chapter are therefore:

- To test a range of different simple Tyr containing keratin model systems by carrying out photochemical experiments looking at the UV response of the amino acid.
- Develop an understanding of the behaviour of tyrosine and its photo-induced radical species in different environments.
- Compare and assess different model systems in relation to the key criteria of simplicity, tuneability and realism, and decide upon an appropriate system for further study.

2.1 Modelling tyrosine environment

Keratin proteins are primarily formed of tightly wrapped helical structures (see section 1.1.1). Given the relative hydrophobicity of tyrosine compared to other amino acids at neutral pH, tyrosine is often present buried within hydrophobic pockets in proteins.[118] Tyrosine units are also present towards the head and tail ends of the protein,[119] in less tightly wrapped globular structures which form linkages with other keratin chains (see Figure 1-2).[120] This presents a range of distinct tyrosine physical environments within keratin, a challenge to accurately model.

As a starting point for investigations, two physical extremes were modelled by using free tyrosine as a solid powder and in aqueous solution. The amino acid samples were irradiated and analysed by EPR spectroscopy. The aim of these initial studies was to observe and characterise photo-induced tyrosine radical species, and to compare how radical species behaved under such different physical conditions.

2.2 Probing the photochemistry of tyrosine in free solution

When photoexcited, tyrosine can fluoresce, decay by non-radiative pathways or undergo intersystem crossing to a triplet state.[121] This triplet state can participate in a range of further reactions, including absorbing a second photon, resulting in the expulsion of a solvated electron and the formation of a tyrosyl radical species.[42] Reactions from the triplet state can lead to the formation of a wide range of products, including dihydroxylphenylalanine (DOPA), fragmentation to other amino acids such as Asp, Gly, Ser, and Ala, and acetic acid.[122-123] Dimerised products are also formed. Section 1.2.1 describes tyrosine photochemistry in detail. The relative yields of these products depend upon oxygen availability, pH, irradiation wavelength and time.[35]

Given the complex photochemistry exhibited by tyrosine even in relatively simple systems, experimental design needs to provide a simple method of comparing overall photochemical degradation under different conditions (for example in the presence of transition metals). Product analysis is impractical given the wide range of potential degradation products, with small quantities making quantitative analysis challenging. Instead, work focused on the observation of intermediate species such as radicals. The identity, concentrations and UV response of radical species can then be compared between different systems.

2.2.1 Solubility limitations

Due to its zwitterionic character, shown in Figure 2-1, tyrosine exhibits relatively low solubility at neutral pH compared to other amino acids. This limits concentration at pH 7 to around 2.5 mmol dm^{-3}.[124] At these concentrations, it proved impossible to observe any radical species by EPR upon UV exposure.

L-Tyr **L-Tyr methyl ester**

Figure 2-1: Structures of L-Tyr and it's methyl ester at pH 7

Solubility was improved by using a methyl ester tyrosine derivative (Figure 2-1), removing the zwitterionic character. However, despite increasing Tyr concentration to 35 mmol dm^{-3}, still no EPR signal was observed. This was attributed to the very short tyrosyl radical lifetime, with a reported rate constant for radical decay of 8×10^8 dm^3 mol^{-1} s^{-1} in water at pH 7.[125] The higher concentration achieved using the esterified derivative did however allow Tyr degradation to be monitored by fluorometry. Results from tyrosine ester fluorometry experiments are compared with other model systems in section 3.8.2. Ideally, a range of techniques would be used to probe tyrosine reactivity, attempts to observe tyrosine radical signals by EPR was therefore continued.

Solubility can also be improved by manipulating pH. At more extreme pH conditions, the zwitterionic character of the amine and carboxylate groups are lost. The amine becomes deprotonated around pH 10 (literature $pK_a = 9.21$).[126] Above pH 10, the hydroxyl group of the phenolic side chain also deprotonates (literature $pK_a = 10.46$). Increasing pH also decreases the rate of phenoxyl radical recombination due to reduced H^+ concentration.[127] This will increase radical lifetime. EPR measurements were therefore carried out on aqueous tyrosine solutions at pH 10.

2.2.2 Observation of radical species in tyrosine solutions at high pH

A 20 mmol dm^{-3} solution of tyrosine in water adjusted to pH 10 with sodium hydroxide was prepared. Aqueous sample size in EPR is severely limited due to high dielectric loss (absorption of microwave energy by solvent). A flat cell was used to minimise sample volume in the cavity.

Aqueous sample was flowed through the flat cell to ensure constant replenishment of fresh sample upon irradiation (see section 7.3.1). Upon irradiation, a weak EPR signal was observed, the black spectrum in Figure 2-2. A 100W Hg arc lamp was used for all irradiation experiments, spectral details can be found in Appendix 4. The signal disappeared rapidly when UV irradiation ceased, accurate kinetic measurements of radical lifetime were not possible due to the weak signal intensity.

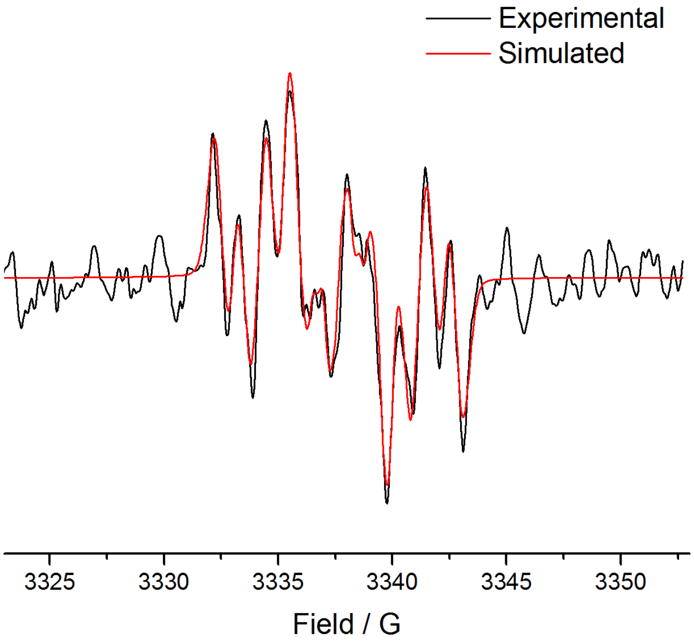

Figure 2-2: EPR spectrum observed upon irradiation of flowing 20 mM solution of tyrosine at pH 10. Red line shows simulated spectrum based on hyperfine values in Table 2-1

2.2.3 Identification of radical species present at high pH

The EPR spectrum shown in Figure 2-2 has a clearly defined hyperfine structure caused by interactions between the unpaired electron of the radical and nearby nuclei. The magnitudes of hyperfine splitting can be a signature of the identity of the radical.

The formation of tyrosyl radicals upon UV exposure is outlined in section 1.2.1. Cocivera et al propose that at high pH, tyrosyl radicals (**1**) hydroxylate to form dihydroxyphenylalanine (DOPA) semiquinone radicals (**3** and **4**) as shown in Scheme 2-1.[128] McCormick et al report hyperfine splitting values for the tyrosyl radical (**1**).[129] These are compared with literature values for semiquinone radicals **3** and **4** in Table 2-1.[128] Experimentally obtained hyperfine values were calculated by optimising a simulation (red line in Figure 2-2) based on literature hyperfine values for a combination of radical species **1**, **3** and **4**.

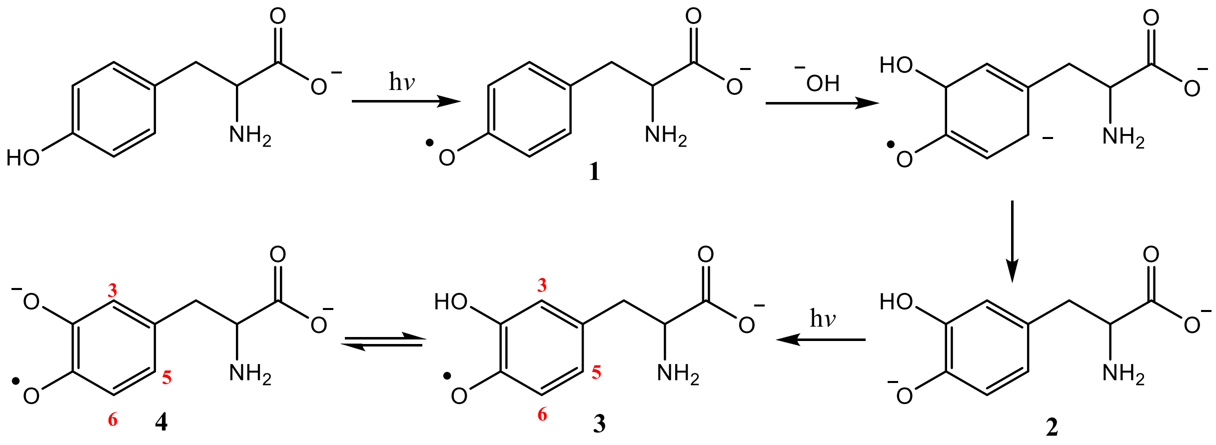

Scheme 2-1: Formation of semiquinone radicals upon UV exposure of tyrosine at high pH. Mechanism adapted from mechanism predicted by Cocivera et al [128] for photooxidation of phenol

Table 2-1: Comparison of observed and reported literature hyperfine values for acidic and deprotonated forms of DOPA radicals

Radical	**Observed hyperfine values**		**Literature hyperfine values**	
	Aromatic H	**β-H**	**Aromatic H**	**β-H**
Tyrosyl radical (**1**)	Not observed	Not observed	6.3, 1.6	15.0
Semiquinone Acid form (**3**)	3.37(5), 0.93(6), 0.32(3)	5.87	3.55(5), 1.12(6), 0.32(3)	5.30
Semiquinone base form (**4**)	1.59(5), 0.90(6), 0.32(3)	3.20	1.55(5), 0.91(6), 0.39(3)	3.70

The small differences compared to literature data could be attributed to variations in temperature, which influences molecular rotation. Hindered rotation on the EPR timescale significantly changes linewidths, and can therefore influence observed hyperfine values.[130] The low signal to noise ratio may also limit the accuracy of the optimised simulation.

Experimentally obtained data matched literature reported hyperfine values for semiquinone radicals **3** and **4** with minimal optimisation. The tyrosyl radical **1** was not observed. The relative contribution to the spectrum for radical **4** is 1.71 times the contribution for radical **3**; at high pH the deprotonated form is favoured. The dominant radical species present at pH 10 are therefore semiquinone radicals **3** and **4**.

2.2.4 Conclusions and limitations of free solution experiments

UV irradiation of free tyrosine solution at pH 10 revealed that tyrosine is rapidly oxidised to DOPA. EPR analysis of irradiated samples confirmed the presence of DOPA based semiquinone radicals: experimental data matched reported literature hyperfine splitting values with minimal optimisation. Radical species are short-lived, and do not persist when the light source is shut off.

Initial solution experiments confirmed that radicals are formed upon irradiation, suggesting a radical decay pathway for tyrosine. However, the short lifetime of radical species doesn't provide a handle to probe the effects of metals or antioxidants on the decay pathway.

The pH used for solution experiments is unrealistic as a model for hair protein environment, which is typically slightly acidic, around pH 4.5-5.5.[131] The high pH will influence the photochemistry of tyrosine: higher [$^{-}$OH] may promote the hydroxylation pathway in Scheme 2-1 compared to experiments at neutral or acidic pH. Esterified tyrosine derivatives can be used under reasonable pH conditions in fluorescence studies, although without EPR analysis the study is more limited.

Free tyrosine or tyrosine ester in solution exhibits largely unhindered rotation on the EPR timescale. Although this can allow defined hyperfine splitting in EPR spectra at high pH, it is an unrealistic model of the more restrictive environment of tyrosine as part of a protein structure. Individual amino acid molecules also do not reflect the polypeptide structure within proteins, and may exhibit significantly different chemical properties.

2.3 Photo-generated radical species in solid amino acids

In contrast to free amino acid solutions, the mobility of tyrosine in solid powders is highly restricted. This may provide a more appropriate model of tyrosine within rigid keratin proteins. Solvent and pH effects are also removed in solid samples. The aims of this investigation are to observe and characterise photo-generated radical species in solid samples, and observe the effect of manipulating amino acid composition and metal content upon radical lifetime.

2.3.1 Observation and characterisation of radicals observed in solid tyrosine powder upon UV exposure

Solid tyrosine powder was exposed to UV within the EPR cavity for a period of 5 minutes, an EPR spectrum was then recorded. A broad EPR signal was observed upon irradiation with an isotropic g-value of 2.0045, as shown in Figure 2-3.

As radicals are randomly oriented in a powder sample with respect to the magnetic field, the spectrum is anisotropic with unresolved principal values of the g-tensor, leading to a single broad peak. Hyperfine splitting is also not resolved due to the restricted motion of radical species.

Comparable g_{iso}-values reported in literature range from 2.0026 to 2.0052 for tyrosine in proteins,[132] with a value of 2.00423 reported for free amino acid (based on simulated data).[133] The value of 2.0045 obtained here is comparable, suggesting that the radical observed is likely to be the tyrosyl radical. Unlike solution measurements, highly restricted mobility prevents the rapid conversion of tyrosyl radicals into semiquinone species as outlined in Scheme 2-1.

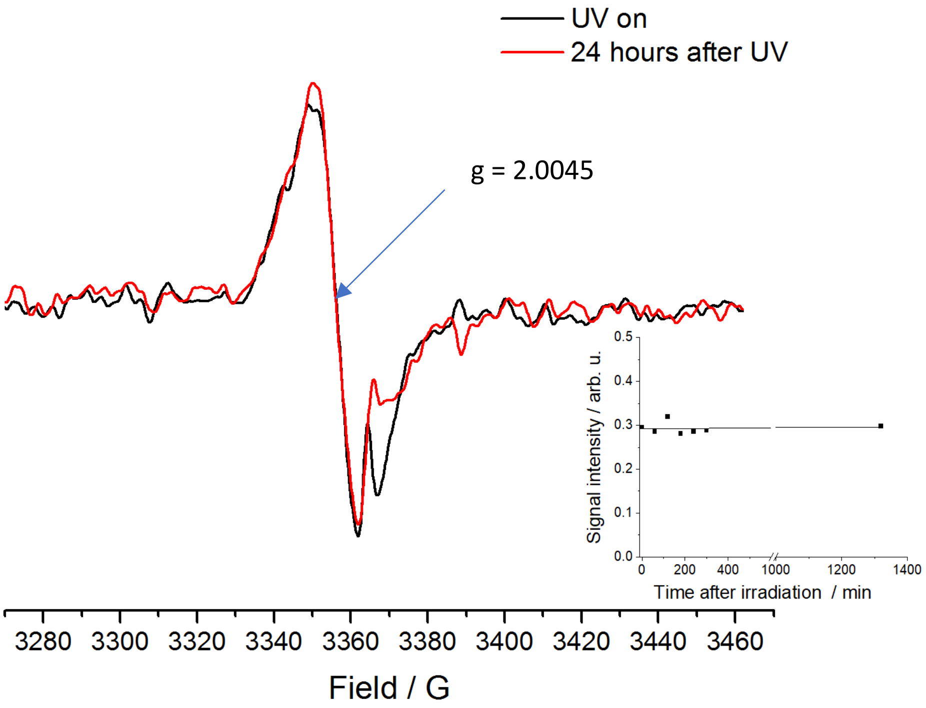

Figure 2-3: EPR spectrum of solid Tyr powder after 5 minutes exposure to 100 W Hg lamp, and 24 hours after lamp shut off. Inset shows change in signal intensity over time after exposure.

In a restricted solid environment, there is little opportunity for interaction between excited tyrosine and other groups, such as metal centres, oxygen and other amino acids. By restricting these interactions, radical lifetime is significantly increased, as fewer decay pathways are available. The signal intensity of a solid tyrosine sample generated after only 5 minutes UV exposure changes little over a 24-hour period following the exposure, as shown in Figure 2-3, inset. The addition of other components to the solid matrix may promote radical reactions, therefore this was investigated.

2.3.2 Introduction of other amino acids to promote tyrosine degradation

A major factor leading to keratin protein damage is the breaking of disulfide bonds in cystine, the dimer of cysteine. The disulfide readily interacts with the excited state of tyrosine, hydroxyl radicals or singlet oxygen, forming sulfur centred radicals, single cysteine and eventually leading to the formation of sulfonic acid (see section 1.2.3).[99] Tyrosyl radicals may also abstract hydrogen from cysteine, leading to the formation of a sulfur centred radical. Studies were carried out upon solid Tyr/Cys amino acid mixtures.

Electron transfer processes between amino acids typically require separations less than 20 Å.[134] In a solid mixture of two amino acids produced through evaporation of a mixed solution, these interactions are only likely at surfaces between different particles. High levels of cysteine were added to tyrosine samples, corresponding to mass fractions of 0.25, 0.5 and 0.75. A pure cysteine sample was also tested. Upon UV exposure, mixed amino acid samples gave a different EPR signal, shown in Figure 2-4. Subtraction of a pure tyrosine spectrum from the composite spectrum results in a radical signal with a shape consistent with asymmetric sulfur-centred radical signals reported in the literature.[135] The g-values shown in Figure 2-4, calculated compared to a DPPH standard, are comparable to that of pure irradiated cysteine (see section 5.5.2) and with those reported in literature for the $g_{\perp}$ component of cysteine thiyl radicals as part of proteins or frozen solutions. These vary from 2.006 to 2.011 for the centre of the signal (2.010 in Figure 2-4) depending on the radical environment.[98] Smissman and Sorenson also report a value of 2.0137 for the saddle point for the methyl thiyl radical, compared to 2.0129 observed here.[135]

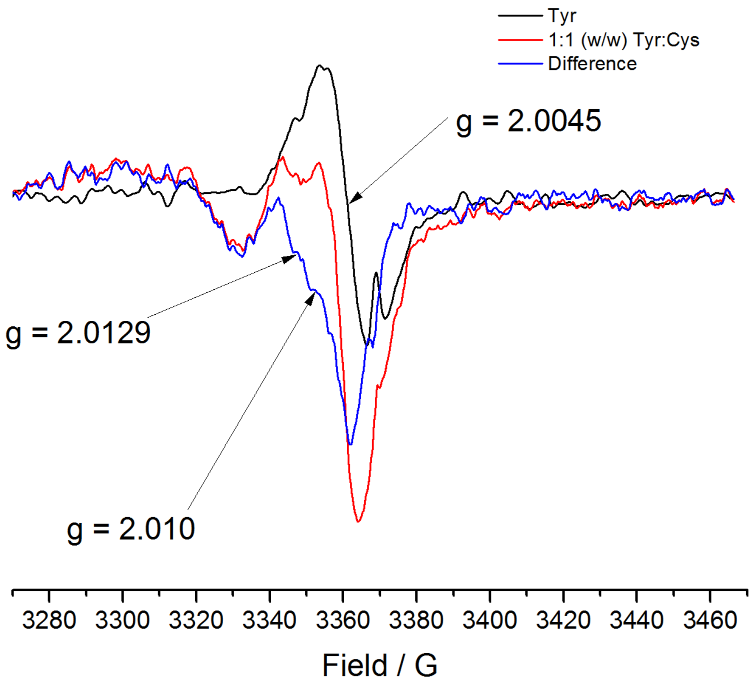

Figure 2-4: EPR spectra obtained upon irradiation of solid tyrosine (black) and 1:1 Tyr:Cys mixture (red). Spectra collected after 5 minute irradiation period. Difference spectrum (blue) is the mixture minus the tyrosine signal.

It is therefore reasonable to conclude that sulfur centred radicals are observed upon irradiation, in addition to tyrosine based radicals. However, pure cysteine (in the absence of tyrosine as a chromophore) shows a similar spectrum. This suggests that sulfur centred radicals are also formed by direct photolysis of S-H bonds in cysteine by UVC absorption. This high energy UV is not present in sunlight, therefore direct cystine photolysis is unlikely to play a significant role within proteins.

2.3.3 Monitoring rate of radical decay in mixed amino acid systems

The extent of radical loss in solid samples over a 24-hour period following UV exposure was compared for different amino acid mixtures. The aim of this study was to determine if significant interactions between different amino acids occur in solid samples, influencing radical lifetime.

Tyrosine based radicals were found to be more stable than cysteine based radicals in pure samples, as shown by much slower decay rate in Figure 2-5 for pure Tyr compared to pure Cys. Consequently, experiments with a range of amino acid mixtures revealed that the decay rate was dependent upon the amount of cysteine present, as shown in Figure 2-5.

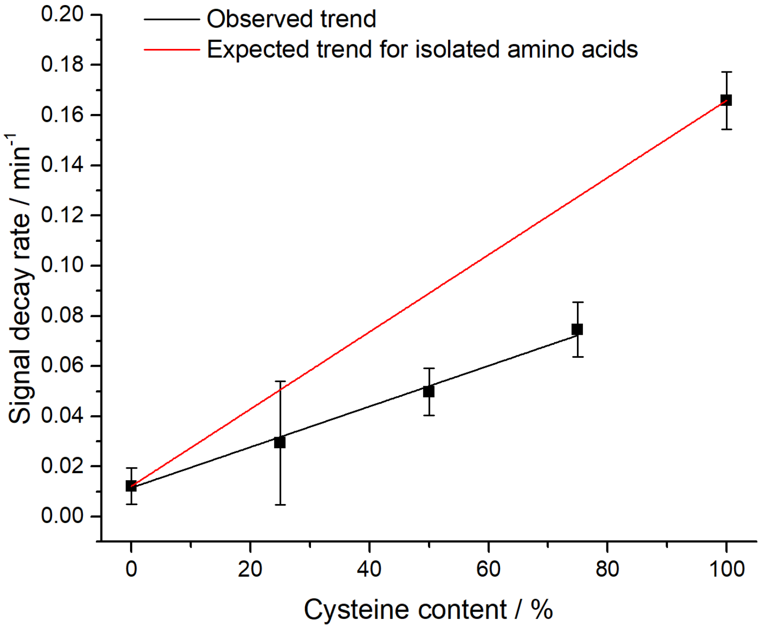

Figure 2-5: The effect of cysteine content on the signal decay rate of solid amino acid powder sample mixtures, compared to expected rate based on observed decay rates of isolated amino acids. Error bars show standard error based on 4 repeat measurements.

If cysteine and tyrosine radical species were purely isolated, then the rate of radical decay would be expected to increase linearly with cysteine content, broadly following the red line in Figure 2-5. However, amino acid mixtures consistently show lower than expected decay rates. This indicates that radical species are not completely isolated, and radical transfer processes between different amino acids in the mixture slow the overall rate of decay of radical species in the system.

Further evidence of interaction between amino acids can be seen when comparing spectral lineshape of mixed samples directly after UV exposure and after 24 hours, as shown in Figure 2-6. By subtracting the spectrum after 24 hours from the one immediately after UV exposure, a similar signal to a tyrosyl radical signal is observed (blue line in Figure 2-6).

Despite cysteine based radicals exhibiting shorter lifetimes based on Figure 2-5, the shape of the difference spectrum indicates significantly greater loss of tyrosine based radicals. Tyrosyl radical degradation is therefore enhanced by cysteine content. This is indicative of a transfer of radical centre from tyrosine to cysteine, likely through hydrogen abstraction or photo-generated reactive oxygen species such as hydroxyl radicals or singlet oxygen. However, the process is very slow in the immobilised solid system.

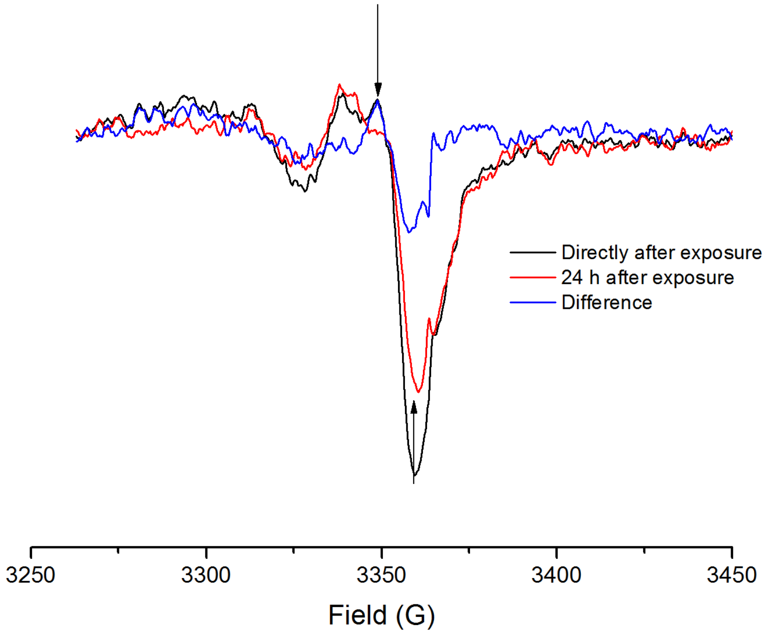

Figure 2-6: Comparison of EPR spectrum of 1:1 Tyr:Cys solid amino acid mixture directly after and 24 hours after 5 min UV exposure. Remaining signal subtracted from initial signal to give the signal lost over the time (blue spectrum)

2.3.4 Introduction of metals

Adding cysteine to solid tyrosine samples has shown that tyrosyl radicals are not completely isolated within solid systems, but can interact with surrounding molecules. Tyrosyl radicals may therefore interact with transition metal ions the in solid phase. The aim of this study was to examine whether the addition of Fe(III) to solid amino acid samples had any effect upon tyrosyl radical degradation following UV exposure.

1000 ppm Fe(III) ($FeCl_3$) was added to samples of tyrosine and mixed Tyr/Cys, by dissolving with amino acids in solution and evaporating the solvent. An artificially high metal content compared to hair (typically around 40-60 ppm)[105] was used to increase the possibility of near-space electronic interactions between metal and tyrosine. Decay rates for samples with and without iron(III) are compared in Figure 2-7.

The general trend of increased decay rate with increased cysteine content remains the same in the presence of Fe(III). However, addition of the metal does not have a consistent effect on all solid samples. From this data, it is not possible to conclude whether iron(III) has any influence over tyrosyl (or cysteinyl) radical lifetime in solid systems. Differences observed are likely to be within measurement error, given that only single measurements for Fe(III) samples were carried out, and comparatively weak signal strength.

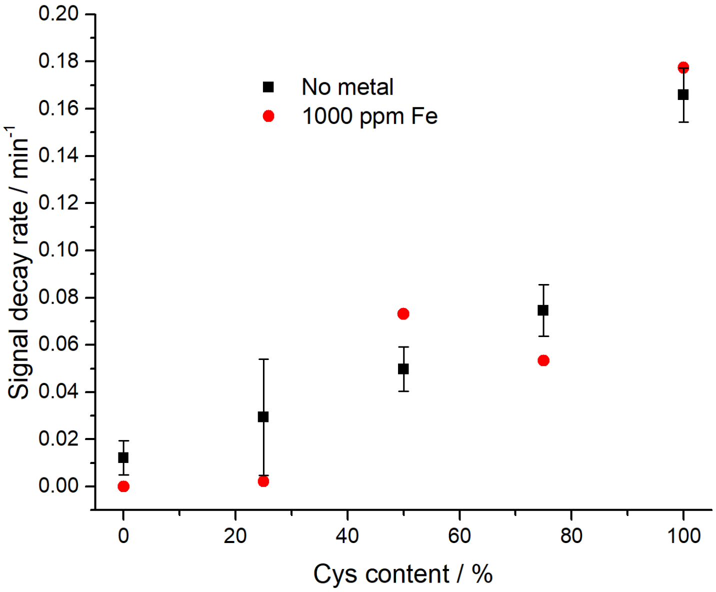

Figure 2-7: Comparison of signal decay rates for solid Tyr/Cys samples with and without 1000 ppm Fe(III). Error bars show standard errors from average of 4 measurements. Fe(III) samples based on single measurements.

The metal concentration in the bulk sample may be too low to influence photochemistry. However, increasing iron(III) concentration further was not practical due to the impact this had upon EPR signal strength because of exchange interactions between paramagnetic metal centres and organic radicals.[136]

2.3.5 Solid powder experiments: conclusions

When exposed to UV, radical species are formed in solid tyrosine powder. This gives rise to a broad EPR signal with a g-value of 2.0045, which matches literature values for a tyrosyl radical. The highly restrictive solid environment results in relatively slow radical decay after exposure.

The rate of radical decay was influenced by the presence of cysteine in the sample. Changing EPR lineshape indicated that radicals transfer from tyrosine to cysteine. Radical decay was also significantly slower in mixed systems than would be expected if Tyr/Cys radicals were isolated. These studies confirm that Tyr radicals can interact with surrounding molecules despite their highly restricted environment.

Slow radical decay limits further studies due to the unrealistic timescale needed to obtain meaningful data. Investigating the effect of metals upon Tyr photochemistry is also hampered by poor interaction in the solid matrix, even at high metal concentration. An alternative system was therefore sought which offered a balance between mimicking the restricted environment of tyrosine in proteins whilst allowing interaction with metal ions and other additives to be investigated.

2.4 Development of colloidal and hydrogel systems

An ideal model system for tyrosine in proteins would exhibit a restricted tyrosine environment. However, to allow homogenous interaction between tyrosine and metals, a solvated system is required. The aim of this section was to develop a system with restricted tyrosine environment, without compromising on intermolecular interactions between metal and tyrosine centres.

2.4.1 Hydrogel systems

Hydrogels consist of a fibrous network of polymers or small molecules surrounded by solvent pockets. This provides an ideal mechanism to restrict tyrosine mobility whilst retaining free diffusion of any added metals or antioxidants through solvent pockets around the fibres.

Many successful tyrosine based hydrogels involve modification of the amino acid side chain, which was considered undesirable. However, an assessment of the literature revealed two promising candidates for tyrosine containing hydrogels.

2.4.2 Supramolecular hydrogels

Low molecular weight gelators (LMWG) are small molecules which, solely through non-covalent interactions, self-assemble in solution into a stable fibrous network.[137] Amino acids have been shown to form LMWG gelator molecules after glycosylation,[138] functionalisation with alkyl chains and quaternary ammonium substituents,[139] and with fluorenylmethyloxycarbonyl (Fmoc) protecting groups.[140] Hydrogels were prepared from Fmoc-Tyr (Figure 2-8, inset) according to a procedure described by Adams et al.[141] Gelation is pH dependent and driven by H-bond stabilised π-π interactions.

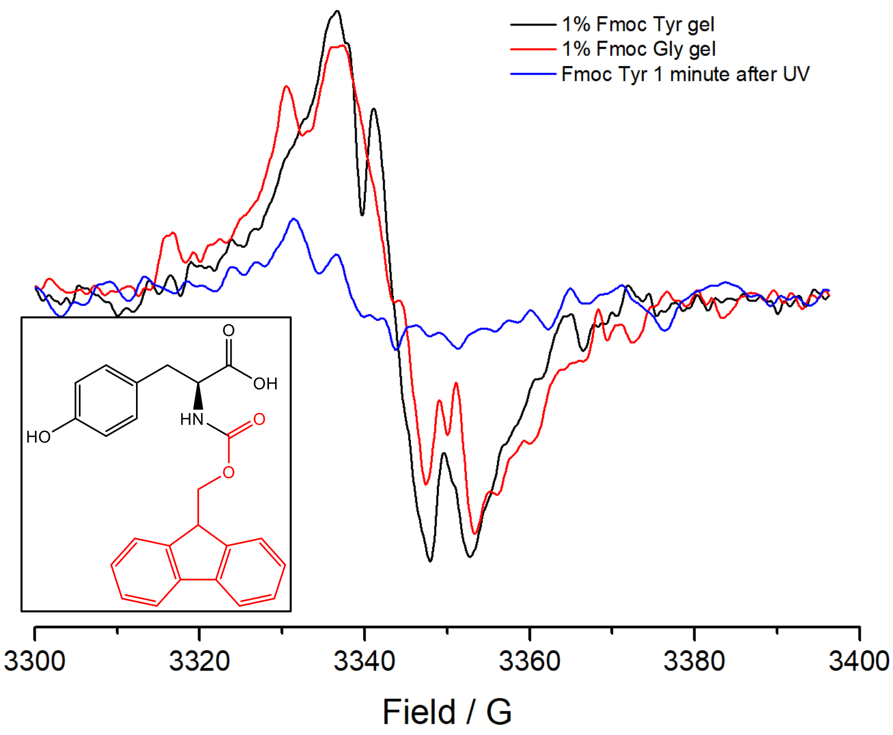

Figure 2-8: EPR spectra obtained during and after irradiation of 1% Fmoc-Tyr and Fmoc-Gly hydrogels. Inset: Structure of Fmoc-Tyr. Fmoc group is shown in red.

When Fmoc-Tyr hydrogel samples were exposed to UV and monitored by EPR, a radical signal was observed, shown in Figure 2-8. The signal is broad, with no defined hyperfine structure, indicative of a restricted radical environment. However, the radical signal does not persist after UV exposure. A spectrum recorded 1 minute after the lamp was shut off shows a drop in peak area of 77%. This suggests greater interaction between the radical and its environment compared to a solid matrix.

However, a control sample of Fmoc-Gly hydrogel also showed a similar signal upon UV exposure (Figure 2-8). This indicates that the observed signal arises primarily from radical species centred on the chromophoric Fmoc group, rather than tyrosine. This is likely a resonance stabilised 9-fluoronyl radical species.

This study shows that hydrogels reduce radical mobility on a microscopic scale, whilst maintaining a free solvent environment for soluble metal ions or other additives. However, an alternative gel system is needed without competing chromophores.

2.4.3 Polymeric hydrogels

Large polymers can also form gel fibres through physical interactions or the formation of covalent bonds.[141] Amphiphilic molecules, such as block copolymers with hydrophobic and hydrophilic "blocks" are capable of self-assembling into gel fibres through hydrophobic interactions, hydrogen bonding, π-π stacking and other non-covalent interactions.[142]

By balancing the hydrophobicity of tyrosine with a suitable hydrophilic block, an amphiphilic polymer could be created. Heise and co-workers report a PEG-Tyr block copolymer system, with varying lengths of tyrosine polypeptide as a hydrophobic block, bound to a hydrophilic PEG chain, as shown in Figure 2-9.[143]

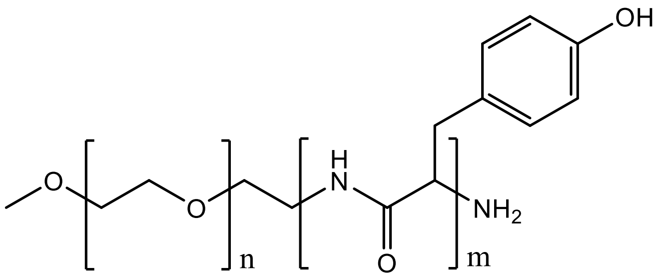

Figure 2-9: PEG-Tyr amphiphilic block copolymer reported by Heise et al [143] n = 44 or 112, corresponding to PEG2000 and PEG5000 respectively. m = 5, 10, 15 or 20

The ratio of hydrophilic to hydrophobic components can be varied by altering the length of PEG used or the length of the tyrosine polypeptide. Heise et al found gelation to occur readily upon heating of PEG_{2000}-Tyr_5 at concentrations at or above 0.86 mmol dm^{-3} to temperatures of 37 °C and above.[143] Longer polymers were also found to form stable hydrogels upon heating to higher temperatures, as described in section 3.3.

Like Fmoc based gels, tyrosine is immobilised within the fibres yet surrounded by free solvent, creating an ideal model for Tyr in keratin proteins. Unlike Fmoc based gels, no additional chromophores are present which may interfere with the photochemistry: PEG does not absorb above 200 nm.[144] The polypeptide chain accurately models the protein chemical environment, unlike single amino acid systems. The response of PEG-Tyr hydrogels to UV irradiation was studied to determine if the system could be used as a model for studying Tyr photochemistry.

2.4.4 Observation of photo-induced radicals in PEG-Tyr hydrogels by EPR

1% (w/v) PEG_{5000}-Tyr_{15} formed a stable hydrogel upon heating to 85 °C for 2 hours. Hydrogel samples were prepared in quartz flat cells or capillaries. Samples were exposed to UV and monitored by EPR. No visible change to gel structure was observed upon UV exposure. A broad EPR signal was observed upon irradiation, as shown in Figure 2-10.

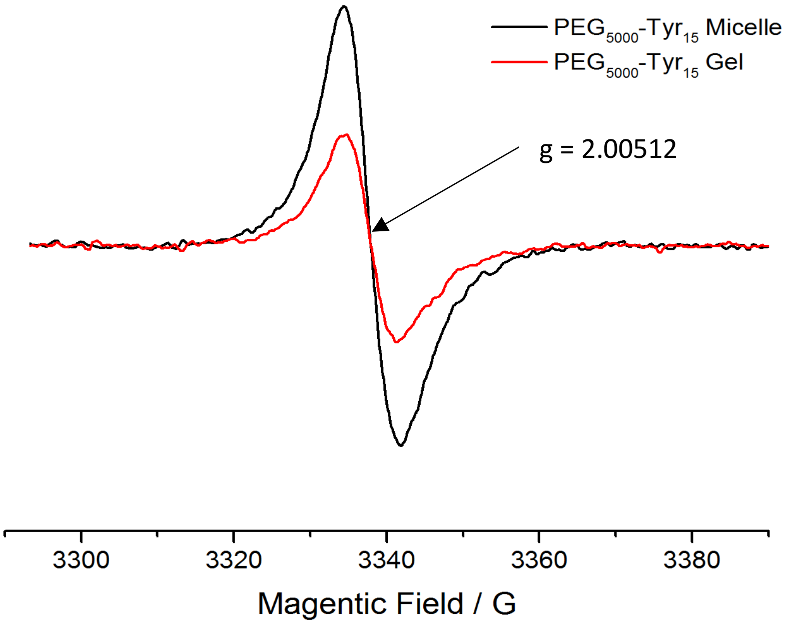

Figure 2-10: EPR signal observed upon irradiation of 10 mg/ml (1.296 mM) sample of PEG_{5000}-Tyr_{15} before and after gelation. g value based on a separate measurement of the same sample with a DPPH internal standard.

The g-value of the signal observed was measured relative to a DPPH standard. The value obtained was 2.00512, which is within the range of different values reported in literature (2.0026 to 2.0052) for a tyrosyl radical in enzymes or proteins[132] and slightly higher than that observed for tyrosine powder (see Figure 2-3). It is possible that the signal corresponds to more than one radical species. The identity of the radical signal is discussed further in section 4.1.

2.4.5 Spontaneous self-assembly of PEG-Tyr copolymers

Experiments revealed that the same broad radical signal was observed in PEG-Tyr samples without gelation (Figure 2-10). The signal observed before gelation is 2.12 times stronger than after gelation, based on the 2nd integrals of the peaks. This is likely due to increased scatter of high energy UV light by the large gel structures reducing the photochemical yield of radical species.

These findings indicate that even before gelation, tyrosine in PEG-Tyr systems is subject to a restrictive environment. It was postulated that the amphiphilic nature of the block copolymer results in spontaneous self-assembly into micelles. The nature of this self-assembly is studied in section 3.2.

2.4.6 Radical stability

Unlike solid samples, the radical signal in PEG-Tyr micelle systems decreased dramatically after irradiation was stopped. Figure 2-11 shows a kinetic trace of radical signal intensity following cut-off of UV from a sample of PEG_{5000}-Tyr_{10} solution (before gelation).

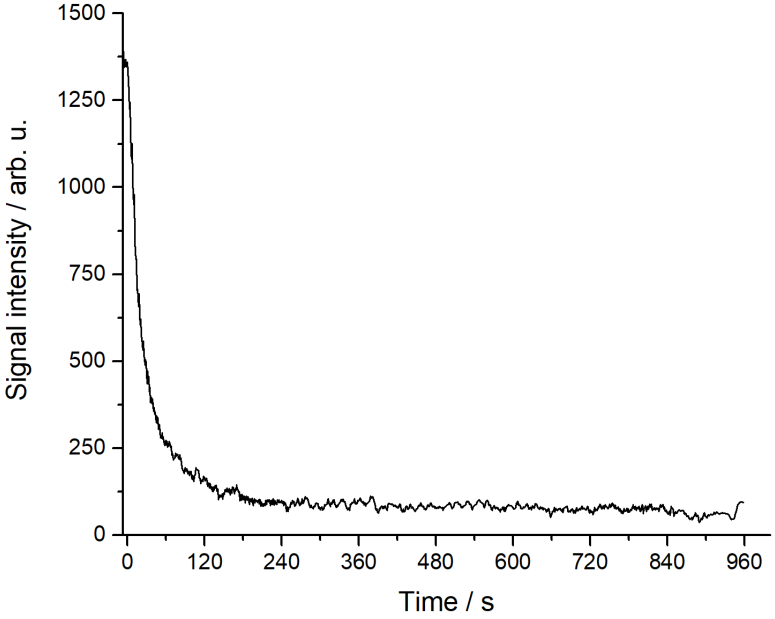

Figure 2-11: Kinetic trace showing decay of UV induced PEG_{5000}-Tyr_{10} radical signal following lamp shut-off (at t=0 s). Average of 4 measurements.

Within 60 seconds of lamp shut off, the signal has decayed to 20% of the initial intensity. A two-component exponential decay curve (Equation 2-1) was fitted to the data. A double exponential was used to model tyrosine based radical species decaying at two different rates, due to the differing environments and reactivity observed in micelle systems (see Section 3.5). Literature studies use a similar approach.[145]

$$y = y_0 + A_1 e^{-x/k_1} + A_2 e^{-x/k_2} \qquad \text{(Equation 2-1)}$$

Average constants for the two rates were $k_1 = 10.41 \pm 1.46\ s^{-1}$ and $k_2 = 53.77 \pm 11.22\ s^{-1}$. Radical lifetime is significantly longer than would be expected for free tyrosine radicals: the rate constant for tyrosyl radical decay is $8 \times 10^8\ dm^3\ mol^{-1}\ s^{-1}$ in the same solvent at the same pH.[125] Radical lifetime is likely prolonged by restricted tyrosine mobility in the colloidal system.

2.5 Development of a suitable model system: conclusions

Intermolecular interactions between tyrosine and other amino acids, oxygen and metal centres are critical to photochemical degradation in proteins. Accurately modelling these interactions is therefore crucial when developing a simplified model system.

The extent of interactions between tyrosine and photochemically generated tyrosine based radicals depends on the physical environment. Experiments with single amino acid solutions and solid powders showed two extremes: in free solution, tyrosyl radicals were too short-lived to observe by EPR (although more stable semiquinone radicals are observed at high pH). Conversely, photo-induced radical species in solid powders persist over extended periods after irradiation, due to severe mobility restrictions and poor intermolecular interactions. Interactions are enhanced through the addition of cysteine; although reactions remain too slow for meaningful study, and metal containing systems cannot be modelled.

Hydrogels and colloidal systems both provide a semi-restricted tyrosine environment, whilst retaining the solvation needed to control metal and antioxidant concentration. PEG-Tyr block copolymers form hydrogels and micellar aggregates, and model the protein polypeptide structure. EPR studies confirm that restricted mobility, UV generated tyrosine based-radicals are observed in PEG-Tyr hydrogels and micellar aggregates. These systems were therefore chosen as appropriate models for detailed studies of tyrosine photochemistry (see Chapter 4).

Additionally, the distinct physical environments of tyrosine in micellar and gel structures provides a unique opportunity to probe the effect of physical environment upon reactivity in chemically identical systems. Further characterisation of tyrosine environment, and its impact upon reactivity, is discussed in Chapter 3.

3. System Characterisation

An analysis of the macroscopic and microscopic surroundings of the amino acid in model systems is key to understanding its photochemical and chemical reactivity. As shown in Chapter 2, PEG-Tyr copolymers present a unique system which can exist as both micellar solutions and gels under identical conditions. This provides an opportunity to compare molecular organisation in these two systems.

When working with model systems, it is important to have some understanding of how realistic the model is. A greater understanding Tyr environment in PEG-Tyr systems will allow results from photodegradation experiments to be related to what may be expected in hair fibres.

The aims of this chapter are therefore:

- Develop a method to quantitatively compare tyrosine environment in different model systems, linking to photochemical reactivity.
- Provide a comparison of macroscale environment in gel and micellar systems and observe changes upon gel formation.
- To characterise aggregate structures and self-assembly in polymer systems.
- Attempt to relate the environment of tyrosine within model systems with keratin protein environments.
- To quantitatively assess the effect of changing tyrosine environment upon photochemical reactivity.

3.1 Overview of Different Tyrosine Containing Model Systems

The two tyrosine sources used in photochemical experiments were monomeric tyrosine methyl ester (see section 2.2.1) and PEG-Tyr block copolymer (Figure 3-1). Polymer samples were prepared by Andreas Heise et al, Dublin City University.[143] The polypeptide is produced by the ring open polymerisation of tyrosine N-carboxyanhydride, which preserves the stereochemistry of the amino acid.[146-147]

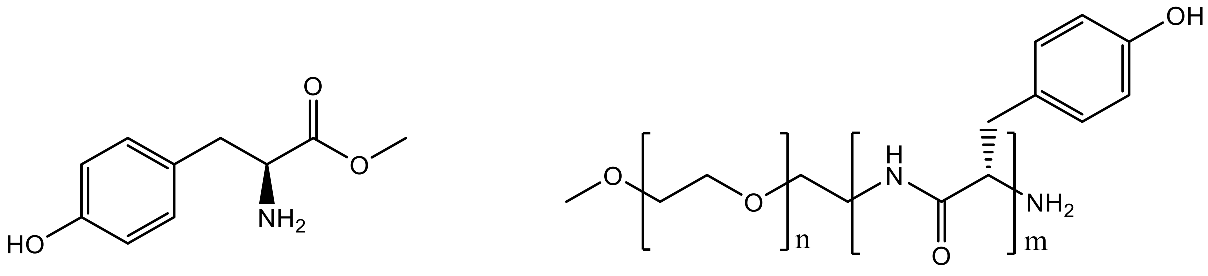

L-Tyr methyl ester **PEG-L-Tyr block copolymer**

Figure 3-1: Tyrosine model systems used in solution phase experiments. For polymer system, n = 44 or 112 (corresponding to PEG$_{2000}$ and PEG$_{5000}$ respectively), m = 5, 10, 15 or 20

The amphiphilic nature of the polymer, with a hydrophilic PEG chain and relatively hydrophobic polypeptide, causes it to self-assemble in solution. This creates a restrictive environment for tyrosine within hydrophobic cores, analogous to tyrosine in hydrophobic areas of keratin proteins. In contrast, tyrosine ester can freely diffuse through solution.

Preliminary photochemical experiments have shown that the different tyrosine environments provided by polymer and monomer systems lead to a different photochemical response. Polymer length affects the photochemical degradation of tyrosine, as well as photochemical dimerization. These differences are outlined in more detail in section 3.8.1. A detailed analysis of tyrosine environments in different polymer systems was performed to understand these differences. Spin labels and probes were used to quantitatively assess and compare the environment of tyrosine in micelle and gel systems, as described in sections 3.4-3.7. Sections 3.2 and 3.3 describe the two distinct states of PEG-Tyr copolymers, micellar aggregates and gels.

3.2 Self-assembly of polymers into micellar type aggregates

The observation of a photo-induced, restricted mobility phenoxyl radical by EPR spectroscopy (see section 2.4.4) indicates a restricted tyrosine environment in aqueous PEG-Tyr solutions. This suggests self-assembly of the polymer. Unfavourable solvent interactions with hydrophobic components of di- or tri- block amphiphilic copolymers typically lead to kinetically trapped aggregates with slow dynamics.[148-149] A study by Wishart et al into the micellization of poly-tyrosine/poly(ethylene oxide) block copolymers showed that PEO-Tyr block copolymers form stable spherical micelles in aqueous solution.[150] Based on these reports, PEG-Tyr copolymers were expected to self-assemble into micelle type structures in aqueous solution.

3.2.1 DLS observations of micelles

The nature of PEG-Tyr aggregate structures was probed through analysis of aqueous polymer solutions by dynamic light scattering (DLS). This technique measures the hydrodynamic radius of particles based on their Brownian motion within the solution. Brownian motion is measured by analysing the time dependence of the intensity of scattered light. Larger particles have slower dynamics, resulting in a slower intensity variation. The hydrodynamic radius depends on any surface groups (such as PEG chains) present, as well as any electrostatic interactions between components in the sample. An advantage of DLS is it enables the sample to be studied in its native environment, rather than in gas or solid phase. However, it gives little information about the shape of micellar structures.

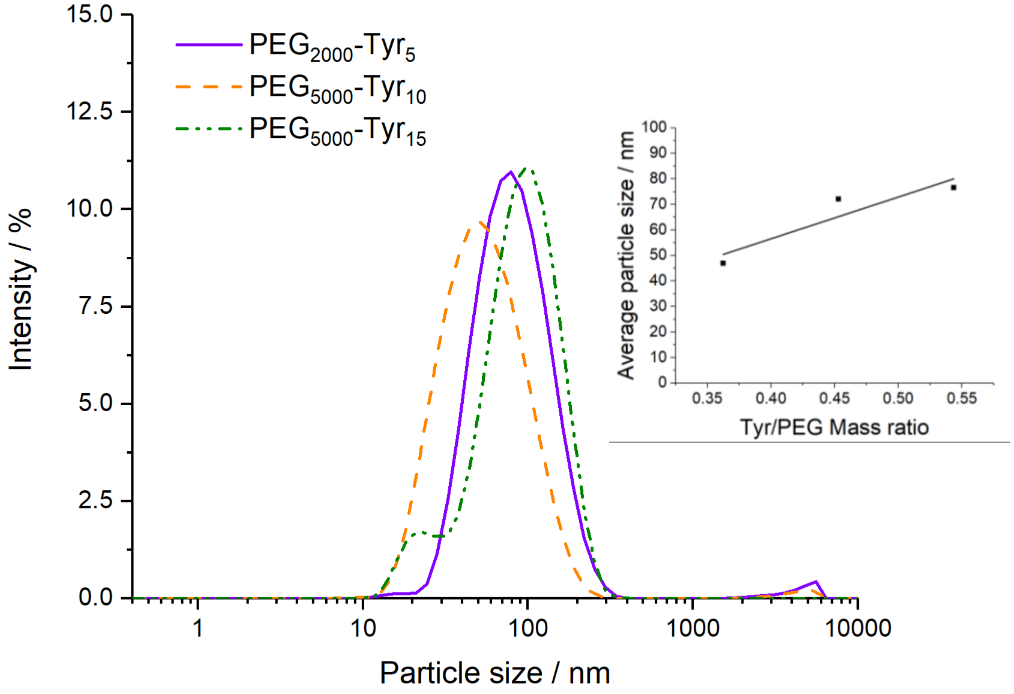

Figure 3-2: DLS size distribution plots (by intensity) for different polymer samples in water. Each plot is an average of 3 measurements.

DLS measurements shown in Figure 3-2 reveal that the size of the micelle remains similar for varying polymer length, but is broadly dependent on the hydrophilic/hydrophobic ratio of the block copolymer, as shown in Figure 3-2 inset.

The volume of the hydrophilic head group, relative to the hydrophobic tail length and overall volume of the surfactant, affects the size, packing and shape of aggregate structures. This relationship is defined by the packing parameter *g* (Equation 3-1), where *V* is the total volume of the surfactant, a_0 is the effective volume of the hydrophilic group and *l* is the hydrophobic tail length.[151] The volume of the PEG chain relative to the overall surfactant volume is large, giving rise to a small value for *g* and consequently spherical micelle structures.[152]

$$g = \frac{V}{a_0 \times l} \qquad \text{(Equation 3.1)}$$

Changes to the hydrophobic component will alter the extent of the intermolecular interactions such as hydrogen bonding and π-π stacking within the hydrophobic core. Greater interaction increases the stability of micelle structures.[150] However, increasing hydrophobic chain length can also lead to changes in aggregate shape.[153]

Changing the size of the hydrophilic component (PEG) can also affect micelle thermodynamic stability. PEG chains interact with each other through van der Waals forces, and with surrounding water molecules by dipolar interactions and hydrogen bonding. Increasing PEG chain length increases the rigidity of the hydrophilic sheath around the hydrophobic core with a greater number of intermolecular interactions.[154] This will increase the thermodynamic stability of the micelle.

Changing the ratio of hydrophilic and hydrophobic components of the copolymer will therefore influence the interactions of both parts which stabilise the formation of aggregates. The change in micelle size observed by DLS reflects the impact hydrophilic/hydrophobic ratio has upon micelle stability.

3.2.2 Determination of critical micelle concentration for PEG-Tyr polymers

DLS can be used to determine the critical micelle concentration (cmc) of diblock copolymers.[155] However, it is not as reliable as some colorimetric techniques, due to the high sensitivity of DLS making results more prone to artefacts.[156] The count rate from the DLS instrument is plotted against concentration, and the cmc is defined as the point at which the line intersects with the baseline count rate. This was carried out for both PEG_{2000}-Tyr_5 and PEG_{5000}-Tyr_{10} copolymers. The aim of this investigation was to ensure that concentrations used for photochemical experiments were above the cmc. Micelle size does not vary significantly over the concentration range studied.

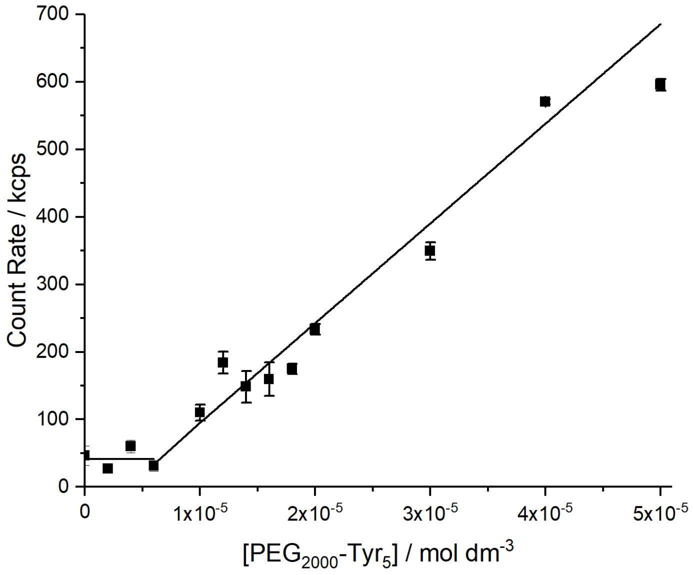

Figure 3-3: PEG_{2000}-Tyr_5 determination of cmc by DLS count rate. Average of 3 measurements shown. Error bars indicate 95% confidence levels.

Figure 3-3 shows that PEG_{2000}-Tyr_5 spontaneously self-assembles above 0.6 × 10^{-5} mol dm^{-3}, equivalent to 0.017 mg ml^{-1}. The same experiment was carried out for PEG_{5000}-Tyr_{10}, with a calculated cmc of 0.5 × 10^{-5} mol dm^{-3}, equivalent to 0.034 mg ml^{-1}. The lower cmc of the longer polymer is likely due to increased hydrophobic interactions within the micelle core and hydrophilic interactions in the PEG shell improving the thermodynamic stability of the micelle.[157]

Photochemical experiments used a concentration range of 0.5 – 5 mg ml^{-1}. Therefore, it is reasonable to assume that the micelle environment remains constant at different concentrations of the same polymer throughout photochemical experiments.

3.2.3 Stability of micelle structures upon UV exposure

Stability of the system to UV exposure is a key consideration, as changes to tyrosine environment during photochemical studies may change its photochemical properties. Further DLS measurements were carried out to confirm that micelle structures remained stable upon UV exposure. Measurements looked at the change in average particle size over a prolonged exposure period. A sample was measured at 2 hour intervals for the first 6 hours, and then after 24 hours' exposure. The results are shown in Figure 3-4.

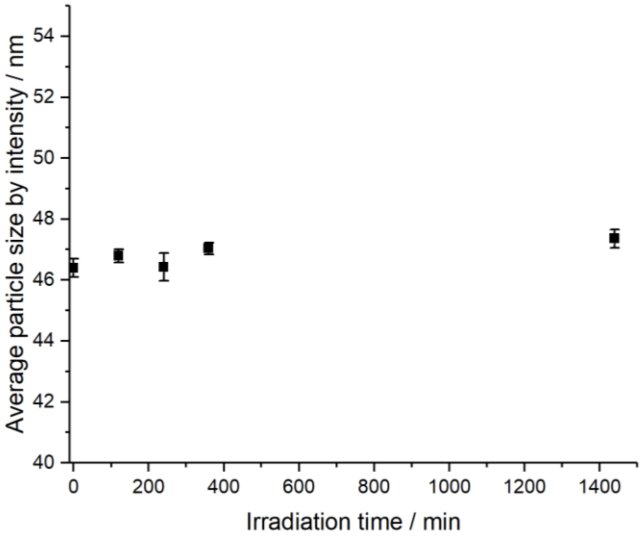

Figure 3-4: Change in particle size of PEG_{5000}-Tyr_{10} micelles upon prolonged UV exposure. Error bars show 95% confidence levels for an average of 3 measurements

The variation in micelle average size shown in Figure 3-4 is very small, with an increase of less than 1 nm over 24 hours falling within measurement error. Micelle structures are therefore stable to UV exposure over relevant timescales. Control experiments have also shown that there is no change to micelle structures (by DLS) after UV exposure, or over a 24-hour period without UV exposure.

Although stable to UV exposure, micelle structure is highly sensitive to changes in temperature. Relatively mild conditions cause the rearrangement of polymers and the formation of hydrogels. The infra-red output of the mercury arc lamp caused a slight increase (< 5 °C) in sample temperature over prolonged exposure. However, based upon Figure 3-4 this was not sufficient to cause micelle breakdown or gel formation. Photochemical studies are therefore possible on both micelle and gel systems.

3.3 Formation of hydrogels

Upon heating, PEG-Tyr copolymers form hydrogels.[143] Unusually, the gel forms on heating rather than subsequent cooling. This shows that energy is needed to break the micelle structures, allowing a more stable gel to form. Structural characterisation (by cryo-TEM) of PEG_{2000}-Tyr_5 hydrogels is reported in literature.[143]

Similar interactions likely drive aggregation in both gels and micelles. Gel fibres are formed due to hydrogen bond interactions between polypeptide backbone, solvent molecules and the tyrosine side chain, as well as π-π stacking. The side chain of tyrosine can act as both a hydrogen bond donor and acceptor, because of the partial delocalisation of a lone pair from the phenolic oxygen around the aromatic ring.[158] The side chain is known to interact with carbonyls on the peptide readily within proteins.[159] The increased magnitude and long-range order of interactions in gel systems improves the thermodynamic stability of the system.

As discussed in section 3.2.1, different length polymers have different kinetic and thermodynamic stability. This results in different gelation conditions, as summarised in Table 3-1. Gel stability was assessed by inversion of sample vials.

The shorter PEG_{2000}-Tyr_5 polymer forms stable hydrogels at concentrations as low as 5 mg/ml, equivalent to a tyrosine concentration of 8.6 mmol dm^{-3}. Increasing the concentration of PEG_{5000}-Tyr_{10} further to promote stable gel formation was not attempted. No gel formation was observed at lower concentrations of longer polymers than those shown in Table 3-1.

Table 3-1: Summary of gelation experiments for longer polymers

Polymer	**Conc. / mg ml^{-1}**	**Temperature / °C**	**Heat time / min**	**Gel formed?**	**Stable?**
PEG$_{2000}$-Tyr$_5$	10	40	60	✓	✓
PEG$_{5000}$-Tyr$_{10}$	10	85	180	✗	✗
PEG$_{5000}$-Tyr$_{10}$	20	85	180	✓	✗
PEG$_{5000}$-Tyr$_{15}$	10	85	120	✓	✓
PEG$_{5000}$-Tyr$_{15}$	20	85	120	✓	✓

3.3.1 Breaking up gel fibres

Gels are stable to mild changes in temperature and pH. At around pH 13, Tyr phenolic -OH groups deprotonate, lowering the hydrophobicity of the Tyr block.[143] The pK_a of the phenolic group is likely different from the values typically reported for the free amino acid (10-10.5) due to the interactions between the side chain and neighbouring groups, which affect ionizability.[160]

Gel structures can be broken up by disrupting PEG-solvent interactions. Addition of a less polar solvent (such as ethanol) or aprotic solvent (such as DMF) leads to a gradual collapse in gel structure. The addition of 50% ethanol is sufficient to completely dissolve gel fibres and micelle structures, as measured by DLS, which shows no significant particles after addition of the cosolvent.

The stability of both micelle and gel systems under the same physical conditions and upon UV exposure enables a quantitative comparison of tyrosine reactivity in two physically distinct, yet chemically identical environments. Before comparing reactivity, tyrosine environment was compared in micelle and gel systems.

3.4 Quantitatively analysing tyrosine environment within model systems.

EPR spectroscopy is a powerful technique which reveals information about the dynamics of a radical centre, as well as the nature of the environment and how the radical interacts with the environment.[161] UV induced radical species are too short-lived for this study: a stable artificial radical centre must be added to the system.

Nitroxide radicals are stable species which exhibit a characteristic 1:1:1 triplet EPR spectrum, with a ^{14}N hyperfine splitting of around 14 G.[162] The nitroxide spectrum is highly sensitive to the dynamics of the molecule on a nanosecond timescale. Slowly tumbling radical species do not completely average anisotropic components of the A and g tensors, which influences EPR line shape.[163] From the line shape it is possible to determine the dynamics of the radical, and therefore the nature of the environment surrounding the probe. Two different approaches to studying the micellar environment in copolymer systems were taken: spin probing and spin labelling.

3.4.1 Assessing the environment within micelle cores by spin probing

A spin probe is a nitroxide containing molecule which is introduced to an environment to probe radical mobility. The spin probe will need to incorporate within hydrophobic centres of micelle and gels, an ideal spin probe will therefore be relatively lipophilic. Several spin probes were attempted. DOXYL stearate and DOXYL cholestane proved too insoluble, forming aggregates with other spin probes. Results from 12-DOXYL stearic acid (Figure 3-5) were more promising.

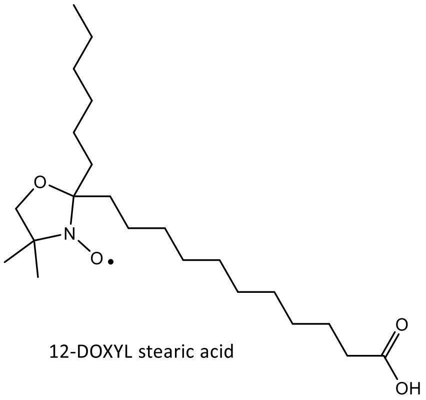

Figure 3-5: Structure of 12-DOXYL stearic acid spin probe

The spin probe was added to a solution of PEG_{5000}-Tyr_{15} in a 1:5 molar ratio. An EPR spectrum of the solution was then recorded and compared to the spectrum of the spin probe in water.

The acidic proton of 12-DOXYL stearic acid slightly improves solubility compared to other spin probes attempted. The position of the nitroxide on the fatty acid chain also influences solubility. The carboxylate pK_a is between 5 and 6, extrapolating from data collected by Rahman et al.[164] Dissociated and undissociated forms of the spin probe will have different hydrophilicity and will locate differently within the colloidal system.[165] Samples of PEG_{5000}-Tyr_{15} containing 12-DOXYL stearic acid were analysed by X-band EPR at both pH 6 and pH 3, to monitor changing affinity. The spectra obtained are compared with the spectrum for the spin probe in water (neutral pH) in Figure 3-6. Spectra were obtained at room temperature.

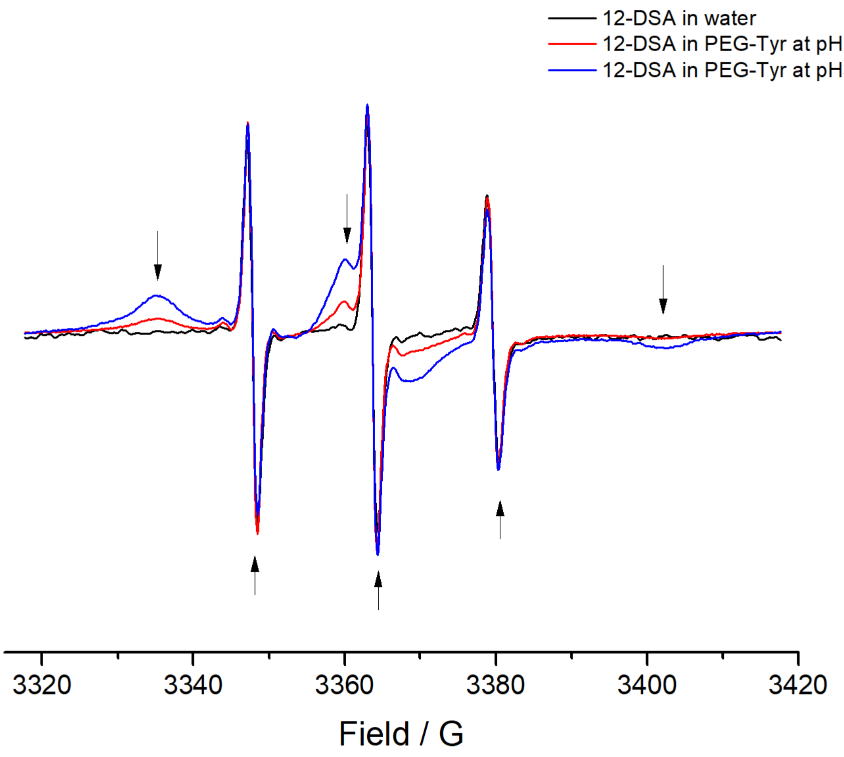

Figure 3-6: Comparison of EPR spectra from PEG$_{5000}$-Tyr$_{15}$ samples containing 12-DOXYL stearic acid spin probe at different pH. Signals normalised by intensity of central sharp peak.

The sharp triplet (upward arrows on Figure 3-6), closely matches free spin probe in water. This indicates that the spin probe is not completely effective at incorporating within micelle structures, leading to a spectrum showing two distinct spin probe environments. The second environment is characterised by broader peaks appearing at low and high field as well as a central broad peak (downward arrows). The line broadening and anisotropy of these peaks is indicative of spin probe in a highly restrictive environment, such as a hydrophobic micelle core.

Spectra in Figure 3-6 are normalised based on the intensity of the central sharp peak, to highlight the pH dependence of spin probe incorporation within micelles. At pH 6, free spin probe dominates. Incorporation of the deprotonated form (dominant at pH 6) into hydrophobic micelles is less favourable due to improved solubility. At pH 3, the neutral form is dominant, uptake of spin probe into micelles is enhanced and the restricted environment becomes more dominant in the spectrum. At pH 3, the ratio of restricted to free spin probe is 9.6, based on double integrals of spectral components.

Nitroxide environment within micelles can be characterised by analysing the slow component of the EPR spectrum. The separation of the broad outer peaks (BOPs) is related to the rotational correlation time of the nitroxide, and consequently the radical mobility. A completely immobilised nitroxide (on the EPR timescale) will give a BOP separation of around 70 G, although this is field and solvent dependent.[166] The spectrum at pH 3 in Figure 3-6 shows a separation of 67.5 G. This corresponds to a highly restricted environment, almost completely immobile on an EPR (nanosecond) timescale.

Although spin probing clearly shows the restricted environment within micelle cores, its accuracy is limited. There is no control over where spin probe molecules are located: some may form aggregates with other spin probe molecules, or may only partially incorporate within PEG-Tyr micelles. No studies were carried out to test if the change in pH required influenced micellar self-assembly. Therefore, a method to achieve a more controlled uptake of nitroxide into micelles was sought.

3.4.2 Spin labelling as an enhanced probing technique

Unlike spin probing, spin labelling involves covalently binding a stable radical species to a molecule of interest to probe its mobility. A nitroxide bound directly to the hydrophobic Tyr chain in PEG-Tyr will give a more accurate and reliable indication of tyrosine environment. Relatively small nitroxide labels ensure that aggregation is not disrupted. This study aimed to develop a method of spin labelling tyrosine residues in PEG-Tyr, and quantitatively analysing tyrosine environment by EPR.

The side chain of tyrosine is relatively unreactive under mild conditions, with most chemical reactions occurring only when the phenol is deprotonated to the phenolate anion.[167] Francis et al report a Mannich type electrophilic aromatic substitution reaction capable of labelling tyrosine with a fluorescent aniline molecule under mild conditions.[168] This has been utilised by Belle et al to attach a nitroxide spin label to a tyrosine residue in a small chloroplast protein.[169]

3.4.3 Spin labelling of tyrosine ester – proof of principle

The labelling of tyrosine with a nitroxide was adapted from the procedure reported by Belle et al.[169] 4-amino-2,2,6,6-tetramethylpiperidinyloxy nitroxide radical (4-amino-TEMPO) was used as a spin label. Initially, the reaction was attempted with free tyrosine ester rather than the polymer, and a non-spin active analogue of the nitroxide, 4-amino-2,2,6,6-tetramethylpiperidine (4-amino-TEMP) in 10mM pH 6.5 phosphate buffer, as shown in Scheme 3-1. This simplification enabled product analysis by NMR and ESI-MS (see Appendix 2).

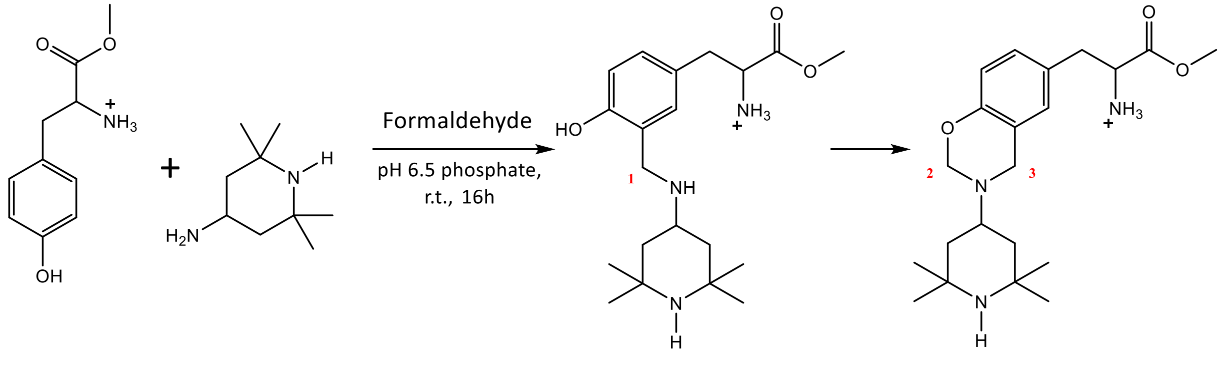

1 **2**

Scheme 3-1: Mannich coupling reaction of tyrosine methyl ester and 4-amino-TEMP with formaldehyde

^{1}H NMR analysis showed characteristic peaks at 4.75, 4.9 and 5.2 ppm, consistent with the formation of both the Mannich bridge intermediate **1** and the benzoxazine product **2** according to literature reports.[170] ESI-MS analysis showed peaks at m/z = 364.2600 and 376.2604 corresponding to the Mannich bridge intermediate and benzoxazine product respectively.

Tyrosine ester was also spin labelled with 4-amino TEMPO. ESI-MS showed a peak at m/z = 390.2372, corresponding to the benzoxazine product in addition to unidentified side products and starting material. As this was a proof-of-principle test, no further attempts were made to purify products or determine yield.

3.4.4 Spin labelling of polymer system – reaction optimisation

Spin labelling of PEG-Tyr with 4-amino TEMPO was attempted in 10 mM phosphate buffer at pH 6.5, however this yielded no labelled product when analysed by EPR spectroscopy. This indicates that tyrosine side chains buried within the core of micelle structures are significantly less chemically reactive than free tyrosine.

After reaction, excess spin label was removed by dialysis. PEG-Tyr micelles are too large to pass through the dialysis membrane (12000-14000 Da). The process could be monitored by EPR spectroscopy: dialysis was complete when no further loss to signal intensity was observed.

Several different solvent systems were attempted: 1:1 phosphate buffer/acetonitrile, methanol, DMF and pure acetonitrile. In less polar solvents, the polymers do not readily self-assemble. Tyr side chains are therefore more accessible. DMF and methanol both showed promising results. The polymer was therefore spin labelled with 4-amino-TEMPO as shown in Scheme 3-2. After reaction, methanol was removed and the sample redissolved in water before dialysis.

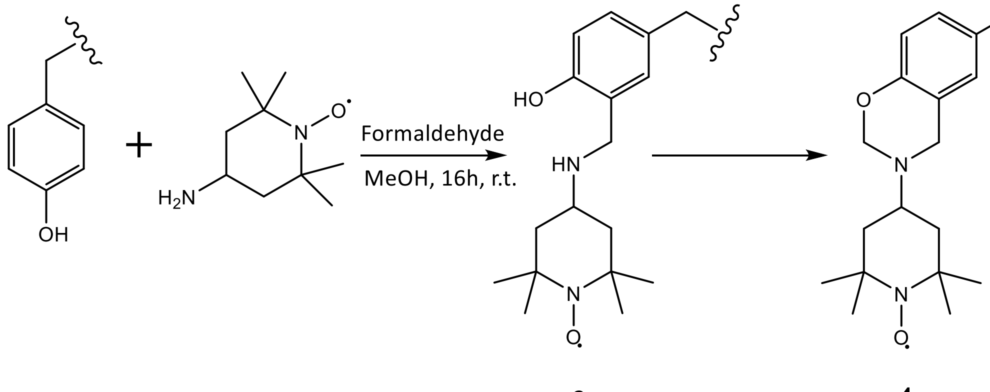

3 **4**

Scheme 3-2: Spin labelling of PEG-Tyr block copolymer tyrosine side chains with 4-amino-TEMPO

3.4.5 Yield of spin labelling reaction

The yield of the reaction was estimated by comparing the signal integral from a micelle EPR spectrum of spin labelled sample to that of a known concentration of free amino-TEMPO obtained under the same experimental conditions. These indicate that 0.3% of available tyrosine residues were successfully labelled. In a PEG_{2000}-Tyr_5 sample at 5 mg/ml, this corresponds to a nitroxide concentration of approximately 25 µ mol dm^{-3}. With 5 tyrosine residues per polymer chain, this means that 1.5% of polymer units are labelled, assuming only a single label per chain. This approximation of yield is very low. However, low yield does not influence the ability to probe Tyr environment by EPR, as the technique can detect stable nitroxide radicals at concentrations as low as 50 nM.[171] A lower yield is preferable as it decreases the likelihood on spin-spin interactions between nearby spin labels, which will influence the EPR spectrum.

3.5 Analysis of Spin Labelled Polymer Systems by EPR Spectroscopy

The environment of the nitroxide label in samples can profoundly affect the EPR spectrum. For radical centres with restricted mobility on a nanosecond timescale, magnetic tensors are not averaged out leading to anisotropy. This manifests through changes in line shape.[163] Interactions between neighbouring unpaired electrons on a nanometre scale can also influence linewidth and shape through exchange and dipole-dipole interactions.[172]

Spin probe studies have shown that nitroxide radicals buried within the core of a micelle structure exhibit significantly restricted tumbling compared to those free in solution. Spin-labelled PEG_{2000}-Tyr_5 was analysed by EPR (Figure 3-7) to identify if direct labelling of Tyr showed similar results.

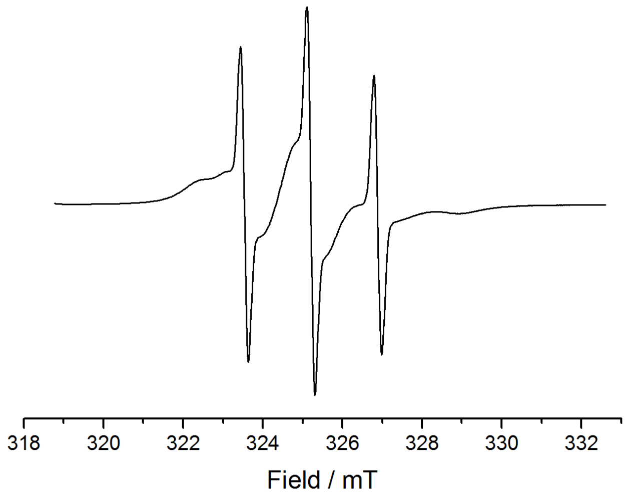

Figure 3-7: X-Band EPR spectrum of spin labelled PEG_{2000}-Tyr_5 micelle sample at room temperature. Polymer concentration 5 mg/ml

The spectrum in Figure 3-7 indicates nitroxides in a range of different environments. The three sharp peaks correspond to nitroxide which is relatively mobile (fast tumbling). Faster tumbling species have better averaged g- and A-tensors, leading to a spectrum similar to the isotropic spectrum of free nitroxide (1:1:1 triplet).

Restricted mobility leads to anisotropy and increased spin-spin relaxation time (T_2). This causes changes to the line shape and broadens the spectrum. The broad peaks at low and high field, and either side of the central sharp peak indicate nitroxide labelled tyrosine in a restricted environment. As the EPR spectrum is so highly sensitive to changes in nitroxide mobility, small differences in environment between systems can be compared.

3.5.1 Modelling nitroxide environment - considerations

To provide a comparison between different tyrosine environments in micellar and gel samples, quantitative information needs to be obtained from spectra. This is achieved by fitting and optimising simulations to experimental data.

By their nature, simulations offer a simplified approximation of the real system. Certain factors are discounted by models to decrease complexity and computation time. Polymeric micelles are often described as "kinetically frozen": the exchange of polymer units between micelle and solution is very slow. It is unlikely these processes impact mobility on the EPR timescale, therefore they were not modelled.[173] Brownian diffusion of micelles may impact the EPR spectrum.[174] Some models such as the Slow Relaxing Local Structure model developed by Freed et al account for such motion.[175-176] To simplify the model, such motion was not considered in this study.

It is unlikely that all labelled tyrosine units will fit into distinct groups corresponding to Tyr within a micelle and a free polymer unit in solution. Micelle concentration, neighbouring groups and the position of tyrosine in the polypeptide chain may influence mobility. In practice, modelling a range of tyrosine environments is challenging, approximation is therefore required. Models were limited to two or three distinct tyrosine components.

3.5.2 Determining Principal Values of the hyperfine and g-tensors

The initial parameters for modelling were determined by analysing a frozen spin labelled PEG_{2000}-Tyr_5 sample by Q-band EPR. The aim of carrying out measurements at low temperature is to prevent averaging of anisotropic parameters by completely immobilising the system. This allows the static parameters (principal values of g and A tensors) to be determined. These parameters can then be applied to simulations of dynamic systems at room temperature.

The magnetic field strength used for frozen experiments is an important consideration, as the electron and nuclear Zeeman interaction components of the spin Hamiltonian are field dependent.[162] Nitroxide radicals have a nuclear spin of ^{14}N $I = 1$, and overall electron spin $S = \frac{1}{2}$. The electron Zeeman interaction term of the Hamiltonian (H_{EZ}) is shown in Equation 3.2.

$$H_{EZ} = \frac{\beta_e}{\hbar} B_0^T g S \quad \text{(Equation 3.2)}$$

Where B_0 is the externally applied magnetic field, g is the g-factor of the unpaired electron and S is the spin angular momentum. At higher fields, the electronic Zeeman interaction becomes the dominant term of the spin Hamiltonian, leading to improved resolution of the three principal values of the g-tensor, g_{xx}, g_{yy} and g_{zz}. High field, high frequency Q-band EPR was selected for EPR analysis of frozen samples. A sample of spin labelled PEG_{2000}-Tyr_5 at a concentration of 5 mg/ml was analysed by Q-band EPR at -185 °C. The spectrum obtained is shown in Figure 3-8.

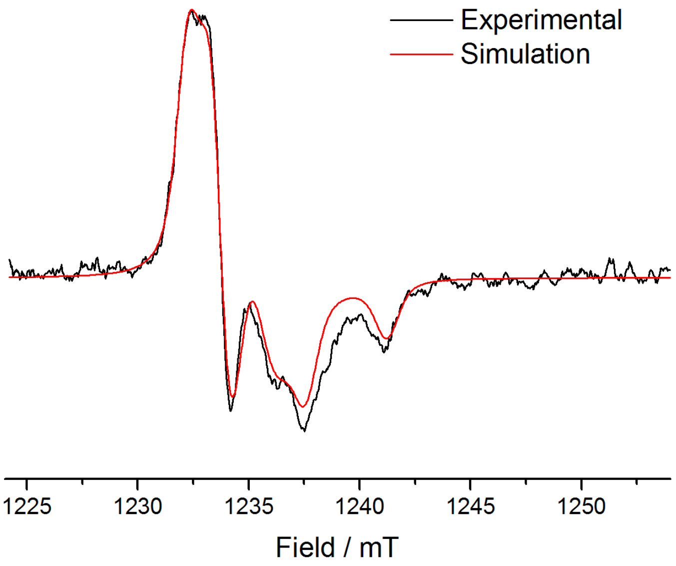

Figure 3-8: Q-band EPR spectrum of spin labelled PEG_{2000}-Tyr_5 at 88 K

A power saturation test was also carried out on the EPR signal: Q-band samples at low temperature are prone to saturation. If the microwave power applied to the sample is too large, an overpopulation of the higher energy spin state occurs as the saturation factor (Equation 3.3) deviates significantly from 1. This leads to a loss in intensity and signal broadening.[136] In Equation 3.3, γ_e refers to the gyromagnetic ratio of the electron spin, B_1 is the strength of the magnetic component of the microwave on the sample, and T_1 and T_2 refer to the longitudinal and transverse relaxation times, respectively.

$$Saturation\ factor = \frac{1}{(1+\gamma_e^2 B_1^2 T_1 T_2)} \quad \text{(Equation 3.3)}$$

The optimal microwave power for measurements was 124 µW, as shown in Figure 3-9, where the square root of microwave power is plotted against signal intensity. At higher microwave power, the signal intensity reaches a peak and then starts to decrease as saturation is observed.

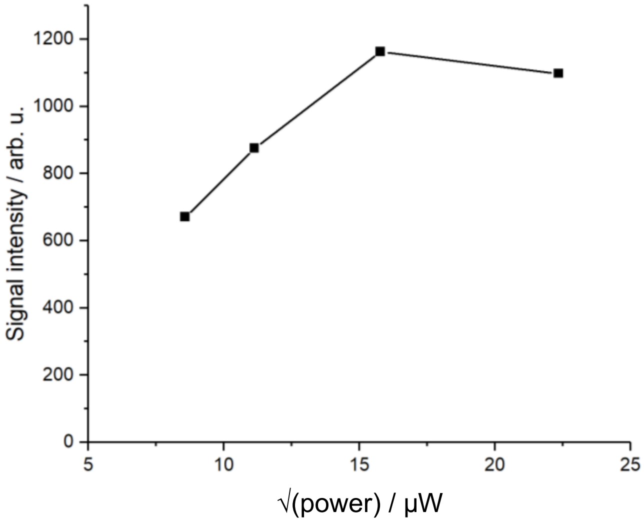

Figure 3-9: Power saturation experiment showing change in EPR signal intensity with microwave power at Q-band

3.5.3 Fitting of Q-band frozen spectrum

The low temperature Q-band spectrum shown in Figure 3-8 is quite weak, due to low spin concentration in the sample. Nevertheless, a simulation was fitted to experimental data using easyspin (pepper function).[177] The simulation was optimised by least squares fitting using Nelder Mead simplex and Levenberg-Marquardt algorithms. The simulated and experimental spectrum are compared in Figure 3-8.

As Figure 3-8 shows, the simulated fit is not perfect, although it offers a reasonable representation of the noisy experimental spectrum. Phase separation and aggregation of the sample during freezing may affect sample homogeneity, which may explain why a single component simulation did not fit perfectly.

Dynamic properties of the nitroxide are removed in frozen samples, allowing static parameters such as anisotropic g-values and hyperfine coupling constants to be derived. These were calculated from the simulation, and are shown in Table 3-2.

Table 3-2: Static Parameters of spin labelled PEG$_{2000}$-Tyr$_5$ nitroxide radical calculated by fitting simulation to Q-band EPR spectrum of frozen solution.

	x	*Y*	*z*
g	2.00917	2.00579	2.00214
A / MHz	21.7278	17.4809	102.858

Each principal axis relative to the magnetic field shows a different value for g and A, revealing that the nitroxide exhibits rhombic symmetry. This is to be expected in the frozen sample, where paramagnetic centres are unable to realign. The hyperfine values for the *x* and *y* axes are very close, indicating that the symmetry is close to axial.

3.5.4 Applying derived static parameters to dynamic (unfrozen) samples – 2 component simulation

Static parameters derived from frozen simulations can be applied to model the system in a dynamic state at room temperature. X-band EPR was used for room temperature measurements, due to practical considerations such as the ability to use a larger volume aqueous sample, allowing comparison between micellar and gel systems. X-band measurements are also sensitive to mobility restrictions on a timescale around 10^{-11} - 10^{-7} seconds, relevant to more dynamic spin-labelled biological systems.[178]

Using static parameters in Table 3-2, a spectrum was simulated and fitted to an experimental spectrum acquired at room temperature for spin-labelled PEG$_{2000}$-Tyr$_5$ micelles. At room temperature, it is also necessary to consider molecular dynamics (tumbling rates). The simulation modelled two different tumbling rates, to account for nitroxide within micelle cores and in a less restricted environment. Given the chemical structure of the labelled tyrosine (Scheme 7-1), and the results in Table 3-2, anisotropic (axially symmetric) rotation is assumed. The rotational diffusion rate D is thus split into $D_\perp$ and $D_\parallel$ for rotation perpendicular and parallel to the principal rotation axis. The simulated spectrum is compared with experimental results in Figure 3-10.

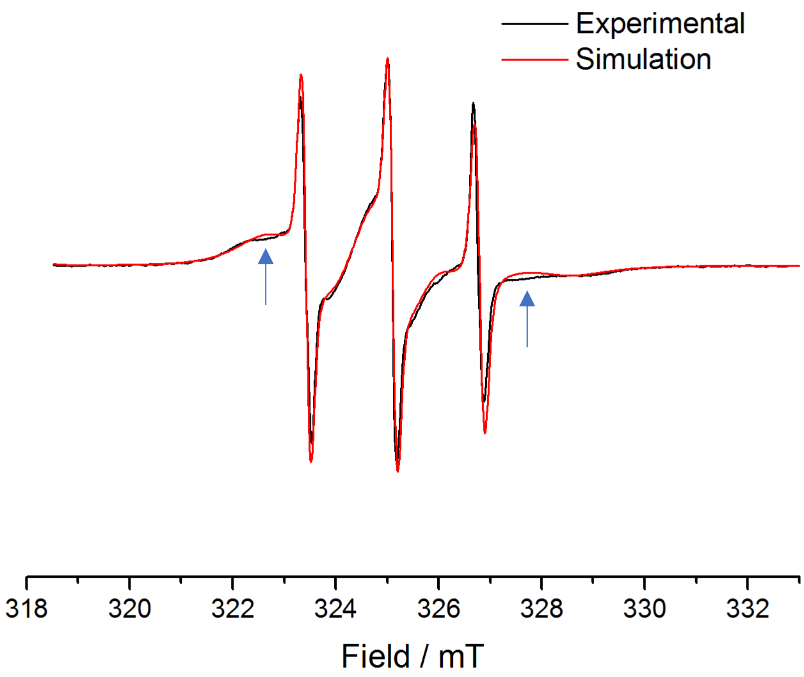

Figure 3-10: Two component simulation of 5 mg/ml PEG$_{2000}$-Tyr$_5$ spin labelled micelle spectrum, compared to experimental spectrum

The optimised simulation shown in Figure 3-10 fits the experimental data reasonably well, optimised parameters are shown in Table 3-3. The ratio of slow to fast component was 7.13, indicating that around 88% of labelled nitroxide is in the more restricted environment.

Table 3-3: Optimised values for logarithm of rotational diffusion tensors of two component spin labelled PEG$_{2000}$-Tyr$_5$ X-band EPR spectrum

	log $D_{\perp}$ / s^{-1}	**Log $D_{\parallel}$ / s^{-1}**
Fast component	9.28	10.83
Slow component	7.52	7.23

The rigid limit of the EPR timescale corresponds to a rotational diffusion rate of around 100 ns (corresponding to a log(D) value of 7). The rapid limit is around 0.01 ns (log(D) = 11). Changes to diffusion rates outside these limits are not reflected in X-band EPR spectra. Both components simulated show restricted rotation on the EPR timescale, and are therefore distinct from free nitroxide in solution. The slower component is almost completely immobilised; it is likely that this corresponds to nitroxide buried within the micelle core.

Aqueous amino-TEMPO solutions (with the same spin concentration as crude labelled product) dialysed under the same conditions showed no EPR signal, indicating that all residual free amino-TEMPO is removed. The fast component therefore likely corresponds to non-aggregated or partially aggregated polymers.

The two-component model fits the slow component poorly, visible around 322.5 mT and 327.5 mT particularly (arrows on Figure 3-10). This highlights that there is a range of Tyr environments within the system, and modelling only two components is an oversimplification. The fitting algorithm attempts to model the distribution of environments by broadening the linewidth of the slow component. Line broadening is limited to either Gaussian, Lorentzian or a convolution of the two functions (Voigtian). The distribution of nitroxide environments in the micelle system does not follow a Normal, Cauchy or Voigt distribution, therefore simple line broadening cannot accurately model the range in nitroxide environments.

3.5.5 Introduction of additional component and improved fitting

In order to improve the modelling of restricted tyrosine environments, a further set of simulations was performed, introducing a third spectral component. Slow mobility radicals were not modelled accurately by a single environment, this additional component is also a simplification. However, inclusion of a greater number of distinct components is impractical computationally. A three-component simulation offers a compromise between simulation quality and computational demand. The simulation is compared to experimental data in Figure 3-11. Dynamic parameters from the optimised simulation are shown in Table 3-4, static parameters shown in Table 3-2 were used for the simulation.

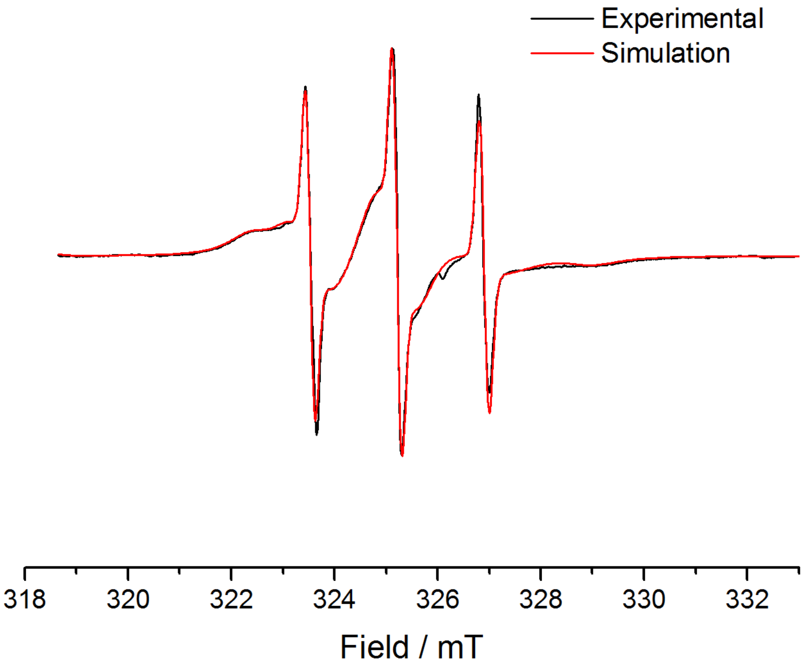

Figure 3-11: Three component simulation of 5 mg/ml PEG$_{2000}$-Tyr$_5$ spin labelled micelle spectrum, compared to experimental spectrum

The three-component model (Figure 3-11) offers a more accurate approximation of tyrosine environment than the simpler two-component model (Figure 3-10). Distribution of the low field broad peaks and the central broad peak are well modelled. Despite these improvements, the three-component simulation is still a simplification, and the high field region around 328.5 mT is not perfectly modelled. The small peak in the experimental spectrum around 326 mT is attributed to defect centres in the quartz flat cell used to hold the sample.

Despite the visual dominance of the sharp EPR lines in the spectrum, the relative area of these peaks is much smaller, with a ratio of around 13:1 for “slow” and “fast” components. This indicates that around 93% of labelled tyrosine is in the more restricted environment. The ratio is significantly higher than in the two-component simulation, where the fitting algorithm likely broadens the “fast” peaks to account for the variation in slow mobility. This will artificially increase the contribution of the fast component. An additional component gives extra scope for achieving a good fit, therefore the fitting process is less likely to result in artificial line broadening. The ratio indicated by the three-component system is therefore more likely to be accurate. Fitting error (measured by the sum of squares of experimental minus simulation) is 0.98%.

Table 3-4: Optimised parameters for nitroxide components of X-band EPR spectrum of labelled PEG$_{2000}$-Tyr$_5$ micelles

	Gaussian Linewidth / mT	**Lorentzian Linewidth / mT**	**log D$_\perp$ / s^{-1}**	**Log D$_\parallel$ / s^{-1}**	**Relative contribution**
"Fast"	0.2198	0.0000	9.5476	9.6372	1.0000
"Slow" A	0.2682	0.4919	7.1023	7.4527	6.5881
"Slow" B	0.6356	0.3140	7.9136	8.4558	6.3433

The results show that the slowest component, "Slow A" is almost completely immobilised on the EPR timescale. In comparison, "Slow B" is more mobile. There is a roughly equal split between the two "slow" components, indicating a relatively broad distribution of tyrosine mobility within the micelle structure.

3.5.6 Validation of model: multifrequency analysis

The validity of the three-component fit was tested by applying log(D) and relative contribution parameters from Table 3-4 to a simulation of a room temperature Q-band spectrum. An experimental Q-band spectrum was recorded and compared in Figure 3-12.

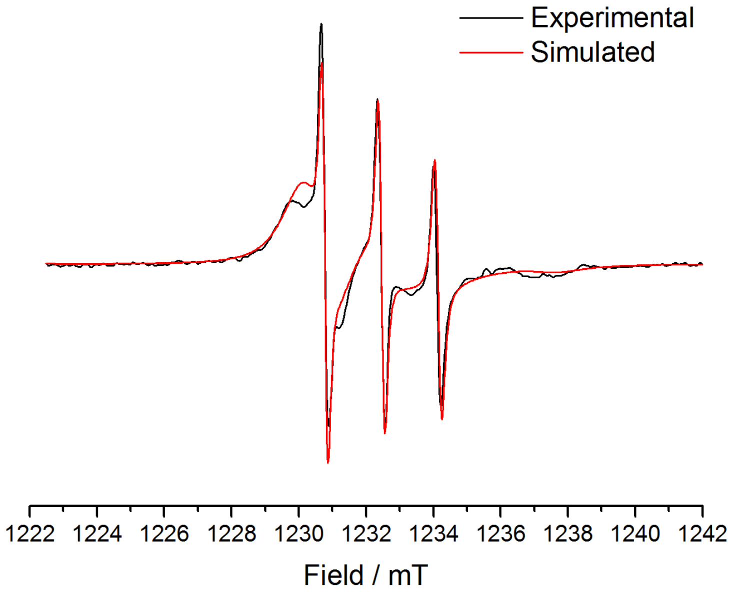

Figure 3-12: Testing the three-component model of PEG$_{2000}$-Tyr$_5$ micelle system - examining the quality of fit in high field Q band EPR measurement

The fit is reasonable but not perfect: although the fast mobility component fits well, the slower components are less well modelled, with the model overestimating mobility in slow components compared to experimental data. The quality of fit may be limited by the comparatively noisy experimental spectrum. A significant peak around 1236 mT attributed to glassware defects was removed through subtraction of a background spectrum, which may influence the quality of fit in the high field region. Despite these limitations, the three-component model provides a sufficient level of accuracy to use for comparisons between systems. Further components will likely offer only marginal improvement whilst significantly increasing the complexity of calculations. Three-component simulation models were therefore used to compare micelle and gel environments.

3.6 Micelle and Gel systems: Comparison of tyrosine environments by EPR spin labelling

At a concentration of 5 mg/ml, aqueous PEG$_{2000}$-Tyr$_5$ samples form gels after heating to 65 °C for 1 hour. Gelation was confirmed by inversion of sample in a cuvette. Spin labelled samples do not show a significant difference in gelation properties compared to unlabelled polymers under the conditions tested. Gelation in the EPR flat cell was confirmed visually.

3.6.1 Gel system: analysis of EPR spectrum

An EPR spectrum of PEG$_{2000}$-Tyr$_5$ was recorded after gelation, and is shown in Figure 3-13. Despite being from the same sample, the spectrum has changed notably compared to the micelle spectrum (Figure 3-11). The restricted mobility environment is particularly clearly defined by broad peaks at low and high field (arrows on spectrum).

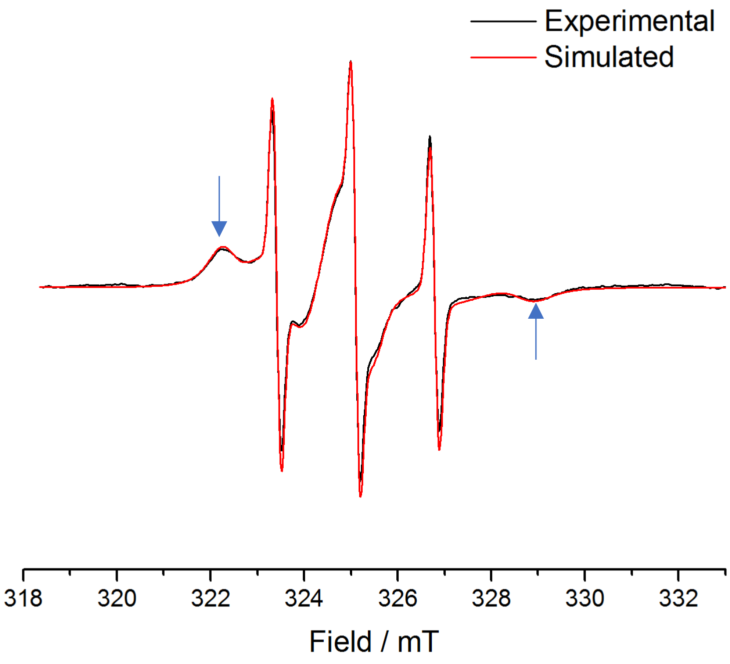

Figure 3-13: Experimental and simulated 3 component EPR spectra of PEG$_{2000}$-Tyr$_5$ spin labelled gel

A three-component model simulation was fitted to the gel spectrum, shown in Figure 3-13. The simulation fitted the experimental data well, with a fitting error of 0.6%. After gelation, there is still a significant "fast" mobility component, possibly corresponding to free polymer in solution or partial aggregate structures. This shows that not all polymers form gel fibres. The optimised rotational diffusion rates, relative contributions and linewidths of each component are shown in Table 3-5. Parameters derived from simulations were then used to quantitatively compare tyrosine environment in micelles and gels.

Table 3-5: Optimised parameters for nitroxide components of X-band EPR spectrum of labelled PEG$_{2000}$-Tyr$_5$ gel

	Gaussian Linewidth / mT	**Lorentzian Linewidth / mT**	**log $D_\perp$ / s^{-1}**	**Log $D_\parallel$ / s^{-1}**	**Relative contribution**
"Fast"	0.2116	0.0169	9.3478	9.4372	1.0000
"Slow" A	0.3732	0.1060	7.0551	7.5709	6.5185
"Slow" B	0.9312	0.0416	7.8551	8.2275	4.9886

3.6.2 Comparison of micelle and gel environments

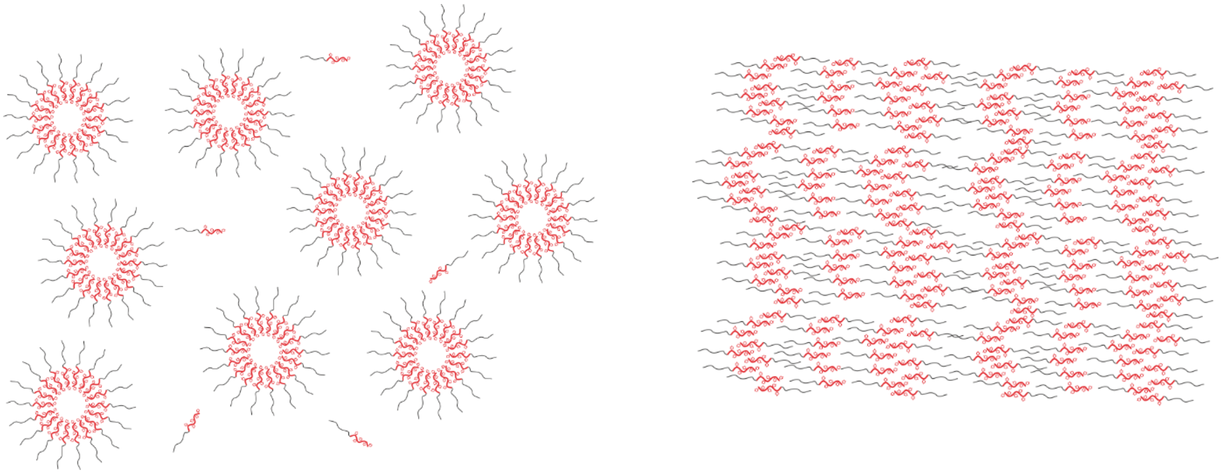

Figure 3-14: Simplified 2-dimensional visual representations of PEG-Tyr micelle and gel systems. Polymers arrange through π-π stacking of tyrosine side chains and other non-covalent interactions, creating immobilised hydrophobic and hydrophilic regions.

A simplified 2-dimensional representation of micellar and gel PEG-Tyr environments is shown in Figure 3-14. Several metrics derived from EPR simulation models could be used to compare the environment of nitroxide labelled tyrosine in model systems. Rotational diffusion rates can be compared between systems to reveal information about the mobility of the radical centre. Linewidths of different components can reveal information about intermolecular interactions.

Changes to the relative contributions of different spectral components indicate bulk changes to the overall mobility of the system.

The primary parameter comparing the environment of a spin label is the rotational diffusion rate, a measure of how mobile the labelled tyrosine is. Mobility will influence the reactivity of tyrosine units: more mobile Tyr can interact with dissolved molecules and neighbouring groups better. However, increased mobility can also lead to more rapid quenching of excited states and radical recombination.

The average mobility of each of the three components of simulation models, (average of parallel and perpendicular terms) is shown in Table 3-6. The average mobility of nitroxide labelled tyrosine in the entire system was then calculated as a weighted average based on the contribution of each component.

Table 3-6: Average rotational diffusion rates for individual components and overall weighted average for micelle and gel systems. Measurement error given in brackets, calculated based upon error in optimised simulation against experimental data

	"Fast"		**"Slow A"**		**"Slow B"**		**System**
	Log D (av) / s^{-1}	**Weight**	**Log D (av) / s^{-1}**	**Weight**	**Log D (av) / s^{-1}**	**Weight**	**Weighted log D (av) / s^{-1}**
Micelle	9.5924	1	7.2775	6.5881	8.1847	6.3433	**7.8567**
	(0.0940)	(0.0098)	(0.0713)	(0.0646)	(0.0802)	(0.0622)	**(0.0770)**
Gel	9.3925	1	7.3130	6.5185	8.0413	4.9886	**7.7698**
	(0.0564)	(0.0060)	(0.0439)	(0.0391)	(0.0482)	(0.0299)	**(0.0466)**

As averages, the values shown as system weighted log D values in Table 3-6 do not offer a true representation of the mobility of individual tyrosine units within micelle or gel systems. They do show the general change in mobility between micelle and gel systems. On average, tyrosine has lower mobility in gel systems compared to micelles, although the difference is small and almost within measurement error. The change in log(D) corresponds to an 18.1% decrease in the tumbling rate, indicating that tyrosine in gel fibres has more restricted mobility.

The slow components of the spectrum become more homogenous on gelation, with the faster "Slow B" decreasing in mobility and the slower "Slow A" increasing mobility. This results in clearly defined broad peaks in the low and high field regions of the gel sample spectrum. The gel system has a more homogenous distribution of tyrosine environments immobilised within fibres compared to the tyrosine immobilised in micelle cores.

The overall ratio of “slow” to “fast” components decreases slightly from 12.93 to 11.51 upon gelation. This suggests that at this polymer concentration, 5 mg/ml (corresponding to 1.72 mmol polymer), and heating time (1 hour), the sample contains free polymers or partial aggregates in solution, in addition to gel fibres. Gel formation is a gradual process, especially at lower polymer concentration.[143] Micelle structures may break rapidly upon heating, with polymers taking a longer time to arrange into gel fibres. This would result in an increase in free polymer / partial aggregates, heating over a longer period may result in these forming gel fibres, although this was not studied at this concentration. Further investigation of changing mobility during the gelation process is carried out in section 3.7.

3.6.3 Relating environment in model systems to protein tyrosine environment

There is limited scope for direct comparison between Tyr environment in model systems and in proteins. Few spin-labelled tyrosine residues are reported in literature, and different spin labels or amino acids will behave differently. However, a single Tyr within a small chloroplast protein CP12 has been successfully spin labelled with a similar nitroxide by Belle et al.[169] The Tyr residue is in a relatively accessible, free part of the protein, making attachment of the spin label more straightforward.[179] The labelled Tyr residue exhibits a slight reduction in mobility on the EPR timescale, giving a rotational diffusion rate of 0.125 ns, equivalent to a log D value of 9.9031 s^{-1}. The Tyr environment in CP12 is therefore significantly less restricted than in PEG-Tyr micelles or gels. However, CP12 is unlikely to be an accurate representation of keratin proteins, which adopt a primarily helical structure.[180]

The inverse central linewidth (ΔH_0^{-1}) of a nitroxide spectrum can also be used as a measure of system mobility and rotational diffusion rate.[181] Experiments with labelled cysteine residues have indicated that nitroxides within helical structures are likely to have a ΔH_0^{-1} of 0.1–0.3 G^{-1}, depending on how exposed the residue is. It should be noted that this is a different spin labelling system, therefore direct comparison with tyrosine labelling may not be accurate. However, it is likely to give some indication of how tyrosine in the model system may compare with tyrosine in keratin proteins. Inverse central linewidth values of the two “slow” components are 0.135 G^{-1} and 0.137 G^{-1}, comparable with helical type protein structures. The environment of tyrosine in PEG-Tyr model systems therefore provides a good mimic of Tyr in keratin proteins.

3.6.4 The effect of polymer concentration

Polymer concentration is known to influence the structural properties of the gel, as well as gelation temperature and time and photochemical reactivity. This may be due to a change in tyrosine environment. Spin labelled polymer was therefore analysed at a higher concentration, to observe any impact of polymer concentration upon tyrosine environment.

EPR measurements on spin labelled micelle systems do show slight differences between samples at different polymer concentrations. The simulated fits of experimental data for micelle systems at both the higher polymer concentration of 10 mg/ml and 5 mg/ml are compared in Figure 3-15. Data has been normalised based on 2nd integrals of the spectra. Average rotational diffusion rates and contributions of the three simulated components are compared for the two concentrations in Table 3-7.

Table 3-7: Comparison of rotational diffusion rates and relative contributions for fitted simulated components of experimental data at different polymer concentrations.

Polymer conc. mg ml^{-1}	**"Fast"**		**"Slow A"**		**"Slow B"**		**System Weighted log D (av) / s^{-1}**
	Log D (av) / s^{-1}	**Weight**	**Log D (av) / s^{-1}**	**Weight**	**Log D (av) / s^{-1}**	**Weight**	
5	9.5924	1	7.2775	6.6	8.1847	6.3	**7.8567**
10	9.2468	1	7.2608	4.1	8.0330	4.5	**7.8947**

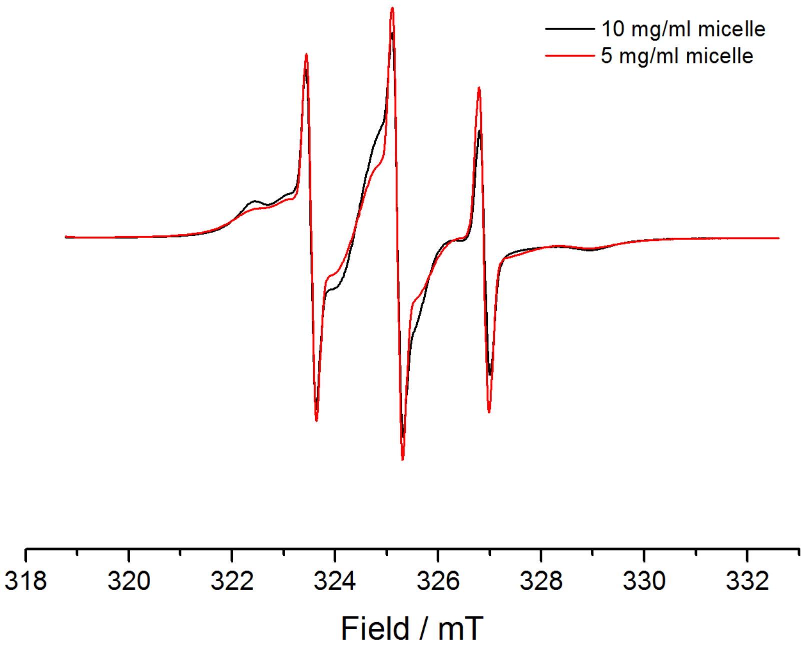

Figure 3-15: Fitted simulations of spin labelled PEG$_{2000}$-Tyr$_5$ micelle spectra at different polymer concentrations

DLS measurements indicate that there is no significant change in micelle size or polydispersity with polymer concentration (see section 4.7.1). Despite this, overall tyrosine mobility (based on average log(D) in Table 3-7) is slightly greater at higher polymer concentration. The difference is less significant than between micelles and gels.

Higher mobility may be due to increased exchange of polymers between micelles in a more dynamic micelle system. Mattice et al use computational modelling to predict a significant increase in exchange between polymeric micelles at higher polymer concentration as the number of micelles in the system increases and exchange processes become more kinetically favourable.[182]

This increase in mobility, potentially driven by increased exchange between micelles, may explain the decrease in gelation time and increase in photochemical reactivity at higher concentration. However, it should be noted that the differences in tyrosine environment are very slight. Environmental factors alone are unlikely to explain the change in photochemical reactivity. The role of reactive oxygen species is discussed in section 4.7.

3.6.5 The effect of polymer length

Changing polymer length influences hydrophobic and hydrophilic interactions which drive self-assembly (see section 3.2). Micelle size is influenced by hydrophobic/hydrophilic ratio (see

Figure 3-2). Polymer length also influences gelation conditions (see section 3.3). The aim of this study was to analyse and compare tyrosine environments in micelles of two different polymer lengths, to determine if changing amphiphilic properties of the polymer influences the environment in the micelle core.

The longer polymer PEG$_{5000}$-Tyr$_{10}$ was also spin labelled, and analysed by EPR spectroscopy. Figure 3-16 shows experimental and simulated EPR spectra for spin labelled PEG$_{5000}$-Tyr$_{10}$ micelles at a concentration of 5 mg/ml. Average rotational correlation times are shown in Table 3-8, compared with the values for PEG$_{2000}$-Tyr$_{5}$ micelles.

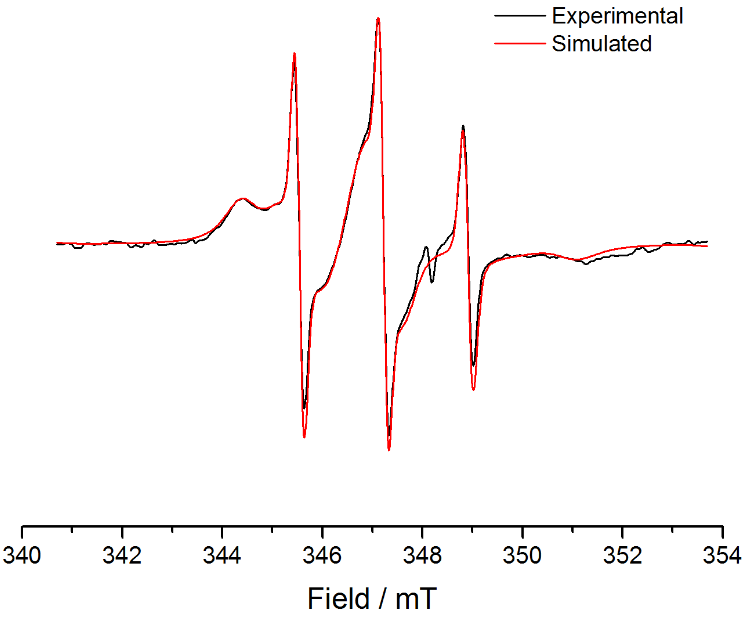

Figure 3-16: Experimental and simulated EPR spectrum of spin labelled PEG$_{5000}$-Tyr$_{10}$ micelles at a concentration of 5 mg/ml

Table 3-8: Comparison of rotational diffusion rates and relative contributions for fitted simulated components of experimental data for different polymer lengths.

Polymer length PEG-Tyr	"Fast"		"Slow A"		"Slow B"		System Weighted log D (av) / s^{-1}
	Log D (av) / s^{-1}	Weight	Log D (av) / s^{-1}	Weight	Log D (av) / s^{-1}	Weight	
2k-5	9.5924	1	7.2775	6.6	8.1847	6.3	**7.8567**
5k-10	9.0860	1	7.0500	5.5	8.0774	7.8	**7.7500**

The three-component simulation does not model the broad peak at 351 mT perfectly. This may be a limitation of the simplified model; the experimental signal is also weaker than for earlier experiments. Generally, the model fits the experimental data well.

Overall mobility of tyrosine in the longer polymer system is lower than the shorter polymer. The longer hydrophobic chain in PEG_{5000}-Tyr_{10} will result in increased intermolecular interactions such as π-π stacking, which create a more rigid, thermodynamically stable micelle core. This results in a more restrictive tyrosine environment, with both simulated slow components more restricted than the shorter polymer. This effect has been observed in other di-block copolymer micelles.[150] This agrees with DLS measurements: the longer polymer gives micelles of smaller hydrodynamic radius, due to the lower hydrophobic/hydrophilic mass ratio (see Figure 3-2). Increased thermodynamic stability also explains the lower cmc for longer polymers (see section 3.2.2).

Changing hydrophilic/hydrophobic ratio is also likely to influence the kinetic stability of micelles. The effect of tyrosine chain length in PEO-block-polytyrosine micelles has been studied by Wishart et al.[150] Generally, a longer hydrophobic proportion results in improved kinetic stability. The hydrophilic component may also influence kinetic stability. PEG chains create a hydrophilic “corona” around the hydrophobic core through interactions between chains and with water molecules. This protects the core from breaking down upon exposure to aqueous medium.[183] A longer PEG chain will improve surface coverage and consequently stabilise the micelle.[154]

3.6.6 Tyrosine environment in model systems: conclusions

By labelling tyrosine residues in PEG-Tyr polymers with a stable nitroxide radical, the mobility of tyrosine in model systems can be probed by EPR spectroscopy. Tyrosine mobility is key to understanding reactivity. Results highlight a distribution of mobility in both micelle and gel systems. This was modelled with a multi-component simulation, approximating 3 distinct tyrosine environments. This 3 component model fitted experimental data well.

Despite significantly different bulk properties, micelle and gel systems exhibit remarkably similar tyrosine environments. However, there are crucial differences. Micelle structures represent a local kinetic minimum, stabilised by the hydrophilic/hydrophobic balance of the polymer and intermolecular interactions. Longer polymers increase thermodynamic stability: hydrophobic interactions make micelle cores more rigid, PEG_{5000}-Tyr_{10} micelles consequently exhibit a more restrictive tyrosine environment than PEG_{2000}-Tyr_5.

At higher polymer concentration, this kinetic stability is reduced: increased exchange between micelles decreases their stability, resulting in a more dynamic system with a slightly less restricted tyrosine environment.

When heated, micelles can rearrange to form a gel with higher kinetic stability than the micelle structures. The tyrosine environment becomes more homogenous, with experimental data showing a narrower distribution of immobilised tyrosine environments, and an overall decrease in mobility, as long-range order develops and the extent of intermolecular interaction between both hydrophilic and hydrophobic components increases.

3.7 Monitoring gelation as it happens

Micelle and gel environments, whilst similar, are distinct when measured by EPR in spin labelled systems. This presents a unique opportunity to monitor the process of PEG-Tyr gel formation. Gelation conditions, polymer length and concentration can all influence the stability of gel fibres.[143] The aim of this investigation is to use EPR spin labelled samples to study the gelation process *in situ* at a particular concentration. This may reveal information about the gelation process and any intermediate structures.

Previous circular dichroism studies have indicated an increase in β-sheet type aggregates upon heating.[143] These may correspond to an intermediate arrangement of polymer fibres, and EPR studies will aim to model the change in tyrosine environment as samples transition from micelles to gels.

3.7.1 DLS measurements – examining changes to particle size upon heating

At a low polymer concentration (1 mg/ml), PEG_{5000}-Tyr_{10} does not readily form gel fibres. Despite this, DLS measurements do show that heating to a temperature of 50 °C over a prolonged period leads to a decrease in average particle size, shown relative to an unheated control sample in Figure 3-17.

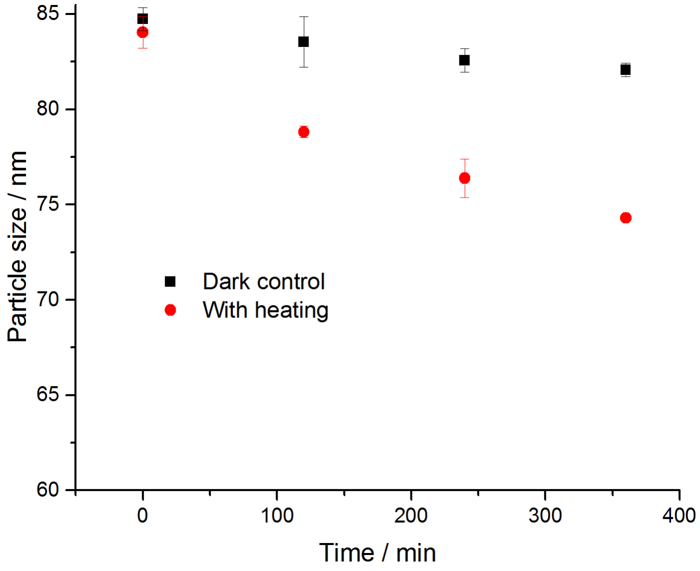

Figure 3-17: DLS measurements of particle size change over prolonged heating to around 50 °C. PEG_{5000}-Tyr_{10} samples at 1 mg/ml. Average of 3 measurements, error bars show 95% confidence intervals

Even at low concentrations, the thermal stability of the micelle structures is limited: distinct structural changes occur upon application of minimal heat. DLS cannot reveal information about structural changes beyond this decrease in micelle size. However, over a 24 hour heating period, DLS measurements indicated the presence of large structures which disrupted the measurement. This was despite the concentration being too low for stable hydrogel formation, and the sample remaining sealed throughout.

At a higher concentration of 10 mg/ml, a stable gel is formed within 10 minutes of heating to 65 °C. Consequently, changes to the system observed by DLS are far more dramatic. Figure 3-18 shows the change in particle size distribution upon heating to this temperature for short periods. The sample was cooled to 20 °C before measuring. The same sample (in a sealed cuvette) was used for all measurements to prevent dust or other contamination affecting the result.

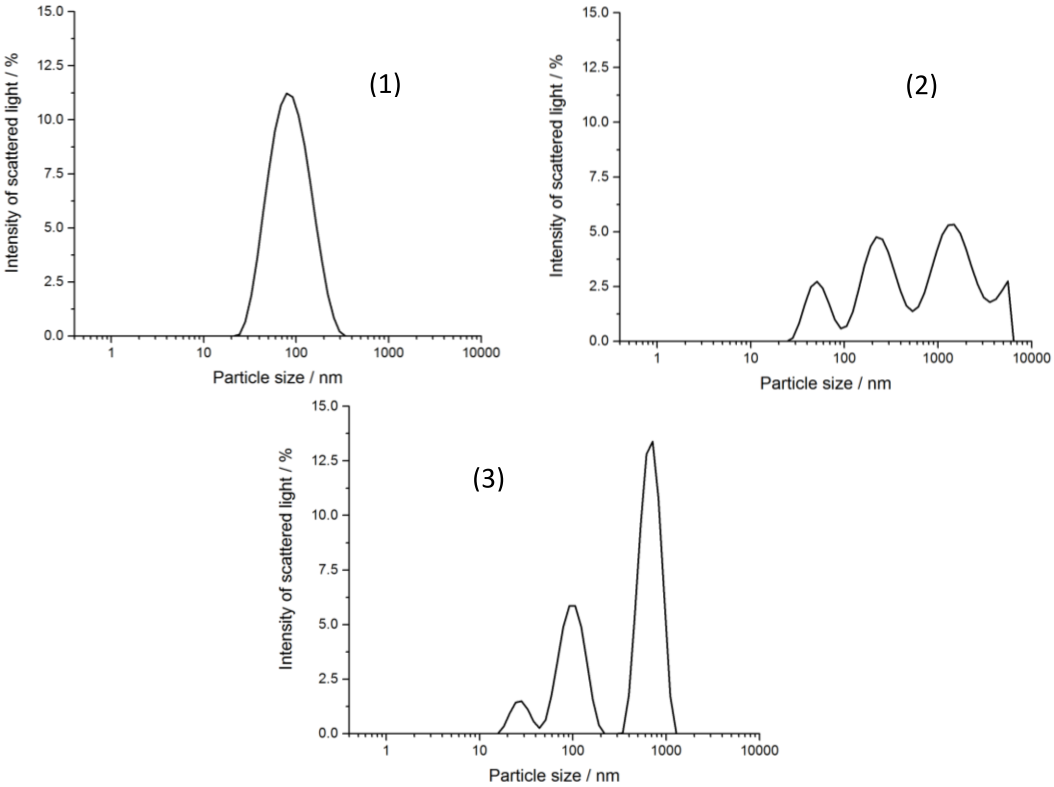

Figure 3-18: DLS measurements of sealed 10 mg/ml PEG_{2000}-Tyr_5 sample before (1), after 30 (2) and 60 (3) seconds of heating at 65 °C

The drastic change in Figure 3-18 indicates a rapid collapse of micelle structure at this higher polymer concentration. The high polydispersity shown in measurements 2 and 3 indicate a range of intermediate structures formed before complete gel formation. The structures remain stable upon cooling: measurements were performed at 20 °C. Intermediate structures are therefore stable, and may be β-sheet type structures predicted by circular dichroism studies.[143] However, DLS becomes unreliable in the presence of large aggregates and reveals no information about their structure.

The change in average particle size was also monitored by DLS over a longer heating period. As fibres form and combine into larger structures, the average particle size measured by DLS increases over the first 3 minutes as shown in Figure 3-19. However, when particle size becomes too large (beyond 3 minutes), DLS is unable to accurately measure the sample due to too much light scatter. DLS therefore does not show the formation of gel fibres, beyond the initial rearrangement into aggregate structures of increasing size. EPR analysis of spin labelled samples was therefore used to monitor gel formation.

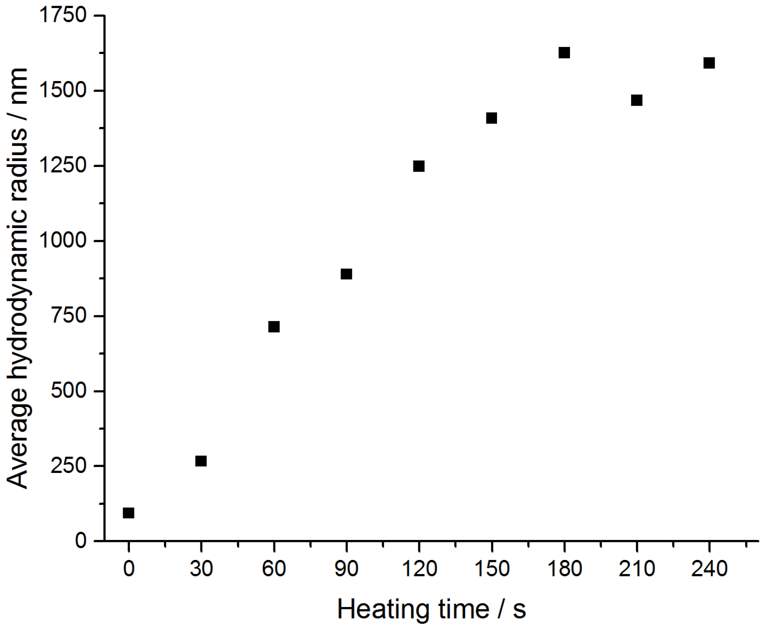

Figure 3-19: Change in average particle size (hydrodynamic radius) upon heating a PEG$_{2000}$-Tyr$_5$ 10 mg/ml sample to 65 °C

3.7.2 Monitoring gelation of spin labelled system by EPR spectroscopy

The EPR spectra of spin-labelled PEG$_{2000}$-Tyr$_5$ micelles and gels are distinct (see Figures 3-11/3-13), despite similar tyrosine environments. Gel fibre formation can therefore be monitored by looking at the changing spectral profile over time upon heating.

Direct monitoring of gelation by *in situ* heating of the sample in the EPR cavity was unsuccessful. At high temperatures (> 50 °C), the increased kinetic energy of the sample resulted in a broadening of spectral features and a loss of clearly defined "slow" and "fast" components. At a polymer concentration of 5 mg ml^{-1}, gel formation takes a considerable time, with micelle breakdown occurring within 20 minutes of heating and a stable gel forming after 60-70 mins of heating to 65 °C, by EPR measurements and visual observation. At polymer concentrations < 5 mg ml^{-1}, or at lower temperature, no gel formation was observed either qualitatively or by changes to EPR spectra over extended periods of up to 24 hours. A further experiment found that at a higher gelation temperature (80 °C), the gel formed very rapidly but continued heating resulted in collapse of gel structure. Optimising these conditions is therefore key to observing gel formation *in situ*. Experiments were therefore carried out at the same concentration as DLS samples, 10 mg/ml.

A spin labelled 10 mg/ml PEG$_{2000}$-Tyr$_5$ polymer sample was monitored over a 20-minute heating period. Given that DLS studies reveal intermediate structures are stable upon cooling, spectra were recorded at room temperature, after heating to 65 °C for 30-240 second periods. Key spectra are shown in Figure 3-20.

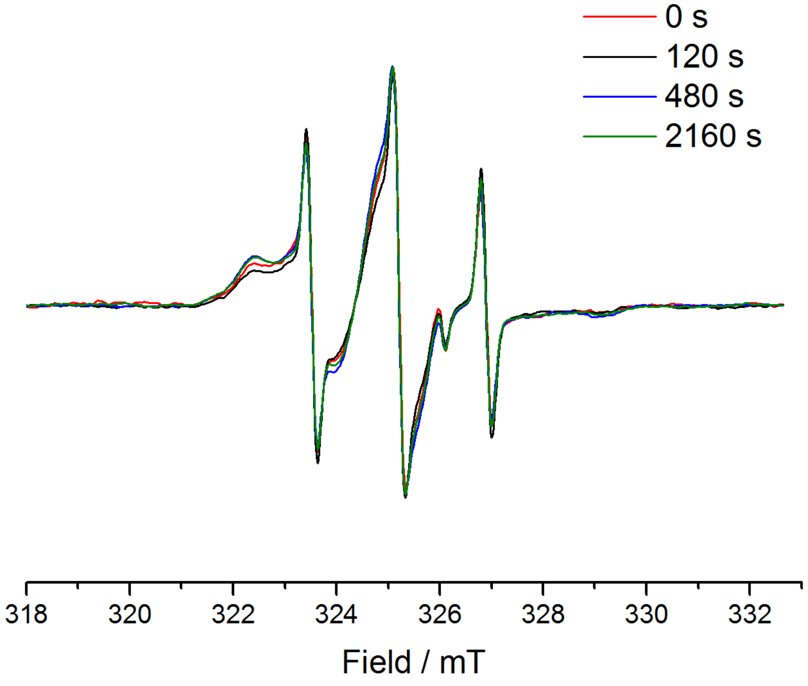

Figure 3-20: Selected experimental spectra throughout gelation process of PEG$_{2000}$-Tyr$_5$. Spectra normalised based on intensity of central sharp peak.

The spectra show a decrease in "slow" components relative to the fast component over the first 120 seconds of heating. This is indicative of micelle structure breaking down. There are still significant immobilised components present after the initial heating period. Individual polymer molecules are unlikely to be present in free solution due to unfavourable solvent interactions with the hydrophobic block. The spectrum after 120 seconds likely reflects intermediate, loosely aggregated structures predicted by DLS measurements (Figure 3-18). These structures appear to exhibit a more mobile tyrosine environment.

With continued heating, there is an increase in immobilised component as the gel fibre forms, with the slowest mobility component gradually becoming more clearly defined. An experiment was carried out to map the change to a 10 mg/ml PEG$_{2000}$-Tyr$_5$ sample upon heating. The sample was heated for short periods, cooled to room temperature and a spectrum recorded. The process was then repeated to give data for 20 mins heating time. Three-component simulations were fitted to experimental data, and the changing ratio of combined "slow" components to the "fast" component are shown in Figure 3-21.

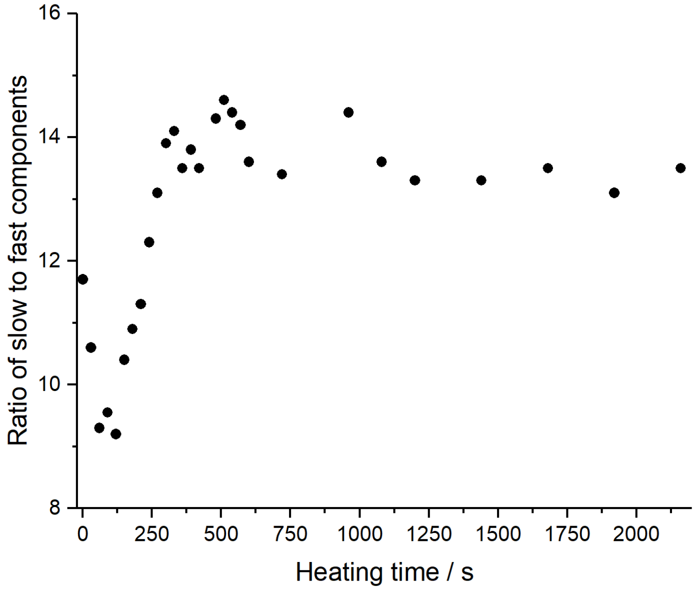

Figure 3-21: Change in combined slow components contribution to EPR spectrum of PEG_{2000}-Tyr_5 relative to fast component upon heating. Polymer concentration 10 mg/ml.

The breakdown of micelle structure is evident from the first 2 minutes of heating: combined slow components decrease by 22% over this time. After that, the contribution of slow components to the overall spectrum rises significantly, increasing by 59% over the subsequent 8 minutes as the gel forms. Beyond this, the EPR data indicates that gel formation is complete, as no significant change is observed with further heating. This agrees with visual observations and inversion tests which show that a stable gel forms in 8-10 minutes at 10 mg ml^{-1} concentration. Subsequent heating does not significantly influence the spectrum, although the data scatter is quite high: likely a result of low intensity signals from small aqueous sample size.

EPR experiments show broad agreement to the DLS measurements, although unlike DLS the formation of gel can be monitored. The initial collapse of micelle structure over the first 2 minutes of heating, and the almost immediate formation of intermediate aggregate structures is shown by both DLS and EPR experiments. However, neither technique reveals the nature of any intermediate structures. Both micelle breakdown and gelation are relatively rapid at the concentration studied, and it is unlikely that a pure intermediate structure is observed by either technique, as gel fibres start to form.

The rapid breakdown of micelle structures upon moderate heating highlights their limited thermodynamic stability. Higher concentration PEG_{2000}-Tyr_5 solutions (20 mg/ml) spontaneously formed gels over several days when left at room temperature. This further confirms that the kinetic stability of gel structures is high compared to micelles or intermediate structures. High kinetic stability explains how further changes to temperature do not lead to the destruction of the gel.

3.8 Photochemical reactivity of micelle and gel systems

EPR spin labelling experiments reveal that the mobility of tyrosine units varies slightly between PEG-Tyr micelles and gels. Considering the large difference in bulk properties of the two structures, this difference is small. However, it may have an impact upon the chemical and photochemical properties of tyrosine. This presents an opportunity to probe how macromolecular assembly can influence reactivity in otherwise identical systems. The aim of this study is to compare photochemical reactivity in PEG-Tyr micelle and gel systems, and with different polymer lengths, to determine how Tyr environment impacts reactivity.

3.8.1 Photochemical radical generation

When exposed to UV, PEG-Tyr samples exhibit an EPR signal consistent with the formation of tyrosyl or semiquinone type radical species on tyrosine side chains (see section 2.4.4). However, the radical signal observed for a micelle sample is significantly stronger than for a gel sample (see Figure 2-10).

This difference may arise from changes to the optical properties of the sample upon gelation. Larger particles scatter light more effectively, and gel samples (particularly at high concentration required for longer polymers) are noticeably less transparent. Increased scatter will decrease absorption and the photochemical yield of radical species. UV-vis absorption spectra were recorded for PEG_{2000}-Tyr_5 micelle and gel samples at a polymer concentration of 5 mg ml^{-1} (Figure 3-22). They show that less light reaches the detector in the gel sample over the entire wavelength range, indicative of increased scatter. At 276 nm (where tyrosine absorbs), absorbance of both samples is very high (transmittance is 0.133% for micelles and 0.116% for gels). At this wavelength, the majority of energy is likely absorbed by tyrosine rather than scattered – the difference between micelles and gel is minimal. However, the reliability of data at high absorbance values is limited, as measurements may be outside the linear range of the detector.

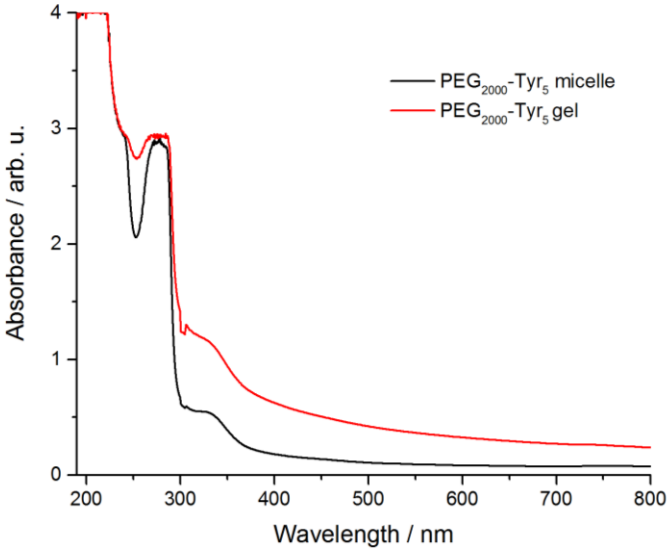

Figure 3-22: UV-vis absorbance spectra for PEG$_{2000}$-Tyr$_5$ 5 mg/ml micelle and gel samples.

Increased light scatter by gels does thus not satisfactorily explain the lower photochemical yield of radical species. The small differences in tyrosine environment measured by EPR spin labelling of micelles, gels and different polymer lengths may influence reactivity. This was tested by measuring tyrosine degradation over a prolonged exposure period in micelle and gel systems. Different polymer lengths in micelle systems were compared, as well as micelle and gel systems.

3.8.2 The effect of polypeptide length upon reactivity in micelle systems

Photochemical degradation was measured in micellar systems of different polymer lengths and compared to degradation in a monomeric tyrosine ester system. Two changes upon UV exposure were monitored by fluorometry: the decrease in tyrosine characteristic fluorescence at 310 nm (λ_{ex} = 276 nm) and the increase in fluorescence corresponding to the photodegradation product dityrosine at 415 nm (λ_{ex} = 320 nm). Sample fluorescence was measured before and after 24 hours of UV exposure. The decrease in tyrosine fluorescence is plotted as a percentage of the original fluorescence in Figure 3-23.

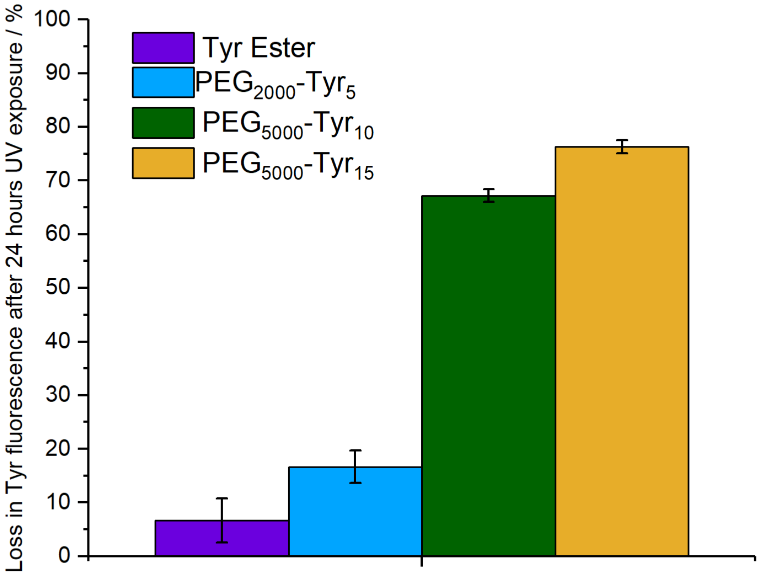

Figure 3-23: Comparison of Tyr photodegradation observed in model systems by monitoring fluorescence emission at 310 nm (λ_{ex} = 276 nm) after 24 hours exposure. Concentration of polymers 0.5 mg/ml (equivalent to [Tyr] = 0.86 mM for PEG$_{2000}$-Tyr$_5$, 0.74 mM for PEG$_{5000}$-Tyr$_{10}$ and 0.97 mM for PEG$_{5000}$-Tyr$_{15}$. Tyr Ester concentration 0.5 mM) Concentration significantly above cmc for all polymers. Error bars show 95% confidence intervals based on 3 repeat measurements.

Despite small variations in tyrosine concentration, there is a significant difference in photochemical reactivity between different polymer systems, and all show higher reactivity than the monomeric tyrosine ester system at a similar concentration.

The lower reactivity in free tyrosine ester systems could be rationalised by considering the process of radical formation. Photo-excited tyrosine needs to collide with an electron acceptor such as another tyrosine or oxygen to enable radical or ROS formation and subsequent degradation.[58] Within tyrosine-rich micelle cores, nearby tyrosine units can act as electron acceptors. Reactive oxygen species generated by oxygen interacting with excited tyrosine residues will be able to more rapidly interact with nearby amino acid residues, further accelerating degradation. In contrast, monomeric systems require diffusion of reactive oxygen species over longer distances, making them less likely to react with Tyr due to their short lifetime.

PEG$_{5000}$-Tyr$_{10}$ micelles are more rigid than the shorter polymer, due to increased intermolecular interactions between Tyr units within the hydrophobic core. This likely contributes to increased photochemical activity, as electron transfer processes occur more readily between Tyr units and ROS can cause more damage within the Tyr rich micelle core.

Tyrosine-tyrosine interactions can be loosely quantified by considering the formation of dityrosine as a photodegradation product, which requires the combination of two tyrosyl radicals. The increase in characteristic fluorescence emission for dityrosine at 415 nm[184] upon prolonged UV exposure was compared for the different model systems (Figure 3-24).

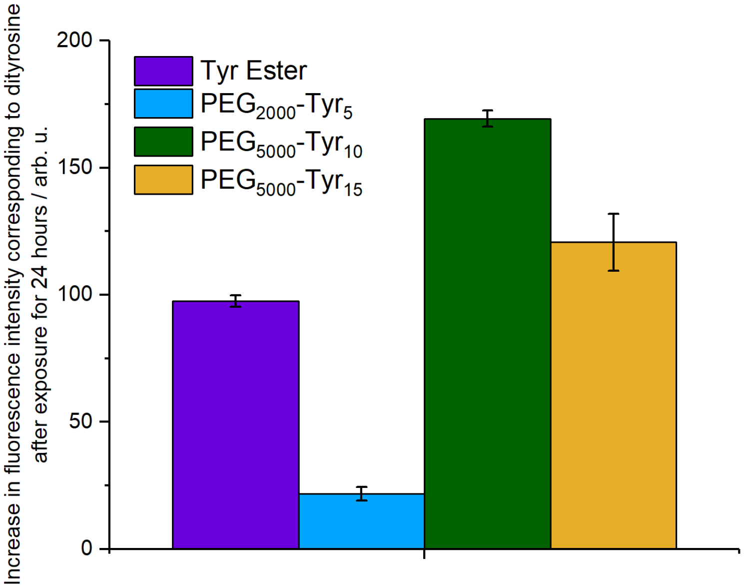

Figure 3-24: Comparison of dityrosine formation observed in model systems by monitoring fluorescence over 24 hours. Concentration of samples as in Figure 3-23, data normalised based on Tyr concentration. Error bars show 95% confidence intervals based on 3 repeat measurements.

The results indicate that despite a lower overall photochemical reactivity, more dityrosine is formed in the tyrosine ester system than the PEG$_{2000}$-Tyr$_5$ system. Based on Tyr-Tyr interactions, this seems to disagree with the results in Figure 3-23. However, it may indicate that Tyr localisation in PEG-Tyr micelles promotes ROS decay pathways in preference to a pathway leading to dimerization.

As polymer length is increased, Tyr-Tyr interactions increase within the micelle core, and consequently more dimers are formed. However, PEG$_{5000}$-Tyr$_{15}$ does not follow this trend. The environment of Tyr within these micelles was not characterised, the change in hydrophilic/hydrophobic ratio may affect micelle stability, which could impact reactivity and dimerization. Terminal amino acids in the chain may exhibit different reactivity: as polymer length increases the proportion of terminal tyrosine units decreases. However, this does not explain the decrease in activity for PEG$_{5000}$-Tyr$_{15}$. The reason for this result is unclear.

3.8.3 Comparison of photochemical reactivity in gel and micelle systems

The polymer model system allows the effect of macromolecular environment on reactivity to be studied. The chemical structure of polymers is not affected by self-assembly, therefore the chemical environment of tyrosine in micelles and gels is identical. Photochemical reactivity was compared for micelle and gel systems, at two different polymer lengths. The results are shown in Figure 3-25.

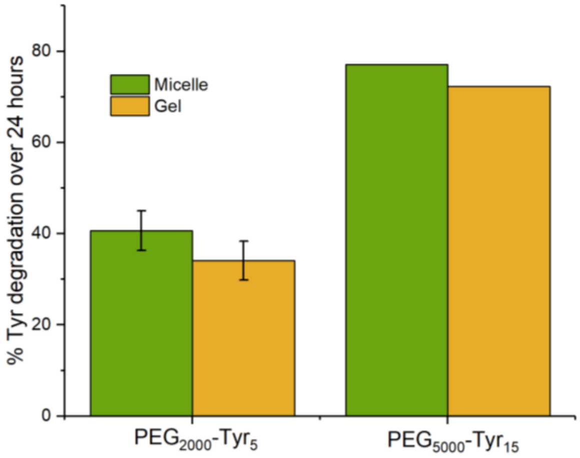

Figure 3-25: Comparison of photochemical reactivity in gel and micelle polymer systems, measured by loss in tyrosine fluorescence after 24 hours UV exposure

Differences are small, and repeat measurements for the shorter polymer highlight a significant margin of error. However, results consistently show slightly lower degradation in gel systems.

Given that the difference is so small between micelles and gels, it could be attributed to increased light scattering in gel systems. Alternatively, it may be due to the difference in Tyr environment shown by spin labelling studies, as environment is known to influence reactivity. In gel systems, higher kinetic stability likely results in less movement of polymer chains, creating a more rigid system (see Section 3.6.2). This will decrease interactions between tyrosine units, which may impact electron and energy transfer processes leading to radical formation and degradation. This agrees with the lower radical yield observed in gel systems (see Section 3.8.1).

In addition to this, reactive oxygen species generated through the interaction of photo-excited tyrosine and oxygen are more likely to react with nearby tyrosine residues than diffuse through the sample as they will be comparatively short-lived. The fibrous structure may limit diffusion through gel samples. Interaction of reactive oxygen species with tyrosine may also be limited by the less mobile tyrosine in gel fibres.

3.8.4 Difference in dityrosine formation

Macromolecular structure may also influence radical combination processes leading to dimerization. Results, shown in Figure 3-26, show the difference between micelle and gel systems is much more pronounced when considering dityrosine formation.

Interaction between neighbouring tyrosine residues is less prolific in the gel systems, because of the more restricted, less dynamic environment revealed by EPR spin labelling studies. However, dityrosine is only a minor degradation product: oxidative pathways are preferred in the presence of oxygen.[58] Lower dityrosine formation in gels likely only accounts for a part of the overall decrease in activity.

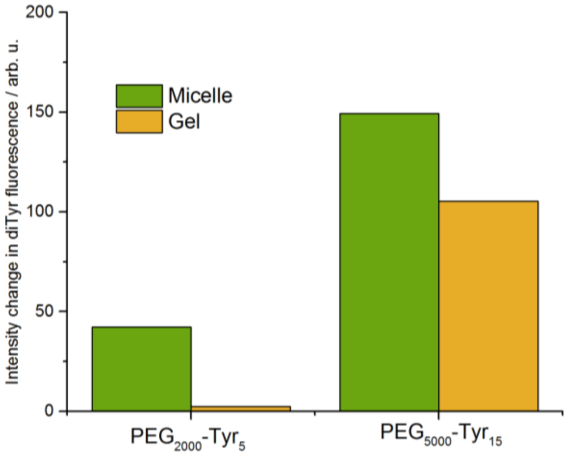

Figure 3-26: Comparison of photochemical reactivity in gel and micelle polymer systems, measured by increase in dityrosine fluorescence after 24 hours UV exposure

3.8.5 The effect of adding iron

A dominant degradation pathway will be via interaction with reactive oxygen species. Direct monitoring of ROS by spin trapping was not possible (see Section 4.9.1). However, ROS formation could be enhanced through the addition of a redox active metal. The effect of macromolecular assembly upon ROS decay pathways can therefore be better understood. Small quantities of the relatively hydrophobic iron(III) acetylacetonate [$Fe(acac)_3$] complex were added to gel and micelle samples of PEG_{2000}-Tyr_5 prior to UV exposure. The difference between systems is significantly enhanced compared to the system without metal, as shown in Figure 3-27.

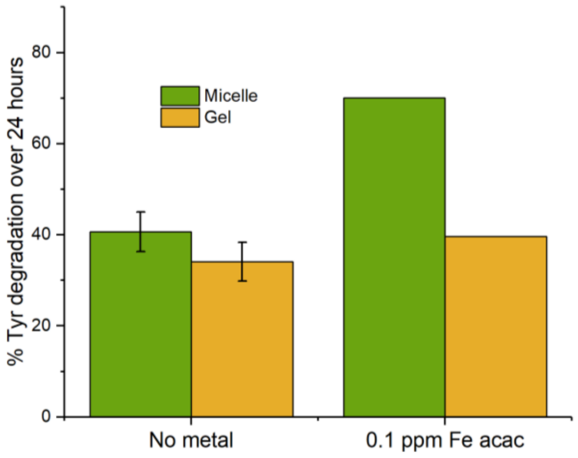

Figure 3-27: Comparison of photochemical reactivity in gel and micelle polymer systems in the presence and absence of 0.1 ppm Fe(III), measured by decrease in tyrosine fluorescence after 24 hours UV exposure

The significant difference in reactivity between gel and micelle exhibited in the metal containing samples confirm the conclusion that diffusion limitation is a major factor for ROS decay pathways in the gel system. This could be diffusion of the metal complex itself, or of reactive oxygen species generated through Fenton and photo Fenton mechanisms. The increase in activity upon addition of the metal is significant in the micelle system. This indicates the important role played by redox active metals in tyrosine degradation, examined further in Chapter 4. There is a less significant increase upon addition of metal in the gel system. Reactive oxygen species generated at metal centres are clearly limited by their ability to diffuse long distances to interact with tyrosine units in gel systems, suggesting parts of the gel are unaffected by the addition of the metal.

3.9 System characterisation: Conclusions

PEG-Tyr block copolymers have been shown to aggregate in aqueous solutions due to their amphiphilic nature. Micellar aggregates exhibit a relatively narrow distribution of particle hydrodynamic radii around 50-80 nm by DLS, dependent on the block ratio of the copolymer. The formation of spherical micelles is in line with other di-block copolymer micelles.

EPR spin probing experiments indicated considerably restricted mobility environment within the core of polymer micelles. Direct spin labelling of tyrosine units on polymer chains was carried out, however chemical reactivity of tyrosine buried within micelle cores was low, therefore labelling was carried out in a less polar solvent which disrupted self-assembly. Spin-label studies have shown that tyrosine in micelles has a range of different mobility, from almost completely immobilised by EPR timescale to only slightly restricted tumbling. Mobility in model systems is loosely correlated to other spin labelling studies of proteins reported in literature, suggesting that tyrosine in model systems is in a similar molecular environment to tyrosine within helical structures in proteins. The model therefore provides a realistic mimic of Tyr in helical keratin proteins, and can be used to probe Tyr photochemistry (see Chapter 4).

Changing polymer concentration alters the dynamics and kinetic stability of the micelle system, due to increased interactions and exchange between micelles. Polymer length influences the hydrophilic/hydrophobic ratio, which also alters the thermodynamic and kinetic stability of micelles. Consequently, the mobility and environment of tyrosine units is affected, which impacts photochemical reactivity.

The limited thermodynamic stability of micelle structures means that upon heating, polymers rearrange into kinetically trapped gel fibres. The gelation process has been monitored in real time by DLS and EPR. Both show a rapid break down of micelle structures upon heating. DLS suggested the formation of large aggregates before stable gel formation, which could be sheet type intermediate structures. The rates of micelle breakdown and gel formation are strongly dependent upon polymer concentration.

The unique properties of the PEG-Tyr system allow a chemically identical molecule to exist in two different states at room temperature: immobilised as a micelle or a kinetically trapped gel. These two systems exhibit very different bulk properties, although the molecular environment of tyrosine is remarkably similar. Spin labelling studies show that micelles exhibit greater mobility and interaction between tyrosine residues. Gels are more restricted, although the environment is more homogenous and gels have improved kinetic stability. A more restricted environment in gels decreases the susceptibility of tyrosine to photochemical degradation, although the effect is small. Gels also limit ROS and metal diffusion.

4. Investigating the photochemistry of tyrosine in model systems

PEG-Tyr micelles in aqueous solution discussed in Chapter 2 and characterised in Chapter 3 provide a reasonable mimic of the physical and chemical environments of tyrosine in a helical protein structure such as keratin. This copolymer system is easily tuneable, allowing polymer length and concentration to be readily manipulated, and the effects of redox metals, antioxidants and other additives to be probed.

The simplicity of the system enables the study of tyrosine photochemistry in isolation, without other chromophoric amino acids such as tryptophan. This enables a better understanding of the key photochemical processes of tyrosine, and how they are influenced by redox metals, antioxidants and oxygen under biologically relevant conditions.

The aims of this investigation are therefore:

- Develop techniques to quantitatively monitor the photodegradation of tyrosine in model systems.
- Investigate the effects of redox active metals (iron and copper) upon the photodegradation of tyrosine, at levels relevant to metal concentrations in hair.
- Probe the mechanism of degradation and understand how metals influence degradation pathways.
- Investigate and quantify the role of oxygen and reactive oxygen species upon tyrosine degradation in model systems.

4.1 Method Development: Observation of a photo-induced radical signal by EPR

Solutions of free tyrosine or tyrosine ester irradiated within the EPR cavity at neutral pH show no EPR signal (see section 2.2.1). The photochemical quantum yield for tyrosine photolysis in air is reported as $\phi = 0.003$.[185] As degradation is highly inefficient, the concentration of radical species is very low. Tyrosyl radicals are also short-lived: they decay with a reported rate constant of 8×10^{8} dm^{3} mol^{-1} s^{-1}.[125] These factors prevent straightforward detection by standard EPR techniques.

Tyrosine environment is sufficiently restricted within PEG-Tyr micelles (as characterised in Chapter 3) to enable the observation of a photo-induced radical signal by EPR, shown in Figure 4-1. Restricted mobility of tyrosine leads to a broad EPR peak, with unresolved hyperfine splitting.

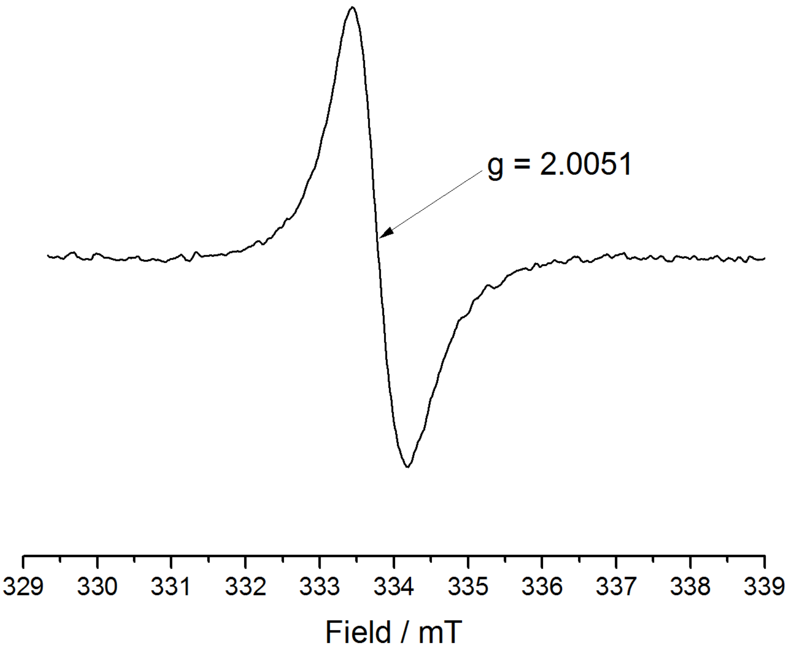

Figure 4-1: Broad EPR signal observed upon irradiation of PEG_{5000}-Tyr_{15} micellar solution at a concentration of 10 mg/ml. g-value calculated using DPPH internal standard. Light source: 100 W Hg arc lamp

The radical signal has a g-value of 2.0051, which falls within a range of reported literature values (2.00423 – 2.00531) for a tyrosyl radical species.[132] g-values for PEG-centred radicals are expected to be lower, based on a literature value of 2.0033 for ethylene glycol (R-C$^{\bullet}$H-R) radicals.[186] Intermediate peroxyl radical species formed upon interaction with oxygen would have higher g-values: alkyl peroxyl radical g-values are typically above 2.01, and vary little with changing R substituent.[187] Transfer of radical centre to the PEG chain via hydrogen abstraction processes is thermodynamically disfavoured as the PEG C-H bond is more stable, based on bond dissociation energies of Tyr-OH (361.916 ± 2.092 kJ mol^{-1}) and ethylene glycol C-H (385.30 kJ mol^{-1}).[188-189] As PEG does not absorb energy at wavelengths >200 nm,[144] the species observed by EPR arise from tyrosine, and are most likely tyrosyl or semiquinone type radicals. The kinetics of radical formation were monitored to reveal more information about radical identity.

4.1.1 Measuring the kinetics of radical formation

The rate of radical formation may reveal more information about the identity of the species. Kinetic measurements were carried out by monitoring the change in signal intensity over time at fixed field (the top of the EPR peak shown in Figure 4-1, at 333.45 mT). The formation of radical species, as shown by the change in intensity at this fixed field, is shown in Figure 4-2.

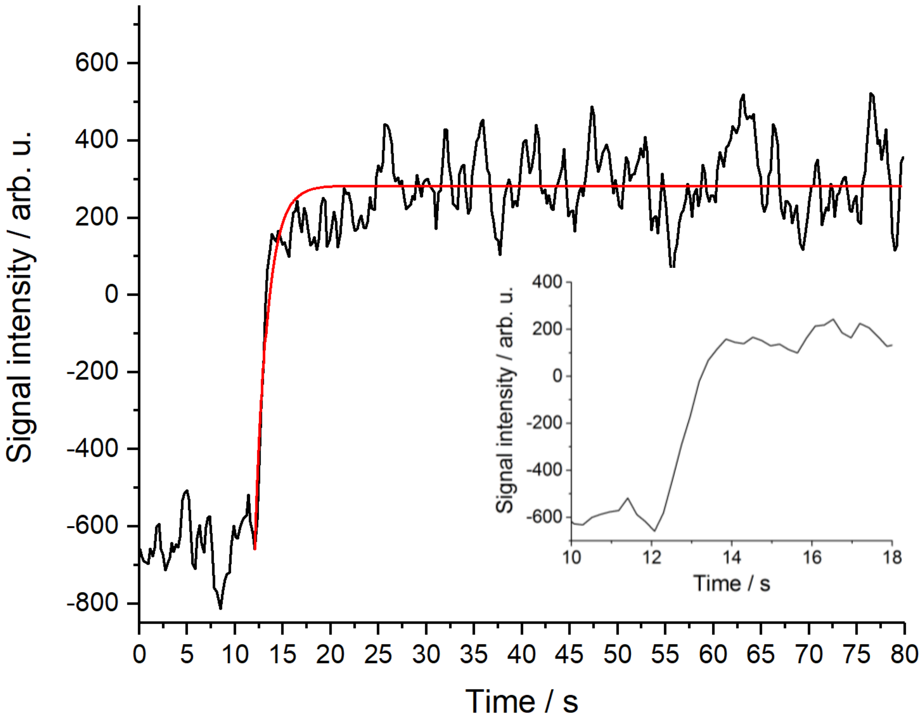

Figure 4-2: Growth in radical signal at 333.45 mT observed by EPR upon exposure of 10 mg/ml PEG$_{5000}$-Tyr$_{15}$. Lamp shutter opened after 12 seconds. Inset shows rapid growth period. Red line shows first order fit of signal growth.

Tyrosyl radical species can form via a biphotonic process, as shown in Scheme 4-1.[42] Tyrosyl radicals also form by the rupture of the O-H bond in excited state tyrosine (Scheme 4-2), driven by vibrationally excited singlet states. Triplet tyrosine can also interact with oxygen, leading to the formation of tyrosyl radicals and superoxide radical anion (Scheme 4-3).[44] Oxidation of triplet tyrosine to form a tyrosyl radical could also occur via interaction with a redox metal centre.

$$TyrOH \overset{hv}{\rightarrow} {}^{1}TyrOH \overset{isc}{\rightarrow} {}^{3}TyrOH \overset{hv}{\rightarrow} TyrO^{\cdot} + H^{+} + e_{aq}^{-} \tag{Scheme 4-1}$$

$$TyrOH \overset{hv}{\rightarrow} {}^{*}TyrOH \rightarrow TyrO^{\cdot} + H \tag{Scheme 4-2}$$

$$TyrOH \overset{hv}{\rightarrow} {}^{1}TyrOH \overset{isc}{\rightarrow} {}^{3}TyrOH \overset{O_2}{\rightarrow} TyrO^{\cdot} + H^{+} + O_2^{\cdot-} \tag{Scheme 4-3}$$

Reported rate constants for the reaction of triplet state tyrosine to yield tyrosyl radicals in aqueous solution at pH 6 are 1.8×10^{5} s^{-1} for Scheme 4-1 and 4.8×10^{9} M^{-1} s^{-1} for Scheme 4-2. The growth curve shown in Figure 4-2 fitted first order kinetics reasonably closely (red curve on Figure 4-2), despite the weak signal and the presence of oxygen. This may indicate that Scheme 4-1 is the dominant pathway. However, the rate of signal growth is significantly slower than expected based on literature values, with a calculated value of 8.42 s^{-1}.

There are several possible explanations for this slower radical formation. Literature values are based on free tyrosine in solution, whereas tyrosine in micelles exhibits significantly restricted mobility which prolongs triplet state lifetime.[190] Radicals observed may be secondary radical species - transfer of radical centre via hydrogen abstraction could move the position of tyrosyl radicals along the polypeptide chain. This would lead to a build-up of radical species on the most immobilised tyrosine residues within micelle cores, where restricted mobility increases radical lifetime sufficiently to enable detection by EPR. Another possibility is that the radicals observed are other more stable phenoxyl based species, such as DOPA semiquinone radicals formed by interaction of tyrosyl radicals with hydroxide ions or hydroxyl radicals (see SCH2-1).[191]

Kinetic measurements were also carried out on systems containing 100 ppm Fe(III) as $FeCl_3$. These showed the same rate of radical formation: the metal does not influence the radical formation process, as far as it is possible to determine from noisy experimental data. Although radical formation appears to follow first order kinetics, the exact identity of the species observed is uncertain. Primary tyrosyl radicals may be rapidly oxidised to DOPA semiquinone species. Fe(III) may accelerate DOPA formation by increasing hydroxyl radical concentration,[191] the fact that this is not reflected in kinetic measurements could indicate that the species observed is not DOPA. The effect of transition metal ions upon photodegradation is examined in more detail in section 4.4.

4.1.2 EPR methods – conclusions

Upon irradiation of PEG-Tyr micelle samples, a broad EPR signal is observed. Based on literature g-values, thermodynamic considerations and kinetic studies, this is tentatively attributed to tyrosyl or semiquinone radicals formed within the restricted environment of the micelle core. Radical signal growth appears to follow first order kinetics and seems unaffected by iron(III) within the limitations of the experiment. This may suggest that a primary tyrosyl species is observed. However, these may rapidly hydroxylate to form more stable semiquinone species, resulting in a similar growth profile.

4.2 Method Development: Observation of tyrosine and dityrosine fluorescence

The uncertainty in the identity of radical species observed may limit the conclusions which can be drawn from EPR experiments. The aim of this section was to develop a complementary analytical method for measuring tyrosine degradation, making use of the intrinsic fluorescence properties of tyrosine.

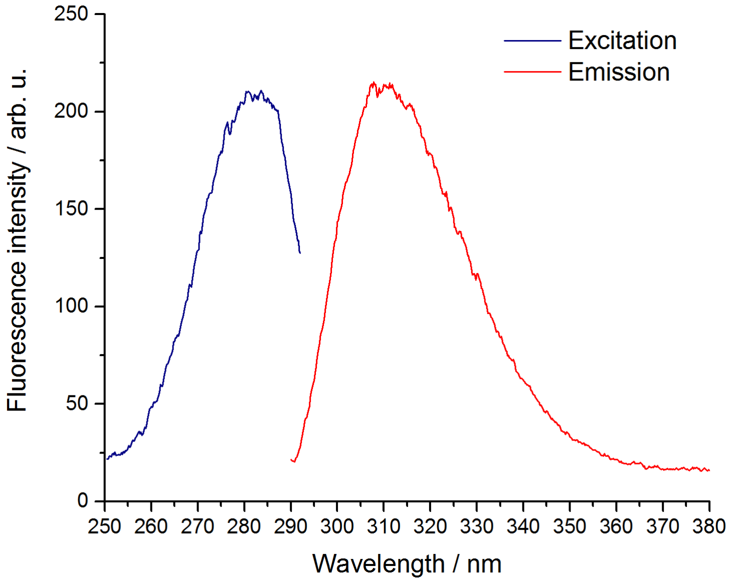

Figure 4-3: Fluorescence excitation and emission spectra for PEG$_{5000}$-Tyr$_{10}$ micellar sample. Measurement polymer concentration = 0.193 mg/ml, equivalent [Tyr] = 0.283 mmol dm^{-3}

The aromatic side chain of tyrosine exhibits characteristic fluorescence at 303 nm, following excitation at 276 nm.[192] Loss in tyrosine concentration through dimerization, or oxidation by hydroxyl radicals or singlet oxygen will lead to a loss in this characteristic fluorescence over time. Hence, fluorescence can be used to monitor the degradation of tyrosine over prolonged exposure to UV light. The fluorescence emission and excitation spectra were recorded for samples of PEG-Tyr micelles, and are shown in Figure 4-3.

Excitation and emission spectra shown in Figure 4-3 show maxima at 281 nm and 310 nm respectively, slightly red shifted from literature reported values for aqueous free amino acid solutions. This is likely due to the different physical environment and solvation in micelle systems: fluorescence spectra are sensitive to molecular environment.[192] As tyrosine is the only fluorophore present within samples, and excitation/emission wavelengths match reasonably with literature values, the observed fluorescence must arise from tyrosine.

4.2.1 Characterisation of dityrosine as a photodegradation product

Observing only changes to tyrosine fluorescence reveals no information about degradation products. Dityrosine, the dimerised degradation product of tyrosine usually formed in the absence of reactive oxygen species[58] (see Scheme 4-8) also has a characteristic fluorescence. With excitation and emission maxima of 320 nm and 405 nm respectively, it is distinct from tyrosine.[184] After prolonged exposure of PEG-Tyr samples, a characteristic fluorescence peak matching these values was observed. The same peak was also detected for aqueous tyrosine ester samples as shown in 2D fluorescence spectra in Figure 4-4.

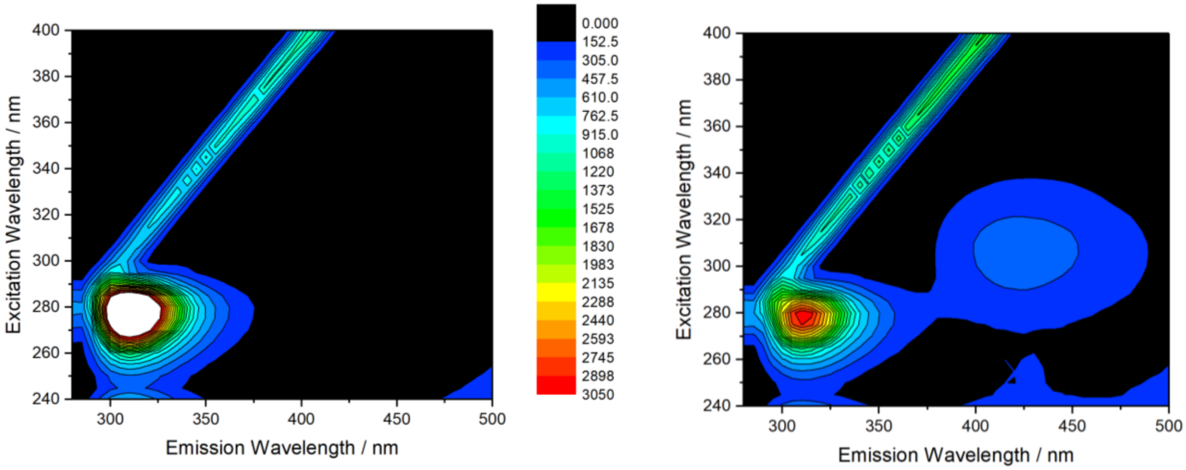

Figure 4-4: 2D fluorescence spectra for 0.5 mmol dm^{-3} tyrosine methyl ester at pH 8.5 before (left) and after (right) 22 hour UV exposure

The 2D fluorescence spectrum of tyrosine methyl ester shows an excitation maximum at 279 nm and emission maximum at 308 nm, very slightly different from values observed with PEG-Tyr samples, likely due to the different environment in polymeric systems.

Following prolonged UV exposure, samples of tyrosine methyl ester were analysed by mass spectrometry (ESI), to confirm the presence of dityrosine. Spectra (Figure 4-5) show the appearance of peaks corresponding to dityrosine $[M+H]^+$ at m/z = 389.1690 (err = 4.3 ppm) and $[M+Na]^+$ at m/z = 411.1510 (err = 0.7 ppm). The two mass spectra shown in Figure 4-5 were obtained from the same sample before and after irradiation. Dityrosine was confirmed as a degradation product, although no other products could be identified by mass spectrometry.

Fluorometry techniques can therefore be used not only to monitor the degradation of tyrosine through the loss of fluorescence emission at 310 nm, but also the formation of dityrosine. Dimer formation will be sensitive to radical concentration in samples, as two tyrosyl radicals need to combine to form dityrosine. However, other reaction pathways are possible for tyrosyl radical species, particularly in the presence of oxygen.

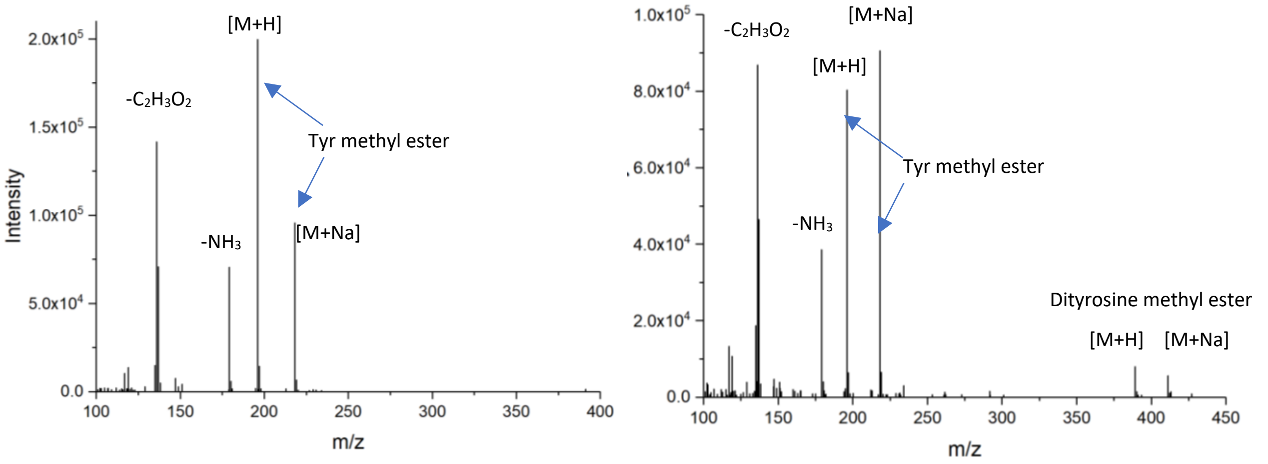

Figure 4-5: ESI-MS analysis of tyrosine methyl ester solution before (left) and after (right) 22 hours UV exposure, showing the formation of dityrosine as a photodegradation product.

4.3 Quantifying tyrosine degradation in PEG-Tyr micelles upon prolonged UV exposure

By monitoring the loss in tyrosyl radical EPR signal over an exposure period of 3 hours, and the loss in tyrosine intrinsic fluorescence over 24 hours coupled with the increase in dityrosine fluorescence, it is possible to quantify the overall photochemical reactivity of tyrosine in different samples. Although the techniques do not reveal absolute yields or identities of degradation products (except dityrosine), they provide a method to compare relative reactivity in the presence of metals, antioxidants and with different polymer systems. Dityrosine formation is dependent upon tyrosyl radical formation, although is more likely when oxygen supply is limited.[58] However, an increase in tyrosyl radical concentration through ROS pathways may lead to increased dimerization. Metals may influence both direct radical production through redox chemistry, and ROS production through Fenton chemistry, as outlined in Scheme 4-4. Photo-Fenton reduction of Fe^{3+} to Fe^{2+} may also occur (box on Scheme 4-4), producing hydroxyl radicals and regenerating Fe^{2+} for Fenton reactions. Initial experiments were carried out without any additives, to test the reproducibility of the techniques.

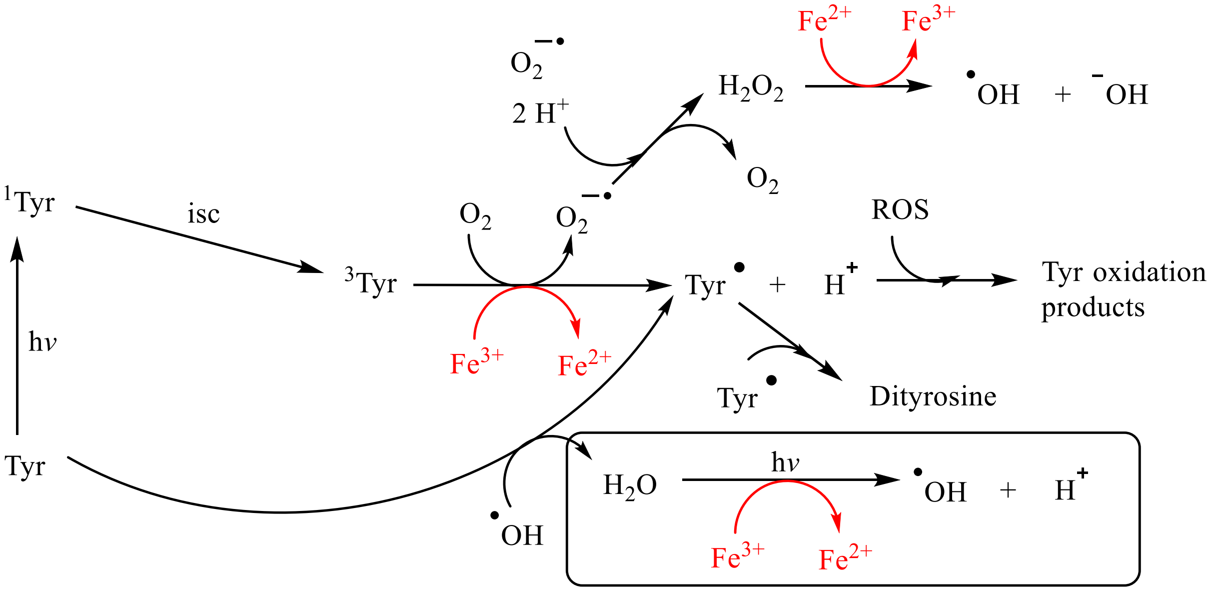

Scheme 4-4: Simplified scheme showing tyrosyl radical production, and potential involvement of redox active transition metal ions.

4.3.1 Prolonged exposure EPR studies of PEG-Tyr micelles

To provide consistency between different measurements, quartz capillaries were used to hold samples in the EPR cavity, rather than flat cells. Although flat cells contain more sample and cavity Q factors are higher, positioning of sample needed to be consistent. This is easier to achieve with capillaries. However, this resulted in a decrease in signal strength compared to Figure 4-1. An EPR signal was also detected in a blank control sample, which was attributed to defect centres in the quartz glassware, overlapping with the tyrosine signal.

To overcome these problems, simple two-component simulations were fitted to experimental data. The quartz signal could then be subtracted from the simulation, leaving only the signal corresponding to tyrosine based radicals. The areas of simulated peaks were then plotted

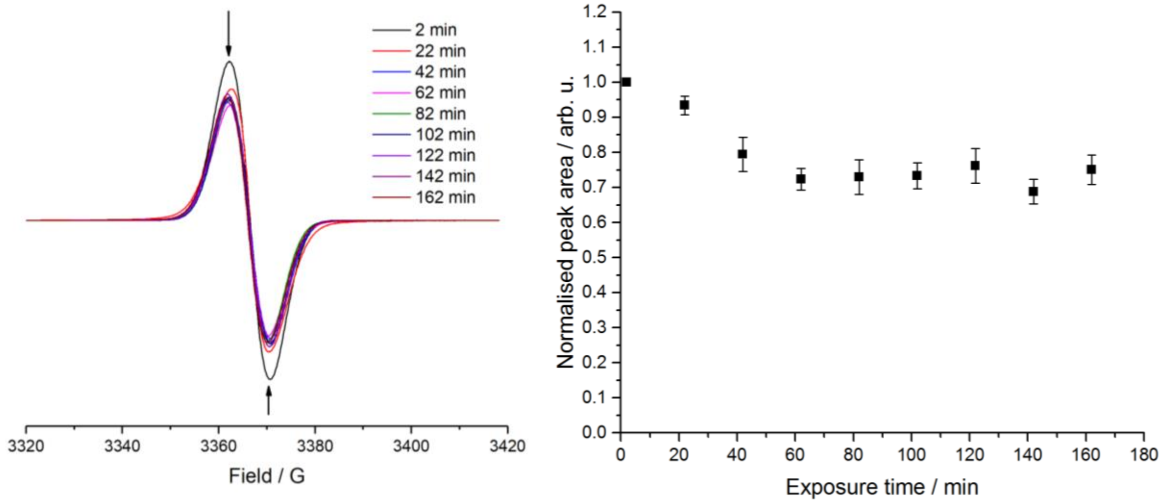

Figure 4-6: Simulated tyrosyl radical signals based on fitted experimental data with quartz signal removed (left). Corresponding change in relative peak area over time (right). Average of 5 measurements, standard error shown.

against exposure time, based on their double integrals. 5 repeat measurements were carried out on a 10 mg/ml PEG$_{5000}$-Tyr$_{15}$ sample, the results are shown in Figure 4-6. A comparison between experimental and simulated data is shown in Appendix 1.

The technique shows reasonable reproducibility, although there is some variation in experimental data, likely due to the weak signal strength. Average standard deviation of normalised peak area data shown in Figure 4-6 is 0.077. There is a significant loss in intensity over the initial hour of exposure, with signal intensity decreasing by around 25% in this time. However, continued exposure after this does not seem to lead to significant degradation.

This suggests that dominant degradation pathways are dependent upon dissolved oxygen. In the narrow quartz capillaries (internal diameter 0.5 mm), diffusion is slow and oxygen is unlikely to be quickly replenished within the sample.[193-194] Exposed surface area to volume ratio is only 0.006 cm^{-1}, therefore interaction between sample and the air is low. Experiments were also carried out in the presence of metals and other additives, which may influence the rate of oxygen depletion or promote tyrosine degradation via other pathways. These are discussed in Section 4.4.

4.3.2 Prolonged exposure fluorescence studies

Unlike EPR studies, samples for fluorometry were irradiated in 1 cm path length quartz cuvettes. The exposed surface area to volume ratio was therefore much higher, at 3.33 cm^{-1} for a 300 µL sample. Replenishment and diffusion of dissolved oxygen is therefore likely to be faster.

Initial experiments used the slightly shorter PEG$_{5000}$-Tyr$_{10}$ polymer at the same mass concentration (10 mg/ml) as the PEG$_{5000}$-Tyr$_{15}$ used in EPR measurements. Samples were tested after the same 3-hour exposure period as EPR studies, and after a prolonged exposure time of 24 hours. The fluorescence of the sample was measured relative to a control sample prepared at the same time but kept in the dark. Degradation after the 3-hour exposure period was 16%. Over a 24-hour exposure period, 52% was observed, as shown in Figure 4-7. Values are quoted to the nearest 1%.

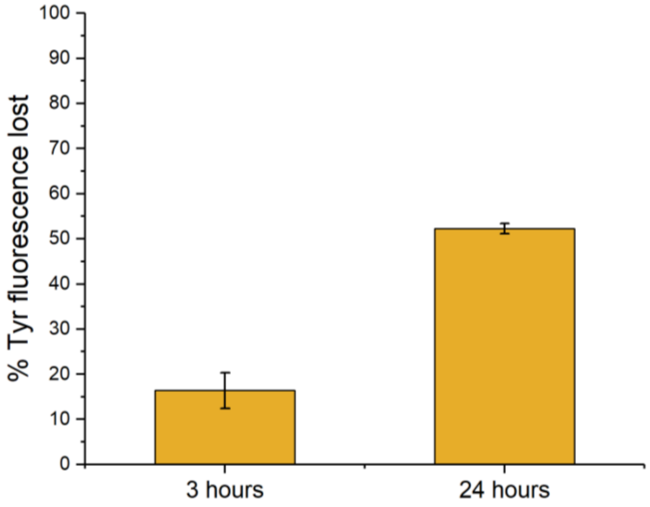

Figure 4-7: Tyr degradation upon UV exposure of 10 mg/ml PEG$_{5000}$-Tyr$_{10}$ aqueous micellar solution. Measured by loss in Tyr fluorescence relative to a control sample. Error bars show 95% confidence intervals based on average of 3 measurements.

Unlike EPR samples, fluorescence measurements show continued degradation throughout the prolonged exposure period. The reason for this discrepancy is likely the difference in the exposed surface area to volume ratio of the sample. In the larger cuvette, there is significantly greater interaction with air above the sample compared to the EPR capillary, leading to faster replenishment of dissolved oxygen and a continued supply for degradation processes. Non-fluorescent degradation products or intermediates may also still exhibit an EPR signal.

Degradation over the initial 3-hour period is however slightly lower than for the EPR sample. It should be noted that the two techniques monitor different species, with EPR detecting phenoxyl radicals formed after oxidation of excited state tyrosine compared to fluorescence from the singlet excited state. Depletion of oxygen may not only affect the degradation of tyrosine but also the formation of tyrosyl radicals via Scheme 4-3.[44] Also, the slightly shorter polymer used in initial fluorescence measurements may affect micellar environment and consequently reactivity, as discussed in Section 3.8.2.

The reproducibility of the fluorescence method for measuring tyrosine degradation was tested by comparing the results of three identical experiments with the shorter PEG_{2000}-Tyr_5 polymer in the presence of Fe^{3+} as hydrophobic iron stearate. The reproducibility test was carried out on a metal containing sample to confirm that fluorescence quenching by the metal wasn't influencing results. For a series of 3 identical PEG-Tyr samples with 0.5 ppm Fe stearate exposed to UV for a period of 24 hours, a mean degradation of 27.27% was obtained, with a standard deviation of 1.68% and a standard error of 0.97%. Further tests were carried out on PEG-Tyr samples containing both iron stearate and BHT antioxidant, giving a percentage error of 1.3%.

4.3.3 Analysing photodegradation products

Attempts to identify degradation products in PEG-Tyr samples by mass spectrometry were unsuccessful, due to the range of multiply charged larger aggregate structures created during ionisation preventing straightforward isolation of degraded PEG-Tyr monomers.[195]

Dityrosine formation through UV exposure can be tracked through fluorescence measurements, as described in Section 4.2.1. However, in the presence of oxygen, degradation pathways other than dimerization are likely to dominate through reactive oxygen species.[58] Singlet oxygen, superoxide and hydroxyl radicals may lead not only to oxidation of tyrosine side chains (observed by loss of Tyr fluorescence), but also damage to overall polypeptide structure through the formation of peroxyl radicals and autoxidation.

Hydroxyl radicals can abstract hydrogen from the α-carbon of an amino acid, leading to the formation of a carbon centred radical. This can undergo further reactions with oxygen, ultimately leading to the oxidative cleavage of the polypeptide backbone, as outlined in Scheme 1-17.[64] This process will not influence tyrosine fluorescence, as the side chains remain intact. Polypeptide cleavage could therefore be used as a measure of ROS activity.

Polypeptide cleavage can be indirectly measured by looking at any change to primary amine concentration following UV exposure. Several fluorometric assays enable the quantification of primary amines in a sample by selectively reacting a non-fluorescent dye with the primary amine to produce a fluorophore. An example of such a dye is fluorescamine, which interacts selectively and rapidly with primary amine groups, as outlined in Scheme 4-5.[196]

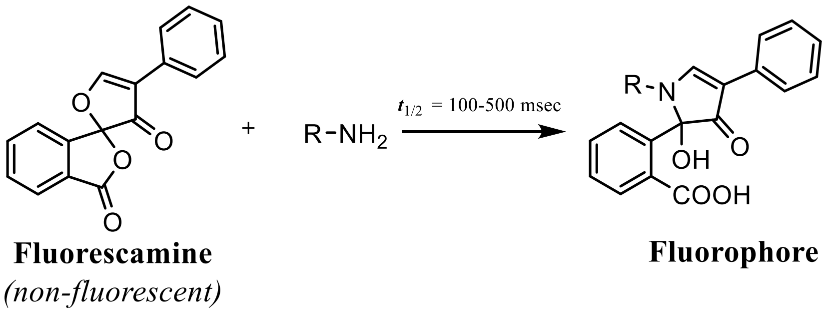

Scheme 4-5: Interaction of fluorescamine with primary amines, forming a fluorophore with λ_{max} (em) = 490 nm and λ_{max} (ex) = 390 nm

Fluorescamine was added to samples of PEG$_{5000}$-Tyr$_{10}$ copolymer according to a reported literature procedure for microscale samples.[197] Results indicated an increase in primary amine concentration over the period of UV exposure, as shown by an increase in fluorescence emission at 490 nm (Figure 4-8). After 4 hours exposure, concentration rises 9% compared to the initial concentration, and up 19% after 24 hours exposure. This shows that autoxidative processes can lead to the breakdown of polypeptide as outlined in Scheme 1-17. Autoxidation is discussed in more detail in Section 4.9.

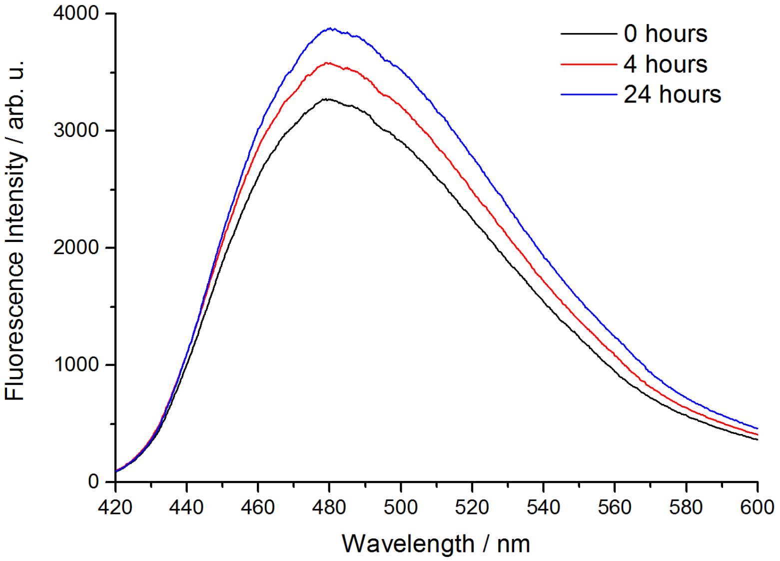

Figure 4-8: Fluorescence emission spectra from Fluorescamine assay analysis of PEG$_{5000}$-Tyr$_{10}$ samples before and after fixed UV exposure periods.

Unfortunately, iron caused significant quenching of dye fluorescence, making results from metal containing systems incomparable. Therefore, although UV exposure does lead to polypeptide cleavage, thus proving the involvement of reactive oxygen species and confirming autoxidation, it was not possible to quantitatively analyse the effect of metals by this method.

Fluorescence studies therefore relied upon analysing only tyrosine loss and dityrosine formation.

4.4 The effect of redox active metals upon tyrosine photochemistry

Redox active metals are known to influence photochemical processes in a variety of ways. Metal centres may quench excited states.[111] They can also act as photosensitisers: earth-abundant iron based photosensitisers are increasingly reported in the literature.[108] Redox metals can increase ROS production via Fenton and photo-Fenton processes,[198] or directly quench radical species through redox interactions.[199] The aim of this investigation is to quantify the effect redox active metal ions have upon tyrosine degradation, particularly those present within hair fibres, Fe^{3+} and Cu^{2+}. The extent of photodegradation in metal containing systems was analysed and compared to metal-free systems. Further studies were therefore carried out to mechanistically assess how the metals affect photochemistry.

4.4.1 The effect of iron upon tyrosyl radical decay

The concentration of radical species in PEG-Tyr systems decreases upon prolonged UV exposure, as shown in Figure 4-6, with the greatest change in the first hour. This likely corresponds to the consumption of dissolved oxygen, after which degradation is slowed as fewer pathways are available. Identical measurements were performed in the presence of 100 ppm Fe(III), added as $FeCl_3$. Figure 4-9 compares the decay over prolonged exposure for metal containing and metal free systems.

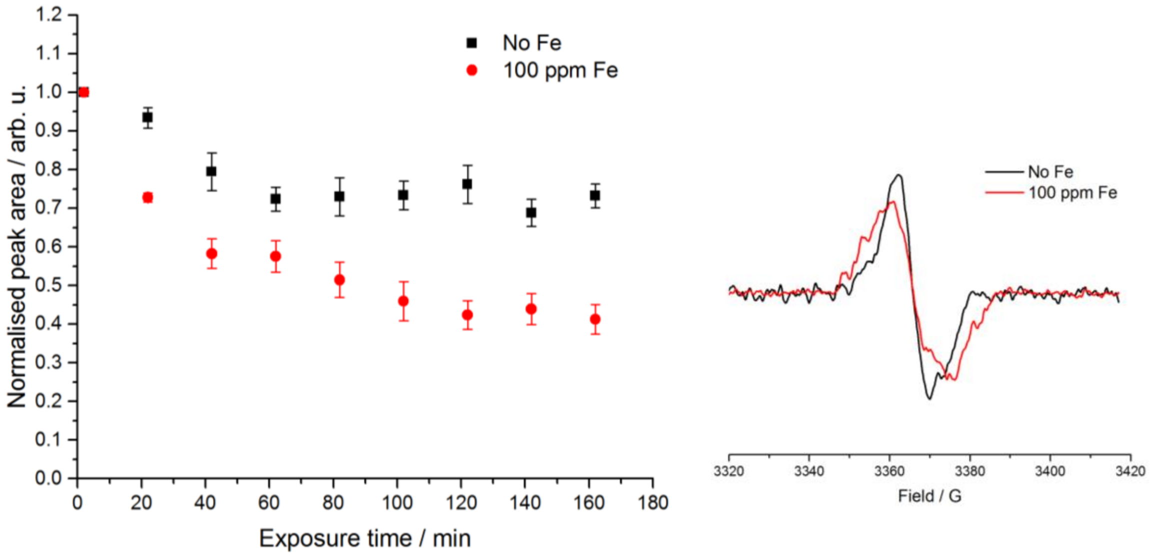

Figure 4-9: Change in radical EPR signal strength (measured by peak area) of photo-induced radicals in 10 mg/ml PEG_{5000}-Tyr_{15} over prolonged exposure, relative to peak area after 2 mins UV exposure (inset). Average of 4 (no metal) or 3 (100 ppm Fe) experimental runs. Standard error bars shown.

The addition of the iron leads to a slight broadening of the EPR signal, as shown in Figure 4-9, inset. This is likely due to collisional exchange interactions between the paramagnetic metal centres and photo-induced radical species.[200] The orbital overlap of paramagnetic centres leads to exchanging spin states between the two unpaired electrons, which become indistinguishable. This leads to a shortening of spin-spin relaxation time (T_2), causing line broadening.[201] The frequency of spin exchange depends on the extent of interaction, with greater orbital overlap ultimately leading to increased EPR line broadening.[202] When 100 ppm Cu(II) (as $CuSO_4$) was added to the sample, the EPR signal was broadened to the point that it was not detectable. This indicates significantly greater exchange interaction between tyrosine and Cu(II) compared to Fe(III), and is suggestive of complex formation between tyrosine/tyrosyl radicals and copper. For this reason, Cu(II) containing samples could not be analysed by EPR.

Figure 4-9 shows that iron(III) has a significant impact upon tyrosyl radical concentration over prolonged exposure. Degradation continues throughout the exposure period, and seems less limited by O_2 consumption. The extent of degradation observed is also significantly higher in the presence of iron, with the signal less than half (41%) its initial intensity after 3 hours. This is mainly driven by a rapid initial decay period over the first 40 mins, where the radical concentration decreases by 42%. Dissolved oxygen is likely used up during this period, and decay pathways involving ROS dominate. The presence of iron significantly enhances hydroxyl radical production, as summarised in Scheme 4-4, by splitting H_2O_2 formed *in situ* from superoxide.[203] Photo-Fenton water splitting by Fe(III) may also increase hydroxyl radical formation (boxed reaction in Scheme 4-4),[198] however this is strongly dependent on the UV absorbing properties of the iron(III) complex, which depends on pH.[204] It is most efficient at pH 3, where (in the absence of other ligands) the $Fe(H_2O)_5(OH)^{2+}$ complex dominates, which absorbs in the UV region.[205] Iron(III) acetate complexes also show absorbance across the UV range (Figure 4-16), although it is uncertain whether they can undergo a similar reaction.

Hydroxyl radicals readily interact with tyrosine, leading to the formation of DOPA and other oxidation products.[206] Higher hydroxyl radical concentration in the presence of iron therefore explains the more rapid decay.

After the initial decay period, the limited availability of oxygen prevents significant further degradation in systems without metal. However, in the presence of iron, radical concentration continues to decrease, losing a further 16% signal intensity over the following two hours of UV exposure. This may be due to continued photo-Fenton formation of hydroxyl radicals, as shown in Scheme 4-4. Iron(III) may also interact directly with excited state tyrosine, leading to tyrosyl radical formation. Tyrosine degradation and dityrosine formation in iron(III) systems were monitored by fluorometry to confirm findings from EPR studies.

4.4.2 The effect of iron upon tyrosine degradation and dimerization

Samples of PEG_{5000}-Tyr_{10} were prepared at a concentration of 0.294 mmol dm^{-3} (2 mg/ml) in 0.1 mol dm^{-3} acetate buffer at pH 5, with 100 ppm Fe(III) added. These were analysed by fluorometry after 3-hour and 24-hour exposure periods, and compared to unexposed control samples.

In the presence of iron, significant fluorescence quenching was observed, making results unpredictable and unreliable. No iron-tyrosine complexation was predicted by speciation calculations at pH 5 (see Section 4.4.4). Quenching mechanisms are therefore likely to be dynamic (collisional energy transfer)[111] rather than static (changed photophysical properties of fluorophore by complexation).[192,207] Experiments carried out with the same concentration of Zn^{2+} rather than Fe^{3+} showed no quenching. Both ions are of a similar size, therefore collisional conversion of excited states to kinetic energy would be expected to be similar for both metals.[111] As this is not the case, another possibility is the transfer of electronic energy from excited Tyr to metal. This would most likely result in metal d-d excitation. As Zn^{2+} has a d^{10} configuration, no d-d transfer bands are possible, hence no quenching is observed. Electronic energy transfer from excited Tyr to iron centres is therefore a more likely quenching pathway.

To overcome quenching effects, iron was removed from samples before fluorometry. This was achieved by increasing the pH to precipitate the metal as $Fe(OH)_3$. Samples were then filtered, and pH adjusted back to 8.5 for analysis (optimal for dityrosine fluorescence).[184] ICP-MS analysis confirmed 100% removal of the iron, and no significant difference in fluorescence intensity was observed between treated iron and control samples.

The results of fluorescence studies indicated that iron increases the rate of tyrosine degradation, as shown in Figure 4-10. Over a 3-hour exposure period, the decrease in fluorescence intensity is around 2.2 times greater in systems with iron present. This is comparable with the effect observed in EPR studies, as shown in Table 4-1. Absolute degradation values are lower in fluorescence measurements, although these are not directly comparable due to different polymer length (see section 3.8.2) and different experimental setup (which impacts sample irradiance).

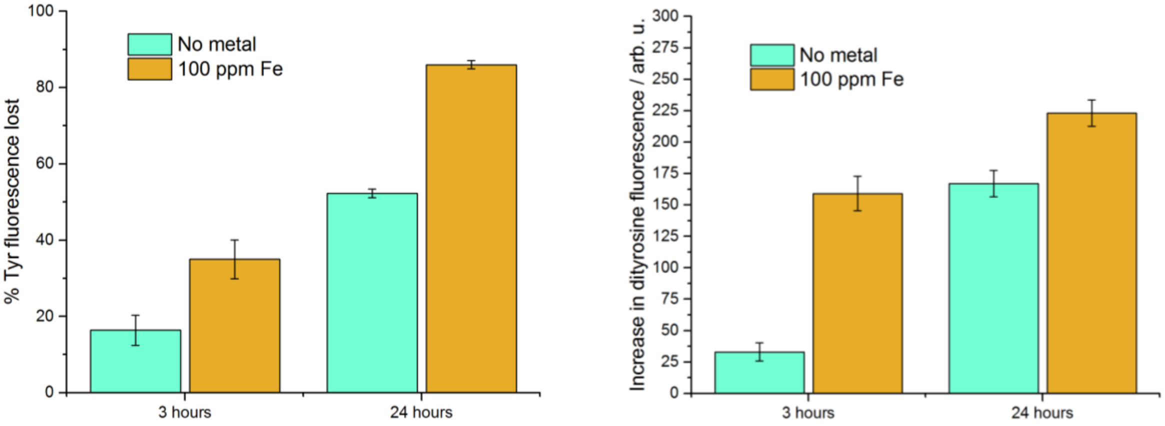

Figure 4-10: Comparison of photodegradation in PEG_{5000}-Tyr_{10} micelles with and without 100 ppm Fe(III), measured by Tyr fluorescence loss (left) and dityrosine formation (right). 95% confidence levels shown, based on 3 measurements. Polymer concentration 2 mg/ml

Table 4-1: Observed Tyr degradation (%D) in PEG-Tyr micellar systems by EPR and fluorescence measurements, with and without 100 ppm Fe(III).

	PEG$_{5000}$-Tyr$_{15}$ EPR radical signal		**PEG$_{5000}$-Tyr$_{10}$ Tyr fluorescence**	
Metal	**%D (Tyr) / 3 hours**	**%D (Fe) / %D (no metal)**	**%D (Tyr) / 3 hours**	**%D (Fe) / %D (no metal)**
-	25	1	16	1
100 ppm Fe(III)	59	2.36	35	2.19

Over a 24-hour exposure, samples containing iron exhibit an almost complete loss in tyrosine fluorescence (86%), suggesting significant oxidation of tyrosine side chains occurs. Continued degradation occurs more readily in fluorescence studies due to the higher surface area/volume ratio of sample compared to EPR capillaries. DOPA, and semiquinone radicals which may contribute to the observed EPR signal, do not show the same fluorescence characteristics as tyrosine, and consequently are not observed in fluorescence experiments.[208]

Fluorescence studies also indicate significantly higher dityrosine formation in iron containing systems (Figure 4-10, right). The dimerization process itself is unlikely to be influenced by metals as it involves only the combination of two tyrosyl radicals, however increased dityrosine formation is indicative of a higher tyrosyl radical concentration in the presence of iron(III). Further investigations were carried out to determine if other transition metal ions present in hair can influence tyrosine photochemistry in the same way.

4.4.3 The effect of copper upon tyrosine photochemistry

Copper is also present in hair fibres.[13] EPR studies were not possible upon copper containing systems, due to exchange interactions leading to line broadening. Like iron, copper also caused significant fluorescence quenching. Unlike iron, the metal cannot be easily removed by precipitation at high pH. Samples were therefore treated using a micro-scale ion exchange column containing Chelex-100 chelating resin, a chelating iminodiacetate based resin with particularly high affinity for Cu^{2+} ions.[209] ICP-MS analysis showed a copper concentration of 0.036 ppm after treatment of a 100-ppm sample (diluted to 14 ppm for analysis), corresponding to a >99% metal removal. No quenching effects were observed after sample treatment.

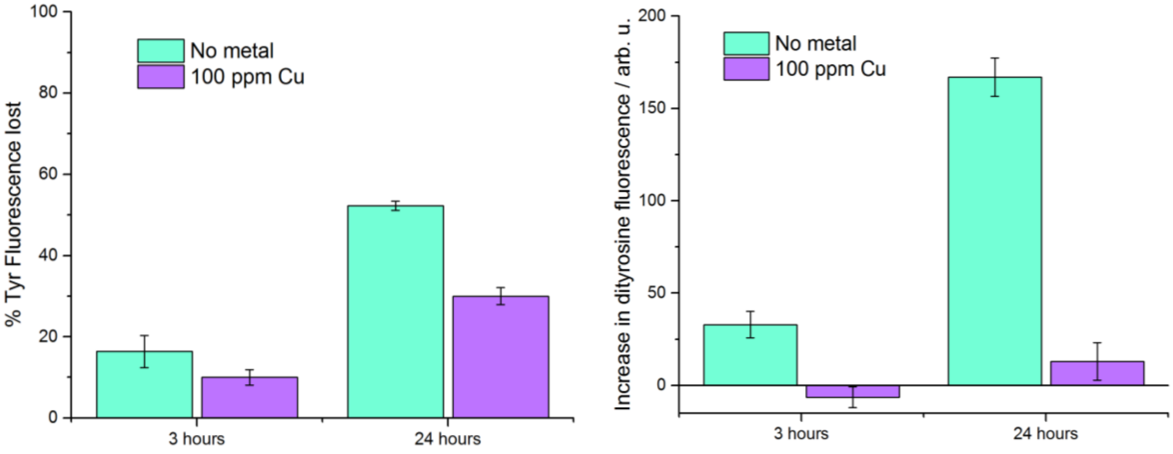

Figure 4-11: Comparison of photodegradation in PEG$_{5000}$-Tyr$_{10}$ micelles with and without 100 ppm Cu(II), measured by Tyr fluorescence loss (left) and dityrosine formation (right). 95% confidence levels shown, based on 3 measurements.

The results of copper photodegradation experiments indicate that copper has a notably different impact upon tyrosine photochemistry. Figure 4-11 shows the loss in tyrosine fluorescence upon UV exposure for PEG$_{5000}$-Tyr$_{10}$ samples, with and without 100 ppm Cu(II). In the presence of Cu(II), degradation is lower by around 40% (38.99% over 4 hours, 42.65% over 24 hours) compared to systems without metal.

A decrease in dityrosine fluorescence emission at 415 nm was observed over the first 4 hours. The reason for this is uncertain, however it can most likely be attributed to experimental error: dityrosine formation over the first 3 hours is negligible. Over 24 hours, dityrosine formation in the presence of copper is 92% lower than in the metal-free system.

Both fluorescence measurements indicate that despite similar redox properties, Cu(II) appears to have the opposite effect to Fe(III) upon the rate of tyrosine photodegradation. Dityrosine formation is significantly suppressed by copper, which suggests the photochemical yield of tyrosyl radicals is lower. In addition to exchange interactions, decreased radical yield may explain the inability to detect a signal by EPR in Cu(II) systems. To explain the difference between the two metals, their speciation within PEG-Tyr systems was considered.

4.4.4 Metal speciation predictions: explaining the differences between iron and copper

Using metal complex stability constants reported by NIST/IUPAC, the speciation of metal ions over a pH range was predicted using MEDUSA software.[210] These are shown in Figure 4-12.

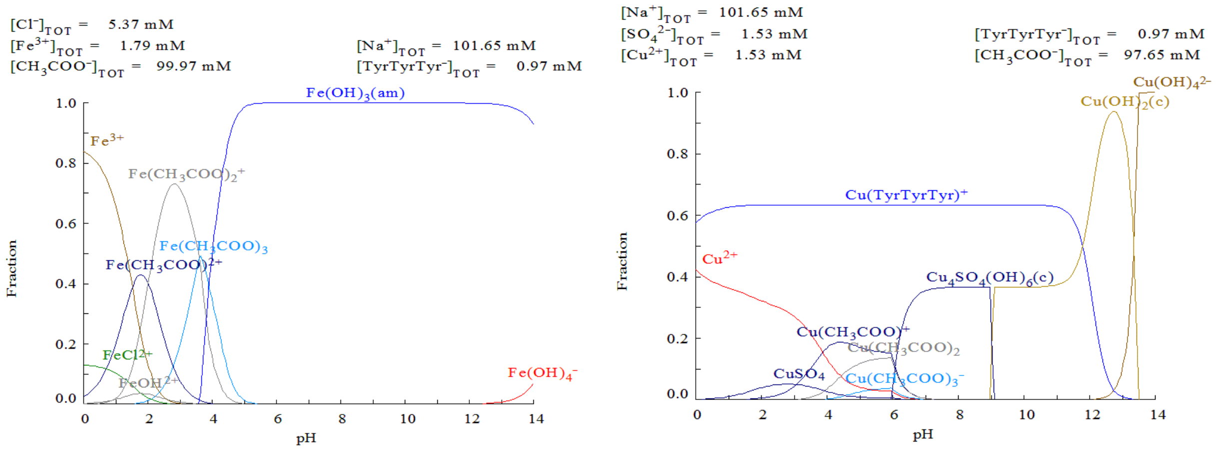

Figure 4-12: Fractional metal speciation plots over pH range 0-14 for iron(III) (left) and copper(II) (right) in PEG-Tyr micelle systems. Photodegradation experiments carried out at pH 5. Plots created by MEDUSA speciation prediction software, based on NIST critical stability data.

The software predicts significant interaction between tyrosine polypeptide and copper(II) over a wide pH range. At pH 5, copper tyrosine complexes are the dominant species. No iron-tyrosine complex formation is predicted, with iron acetate complexes dominant at low pH, and $Fe(OH)_3$ precipitate forming at high pH.

Crystal structures reported in the literature show that complexation occurs between copper centres and the oxygen and nitrogen units within the polypeptide, rather than with tyrosine side chains, as shown in Figure 4-13.[211] However, the structure is distorted slightly, attributed to cation-π interactions between the metal and phenol group. Orbital overlap leads to fluorescence quenching, increases exchange interactions and changes the photochemical properties of the tyrosine units.[212]

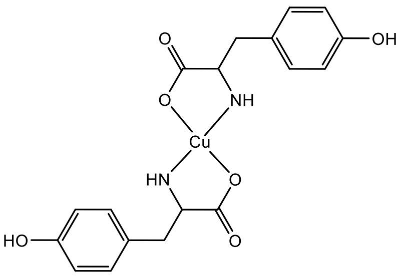

Figure 4-13: Complex formation between tyrosine and copper(II)

Copper complexation to tyrosine will therefore alter the fate of excited state tyrosine molecules. The percentage of tyrosine units within the system which form complexes with copper is likely to be high: the Cu:Tyr ratio is 0.536. Depending on the nature of Cu-Tyr complexes, all Tyr units may interact with a metal centre. Most notably, complexation will enable static quenching of tyrosine excited states by the metal centre.[111] This will result in significant loss in excited state population, which will decrease the photochemical yield of radical species and other degradation products. Although copper(II) can act as an electron acceptor like iron(III) to promote radical formation (see Scheme 4-4), this effect is masked by the static quenching of excited states.

4.4.5 The effect of iron(III) and copper(II) upon tyrosine photochemistry: conclusions

Both iron(III) and copper(II) have a significant impact on tyrosine photochemistry. Iron increases degradation by a factor of 2.2, measured by radical degradation (EPR) and loss in Tyr fluorescence. This was attributed primarily to increased ROS production by Fenton and photo-Fenton chemistry. Increased dityrosine formation also indicated that tyrosyl radical formation was enhanced, suggesting redox interactions between excited state tyrosine and the metal centre.

Copper(II) has the opposite effect upon tyrosine degradation in model systems, with a 40% reduction in activity compared to metal free systems. Dityrosine formation was almost entirely suppressed, indicative of decreased tyrosyl radical yield. Metal speciation predictions indicate the dominant metal species at pH 5 is a copper(II) tyrosine complex. The exact nature of the complex was not determined. Complex formation leads to cation-π interactions, which increases static quenching of excited states, disfavouring other degradation pathways such as radical formation and interaction with oxygen.

Bulk metal concentrations used in these experiments are high relative to the concentration of metals in hair fibres. This enhances the differences between systems, allowing mechanistic interpretation. However, it may not provide a realistic model of metal interaction in hair proteins. Further studies were needed to determine if iron acts in a similar way at realistic metal concentrations.

4.5 Changing metal concentration: the effect of iron at concentrations relative to hair proteins

For a 2 mg/ml polymer sample with 100 ppm metal, the metal concentration in terms of bulk solid material equates to approximately 50000 ppm. In reality, the majority of metal will be free in solution, not adsorbed onto polymer chains. The amount of metal interacting with tyrosine is likely to be much lower.

By comparison, levels of iron found in hair fibres are typically around 40-60 ppm,[105] although levels of copper and iron can reach 200 ppm.[13] The observed effects of the metals in Section 4.4 may therefore be enhanced compared to real systems.

When bulk metal concentration was varied, the extent of tyrosine degradation in PEG$_{2000}$-Tyr$_5$ systems varied for both copper and iron, as shown in Figure 4-14. Measurement error is quite high (Figure 4-14 shows 95% confidence intervals based on a minimum of 3 measurements). Consequently, when metal concentration was decreased by a factor of 100 to 1 ppm (around 500 ppm in solid material), results were indistinguishable from metal-free systems.

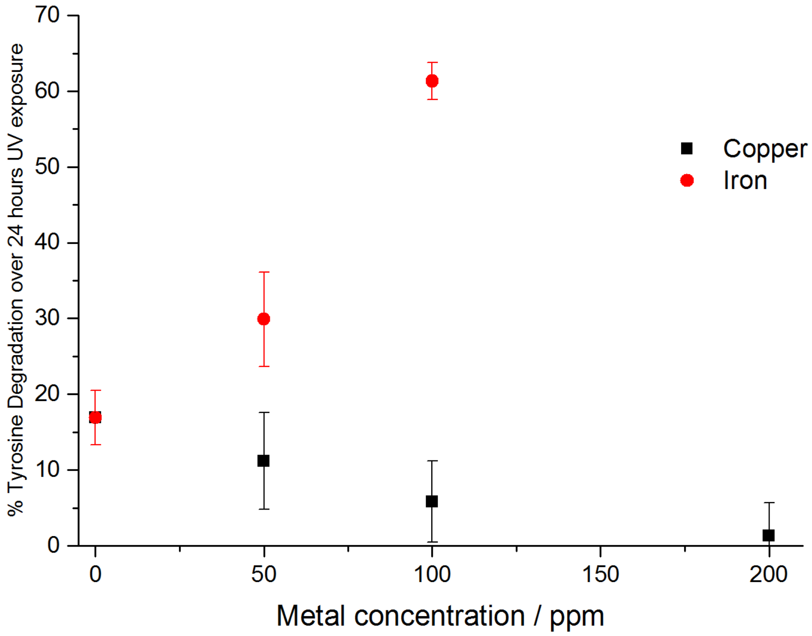

Figure 4-14: The effect of varying bulk metal concentration upon tyrosine degradation for iron and copper. Error bars show 95% confidence intervals.

Metals can influence only tyrosine units close in space: orbital overlap is needed for electron transfer, ROS generated at metal centres are diffusion limited. Within biological materials, hydroxyl radicals and superoxide do not diffuse more than a few nanometres,[213] singlet oxygen may travel up to 70 nm.[89] Values are likely to be similar (possibly slightly longer)[214] for PEG-Tyr systems, potentially allowing some diffusion of ROS between micelles.

Copper-tyrosine complexation localises the metal within the micelles. However, metal concentration (1.53 mmol dm^{-3} at 100 ppm) is lower than tyrosine concentration (3.44 mmol dm^{-3} for 2 mg/ml PEG_{2000}-Tyr_5 sample). Tyr units not complexed to copper will not be affected by static quenching mechanisms. However, they may be close enough within micelle cores to be influenced by the metal's redox properties. These two processes will have conflicting impacts upon the rate of tyrosine degradation.

Conversely, the soluble iron complexes predicted in model systems are freely diffusing through the bulk solution, not partitioned within micelle cores. Interaction between the metal (or metal generated ROS) and tyrosine is therefore limited. Iron within micelle cores may increase the impact of the metal upon Tyr photochemistry.

4.5.1 Hydrophobic iron salts: partitioning metal within micelles

Keratins are not metalloproteins, therefore any iron or copper present is likely exogenous[215] or from degraded enzymes within the fibres.[101] The exact nature of iron complexes in hair fibres is uncertain, although iron(III) doped keratin leads to complexes with glutamate and aspartate residues, as well as Fe-S complexes with cysteine.[216] Iron-carboxylate complexes are therefore reasonable to use in a model system.

Increasing hydrophobicity of the iron complex may encourage partitioning within micelle cores. This will increase interactions between the metal and neighbouring tyrosine units. Iron(III) stearate (Figure 4-15) was added to micellar PEG-Tyr in low concentrations. This complex is poorly soluble in water and is hence incorporated into micelles. Figure 4-16 shows the effect of varying iron(III) stearate concentration upon tyrosine degradation in 2 mg/ml PEG_{2000}-Tyr_5 micelles.

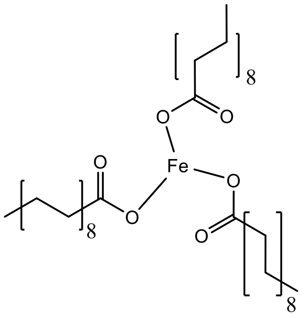

Figure 4-15: Structure of iron(III) stearate. Hydrophobic alkyl chain encourages localisation within micelles, metal-carboxylate interaction mimics iron complexation in protein

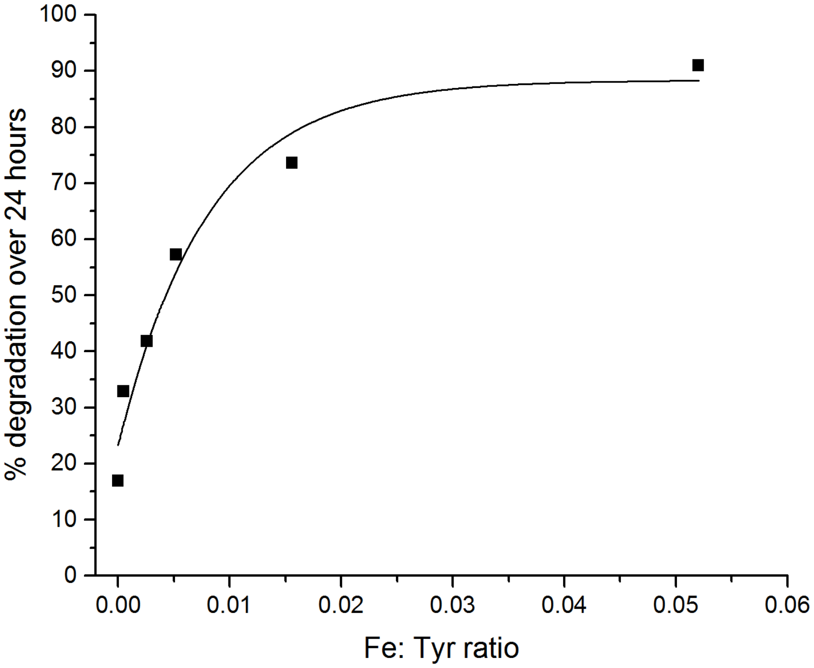

Figure 4-16: Effect of iron(III) stearate concentration (expressed as Fe:Tyr ratio) upon tyrosine degradation in PEG_{2000}-Tyr_5 micellar systems at 2 mg/ml. Measured by decrease in tyrosine fluorescence over 24 hours UV exposure.

Figure 4-16 shows that even at very low metal concentration, degradation is significantly higher than in metal free systems. For comparison, samples with 100 ppm $FeCl_3$ have a Fe:Tyr ratio of 0.52. Concentrations of iron stearate used range from 0.1 ppm to 10 ppm. Increasing hydrophobic iron concentration beyond 10 ppm was not possible due to poor solubility. Activity is significantly enhanced at metal concentrations relevant to iron in hair fibre: 0.1 ppm in solution equates approximately to 50 ppm in solid material.

Localising iron near tyrosine significantly increases its ability to influence photochemical processes. The increase in ROS concentration within micelles because of iron, as well as greater direct metal-tyrosine interaction both contribute to significantly higher degradation. Further mechanistic studies in sections 4.8-4.9 examine these processes in detail by introducing antioxidants and excluding air. Using a hydrophobic iron salt has shown that the metal can have a significant effect upon tyrosine photochemistry at hair protein relevant concentrations.

Degradation reaches a limit around 85%: some tyrosine residues within the polypeptide chain are less susceptible to damage. The different chemical environment of terminal amino acids attached to the PEG group may influence photochemical reactivity. This may partially explain (along with differences to physical environment discussed in Chapter 3) the difference in activity between different polymer lengths.

4.6 Iron complexes as chromophores: mechanistic studies

In addition to redox interactions between iron and excited tyrosine (leading to radical formation) and oxygen (leading to ROS production), other potential effects of metal species must be considered. Iron(III) acetate complexes are known to absorb UV and visible light.[109] The aim of this investigation is to determine whether the absorption of visible light by the metal carboxylate complex can photosensitise tyrosine excitation.

UV-vis absorbance measurements of 100 ppm $FeCl_3$ solutions in acetate buffer show absorbance bands extending into the UVA and visible spectrum (Figure 4-17). This is in line with reported literature absorbance maxima of 337.5 nm and 465 nm for iron(III) acetate complexes,[217] indicating that the buffer displaces chloride ligands, stabilising Fe(III) solubility.

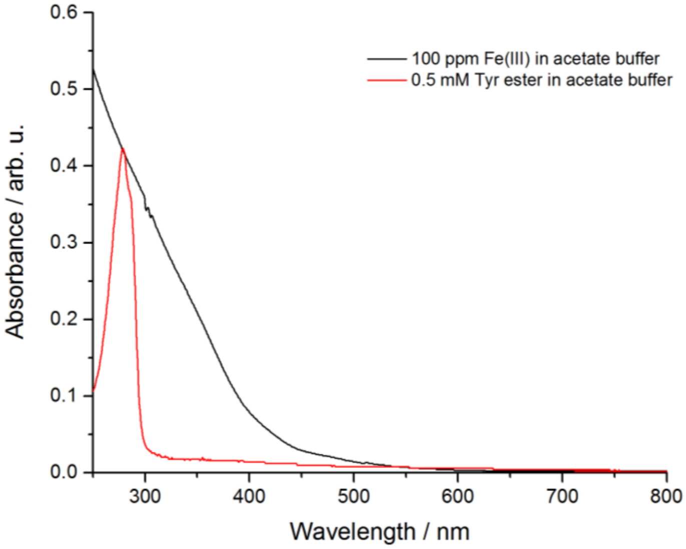

Figure 4-17: UV-vis absorption spectra of 100 ppm iron(III) and 0.5 mM tyrosine ester in pH 5 acetate buffer

Compared to an acetate buffered system model system containing only tyrosine ester (red spectrum on Figure 4-17), the iron(III) acetate complexes present at pH 5 ($Fe(CH_3COO)_3$ or

$Fe(CH_3COO)_2^+$) predicted based on Figure 4-12 show significant absorption extending into the visible range. At the high metal concentrations used for “bulk” iron experiments, this absorbance is significant compared to that of tyrosine itself. This widens the spectrum of light energy absorbed by samples, a series of experiments were performed to determine if photosensitisation by metal complexes influences tyrosine degradation.

4.6.1 Wavelength filters: iron complexes as photosensitisers

As indicated in Figure 4-17, direct absorption of light by tyrosine only occurs below 300 nm wavelength, in the UVB region. Tyrosine degradation via direct tyrosine excitation can therefore only occur by absorption of this high-energy UV light. If iron(III) acetate complexes can act as photosensitisers, then UVA and the shorter wavelengths of visible light may also indirectly cause damage to tyrosine, as outlined in Scheme 4-6.

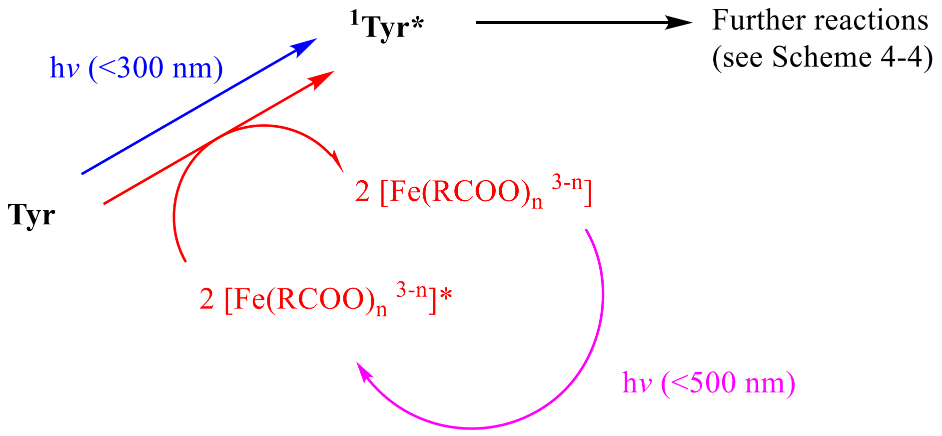

Scheme 4-6: Excitation of tyrosine through energy transfer from photo-excited iron(III) acetate complexes

Photodegradation experiments were carried out where the higher energy UVB (and UVC) light was removed from the incoming light source using a 335 nm wavelength filter. A further set of experiments used a 420 nm filter to remove all UV light. The results of all experiments on systems with and without 100 ppm Fe(III) are shown in Figure 4-18.

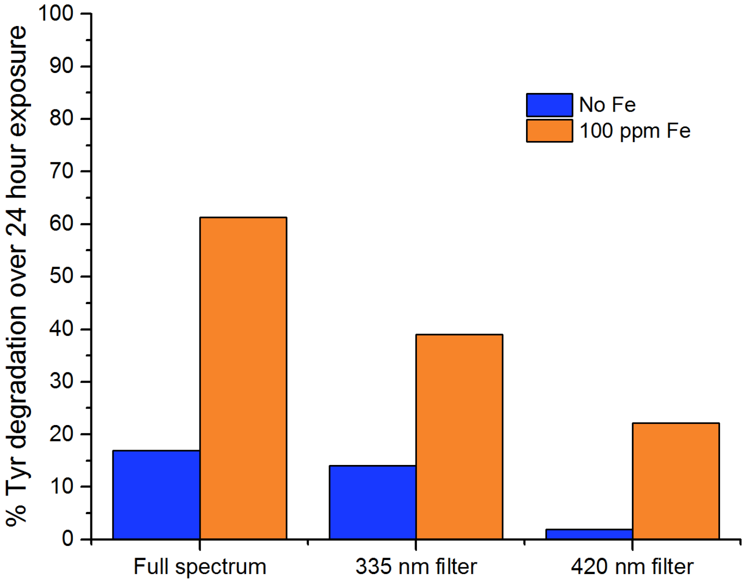

Figure 4-18: Tyr degradation over 24 hours (measured by loss in Tyr fluorescence relative to a dark control) with different wavelength filters, with and without 100 ppm Fe(III) as $FeCl_3$

Results show that as higher energy UV wavelengths are removed from incoming radiation, Tyr degradation decreases. In the absence of metal, no significant (<2%, 2σ = 3.82%) degradation is observed over 24 hours when all UV light is removed by a 420 nm filter. This indicates that in the absence of metal, degradation requires direct UV absorption by tyrosine. Interestingly, despite blocking out the higher energy UV light, the 335 nm filter has little effect upon Tyr degradation in the non-metal system. This result is anomalous, the most likely explanation is that the filter cut-off gradient (50% transmission at 335 nm) may not be sufficiently steep to remove all UVB, allowing some direct absorption by Tyr.

When iron(III) is present, results follow a similar trend, indicating that direct tyrosine absorption still plays a significant role in Tyr degradation in the presence of metal. Unlike metal-free samples, when UV light is excluded in iron(III) systems with a 420 nm filter, significant degradation (22.2%) is still observed over 24 hours. This shows that visible light absorption by iron(III) carboxylate complexes contributes to tyrosine degradation.

This contribution may be via direct energy transfer processes (as shown in Scheme 4-6), or through increased ROS production. Carboxylate ligands can act as catalysts for photo-Fenton water oxidation to produce hydroxyl radicals (see Scheme 4-4) by extending the usable wavelength range into the visible spectrum.[218] The absorption of visible light by iron(III) acetate complexes may therefore increase hydroxyl radical production.

A combination of direct energy transfer from excited iron complexes and catalysed photo-Fenton processes explain degradation by visible light absorption. Based on a comparison with full spectrum irradiation in Figure 4-18, at least 35% of degradation could be attributed to this process. For high concentration $FeCl_3$ experiments, this corresponds a significant proportion to the overall effect of metal on the system. In the context of protein degradation, iron-carboxylate complexes could facilitate significant degradation of amino acid side chains and the polypeptide backbone by catalysing photo-Fenton processes, although absorption of visible light in hair with high melanin concentrations may be limited.

4.7 Further studies into ROS involvement: The effect of polymer concentration

Comparisons between EPR and fluorescence data (section 4.3) and the findings of visible light experiments in the presence of iron(III) carboxylate complexes (section 4.6) strongly indicate that reactive oxygen species such as hydroxyl radicals, singlet oxygen and superoxide radicals play a critical role in degradation. The effect of iron(III) could also be attributed to other factors: direct energy transfer between metal complexes and tyrosine (Scheme 4-6) could be the primary mechanism.

The aim of this section, and sections 4.8-4.9 is to provide further experimental evidence for the involvement of ROS in tyrosine photooxidation. Changing polymer concentration will not influence Tyr environment, but will increase the number of micelles and ROS production (Scheme 4-4). If micelles are isolated environments, increasing Tyr concentration will have no impact upon the degradation rate. Increased ROS diffusing between micelles will however lead to increased degradation.

4.7.1 The effect of polymer concentration upon self-assembly

The physical environment of tyrosine can have a significant impact upon reactivity, as studied in Chapter 3. Polymer concentration can affect the nature of aggregates, with liposomes and bilayers forming at higher concentrations.[219] Such changes will significantly impact Tyr photoxidation. As this study focuses on the role ROS play in degradation, changes to macromolecular structure are undesirable. DLS measurements were therefore carried out at a range of different polymer concentrations, to identify any major structural changes over the concentration range studied.

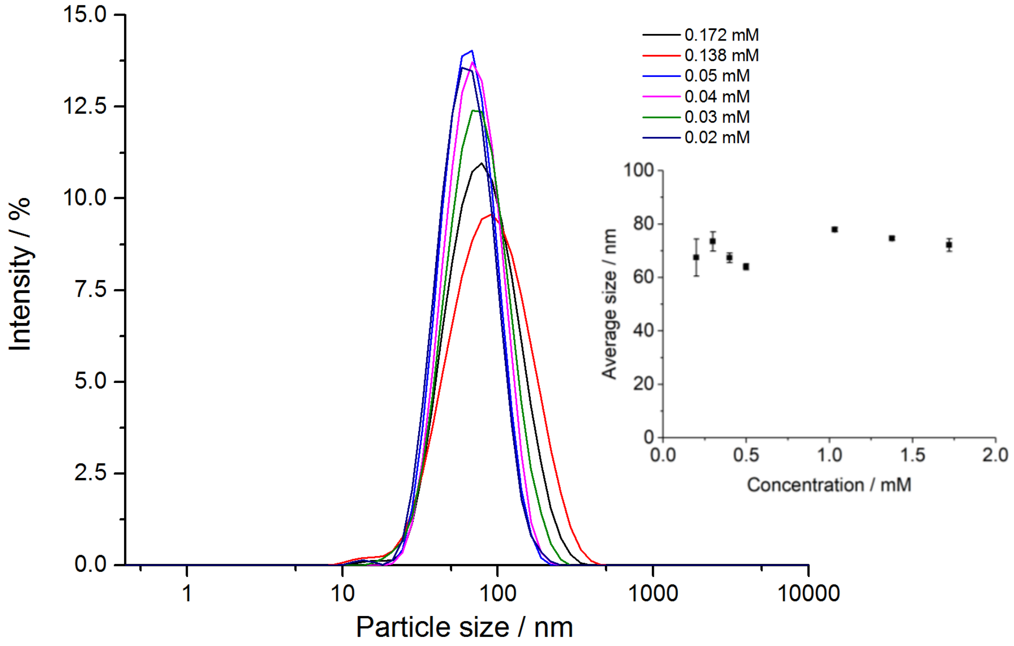

Figure 4-19: Particle size distribution by light scattering intensity for PEG$_{2000}$-Tyr$_5$ micelles at varying concentration. Inset: average particle size against concentration, average of 3 measurements. 95% confidence levels shown

Figure 4-19 shows that as polymer concentration changes, there are slight variations in average micelle hydrodynamic radius, although the data does not follow a clear trend. The average particle size across all concentrations in Figure 4-19 is 70.98 nm, with a variation of ±9.86%. Compared to changes observed in DLS measurements upon thermal rearrangement of polymers (see section 3.7.1), this variation is small, and is therefore unlikely to represent a significant structural change to micelles. EPR spin labelling measurements also indicate that changes to tyrosine environment as polymer concentration changes are small (see section 3.6.4). Any difference in photochemical activity over this concentration range is therefore unlikely due to changes in tyrosine environment.

4.7.2 The effect of polymer concentration upon photooxidation

Increasing polymer concentration increases the number of micelles present within the sample. Polymeric micelles are often described as “kinetically frozen” due to the relatively slow exchange of polymer units between micelles.[220] Practically, this means that photo-excited tyrosine species have lifetimes too short to diffuse between micelles, and as such most likely react with other species within the immediate micellar environment. Micelle systems could therefore be described as isolated, without direct interaction between micelles. Increasing the number of micelles present would therefore not change the rate of photooxidation.

In metal free systems, reactive oxygen species are produced through the interaction of photo-excited tyrosine and oxygen. Increasing tyrosine concentration will therefore increase ROS production, assuming an excess of oxygen is present. Unlike excited tyrosine species, ROS are small enough to diffuse between micelles, although their short lifetime may limit diffusion distance. At higher micelle concentration, more ROS are produced, and diffusion between micelles is more favourable. Therefore, increased photooxidation would be expected.

Photodegradation measurements were carried out at a range of polymer concentrations, with and without 0.5 ppm hydrophobic Fe(III). The results are summarised in Figure 4-20.

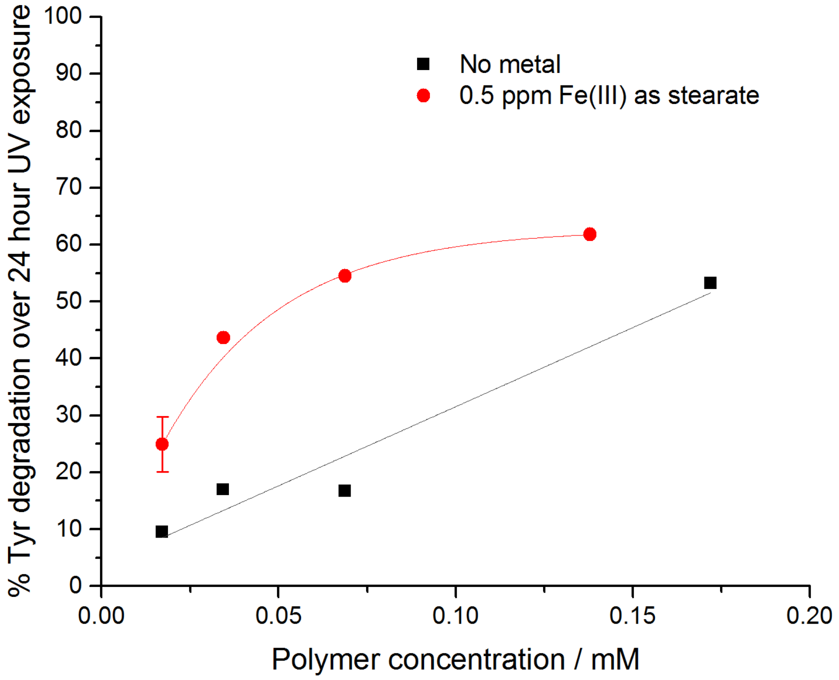

Figure 4-20: The effect of PEG$_{2000}$-Tyr$_5$ concentration upon photooxidation rate in metal free and hydrophobic iron(III) systems.

As predicted, polymer concentration influences the extent of photodegradation over a 24-hour exposure period, with increased degradation at higher concentrations. Although the number of data points is limited, the relationship appears to be linear. This proves that micelles are not isolated systems, and provides further evidence for ROS diffusing between micelles.

The effect of polymer concentration is different in the presence of hydrophobic iron(III). In iron(III) systems, hydroxyl radical concentration is increased, leading to increased degradation relative to metal-free systems. If this were the sole effect of the metal, then the increase in ROS concentration due to 0.5 ppm iron(III) would be constant for varying polymer concentration. Although the number of data points is limited, this does not appear to hold true, indicating that direct metal-tyrosine interactions must also influence the photochemistry of the system.

Therefore, Fe(III) is capable of accelerating Tyr degradation both via direct interaction with tyrosine, and through increased ROS production. The relative contributions of both pathways are unclear and likely depend on partitioning of metals within the micelle. Further studies were carried out in air-free systems and with antioxidants, to control ROS production.

4.8 Mechanistic studies: the effect of excluding air upon Tyr degradation

Without oxygen, most literature reports indicate that the primary photodegradation product of tyrosine is the dimerised product dityrosine, formed through the combination of two tyrosyl radicals Scheme 4-7.

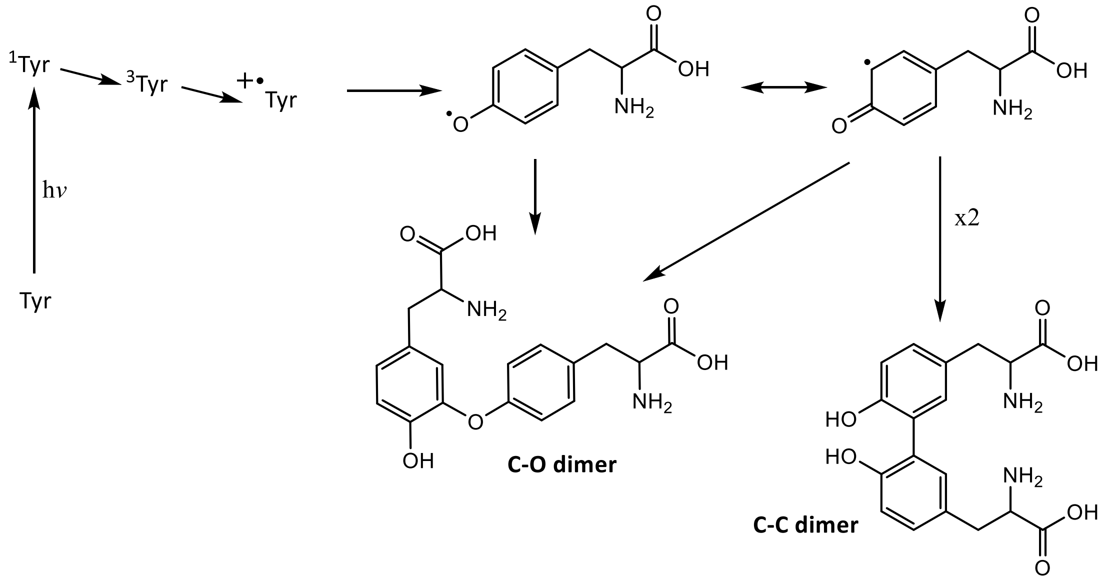

Scheme 4-7: Formation of dityrosine from photo generated Tyr based radicals. Either C-O or C-C linked dimer can form.

Iron(III) accelerates tyrosyl radical formation and overall Tyr degradation through increased ROS production and direct metal-Tyr interaction. The aim of this study was to examine the effect of direct metal-Tyr interactions upon the radical decay pathway by limiting ROS pathways and examining how partitioning of metal within micelles influences reactivity.

4.8.1 Choice of iron(III) salts: modelling direct metal-Tyr interactions

Concentrations as low as 0.1 ppm of iron(III) stearate influence Tyr photodegradation (see Figure 4-16). This was attributed to partitioning of the highly hydrophobic metal salt within micelle cores, near tyrosine residues. This increases the chances of direct metal-Tyr interaction as well as providing a localised source of hydroxyl radicals.

Less efficient partitioning within micelle cores may result in lower direct metal-Tyr interaction. This will decrease the significance of direct interactions upon the impact of iron in Tyr degradation, the effect of the metal will be more dominated by ROS pathways. Excluding air or adding antioxidants will therefore have a larger impact upon degradation than in a system with more direct metal-Tyr interaction.

Decreased partitioning of the metal centre in the micelles can be achieved by altering the hydrophobicity of the metal complex. Acetylacetone is poor at partitioning in non-ionic surfactant micelles (Triton 100-X) compared to other diketones[221] and stearic acid,[222] although literature partitioning data varies significantly for stearates. It was expected that partitioning within PEG-Tyr micelles would follow a similar trend, and Fe(acac)$_3$ (Figure 4-21) will therefore partition less effectively within micelles.

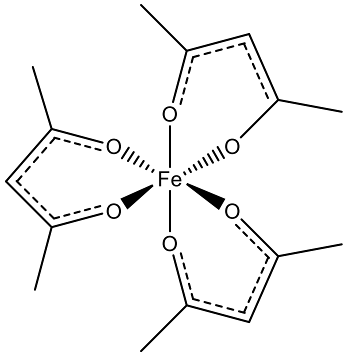

Figure 4-21: Structure of Fe(acac)$_3$ complex

Experiments found that Fe(acac)$_3$ significantly enhanced Tyr degradation at low concentrations (see Figure 4-22). This increase in activity is most likely due to increased hydroxyl radical production by the metal. It may be more effective than higher concentrations of FeCl$_3$ due to the lack of chloride, which can inhibit photo-Fenton processes.[204] The contribution of direct metal-Tyr interactions was investigated by comparing the effect of excluding air upon degradation in systems containing the same concentration of iron(III) as either partitioned Fe(stearate)$_3$ or non-partitioned Fe(acac)$_3$.

4.8.2 Comparing degradation in oxygen free samples, with different iron(III) complexes

Degassed samples of 0.174 mmol dm^{-3} PEG$_{2000}$-Tyr$_5$ containing 0.5 ppm Fe(III) as either stearate or acetylacetonate were sealed and irradiated for 24 hours before being analysed by fluorometry. All samples were in 0.1 mol dm^{-3} acetate buffer at pH 5. Tyr degradation and dityrosine formation was measured, relative to control samples kept in the dark over the same period. Results are shown in Figure 4-22.

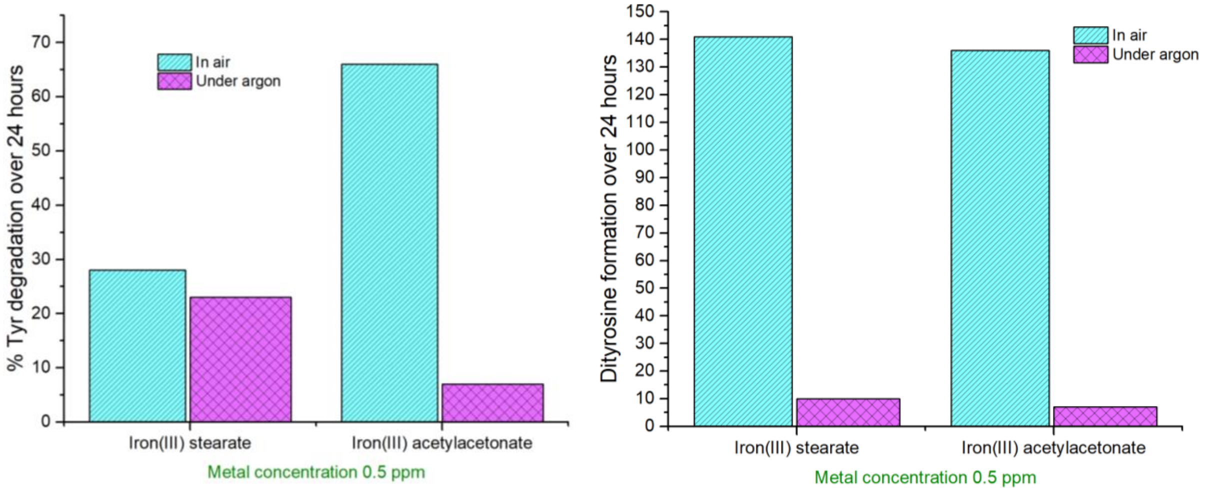

Figure 4-22: The effect of excluding air upon Tyr degradation (left) and dityrosine formation (right) in the presence of 0.5 ppm iron(III) as stearate or acetylacetonate complexes. PEG$_{2000}$-Tyr$_5$ concentration 0.172 mM.

In all experiments, lower degradation was observed in the absence of air. Table 4-2 summarises the effect of excluding air on photooxidation processes. Data is also shown for a metal-free sample of PEG$_{5000}$-Tyr$_{10}$ at a concentration of 0.293 mmol dm^{-3}.

Table 4-2: Loss of photochemical activity in air free samples, compared to identical samples in air. Based on fluorescence data, rounded to nearest %.

% activity suppressed by excluding air	**PEG$_{5000}$-Tyr$_{10}$, no metal**	**PEG$_{2000}$-Tyr$_5$, 0.5 ppm Fe(stearate)**	**PEG$_{2000}$-Tyr$_5$, 0.5 ppm Fe(acac)$_3$**
Tyr degradation	94	18	89
Dityrosine formation	87	93	95

Considering tyrosine oxidation, both metal containing systems are less affected by the exclusion of oxygen than the metal-free system. This indicates that direct metal-tyrosine interactions play a role in Tyr degradation. Furthermore, the localised iron(III) stearate is much less influenced by the exclusion of oxygen. Direct interaction between iron and tyrosine is significantly enhanced when the metal is immobilised within the micelle, contributing more to overall degradation. Excluding oxygen therefore has less impact compared to Fe(acac)$_3$, where increased activity primarily arises from increased ROS production.

Although dityrosine formation does occur in the absence of oxygen, in agreement with literature,[58] its formation is significantly suppressed. This is indicative of lower radical yield, as excited state tyrosine cannot transfer an electron to molecular oxygen, as shown in Scheme 4-4. Despite increased dityrosine formation compared to metal-free systems (see section 4.4.2), iron(III) samples are affected in a similar way when air is removed. This suggests that metal complexes are not effective electron acceptors as suggested in Scheme 4-4. Increased activity by direct metal-Tyr interaction could therefore arise from photosensitisation of tyrosine by metal complexes as suggested in Scheme 4-6.

4.9 Mechanistic studies: the effect of antioxidants upon Tyr photooxidation

Experiments comparing tyrosine degradation in air-free systems have shown that interaction with oxygen and the formation of reactive oxygen species play a key role in tyrosine photodegradation. Interaction with hydroxyl radicals can lead to the formation of peroxides on the polypeptide chain (see Scheme 1-17).[64] Singlet oxygen can react with tyrosine, leading to endoperoxides and hydroperoxides on Tyr side chains.[58] This can lead to autoxidation of side chains and the polypeptide, outlined in Scheme 4-8.[223]

These chain processes can be particularly damaging as only the initiation step requires UV input, and the reaction can propagate until the chain is broken. This initial creation of hydroperoxides can therefore lead to significant damage to polypeptide structure and amino acid side chains. This is likely accelerated in the presence of iron(III) due to increased hydroxyl radical concentration.

Antioxidants break the autoxidation cycle, slowing the rate of oxidative damage. They can act as reducing agents, replacing the role of RH in Scheme 4-8 and preventing the formation of R˙ radicals. Antioxidants can also quench or inhibit singlet oxygen formation,[224] and some inactivate pro-oxidative metal centres.[225]

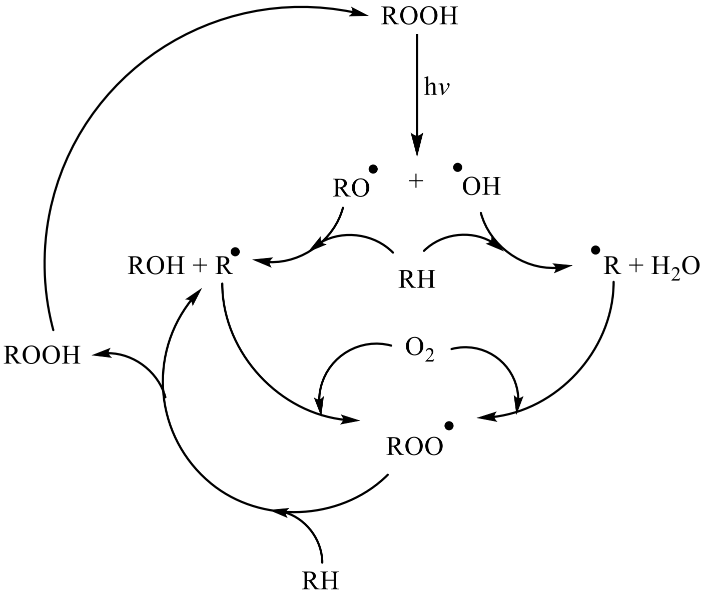

Scheme 4-8: General scheme for autoxidation, initiated by photolysis of hydroperoxide

The aims of this investigation were to attempt to identify and quantify ROS within model systems, and probe the effectiveness of antioxidants at preventing autoxidative pathways (compared to excluding air entirely). This enables degradation from autoxidative processes to be quantified relative to overall degradation.

4.9.1 Attempts to identify and quantify reactive oxygen species by spin trapping

Initial studies focussed on the spin-trapping of reactive oxygen species using the nitrone spin trap DMPO (Scheme 4-9), in an attempt to quantify photo-generated ROS. Spin trapping reactions are typically very rapid ($k \approx 10^9$ M^{-1} s^{-1} for hydroxyl radical trapping),[226] spin traps effectively quench ROS, forming radical adducts which can be quantified by EPR. Radical adducts were identified based on comparison to literature reported hyperfine splitting patterns, as shown in Figure 4-23.[227-229] However, prolonged UV exposure and the presence of metal ions caused degradation of spin adducts. Quantitative spin trapping was therefore not possible.

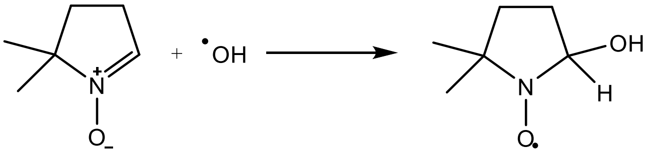

Scheme 4-9: Spin trapping of hydroxyl radical by DMPO

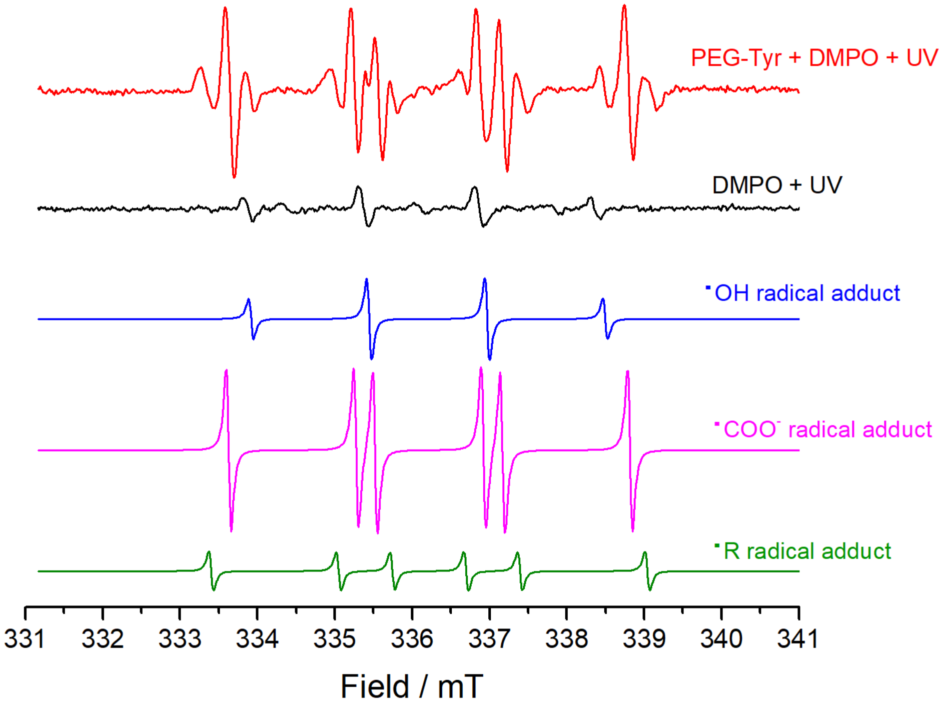

Figure 4-23: EPR spectrum of PEG_{2000}-Tyr_5 micelle system in the presence of DMPO spin trap after 5 min UV exposure (top). Contributions from various radical adducts shown.

Although spin trapping could not be used quantitatively, the results do confirm the presence of hydroxyl radicals formed upon UV irradiation. A lower concentration of hydroxyl radical adducts are detected when spin trap is irradiated in water, indicating that not all hydroxyl radical adducts in the system derive from Tyr generated hydroxyl radicals. No radical adducts are observed in non-irradiated (metal free) samples. This agrees with proposed degradation mechanisms and the results of other investigations. They also confirm the presence of carbon centred radicals ($R^•$), indicating that the system may be subject to autoxidative degradation (Scheme 4-8). However, due to the susceptibility of spin adducts to degradation or further reactions, quantitative analysis of ROS concentration in different systems was not possible. Antioxidants were considered as an alternative to spin trapping, to quantify the impact of ROS upon photooxidation.

4.9.2 Butylated hydroxytoluene (BHT) as an antioxidant in photochemical experiments

The hydrophobic micelle cores in PEG-Tyr model systems show that localisation of metal complexes has a significant effect on their activity (see section 4.5.1). An ideal antioxidant would therefore also be localised within micelles. Small molecules were preferred as these are less likely to disrupt self-assembly. Butylated hydroxytoluene (BHT) (Figure 4-24), was identified as a suitable candidate. It is relatively hydrophobic,[230] and acts by donating the phenolic proton to quench peroxyl radical species. This creates a phenoxyl radical which is stabilised through conjugation to the aromatic ring and steric hindrance provided by the tert-butyl groups in *ortho* positions.[231] This decreases O-H bond strength: bond dissociation energy in BHT is 339 kJ mol^{-1}, significantly lower than Tyr (362 kJ mol^{-1}).[188,232]

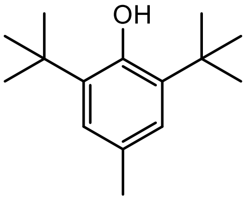

Figure 4-24: Butylated hydroxytoluene (BHT) structure

Different BHT concentrations were added to PEG-Tyr micelle samples. These were exposed to UV and degradation was monitored relative to unexposed control samples. Experiments were

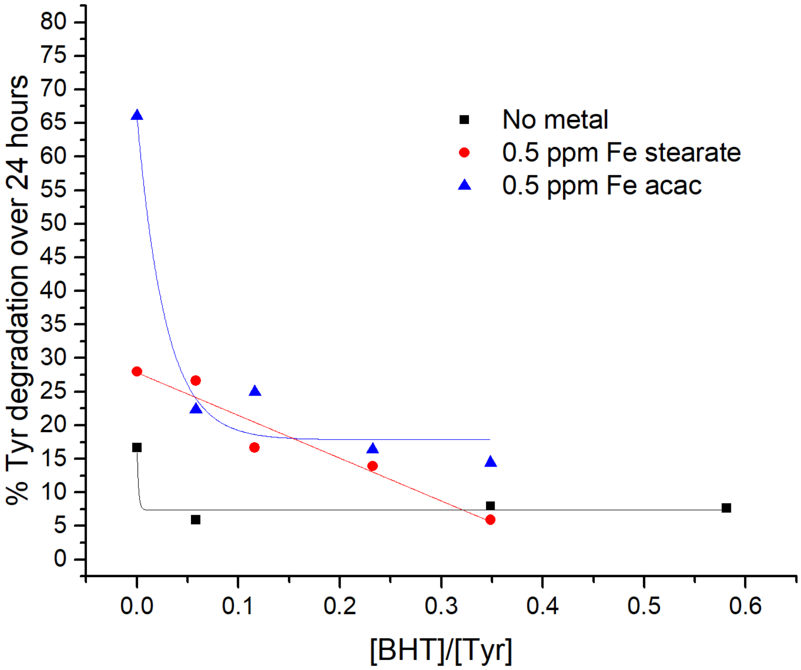

Figure 4-25: The effect of varying BHT concentration upon Tyr degradation in different PEG$_{2000}$-Tyr$_5$ micellar systems. Polymer concentration 0.172 mM.

carried out in systems without metal, and systems with 0.5 ppm Fe as hydrophobic stearate or acetylacetonate complexes. The results are summarised in Figure 4-25. The trendlines shown are illustrative and not intended to represent an accurate model of the activity change.

BHT has a significant impact upon the observed photodegradation of tyrosine over a prolonged exposure period. This is likely due to it's antioxidant properties, however BHT may also act as a competing chromophore which could mitigate Tyr degradation. This is true not only in metal free systems, but also when iron(III) is present as acetylacetonate and stearate complexes. However, the different iron complexes exhibit a notably different response to the antioxidant. The effect of adding in a low concentration of BHT (0.05 mmol dm^{-3}) is compared in Table 4-3. An effective antioxidant will break the autoxidation cycle (Scheme 4-8) and will therefore be active at low concentrations.

Table 4-3: The effect of BHT in low concentration upon Tyr degradation over 24 h in 0.172 mM PEG$_{2000}$-Tyr$_5$ micellar systems

System	**% deg. No BHT**	**% deg. 0.05 mM BHT**	**% deg. suppressed by antioxidant**
No metal	16.7	5.9	64.7
0.5 ppm Fe(stearate)	28.0	26.6	5.0
0.5 ppm Fe(acac)	66.0	22.4	66.1

Both metal-free and Fe(acac)$_3$ systems show a rapid drop-off at low antioxidant concentration. This is indicative of BHT effectively quenching peroxyl radicals, thus breaking the autoxidation cycle. The activity in both systems drops by a similar amount (around 65%) upon BHT addition, indicating that this significant amount of observed degradation arises from autoxidative processes.

As the concentration of antioxidant is increased, the metal-free system shows no further decrease in activity. Experiments in an inert atmosphere have shown that some degradation still occurs in the absence of oxygen (see section 4.8). Based on literature reports and experimental findings, air-free degradation is likely via tyrosyl radicals resulting in dityrosine formation. However, in antioxidant systems, oxygen is still present, and could therefore interact directly with tyrosine, leading to the formation of reactive oxygen species and encouraging tyrosyl radical formation (see Scheme 4-4). Although BHT breaks autoxidation and can act as a radical scavenger, it does not effectively stop all oxygen mediated degradation, and is therefore less effective than excluding air altogether.

By comparison, the addition of a low concentration of BHT to iron(III) stearate containing samples results only in a modest drop in activity. As antioxidant concentration is increased, activity drops off gradually, however the stearate system follows a notably different profile than metal-free and Fe(acac)$_3$ samples. Air free experiments also showed a significantly different result for Fe(III)stearate. The role of oxygen is notably less significant when the metal is localised near tyrosine residues. Consequently, autoxidative processes play a lesser part in overall degradation, with direct metal-tyrosine interactions more significant. As antioxidant concentration is increased, both iron(III) systems show continued decrease in activity. This is likely due to increased scavenging of hydroxyl radicals.[233] BHT has also been shown to interfere with iron complex formation,[234] suggesting possible direct interactions between antioxidant and the metal which may influence iron's activity.

Experiments with antioxidants are in broad agreement with the results from air-free experiments, confirming that oxygen and reactive oxygen species play a significant role in photodegradation. A large proportion of observed activity in Fe(acac)$_3$ and metal free systems can be attributed to autoxidative processes, which are effectively halted by the antioxidant. However, by comparing to air free experiments, it is apparent that BHT does not halt all oxygen mediated degradation. Localised iron centres are capable of direct metal-tyrosine interaction, this activity is less influenced by air exclusion or antioxidants.

4.10 Key findings and conclusions: Photochemistry of tyrosine in model systems

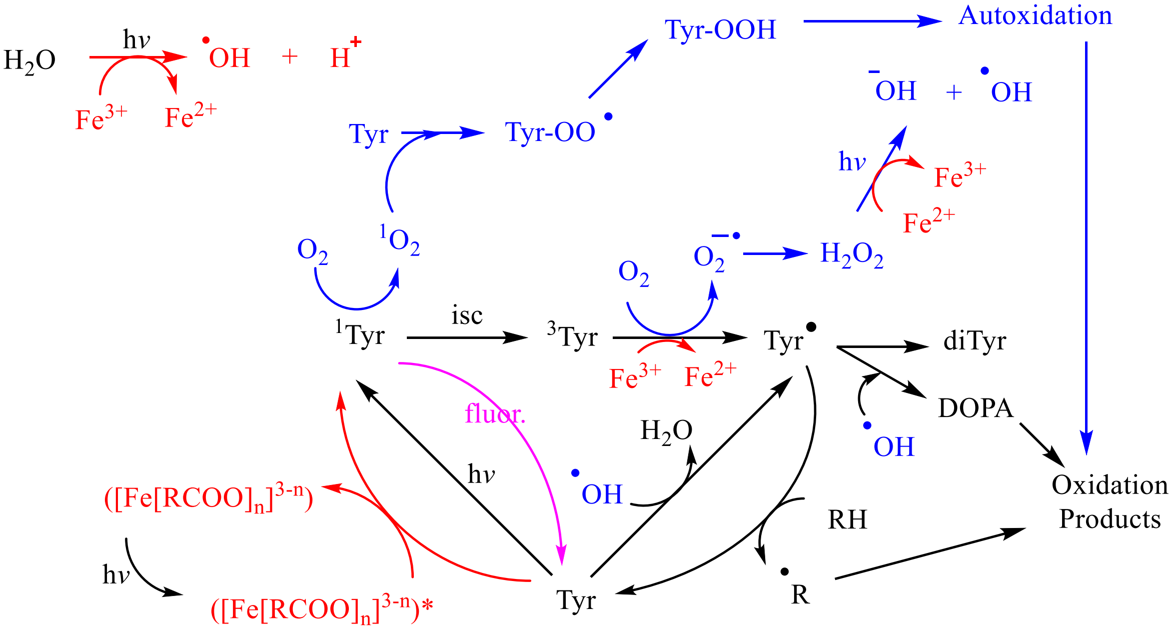

Scheme 4-10: Summary of tyrosine degradation in model systems. Oxygen dependent pathways are shown in blue, the involvement of iron is shown in red.

Tyrosine degradation upon prolonged UV exposure was monitored both by EPR (change in tyrosyl based radical concentration) and fluorescence spectroscopy (decrease in tyrosine fluorescence, dityrosine formation). Both techniques showed that the addition of iron(III) significantly increases the extent of degradation, by around a factor of 2.2 for 100 ppm bulk Fe(III).

Oxygen availability was found to be critical to degradation. Although some degradation occurs in oxygen free systems, when oxygen is absent or limited (as in EPR measurements), degradation is suppressed by up to 90%. Most tyrosine photodegradation therefore proceeds via oxygen and ROS involving pathways, outlined in Scheme 4-10.

Antioxidant experiments show a similar picture, with metal-free and non-localised Fe(acac)$_3$ samples exhibiting a 65% drop in degradation even at catalytic levels of BHT. This indicates that autoxidative processes play a key role in systems both with and without iron(III).

Direct metal-tyrosine interactions also play a critical role, most notably when iron(III) is localised near tyrosine residues. Experiments with hydrophobic iron(III) stearate show significant activity enhancement at concentrations as low as 0.1 ppm, proving that the metal can catalytically influence tyrosine degradation at levels comparable to iron in hair proteins. Excluding air or adding antioxidants has a reduced impact upon localised iron(III) activity.

Direct interactions between the metal and tyrosine include metal carboxylate complexes acting as photosensitisers by visible light absorption, as well as direct oxidation of excited states. Direct interactions between copper(II) and tyrosine in Cu-Tyr complexes lead to static quenching of excited states, and a decrease in activity compared to metal-free systems. The effect of localised copper at catalytic concentrations was not studied, and may be different compared to high bulk concentration.

5. Monitoring Radical Species in Hair Proteins

Studies with PEG-Tyr model systems have revealed information about the mechanisms of tyrosine photodegradation, roles played by transition metal ions and reactive oxygen species, and the importance of tyrosine mobility. The photochemistry of tyrosine will likely strongly reflect the overall photochemistry of keratin proteins, given its high abundance relative to tryptophan and phenylalanine.

Whilst model systems provide a good mimic of tyrosine within restricted keratin proteins, the overall photochemistry of hair fibres will involve other factors. Less abundant chromophoric amino acids such as tryptophan, as well as melanin pigment and lipids within the fibres will also exhibit a photochemical response.

To better understand how the photochemistry in model systems may relate to the photochemistry in hair proteins, some understanding of how keratin in hair fibres responds upon irradiation is needed. Solvation is significantly limited in hair compared to model systems. However, hair responds to changes in ambient humidity (which can vary significantly). This results in a significant change to water content. This may influence diffusion and activity of oxygen and its reactive species such as hydroxyl radicals, superoxide and singlet oxygen, shown to cause significant damage in model systems.

The aims of this chapter are therefore:

- To observe and characterise the response of hair proteins to UV stimulus, and any degradation of fibres occurring from prolonged exposure.
- Link observations from hair fibre experiments with results from model systems to improve understanding of photochemical processes within the real system.
- To monitor the effects of changes in hair water content upon the photochemistry of hair proteins.
- Investigate the use of antioxidants and the exclusion of oxygen to confirm if the role of reactive oxygen species in degradation mechanisms is similar to model systems.

5.1 Overview of hair structure and considerations on its photochemistry

Keratin proteins make up around 80% of hair fibres,[10] with tyrosine the main chromophoric amino acid present (see section 1.1). It is likely that the photochemistry of tyrosine will contribute significantly to the overall photochemistry of the hair fibre, hence model systems focused on investigating tyrosine photochemistry.

However, other components of hair fibres may also contribute to their photochemistry. The most notable is melanin, a pigment produced by the oxidation and polymerisation of tyrosine and cysteine amino acids. Melanogenesis is a process induced within hair and skin as a response to UV exposure. Eumelanin has a strong UV protective effect, effectively dissipating absorbed light at harmful wavelengths.[78]

Melanin levels in hair and skin vary significantly by type and colour. UV exposure has become an increased risk in the last few decades.[235] Although UV damage to hair proteins does not present the same risks as skin damage, it can change the cosmetic properties of fibres, of increased interest as people become more conscious of such factors.

A study of keratin photochemistry in hair fibres therefore needs to exclude the photochemistry of melanin. The photochemical response of melanin was characterised by comparing two hair samples: one “natural white” sample (containing low melanin levels), and a “mid-brown” sample with high melanin levels.

Studying keratin photochemistry requires that hair fibres should, as far as possible, be kept intact for analysis. Destruction of hair fibres will alter the environment of hair proteins, thereby preventing an assessment of keratin in its native environment. This limits the analytical techniques available, as many require destruction of the sample. EPR spectroscopy provides a useful, non-invasive method of observing photo-induced radical species in intact hair fibres.

5.2 Observation of radical species in hair by EPR spectroscopy

EPR studies into paramagnetic species present in hair fibres have been carried out before, although many studies focus on either the strong intrinsic melanin signal[236] or paramagnetic metal centres such as copper which are present in the fibres.[104] White hair, with very little or no melanin has a very weak intrinsic EPR signal, as reported in the literature.[237] Figure 5-1 compares intrinsic EPR signals without irradiation of 130 mg of white and brown hair, cut into 4 cm lengths and placed vertically into the X-band EPR cavity in a 5 mm quartz EPR tube.

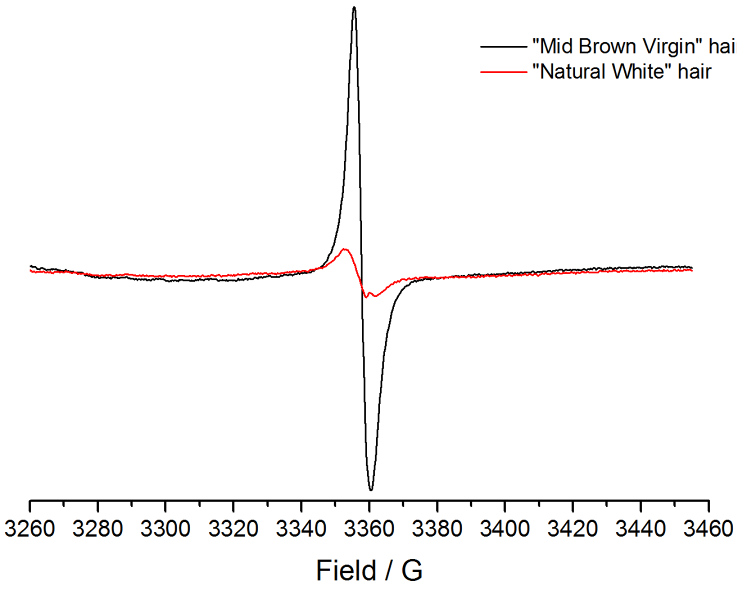

Figure 5-1: Comparison of initial intrinsic X-band EPR signal of natural white and mid-brown virgin hair samples. Spectrum recorded before any UV exposure, intensity corrected for small variation in sample mass.

Radicals are immobilised in a solid-like environment, resulting in a range of orientations relative to the applied fields. This gives rise to broadening and unresolved hyperfine splitting in the EPR spectrum, resulting in a single, broad EPR peak. This prevents easy identification of species by hyperfine interactions.

2nd integrals of the spectra in Figure 5-1 reveal intrinsic radical concentration in the brown hair sample is 2.82 times greater than the white hair sample. The simple linewidth is 1.75 times greater in the white hair sample, from a simple simulated fit using PEST WINSIM.[238] The g-value of the radical signal observed in brown hair is 2.0055, similar to literature reported value for melanin (2.004).[237]

The signal for white hair is significantly smaller, confirming that white hair has very little/no melanin content. The g-value for the white hair signal is similar, but shifted slightly, at 2.0060. The closest literature reported value for tyrosyl radical species in a protein is 2.0053.[132] Tryptophan based radicals are typically lower, around 2.0026-2.0028,[239] whereas lipid peroxyl and carbon centred radicals are 2.014 and 2.004 respectively.[240]

The identity of the radical signal observed in white hair cannot therefore be assigned conclusively based on g-value, although it is comparable to literature values for a tyrosyl radical. Kirschenbaum et al report that white hair and milled wool keratin has a weak intrinsic EPR signal, attributed to highly immobile, long-lived amino acid based radicals such as tyrosyl radicals.[237] The observed spectrum is likely a combination of tyrosyl species and small amounts of Trp, lipid or melanin radical species.

5.3 Reproducibility tests

A key aim of this study is to investigate the effect of light upon radical species in hair fibres. This can be monitored by looking at changes to the intrinsic EPR signal upon irradiation. However, this intrinsic signal is weak in white hair samples, resulting in comparatively noisy EPR spectra. This gives rise to a degree of scatter in the data, although the trends remain clear. The reproducibility of radical build-up and decay was tested by taking three different samples of white hair and monitoring the change in EPR signal intensity over a two-hour exposure period at ambient humidity followed by a further 24 hours after the lamp was switched off. Figure 5-2 shows the average and 95% confidence intervals for the signal growth and decay measurements.

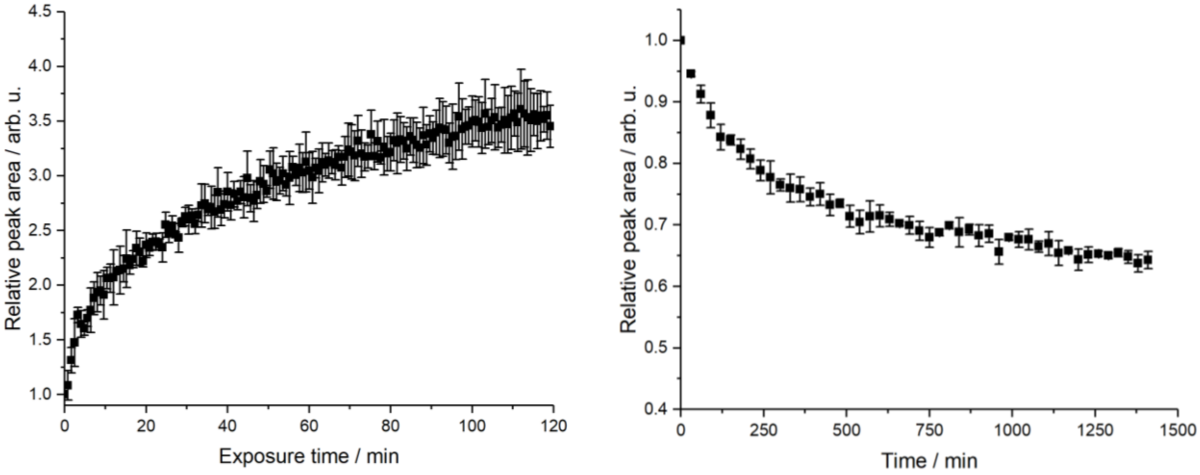

Figure 5-2: Mean and 95% confidence intervals for white hair signal growth (left) and decay (right) measurements. Data have been normalised - initial intensity before exposure (for growth curve) and maximum intensity upon lamp switch off (for decay curve) set as 1.

The data scatter and confidence intervals are considerably larger for the signal growth data. This is likely due in part to the different time resolutions involved. For decay measurements, slower scans were taken at longer intervals to reduce background noise. This results in reasonably good reproducibility for decay measurements. The 95% confidence intervals shown correspond to an average error of ±1.9%.

However, the data for growth measurements shows considerably higher variation, with 95% confidence intervals corresponding to an average error of ±5.8%. Although the intensity of the observed signal has been corrected for slight variation in the sample mass, it is possible that some error arises through slight differences in sample and lamp positioning, causing changes to the amount of sample exposed to light energy within the EPR cavity. In addition to this, the short scan times and relatively low signal intensity for growth measurements leads to noisy EPR signals, which will influence the quality of the data.

Overall, an error margin of 5.8% is reasonable considering the weak signal, however useful comparison of signal growth between systems may be limited, depending on how distinct the data are. However, the reproducibility for decay measurements is significantly better, and should allow for a confident comparison between samples.

5.4 Photochemical response of radical species in hair

The aim of this investigation is to examine the change in radical concentration observed by EPR upon irradiation. As the intrinsic signals observed in Figure 5-1 for brown and white hair arise from different species, they are likely to respond differently to UV. Brown hair, with high melanin content, would be expected to reflect the photochemical response of the dye, whereas white hair would show the response of protein based radical species.

Radical centres in eumelanin pigment are likely to arise from the redox equilibrium between hydroquinone/quinone and semiquinone radical forms of the main melanin polymer repeat unit, as outlined in Scheme 5-1.[80]

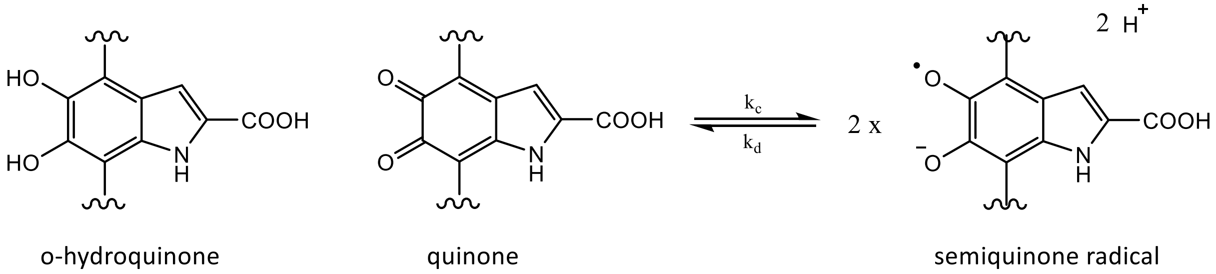

Scheme 5-1: Redox equilibrium between hydroquinone/quinone and semiquinone radical forms within melanin

This equilibrium is known to be sensitive to external stimuli, such as complexation with diamagnetic metal ions such as Zn^{2+},[80] changes in pH, reducing or oxidising agents as well as irradiation.[241] Upon exposure to light, the equilibrium is likely to shift, which will influence the radical signal observed by EPR.

For white hair samples, the intrinsic signals are attributed to radical species on keratin proteins. These are most likely tyrosyl species, based on g-values and abundance in keratin, although other species may also contribute to the signal. As discussed extensively in Chapters 2 and 4, tyrosine forms radical species upon exposure to UV. Unlike model systems, radicals in hair samples are relatively stable, with intrinsic species present before exposure.

The UV response of brown and white hair samples was monitored, to compare differences between melanin and keratin based radical species.

5.4.1 Growth of signal intensity upon exposure to UV light

Upon exposure to the full spectrum of a 100 W Hg lamp coupled to an X-band EPR cavity, the intensity of the radical signal from both natural white and mid-brown hair samples increased significantly over time. The intensity of the EPR signal (measured by 2nd integral intensity of the spectrum) was monitored by recording a spectrum every 0.8 minutes over a 2-hour exposure period. Figure 5-3 shows the change in peak area relative to the initial measurement. The datasets have been normalised to an initial signal intensity of 1, (the initial EPR signal area for the brown hair is 2.82 times greater than white hair).

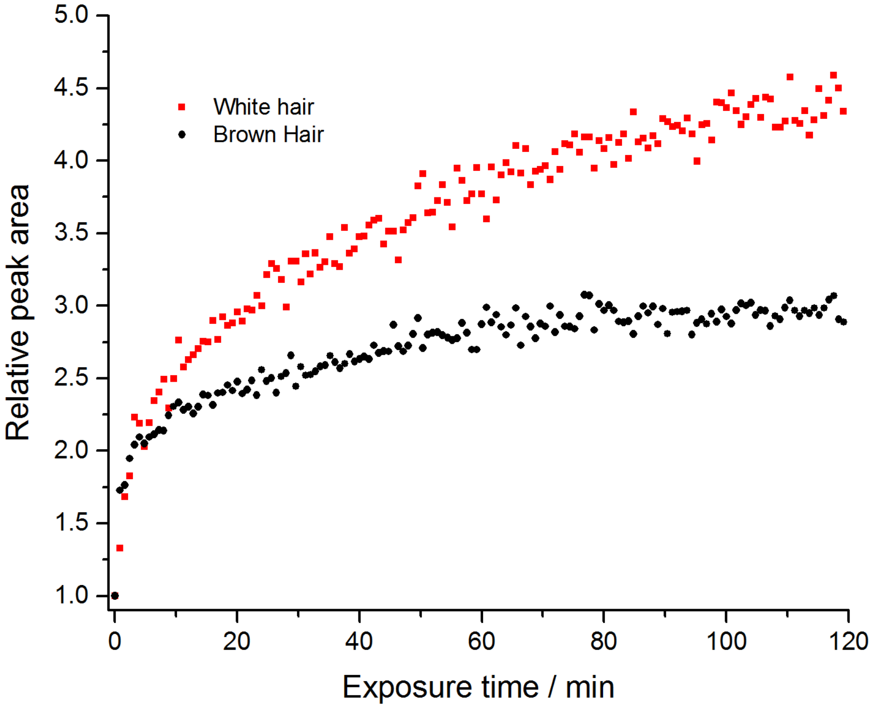

Figure 5-3: Comparison of EPR signal growth upon exposure of mid-brown and natural white hair samples to the full spectrum of a 100 W Hg lamp

Notably, the rate of increase in radical signal is different for white and brown hairs. This different response to UV highlights the different identities and chemical environments of the radical species in the two hair samples.

For the white hair, the change appears to be a gradual increase over time. Based on the mechanisms for tyrosyl radical formation discussed in section 4.1.1, and studies with model systems in Chapter 2, tyrosyl radicals form rapidly upon UV exposure. Keratin proteins adopt a tightly coiled structure.[242] Tyrosine and tryptophan both have hydrophobic side chains, therefore are likely to be buried within hydrophobic centres in the protein. Tyrosyl radicals formed in such a restrictive environment will be long-lived: radical quenching, recombination or onward reactions are likely to be slow (see experiments with solid amino acids, Chapter 2). This results in a build-up of radical concentration over time. Over the two-hour exposure period, the increase amounts to 4.48 times the initial intensity (this figure is from the average of the last three data points, due to the scatter in data because of the weak signal).

In comparison, the brown hair sample shows a much more rapid change initially, with an increase of 73% in the first 0.8-minute measurement interval, compared to only 33% for white hair. However, after this initial rapid increase, the intensity change plateaus, so that after 2 hours, the intensity is only 2.95 times the initial intensity (average of the last three data points taken). The very rapid initial change is consistent with the comproportionation/ disproportionation equilibrium of melanin semiquinone radicals in Scheme 5-1. UV exposure shifts the equilibrium to the radical form and consequently an increase in observed radical signal. This is similar to the "zinc effect": complexation of semiquinone melanin species to Zn^{2+} pulls the equilibrium to the right, causing a rapid increase in radical concentration.[80]

Over a longer irradiation time the signal continues to increase gradually (see Figure 5-3), after 2 hours this secondary increase accounts for a significant proportion of the overall change. As the shift in equilibrium leading to semiquinone radical formation is very rapid, it is likely that this slower increase corresponds to the formation of different radical species. This could be a build-up of keratin-based radicals as seen in white hair, or the formation of longer-lived melanin radical species (see section 1.4).

5.4.2 Kinetic measurements of rapid initial signal growth

The initial intensity change when the sample is exposed to UV can be monitored by kinetic EPR measurements. This can achieve a temporal resolution of <0.3 seconds, although very fast measurements become significantly affected by noise. The change in signal intensity from brown and white hair samples over the first 60 seconds of UV exposure was monitored by this technique, the kinetic trace is shown in Figure 5-4. As with Figure 5-3, data is normalised based on the initial signal intensity before UV exposure, set at 1.

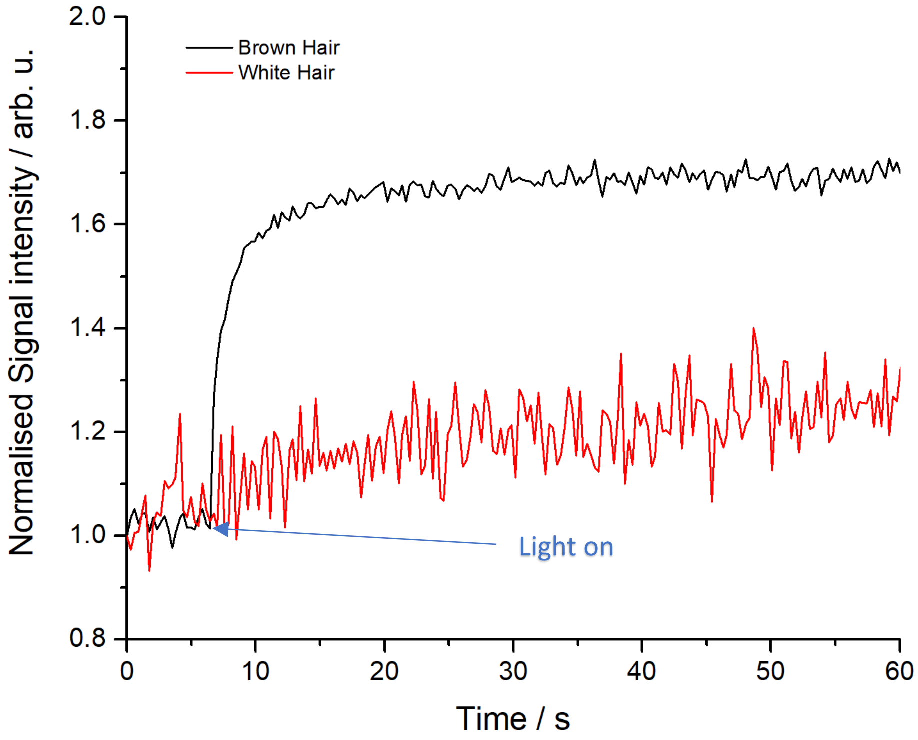

Figure 5-4: Kinetic EPR traces showing the change in height of observed peak upon UV exposure of brown and white hair samples.

As shown in Figure 5-4, the increase in signal intensity occurs very rapidly in the brown hair upon exposure to light. This is in close agreement with the findings of Kirschenbaum et al, who carried out a similar experiment on melanin extracted from brown hair.[243] They conclude that the rapid change is due to the formation of semiquinone radicals from hydroquinone and quinone, as outlined in Scheme 5-1.

Absorption of light by quinones leads to the production of singlet excited states which undergo intersystem crossing to triplet states.[244] Hydroquinones within the pigment then act as hydrogen donors, leading to the formation of two semiquinone radicals.[245] Irradiation increases comproportionation rate (k_c in Scheme 5-1) without influencing the reverse reaction rate. This shifts the equilibrium towards the semiquinone state, increasing radical concentration.

When a white hair sample was measured under the same conditions (the red trace on Figure 5-4), no rapid increase was observed when the sample was exposed to the light, however a gradual increase over time was seen. This is consistent with an absence of melanin, with radical species forming in keratin proteins.

5.4.3 Decay of radical species following UV exposure

With prolonged UV exposure, samples of brown and white hair show significant growth in concentration of radical species. In the case of brown hair, this is initially due to the rapid formation of semiquinone radicals within melanin pigment, however slower forming species are also observed over longer exposure time. In the absence of melanin, the slow forming species in white hair are attributed to protein based radicals.

Radicals in these two different environments are likely to exhibit different stabilities or lifetimes. After irradiating samples for two hours, the lamp was shut off rapidly and the decay in radical signal over time was monitored. Figure 5-5 shows the change in radical signal as measured by the peak area (2nd integral) over 2 hours irradiation followed by measurements every 30 minutes over a 24-hour period after the lamp was shut off, for white and brown hair samples. The initial signal intensity prior to irradiation was normalised for both samples, Figure 5-5 shows the change relative to the initial intensity.

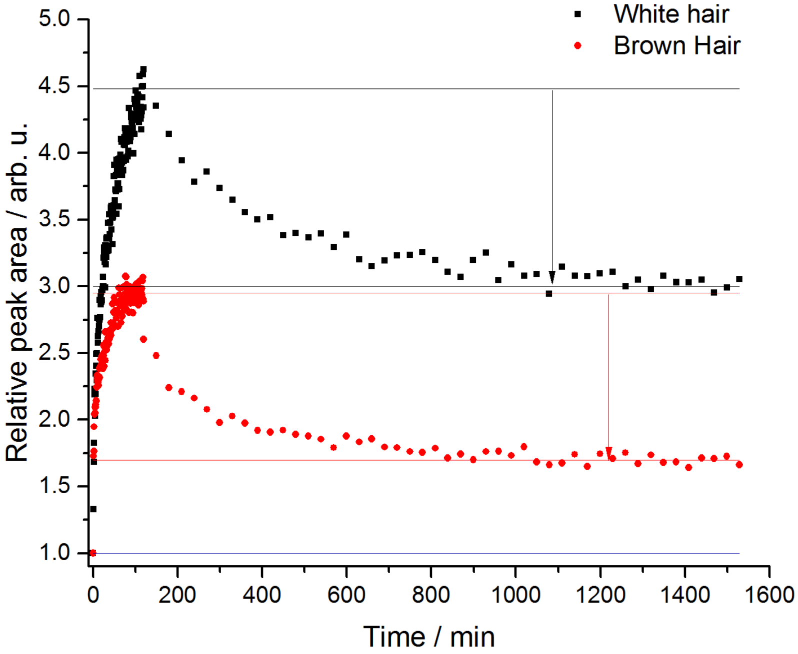

Figure 5-5: Change in EPR signal intensity during and after irradiation of brown and white hair samples. Lines show initial intensity (blue), maximum intensity after irradiation and intensity after 24 hours without light (average of the last 3 data points)

Unlike the rapid loss of signal observed in PEG-Tyr model systems, radicals in hair samples seemed more persistent. Although both samples show significant loss in radical concentration after exposure, neither return to pre-irradiation levels after 24 hours. Although there are hydrophobic environments in micelle and gel model systems, the sample is still relatively mobile and highly solvated compared to keratin in hair proteins, which explains the much shorter radical lifetime in model systems.

Over 24 hours, white hair loses 33.1% of the maximum signal intensity (at the point of lamp switch off), compared to a slightly higher 42.4% for brown hair. Radical concentration after 24 hours is 1.7 times initial concentration for brown hair, compared to 3.0 times for white hair. Initial radical concentration is 2.82 times higher in brown hair due to melanin based semiquinone radicals. Photoinduced radicals therefore decay more rapidly in brown hair, which may indicate that they are primarily melanin-based species rather than longer-lived keratin radicals. However, a significant proportion of radicals in brown hair do not rapidly revert to non-radical forms as suggested by Scheme 5-1.

A rapid change in melanin radical concentration would also be expected for the brown hair sample when lamp is switched on/off due to the melanin equilibrium, however this is not resolved in Figure 5-5. Kinetic measurements with improved time resolution were carried out. As anticipated, the signal of the brown hair sample showed a pronounced rapid decrease upon cessation of irradiation, as shown in Figure 5-6. No rapid drop changes were observed in white hair samples, as radical species build up and decay over longer timescales.

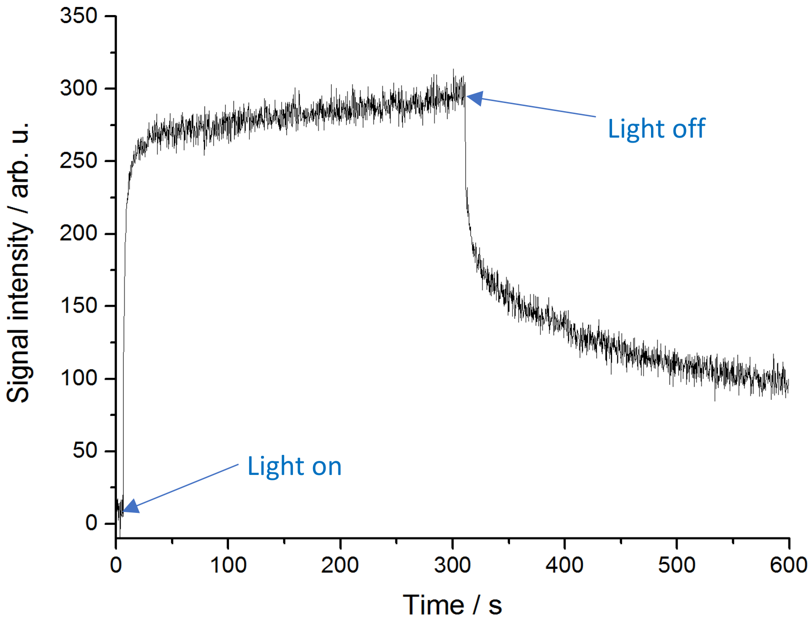

Figure 5-6: Kinetic EPR trace showing rapid response to light stimulus of melanin in brown hair sample. Initial intensity set at zero.

5 minutes after the lamp is shut off, the signal has decayed to approximately 30% of the maximum intensity after 5 mins irradiation. This is significantly different to Figure 5-5, which shows only a drop to around 58% after 24 hours. This can be explained by considering the rates of formation and decay of different radicals. Several radical species can form within melanin pigments. These include neutral and deprotonated semiquinone radicals as outlined in Scheme 5-1. These are formed relatively rapidly due to the effect of light upon the redox equilibrium. However, the reverse process has been found to be a lot slower within the restricted environment of melanin pigments. The anionic semiquinone radical has a half-life of around 6 hours.[81] Other melanin radical species include indolyl radicals, and species produced by electron hole pair formation in the semi-organised melanin structure (see section 1.4). Recombination of electron-hole pairs is very rapid, and likely accounts for the rapid drop in intensity observed upon lamp shut-off in Figure 5-6.

No rapid decrease is observed in the white hair sample, providing further evidence that intrinsic and UV-induced radicals in white hair are buried within protein structures and are consequently longer lived.

These comparative experiments have shown that radical species formed in white hair upon UV exposure are distinct from melanin-based radicals. Radicals in white hair are longer-lived and build up concentration over longer exposure times, suggesting immobilised tyrosyl or other keratin based radicals. In brown hair, some radicals form and decay very rapidly, likely a result of changing redox equilibrium and the creation/recombination of electron-hole pairs. Some melanin radicals are longer-lived: it takes time for the redox equilibrium to be restored following irradiation, and longer lived indolyl species may also form. However, melanin based radicals decay more rapidly than keratin based radicals.

The focus of the project has been investigating the photochemistry of tyrosine, and the involvement of transition metals in photochemical processes. This has been studied extensively in model systems (see Chapter 4). Therefore, the bulk of investigations carried out with hair samples used white hair, as radical species likely derive from tyrosine residues in keratin (based on g-values). Information on metal content was not available for white hair samples, therefore no studies investigating the effect of iron(III) or copper(II) could be carried out. Radical behaviour is very different in solid samples, free solution (see Chapter 2), PEG-Tyr micelles and hair fibres. This shows that solvent environment has a significant impact upon radical lifetime and reactivity. Hair moisture content changes significantly with humidity.[246] An investigation into how humidity influences protein-based radicals in hair was therefore carried out.

5.5 Investigating the effect of humidity upon radical formation in hair proteins

Tyrosine-based radical lifetime depends heavily on solvation. In free solution and highly solvated PEG-Tyr micelle/gel systems, radical species decay rapidly following UV exposure (see Section 2.4.6). In contrast, radical species in solid tyrosine powder (see Section 2.3.1) and poorly solvated hair keratin (see Figure 5-5) persist for many hours after irradiation.

Hair has a reasonably high moisture content of around 14% by weight at 20 °C and 65 % relative humidity.[10] The moisture content can vary significantly with changing relative humidity, as hair is quite hygroscopic.[246] This leads to changes in tensile strength and stretching ability, a property exploited by hair hygrometers.

In addition to changing mechanical properties, high humidity environments accelerate photobleaching.[247] Reactive oxygen species can diffuse further in a more highly solvated environment, increasing the potential for damage throughout hair fibres.[248] Proton coupled electron transfer processes are improved through hydrogen bonded, water containing gaps.[249] Water trapped between keratin fibres at higher humidity may therefore facilitate electron transfer processes.

Existing studies into the effects of sunlight upon hair proteins at different humidity have relied on indirect analysis of properties such as tensile strength and fibre swelling. The cleavage of polypeptides and disulfides within the keratin decreases the rigidity of the fibre. Results in the literature are contradictory, with swelling measurements indicating highest damage at intermediate humidity[250] and tensile strength measurements showing higher degradation at high humidity.[251]

This investigation aims to build upon and clarify existing literature studies by looking directly at photo-induced radical species in hair in different humidity environments. These radicals are intermediates in degradation reactions. The shape of EPR spectra reveals information about the identity of primary and secondary radical species, which can be used to compare radical transfer processes. Rates of radical formation and degradation therefore reflect the overall rate of photodamage in hair proteins, without requiring the extended exposure times of tensile strength measurements.

5.5.1 Achieving a controlled humidity environment

Controlling humidity over the course of prolonged UV exposure and radical lifetime measurements within the EPR spectrometer presents a challenge. Hair samples were sealed in a quartz EPR tube after 2 hours equilibration at the required humidity. The equilibration time was significantly longer than needed: other studies use 1 hour,[246] equilibration is reached within 20 minutes, even for extreme changes (>50%) in relative humidity.[252]

A surprising range of different humidity levels were achievable by utilising the daily variation of ambient humidity levels within the laboratory, which typically ranged from 50-70% depending on weather conditions. For experiments outside this range, artificially controlled humidity environments were created by using a polyethylene glove bag (Aldrich AtmosBag). The sample could be placed within the bag, along with the EPR tube and humidity probe, and equilibrated to a controlled humidity level. This was achieved by using a combination of dry compressed air blown into the bag, warm water reservoirs placed within the bag, and bubbling inlet gas through a saturated salt solution.[253] The set-up is outlined in Figure 7-3.

Dry air samples were prepared by blowing dry air directly into the bag from the lab compressed air supply. Hair samples were equilibrated before sealing into the EPR tube within the glove bag. The sealed tubes could then be removed and photodegradation experiments performed in the EPR spectrometer.

5.5.2 The effect of humidity upon radical identity: Interpreting EPR lineshape

Both the intrinsic and the UV induced EPR signal for white hair samples matches what would be expected for a tyrosine-based phenoxyl radical, based on g-values and the broad symmetric lineshape (see section 5.2). These are likely primary radicals formed directly through oxidation of photo-excited tyrosine species.

Radical transfer processes from tyrosyl species will lead to the formation of secondary radicals within the hair. These may include sulfur-centred species from disulfide cleavage. Formation of secondary radicals will likely depend on the rate of electron transfer processes and the diffusion of hydroxyl radicals and singlet oxygen (see Section 4.7). Increased water content may influence these processes. Sulfur-centred radicals give a distinct asymmetric EPR spectrum, shown in Figure 5-7.[135] Peroxyl radical species may also exhibit a similar EPR signal.[264]

The g values shown on Figure 5-7 are calculated based on a DPPH standard at g = 2.0036. The tyrosyl radical has a different EPR spectrum to cysteine based radicals, which show an asymmetric spectrum slightly shifted to lower field, with some broader features in the lower field region. Of particular note is the distinctive peak at g = 2.0164 in the sulfur radical spectrum. This is shifted by 13 Gauss from the maximum of the tyrosine peak.

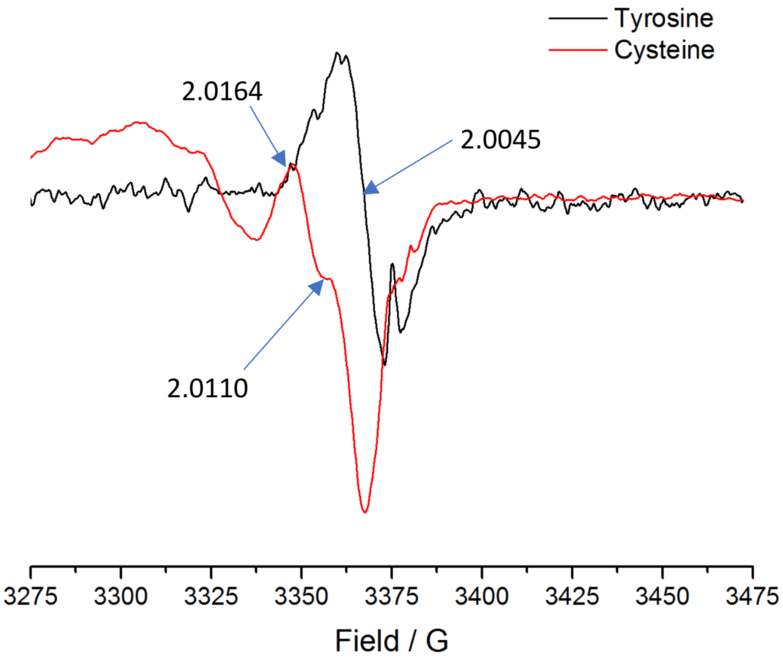

Figure 5-7: EPR spectra of solid powder cysteine and tyrosine amino acid samples after 20 minutes exposure to 100 W Hg lamp.

A qualitative interpretation of spectral lineshape may therefore reveal details about the nature of radicals observed, and if this changes over time. EPR spectra were recorded for hair samples at different humidity, and the lineshape was compared to determine if humidity can influence the formation of secondary sulfur based radicals. EPR spectra of white hair samples in dry air and at 100% relative humidity after 2 hours exposure are shown in Figure 5-8. Spectra have been normalised based on the intensity of the largest peak.

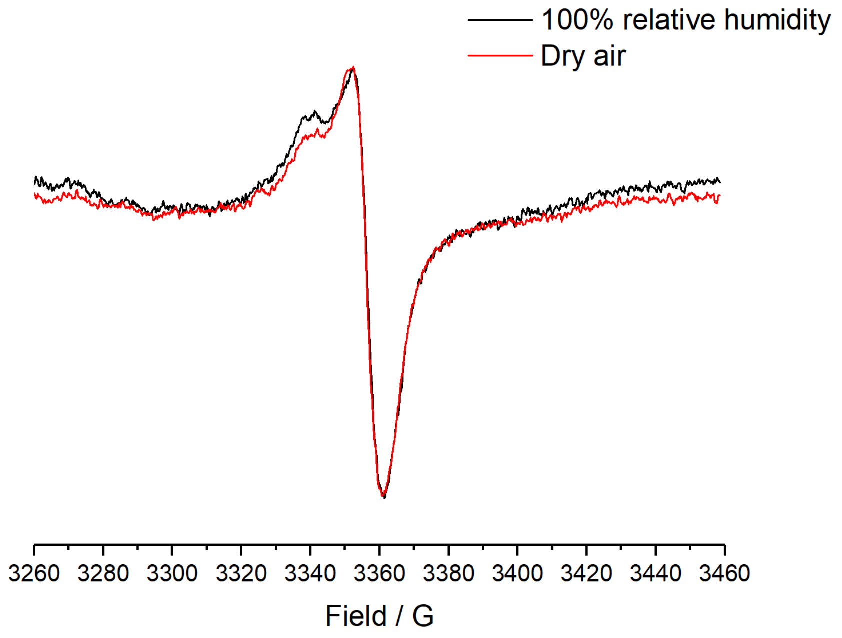

Figure 5-8: Comparison of EPR lineshape for hair samples after 2 hours UV exposure in dry air and 100% relative humidity

A key feature of both spectra is the shoulder peak at around 3340 G. This is shifted by 13 Gauss from the top of the central peak. The separation between the two peaks matches the difference in tyrosine and cysteine spectra (Figure 5-7). The shoulder peak could therefore arise from a cysteine based sulfur centred radical. Another possibility is that the signal corresponds to a peroxyl radical formed by the interaction of a carbon or sulfur radical with oxygen. This could be confirmed by using samples saturated with isotopically labelled oxygen, which may influence EPR line splitting.[265] However, this was beyond the scope of this study as both secondary radical species provide a measure of how labile the system is.

With the powerful 100 W Hg lamp used, it is likely that some sulfur radicals are formed by direct absorption of high energy UV light by disulfides. However, lamp output below 270 nm is minimal, and cystine molar absorptivity in the 270-280 nm region is an order of magnitude lower than tyrosine.[254] Secondary photochemical processes are likely to be the main driving force behind disulfide cleavage.

The shoulder peak at 3340 G is significantly larger (relative to the central peak) at higher humidity, corresponding to a greater proportion of secondary radicals. Sulfur radicals may be formed indirectly through electron transfer from excited Tyr/Trp, interaction with hydroxyl radicals and superoxide, whereas peroxyl radicals require interaction with oxygen (see Scheme

1-2). These results indicate that electron transfer processes and diffusion of oxygen and reactive oxygen species are enhanced at higher humidity.

Hair fibres readily absorb moisture from the air, and increased water content around keratin proteins at higher humidity levels is likely a key factor in photochemical reactivity. As shown in model systems, a more solvated environment increases radical reactivity and photochemical degradation via both radical and ROS (hydroxyl radical, singlet oxygen) pathways (see Chapter 4). This will lead to increased secondary radical formation at the many disulfide cross linkages in keratin proteins. Disulfides are easily reduced (by electron transfer) to thiol radicals and thiolate anions, or oxidised (through interaction with hydroxyl radicals) to form a disulfide radical cation. Although the proximity of the two sulfur-centred radical centres formed means the most likely outcome is recombination,[59] there are a wide variety of potential degradation pathways from a cysteine based radical, ultimately leading to the formation of sulfonic acid and Bunte salts (see section 1.2.3).[99] This irreversible breakdown of disulfide bonds critically weakens the protein.

In addition to this, hydroxyl radicals can promote oxidative cleavage of the polypeptide protein backbone by abstracting the α-hydrogen from an amino acid residue. This forms a carbon centred radical on the peptide backbone which can interact with oxygen further, leading to peroxyl formation and peptide cleavage (see Scheme 1-17).[64]

Peptide cleavage and disulfide breakdown will manifest as a loss in hair strength, and an increase in swelling as fibres lose their structural integrity. Literature studies show greater loss in tensile strength upon UV exposure at high humidity.[251] This is in agreement with the results in Figure 5-8, showing greater disulfide cleavage at higher humidity. However, literature studies indicate a decrease in fibre swelling at higher humidity after UV exposure. This could arise from an increase in protein cross-linking reactions or increased protein loss from the fibre.[250] Both processes will occur more readily in a labile system: the findings of EPR studies are therefore in agreement with tensile strength and fibre swelling measurements in literature.

5.5.3 Monitoring the growth of radical signal upon UV exposure – the effect of humidity

Radical reactivity was monitored more directly by looking at the formation and lifetime of photochemically generated radical species under controlled humidity. A more labile system would be expected to show more rapid radical degradation and shorter radical lifetime. Hair samples placed into the EPR cavity were exposed to a 100 W Hg lamp for a period of two hours, and the change in the observed EPR signal was monitored as outlined in section 5.4.1. There is no significant change in the initial radical concentration (before UV exposure) in hair samples with changing humidity. Slight variations are likely due to small differences in sample mass and position in the EPR cavity. Figure 5-9 shows the growth in radical concentration for each humidity measurement, based on the double integral of the EPR signal.

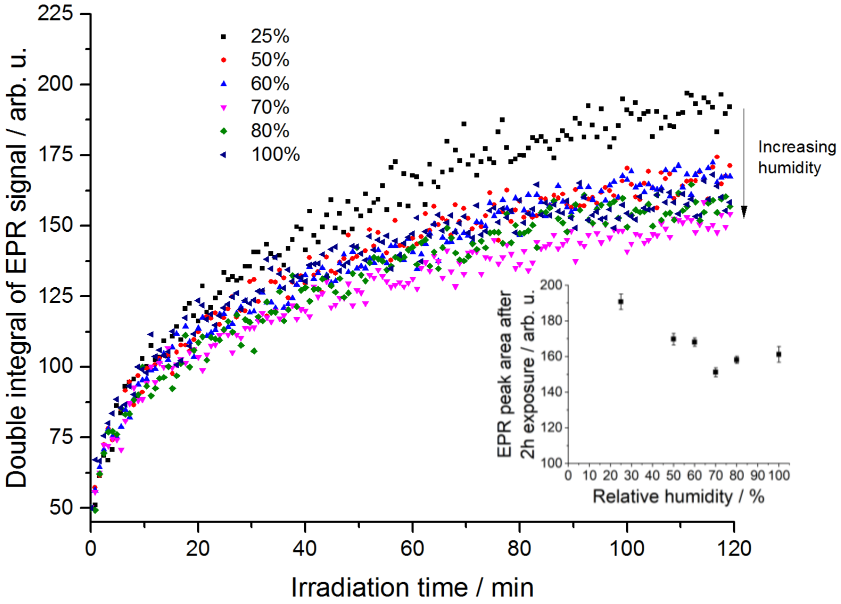

Figure 5-9: Change in radical concentration in white hair samples over a 2-hour irradiation period at different relative humidity levels.

All samples show a significant increase in radical concentration over the exposure period, and changing humidity does influence radical growth. However, radical concentration increases less than previously observed for white hair samples (Figure 5-3). Humidity was not controlled for measurements in Figure 5-3, and the sample tube was not sealed. Oxygen availability could be a limiting factor for radical formation in sealed tubes. However, no direct comparison between open and sealed tubes was performed. All humidity controlled measurements used sealed tubes.

Figure 5-9 (inset) shows the maximum signal intensity after UV exposure (from the average of the last five data points of each measurement, 95% confidence intervals shown). As humidity increases, the stable radical concentration after 2 hours exposure generally decreases, although the scatter in data is high and differences are less distinct at higher humidity.

5.5.4 Analysis of radical concentration and rate of formation at different humidity

To quantify the effect of humidity upon the extent and rate of signal growth, and to remove uncertainty arising from data scatter, exponential growth curves were fitted to the experimental data. It was found that first order exponential growth relationship (Equation 5-1) fitted the data reasonably well, if the first three data points were excluded from each set. These points describe an initial rapid growth process, possibly due to small amounts of melanin pigment present within the hair fibres, therefore exclusion from a study of slower forming protein radicals was considered reasonable.

$$y = Ae^{-kt} \qquad \text{(Equation 5-1)}$$

The magnitude of the pre-exponential term *A* in Equation 5-1 is an indication of how much the radical signal grows over time. The rate constant *k* describes the rate of growth. Both measures are shown in Table 5-1 and Figure 5-10.

Table 5-1: Parameters from first order exponential fitting of radical formation data at different relative humidity levels

Relative Humidity / %	**A**	**k / s^{-1}**
25	-117.26	0.02107
50	-89.48	0.02188
60	-96.68	0.01709
70	-74.78	0.02040
80	-85.69	0.02068
100	-75.26	0.02870

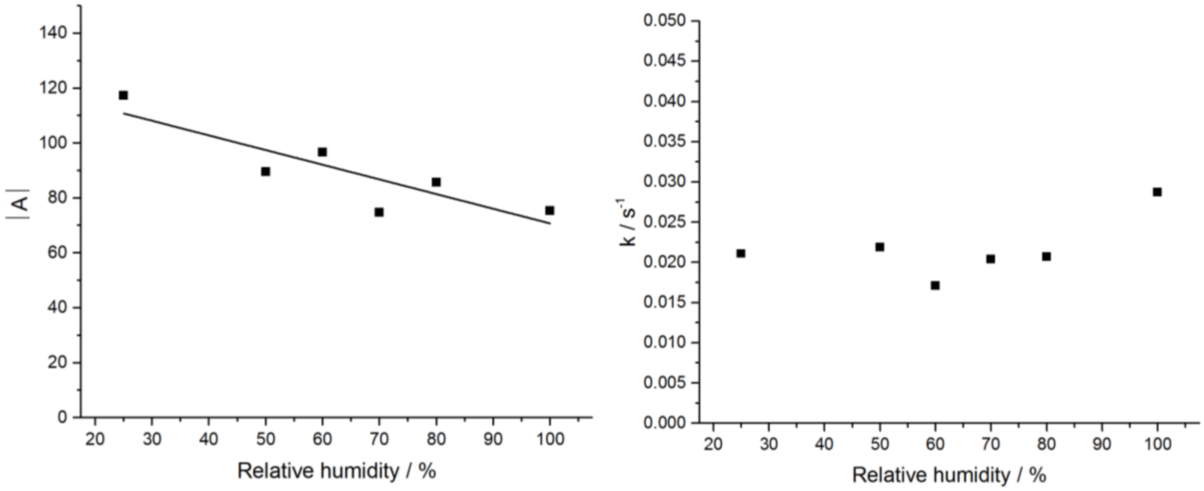

Figure 5-10: Difference in the extent of radical EPR signal growth (left) and rate of growth (right) derived from first order exponential fits of experimental data.

The relative humidity of samples does not seem to have a significant impact upon the rate of radical formation. This indicates that the accessibility of oxygen species is not a limiting factor to radical formation in low humidity environments. Radicals observed are therefore likely formed through primary processes. Secondary radical species are also likely to form, and are less likely to follow first order kinetics. Of particular importance in the breakdown of keratin proteins are sulfur-centred radicals formed as a result of interaction between photochemically generated reactive oxygen species and cystine.

At very high humidity (100%), there is an increase in rate. This may correspond to an increase in the rate of secondary radical formation through ROS diffusion. However, the trend is not observed for other humidity measurements and no certain conclusion can be drawn from a single data point.

The extent of radical growth decreases with humidity, with the pre-exponential multiplier following a similar trend to the analysis of raw data in Figure 5-9. Increasing humidity leads to a lower stable radical population in hair samples upon UV exposure. At higher humidity, photoinduced radical species within hair proteins can react faster and are consequently shorter-lived, limiting build-up of radicals within hair. Absorption of water by keratin proteins will increase the solvation of amino acids in the protein, particularly those within the outer cuticle layer. This will allow greater interaction between radical centres and photochemically generated singlet oxygen, superoxide or hydroxyl radicals. This will lead to greater reactivity and shorter lifetimes. The lifetime of radicals can be monitored by looking at the decay of radical species after the UV stimulus is removed.

5.5.5 The effect of humidity upon the lifetime of photoinduced radical species in hair proteins

In addition to comparing the growth of radical species upon UV exposure in hair samples at different humidity, experiments also monitored their decay after irradiation ceased. The longer timescales involved for signal decay permit slower scans which reduce the background noise levels of spectra. This significantly reduces the scatter of data, as outlined in section 5.3.

The removal of the UV stimulus allows the lifetime of photoinduced radical species to be studied. From section 5.5.3, the lower radical concentrations at higher humidity were thought to indicate greater reactivity due to improved interaction with dissolved oxygen and other species. If this is the case, then the radical signal would be expected to decay faster at higher humidity levels once irradiation is stopped.

The decay of radical concentration was monitored for a period of 24 hours after the light source was removed, as outlined in section 5.4.3. The decay profiles for samples at different humidity are shown in Figure 5-11. As after 2 hours exposure, samples at different humidity

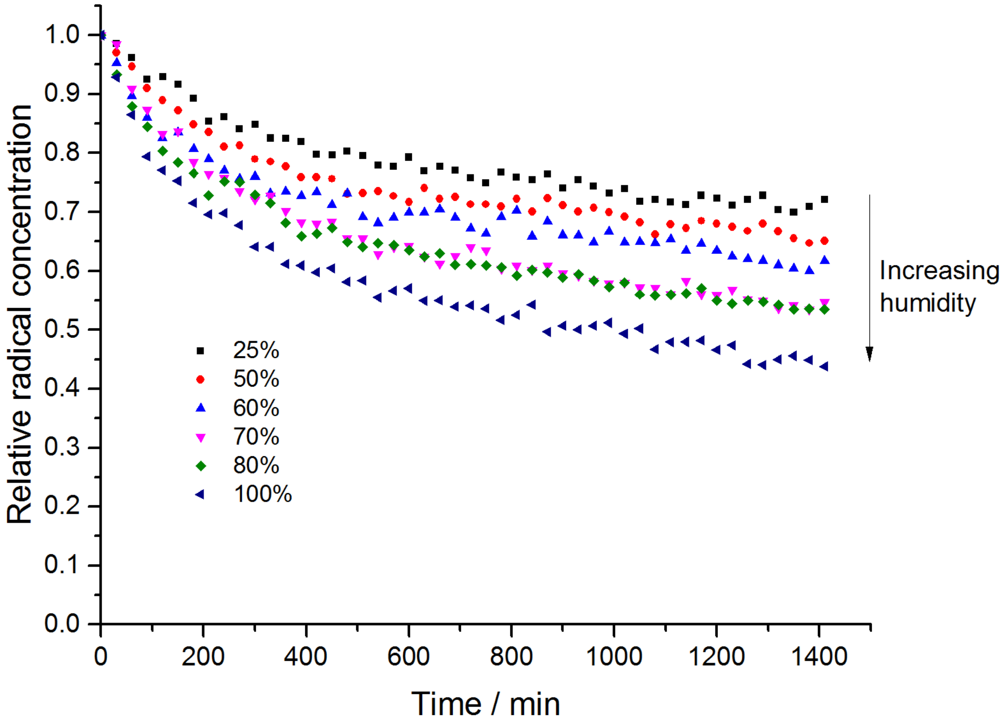

Figure 5-11: Comparison of radical decay profiles following lamp shutdown for hair samples at different humidity, measured by the 2nd integral of the EPR radical signal.

had different radical concentrations, the figure shows the radical concentration relative to the maximum concentration achieved at the point of lamp switch-off.

Unlike radical formation, the decay of radical species is unlikely to follow first order kinetics, and therefore doesn't fit a single term exponential decay profile. Several different radical decay processes are likely to occur including direct recombination and radical elimination. Interaction with oxygen, metal centres and hydrogen abstraction from other amino acids could transfer the radical centre to another part of the protein, leading to further radical products and ultimately disulfide or peptide cleavage.[92] Electron-proton transfer processes may also occur across relatively long distances, leading to the quenching of some radicals and the formation of others.[249]

Despite the many different processes likely contributing to the change in radical signal, the trend with increasing humidity is clear when looking the decay of radical species: at higher humidity, radicals decay more rapidly.

Qualitative analysis of radical lineshape and quantitative data from radical growth and decay measurements all indicate a significantly more labile, reactive tyrosine environment in hair keratin at high humidity. This can be attributed to water uptake into keratin proteins, providing greater solvation and a mechanism for the diffusion of oxygen and reactive oxygen species. This has been shown to influence reactivity in model systems. The role of reactive oxygen species is discussed further in section 5.6. The findings agree with literature tensile strength and swelling measurements, although provide a more direct mechanism to probe the effects of humidity on keratin photochemistry.

5.6 Investigating the role of oxygen in keratin radical reactivity

A critical mechanism for the formation of secondary radicals on cysteine residues or within the polypeptide chain will be the formation of reactive oxygen species at photoexcited aromatic sites, which then diffuse to other parts of the protein to cause wide ranging oxidative damage. ROS can lead to the formation of hydroperoxides on amino acid side chains or the polypeptide

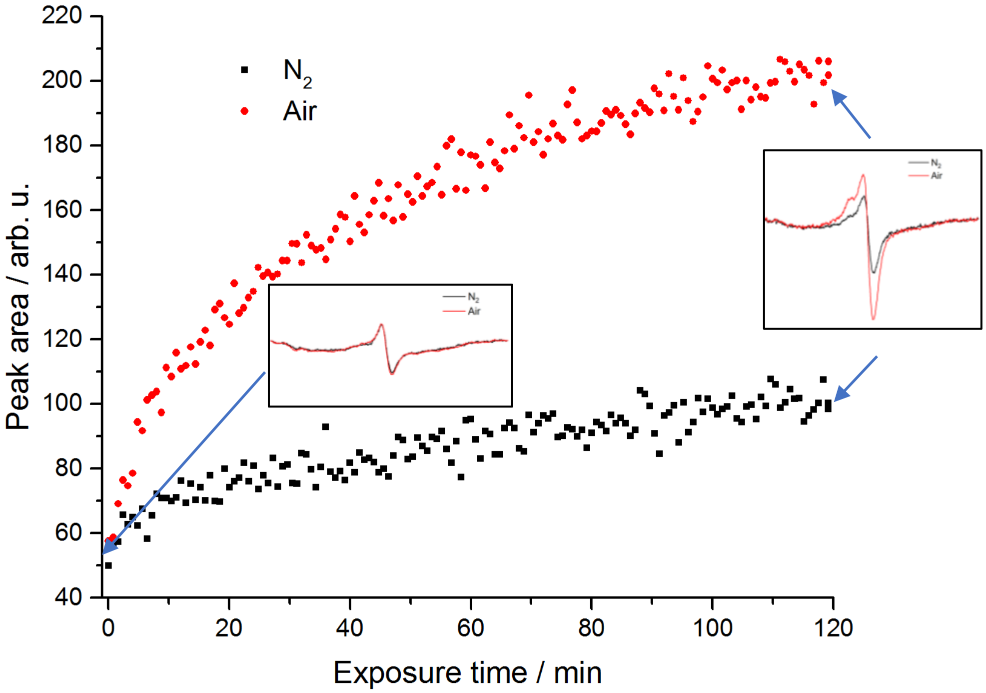

Figure 5-12: Comparison of spectra before and after 2 hours UV exposure, and the change in signal intensity during exposure, for white hair samples at low humidity in air and an inert atmosphere.

backbone which promote autoxidation (see section 4.9), leading to extensive protein damage. By comparison, direct electron transfer can only move the radical centre.

As with model systems (section 4.8), photochemical experiments were carried out on hair samples in an oxygen-free environment. The aim of this was to quantify the role of oxygen species in radical formation and reactions in hair proteins.

The degassing was performed using the same set-up as for humidity controlled experiments, shown in Figure 7-3. The bag, containing the white hair sample, was evacuated and filled with nitrogen gas 4 times. N_2 gas was blown into the sample tube directly via a needle to ensure expulsion of air. The sample was sealed, removed from the bag and photochemical EPR measurements taken. Figure 5-12 compares the initial signal spectrum, that after 2 hours exposure and the growth curves of the radical signal with that of a control sample treated in the same manner with dry air rather than N_2.

The intensity of intrinsic radicals within keratin proteins seems unaffected by the absence of oxygen, with the initial EPR spectra being almost identical. However, when samples are irradiated, there is a significant difference in the response. The air containing sample shows significant signal growth, resulting in a relatively strong, asymmetric EPR signal after 2 hours exposure, indicating the formation of phenoxyl and sulfur centred radical species.

In contrast, the sample under an inert atmosphere shows a modest increase in signal intensity over the same time, resulting in a slightly increased signal after 2 hours which qualitatively shows much less sulfur character than the sample in air. This highlights the importance of oxygen in two crucial processes of keratin photodegradation: the formation of radical species on aromatic amino acids after photoexcitation; and the transfer of radical centre via reactive oxygen species to other parts of the protein such as disulfides.

Based on the relative changes in intensity over the period of UV exposure, interactions between photoexcited amino acid residues and oxygen are responsible for around 68% of the increase in radical species observed. This is lower than in model systems, where excluding oxygen reduces observed tyrosine degradation by around 90% (see section 4.8.2), although this was from fluorometry, not EPR measurements.

The presence of localised iron(III) in model systems reduces the effect of oxygen exclusion, due to direct metal-tyrosine interactions. Iron(III) and other redox active metals are present in hair fibres, which may explain why excluding oxygen is less effective in hair samples than model systems. However, the coordination environment of iron(III) in hair keratin is uncertain, and the metal content of white hair samples used was not known. Further studies could probe a series of white (melanin free) hair samples with different metal content.

5.6.1 Radical decay: the role of oxygen

Oxygen can interact with photo-excited tyrosine and tyrosyl radicals, leading to the production of hydroxyl radicals, superoxide and singlet oxygen. Once the UV stimulus is removed, the concentration of reactive oxygen species in the sample is likely to drop rapidly, as they are short-lived, with singlet oxygen degrading in hair on a microsecond timescale.[255] However, molecular oxygen itself is involved in a range of photodegradation processes of tyrosine, tryptophan and cystine based radicals. This typically involves the formation of hydroperoxides and highly reactive peroxyl radical species on amino acid side chains or the peptide backbone which can form an autoxidative cycle, leading to extensive damage to the protein and amino acid side chains.[64,58] The loss in radical intensity after 2 hours UV exposure was therefore monitored in systems with and without oxygen present, as outlined in section 5.4.3. The normalised decay profiles are plotted in Figure 5-13.

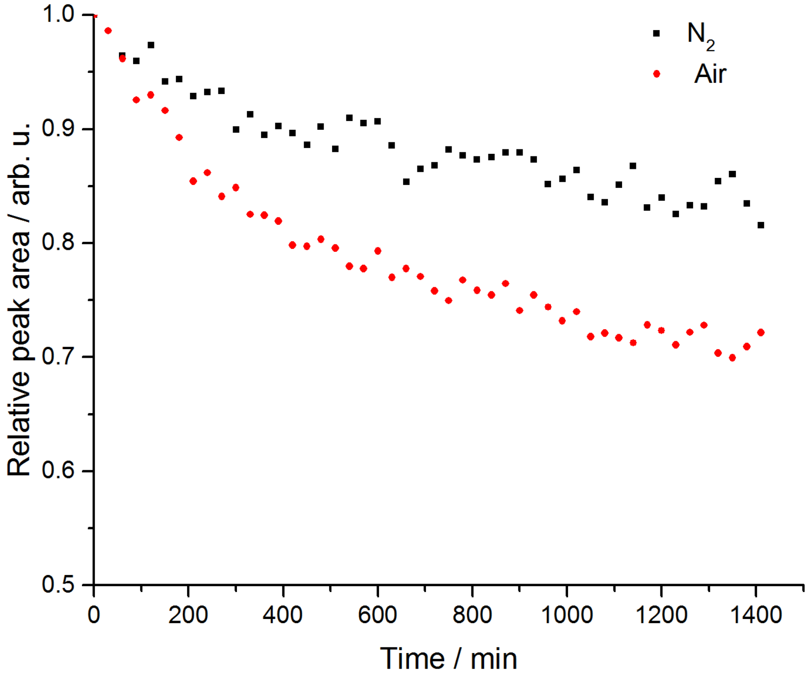

Figure 5-13: Comparison of EPR signal decay after 2 hours UV exposure, for white hair samples at low humidity in air and an inert atmosphere.

The results clearly show that keratin based radicals decay more rapidly in the presence of oxygen. In the absence of oxygen, radicals likely simply revert to their starting form through recombination or hydrogen abstraction. In the presence of oxygen, further degradation pathways are available, some of which lead to hydroperoxide formation and autoxidation. These processes are likely to contribute significantly to the observed radical decay in the presence of oxygen.[58]

5.6.2 Air free experiments: conclusions

Oxygen free samples showing significantly inhibited radical formation and reactivity compared to control samples in air. This agrees with the well-documented importance of oxygen and reactive oxygen species on the formation and reactions of radicals within biological systems. Formation of radical species on aromatic amino acid residues is facilitated through interactions between excited states and oxygen, leading to the formation of reactive oxygen species. Reactive oxygen species facilitate transfer of radical centres, leading to increased cleavage of disulfides and polypeptide backbone. Oxygen can also interact with radical species, leading to the formation of peroxyl radicals. Autooxidation cycles lead to the degradation of amino acid side chains, disulfide bonds and the polypeptide backbone. The drop in activity caused by the removal of oxygen is mitigated slightly compared to model systems, possibly due to the presence of redox active metals in hair.

5.7 Investigating the effect of antioxidants on keratin photochemistry

Excluding oxygen from hair is not a practical possibility as a method of slowing degradation. A wide variety of antioxidant species are added to commercial haircare and other cosmetic products. Antioxidants act by breaking the damaging autoxidative cycle (see section 4.9), limiting further radical production oxidative damage.[256] Greater radical production in oxygenated hair samples is attributed to these autoxidative processes and the role of ROS in general. The aim of this experiment was therefore to test whether a common antioxidant influenced the formation and degradation of radical species upon irradiation.

5.7.1 Selection of antioxidant

An important consideration for antioxidant selection is uptake into the hair fibres. Data from previous studies carried out by P&G identified several candidates which showed good penetration into hair fibres at pH 4. Butylated hydroxytoluene (BHT) used as an antioxidant in model systems is too hydrophobic. Limitations of the EPR technique also prevented antioxidants with certain functionalities being used. As the study detects phenoxyl and sulfur-centred radical species, antioxidants containing phenol, hydroquinone or thiol functionalities could interfere. A study with n-acetylcysteine revealed significantly enhanced sulfur radical concentration in treated hair after 2 hours UV exposure. Similarly, phenoxyl based antioxidants such as resveratrol and salicylic acid were ruled out due to their likelihood of direct UV absorption and radical formation (for example, trans resveratrol has an absorption maximum at 304 nm in water).[257] Based on these criteria, sorbic acid was selected for antioxidant tests (Figure 5-14).

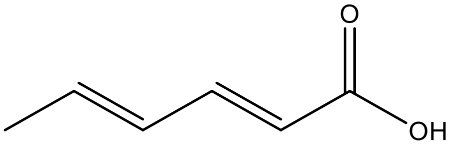

Figure 5-14: Structure of Sorbic Acid

5.7.2 Introducing antioxidant into hair samples

The uptake of antioxidants into hair fibres is dependent on pH. Changes to protonation within keratin fibres influences intermolecular interactions, leading to swelling of fibres and easier penetration of additives such as metal ions and antioxidants.[258] The best uptake of antioxidant was found to occur around pH 4.

A saturated solution of sorbic acid (14.27 mmol dm^{-3}) was prepared in water. Based on the reported pK_a of sorbic acid of 4.76, the pH of the solution was 3.31. This is slightly more acidic than the ideal of around 4, and significantly more acidic than the pH of cosmetic hair treatments. Therefore, uptake of antioxidant is likely to be higher than expected under normal washing conditions. The effects of the antioxidant are therefore likely to be easier to observe after a single treatment of the hair. Unfortunately, actual uptake of antioxidant into hair fibres is unknown.

5.7.3 Effect upon intrinsic radical concentration

A sample of white hair was treated by soaking in antioxidant solution, before drying and equilibrating to 70% RH. A control sample was prepared in the same way by soaking in dilute HCl at pH 3.3. The intrinsic EPR signal of the two hair samples was then compared, and is shown in Figure 5-15. The mass of both hair samples is the same, 130 mg.

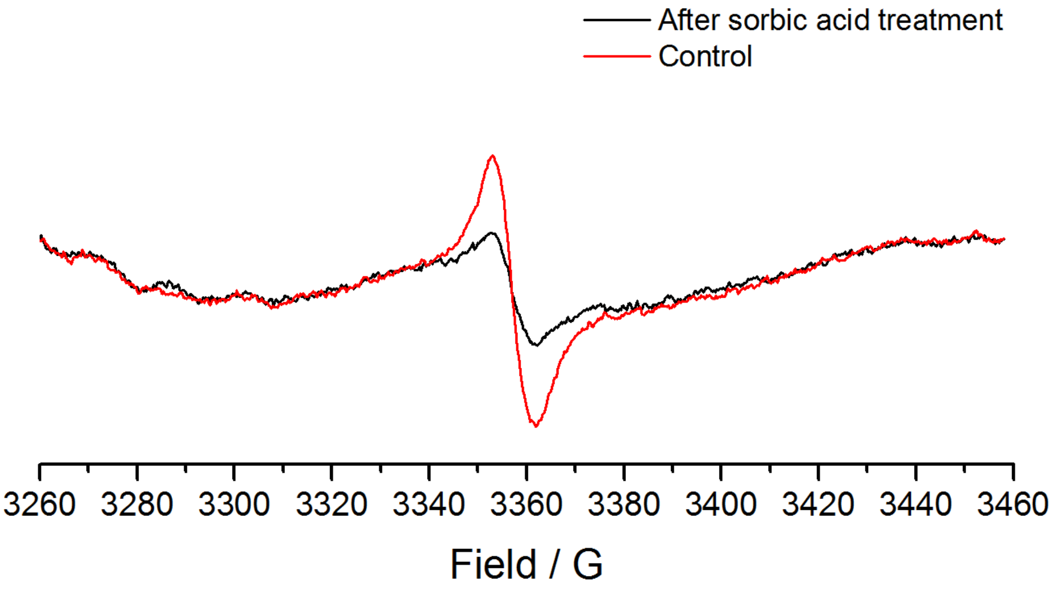

Figure 5-15: Comparison of initial intrinsic EPR signal intensity for hair samples with and without sorbic acid treatment

There is a significant decrease in the intrinsic keratin signal observed by EPR following sorbic acid treatment. This indicates that the stable radical species present within keratin fibres are influenced by the addition of the antioxidant. As autoxidative processes rely on irradiation, this decrease is likely a result of direct reaction between antioxidant and radical species.

5.7.4 Effect of antioxidant upon UV response

Studies have shown that sorbic acid can interact with triplet excited states of organic molecules, quenching reaction pathways which proceed via a triplet state. This occurs through energy transfer from the triplet state to the diene.[259] If radicals are formed by interactions with triplet state excited tyrosine (or tryptophan) then sorbic acid would be expected to influence the process. In addition to this, sorbic acid may suppress the formation and activity of reactive oxygen species.[260] These factors may suppress UV induced radical formation.

The increase in radical concentration in treated hair samples upon UV exposure was monitored over time: the growth in radical concentration is compared in Figure 5-16. Samples were exposed to UV light in the EPR cavity, and the change in signal strength monitored over time.

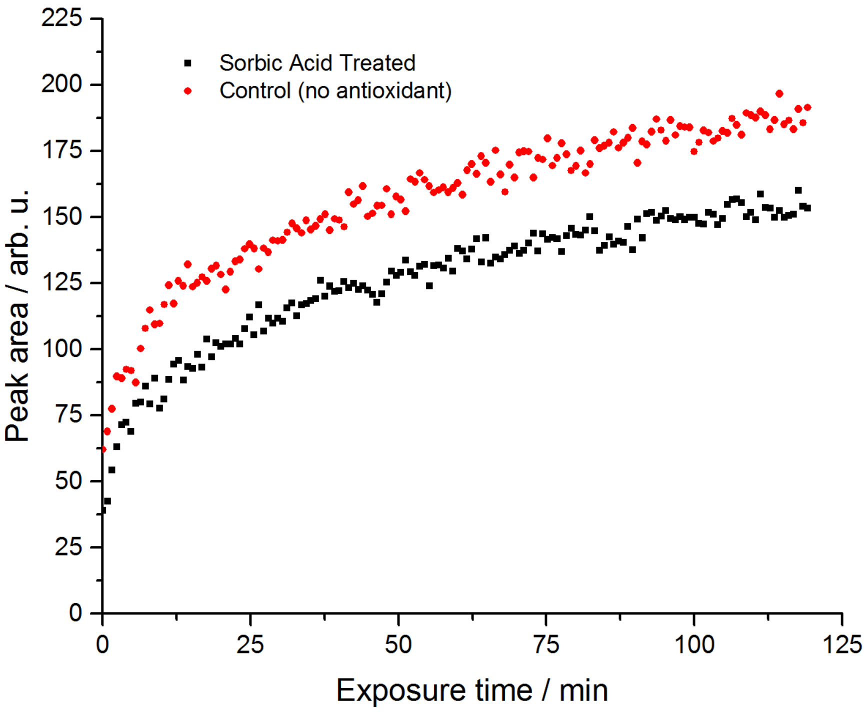

Figure 5-16: Growth of EPR radical signal in hair with and without sorbic acid treatment upon UV exposure

Although the overall radical concentration is lower after 2 hours UV exposure for the treated hair sample, the growth curves follow very similar profiles. First order exponential growth curves were fitted as described in section 5.5.4 and revealed no significant difference in the rate. The extent of growth, measured by the pre-exponential term, was slightly lower in the treated hair (although within fitting error), as summarised in Table 5-2.

Table 5-2: Parameters from first order exponential fitting of radical formation data for treated and untreated samples

Sample	**A**	**k / s^{-1}**
Control	-101.44	0.02115 (±0.00123)
Sorbic Acid treated	-91.63	0.02132 (±0.00103)

The effect of antioxidant upon radical formation was also measured by looking at the difference between the two growth curves over time. An increase in the gap between the curves over time indicates the antioxidant is influencing the formation of radical species. Figure 5-17 shows the difference between the EPR peak size between the treated and untreated samples over the 2-hour irradiation period.

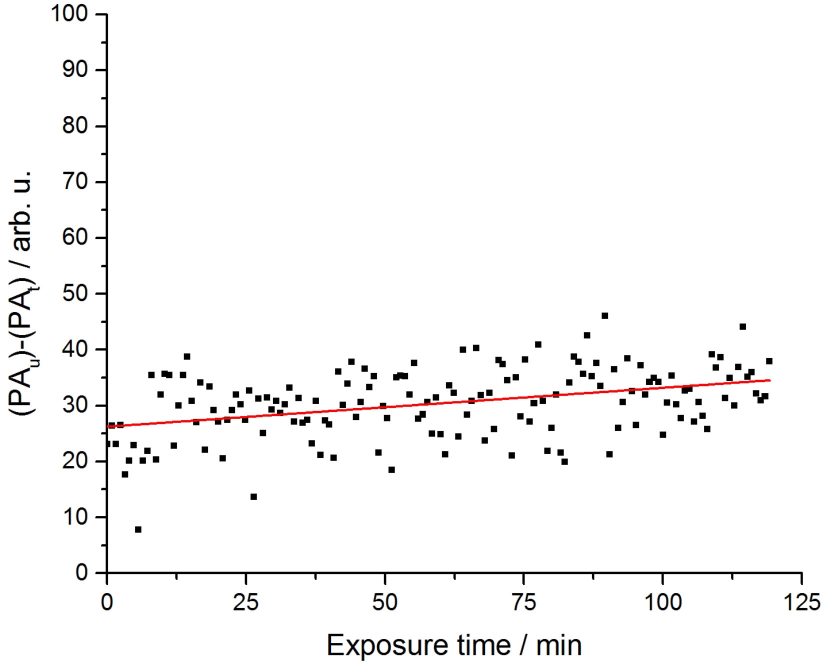

Figure 5-17: Difference between EPR signal peak area for untreated (PA$_u$) and sorbic acid treated (PA$_t$) hair samples throughout 2-hour exposure time

Although there is a gradual increase in the gap between growth curves, shown in Figure 5-17, the difference is very small. This, along with the similar parameters in Table 5-2, indicates that the antioxidant only has a weak protective effect against radical formation in hair fibres.

Sorbic acid is capable of readily quenching triplet states due to its relatively low triplet excited state energy.[261] However, much of the photochemistry likely proceeds from singlet excited tyrosine. Singlet oxygen is produced in proteins by singlet-singlet energy transfer, a process which can occur over much greater distances than triplet-triplet energy transfer.[52-53] Singlet oxygen is highly reactive and capable of forming hydroperoxide species on protein side chains, initiating autoxidation and the formation of radicals.[92] In addition to this, singlet oxygen reacts readily with disulfides, leading to S-S fission.[99] Singlet oxygen mediated lipid peroxidation reactions proceed faster than radical mechanisms.[262]

Sorbic acid should break autoxidative processes, leading to a significant reduction in radical production – as observed when oxygen is excluded. This may indicate that photodegradation in hair is mainly stoichiometric rather than an autoxidative process: antioxidants are less effective at influencing stoichiometric reactions due to their low concentration. However, a likely explanation for the antioxidant not having this effect is poor uptake into hair fibres. It was not possible to determine the concentration of the antioxidant in hair fibres. Future studies will need to optimise conditions and develop a method to monitor antioxidant uptake.

5.7.5 Effect of antioxidant upon radical decay

Antioxidants are most effective at breaking autoxidative cycles. These are initiated by photolysis of hydroperoxides (see section 4.9). Carbon centred radicals react with oxygen rapidly to form peroxyl radicals,[263] which then abstract hydrogen from neighbouring molecules, leading to the regeneration of carbon centred radicals. Loss in radical concentration is limited by oxygen availability and the rate of recombination and termination processes. The drop in intrinsic EPR signal in antioxidant treated hair suggests that the antioxidant can directly quench radical species.

Results from signal growth measurements suggest that the addition of sorbic acid has very little effect upon autoxidative processes, as radical signals grow at a similar rate to untreated hair. This is likely due to a relatively low uptake of antioxidant into hair fibres. The decay of radicals following UV exposure was also monitored by EPR. Signal decay measurements are less influenced by noise, the aim was therefore to confirm whether sorbic acid treatment had any impact upon autoxidative processes and radical concentration.

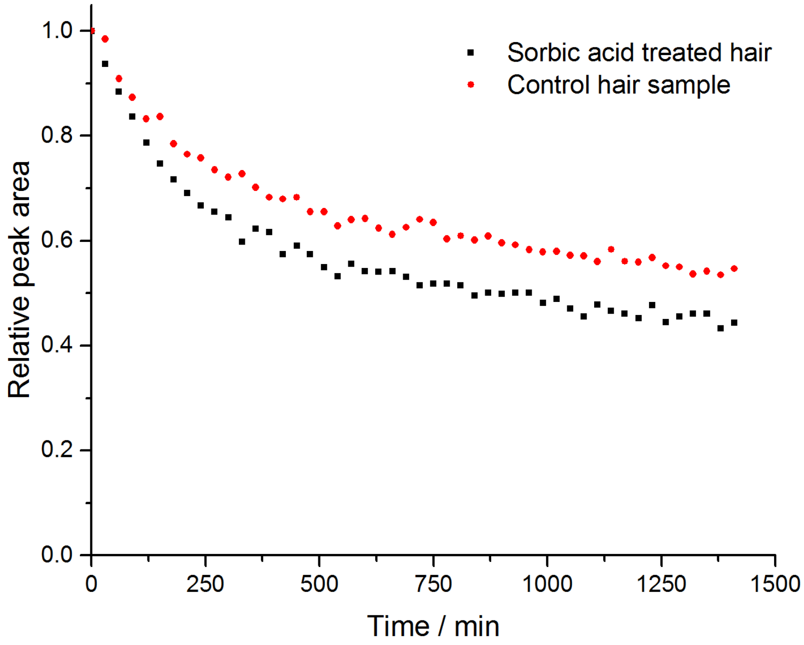

Figure 5-18: Change in peak area over 24 hours following UV exposure, relative to intensity at lamp switch off, for sorbic acid treated and untreated hair samples

As with signal growth measurements, both samples show similar results. However, radical species decay more rapidly in sorbic acid treated hair. The difference is small, which could indicate uptake into hair fibres is poor. However, it may also indicate that autoxidative processes are not as significant in hair proteins compared to model systems. Further optimisation of antioxidant uptake in hair samples is needed to confirm the role of autoxidative processes in hair proteins.

5.8 Photochemically produced radicals in hair proteins: conclusions

There are a variety of different components within hair fibres which may respond to light. Melanin, present in brown hair samples, exhibits a rapid response to irradiation in EPR as light influences the equilibrium between non-radical quinone/hydroquinone and semiquinone radicals. Short-lived electron-hole pairs are also created within the pigment, which decay rapidly following irradiation. In contrast, semiquinone and indolyl radicals are longer-lived.

White hair samples (low melanin content) also show an intrinsic radical EPR signal consistent with tyrosine based radicals on keratin proteins, based on spectral lineshape and g-value. The response of protein based radicals in white hair is significantly different from melanin in brown hair.

Following exposure of white hair, the features of the EPR signal matched that of phenoxyl radicals (from tyrosine) and sulfur centred radicals formed by disulfide cleavage. This is indicative of ROS formation by excited Tyr, which diffuse and break disulfide bonds. The process was accelerated at high humidity.

Radical lifetimes in hair samples decrease with increasing humidity, suggesting a more reactive system with higher water content. Diffusion of ROS and electrons between is facilitated by water layers present at higher humidity between protein fibres. This accelerates radical transfer and degradation reactions, resulting in increased protein degradation at higher humidity. These findings agree with protein loss and tensile strength measurements.

Excluding oxygen significantly reduced radical production, highlighting its crucial role in radical formation and protein damage. The addition of an antioxidant had some impact upon radical production and degradation, however its effect was limited by poor uptake into hair fibres. Further experiments could optimise the uptake of sorbic acid, or test the impact of other antioxidants upon radical formation and autoxidative processes in hair.

6. Conclusions and Further Work

As a highly abundant, photochemically active amino acid in keratin fibres, tyrosine photochemistry was studied in detail using simplified model systems. Tyrosine reactivity and radical lifetime was found to be strongly dependent upon environment. PEG-Tyr block copolymers provide a mimic of both the chemical (polypeptide) and molecular environment of tyrosine in predominantly α-helical keratin proteins.

Characterisation of model systems revealed that polymers self-assembled into micelles in aqueous solution, as well as forming stable hydrogels upon heating. This provided a unique opportunity to probe the effect of the different molecular environments upon the reactivity of tyrosine in chemically identical systems. Spin-labelling of tyrosine enabled a quantitative analysis of tyrosine environment within model systems, showing that micelles and gels have a similar molecular environment despite significantly different bulk properties. Gels exhibit a narrower distribution of tyrosine mobility, indicative of a more homogenous environment compared to less stable micelle structures. This distinction enabled the direct study of gelation process by EPR, a study which could be expanded to investigate intermediate structures and the effect of temperature, concentration and polymer length upon gel structures. Limitations of spin labelling included relatively low spin concentrations in samples, and the use of simplified models. Future work could improve the simulation model beyond three components, possibly making use of more complex theory such as the slow relaxing local structure model, which accounts for the Brownian diffusion of micelles.

Polymer concentration and length in micelles also influences tyrosine environment due to changes in micelle stability. Further studies could use spin labelling to probe a wider range of polymers and concentrations, to develop a more detailed picture of how micelle structure and stability influence molecular environment within micelle cores.

The similar environment of tyrosine in micelles and gels results in similar photochemical reactivity, although gels appear slightly less reactive overall. Different products also dominate in gels, with significant suppression of dimerization. Developing methods such as HPLC-MS to analyse and quantify other photodegradation products in model systems would allow more detailed understanding of how molecular environment influences tyrosine reaction pathways.

Upon prolonged exposure to UV, tyrosine oxidises to form DOPA, dityrosine and a range of other degradation products. This process was monitored through changes in intrinsic tyrosine fluorescence and photo-induced radical concentration. Both showed a gradual loss in tyrosine concentration over time.

Fe(III) and Cu(II) can influence tyrosine photodegradation. At high metal concentrations, copper-tyrosine complex formation leads to quenching of excited states, slowing degradation. Fe(III) does not form complexes with tyrosine under the conditions studied, and significantly enhances tyrosine photodegradation in model systems.

When direct absorption by tyrosine was prevented by filtering out UV light, iron(III) containing samples still showed significant degradation, indicating that the iron(III) acetate complexes predicted by speciation plots can absorb visible light and catalyse the production of reactive oxygen species or sensitise tyrosine.

Oxygen was found to be critical to degradation in model systems: excluding air decreased degradation by up to 90 %. However, partitioning iron(III) within micelle structures near tyrosine residues decreased the significance of oxygen pathways, as a result of increased direct redox chemistry between tyrosine and iron. These experiments proved that iron(III) is capable of catalytically enhancing tyrosine photodegradation at concentrations similar to the 40-60 ppm found in hair fibres. Future work could replicate the studies carried out with hydrophobic iron(III) salts with copper(II).

Antioxidants were found to be highly effective at slowing tyrosine degradation in model systems, suggesting that ROS formation and autoxidative processes dominate degradation. Further work could utilise these model systems to compare the activity of different antioxidants and concentrations, to aid in developing effective treatments for hair.

Studying protein photochemistry in human hair samples is limited owing to the dominance of melanin in most hair. However, by using white hair with minimal melanin content, intrinsic and photo-induced radical species were observed by EPR consistent with protein based radicals. These signals were influenced by the relative humidity and water content of hair fibres. Studies showed that at increased humidity, radicals were more highly reactive, contributing to greater damage to fibres. This study could be expanded to investigate other markers for protein damage, such as HPLC-MS based protein loss measurements or colorimetric assays, to correlate findings with EPR studies.

Protein radical formation in hair fibres is strongly dependent upon oxygen availability, however seems less affected by antioxidant treatment. This may indicate that autoxidative processes, which dominated in model systems are less significant in hair fibres. These processes are strongly dependent upon the ability of ROS to diffuse, and are likely humidity dependent. A broader study is needed to optimise the uptake of antioxidant into hair fibres, compare the effects of different antioxidants and confirm the significance of autoxidative processes in photo-induced radical formation and reactivity in keratin.

Despite significant findings in model system studies, it was not possible to investigate the effects of transition metal ions upon protein photochemistry in hair samples. A suitable range of melanin-free, iron/copper containing hair samples was not available, but could form the basis of future studies.

7. Experimental

7.1 Chemicals

All chemicals were used as supplied by Sigma-Aldrich (amino acids, tyrosine methyl ester hydrochloride, metal salts, buffer salts, spin probes, 4-amino-TEMPO, antioxidants), Fisher Scientific (glucano delta lactone), Fluorochem (Fmoc protected amino acids), TCI (iron(III) stearate). Ion exchange resin (Chelex 100) was obtained from the Dow Chemical Company. DMPO spin trap was prepared within the Chechik group. PEG_{2000}-Tyr_5, PEG_{5000}-$Tyr_{10/15/20}$ were obtained from the Prof. D. Adams group (Liverpool, UK (now Glasgow, UK)). All aqueous samples and buffer solutions were prepared using Milli-Q water. Other solvents used were of analytical grade.

7.2 Instrumentation

X-band EPR spectra of free amino acid solutions, solid amino acid solids, PEG-Tyr hydrogels and micelles, kinetic measurements, and hair samples were recorded on a JEOL JES RE-1X EPR spectrometer. Spin probe studies were performed on a Bruker EMX micro X-band EPR spectrometer. Spin labelled systems were analysed at X-band by a JEOL JES-X320 spectrometer. Q-band measurements were recorded on the JEOL JES-X320 equipped with a JEOL SQ5 Q-band microwave unit.

Fluorescence measurements were performed on a Hitachi F-4500 fluorescence spectrophotometer using quartz cells 1 × 1 cm. UV-vis spectra were recorded on a Shimadzu UV-1800 UV-vis spectrophotometer, using quartz cells with 1 cm pathlength. DLS measurements were performed at 25 °C using 173 ° a non-invasive backscatter method on a Malvern Instruments Zetasizer Nano ZS particle size analyser, using 1 cm glass or disposable plastic cuvettes.

ICP-MS analysis was carried out at the Biorenewables Development Centre, University of York, using an Agilent 7700x ICP-MS. Samples were run in HMI (high matrix introduction) mode, due to the presence of PEG and buffer. pH measurements were performed on a Jenway model 3505 pH meter.

Mass spectrometry was performed on a Bruker Micro-TOF with ESI at the mass spectrometry centre for excellence, University of York. NMR spectra were recorded on Bruker ECX-400 MHz and Bruker ECS-400 MHz machines.

7.3 Chapter 2: Experimental Procedures

7.3.1 EPR analysis of tyrosine and tyrosine methyl ester solutions

Solutions of L-tyrosine (2.5 mmol dm^{-3}, 100 mL) and L-Tyr methyl ester (35 mmol dm^{-3}, 100 mL) were prepared, and adjusted to either pH 7 or pH 10 by adding small volumes of 5 mol dm^{-3} NaOH.

Due to the high dielectric loss of water, a quartz flat cell was used for aqueous solution EPR measurements. Samples were irradiated *in situ* within the EPR cavity using a 100 W Hg vapour arc lamp (Ushio USH-102DH, see appendix 4). Samples were continuously flowed through the flat cell within the EPR cavity as shown in Figure 7-1, to replenish the low volume of sample exposed to UV. Samples were degassed by bubbling N_2 through the reservoir. EPR spectra were recorded before, during, and after irradiation. EPR parameters (average of 15 scans, room temperature): power = 1 mW; scan time = 60 s, sweep width = 3 mT; modulation width = 0.05 mT; time constant = 0.1 s.

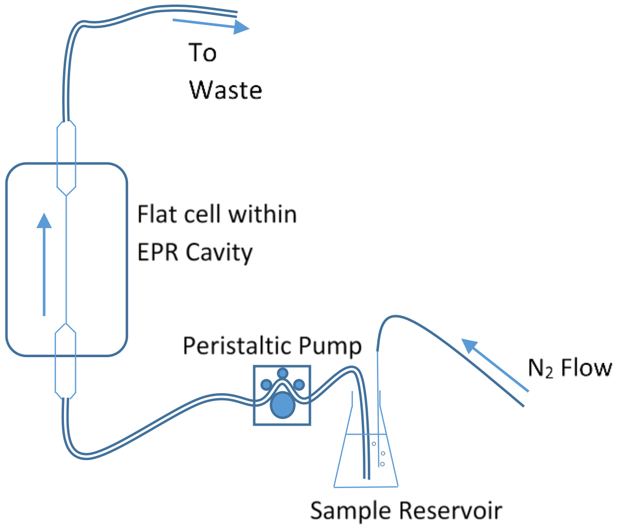

Figure 7-1: EPR flow system used for free amino acid aqueous solutions.

7.3.2 EPR analysis of solid amino acid powders and mixtures, with and without Fe(III)

Amino acid mixtures were prepared by dissolving the desired mass ratio of Tyr/Cys in water, then evaporating the solvent under reduced pressure. $FeCl_3$ was also added to solutions to give a mass concentration of 1000 ppm after drying.

Solid powders were placed into 5 mm (outer diameter) Suprasil® quartz tubes, and packed to a height of 4 cm by gently tapping the tube several times. For experiments under inert gas, a capillary was placed into the sample tube after loading the sample and argon gas blown through for 2 minutes before sealing.

Samples were placed in the EPR cavity and a spectrum was recorded. Samples were then irradiated within the cavity for 4 minutes with a 100 W Hg lamp, then a further spectrum was recorded. The lamp was switched off, and further spectra were recorded at 1-hour intervals. EPR parameters (average of 10 scans, room temperature): power = 1 mW; scan time = 90 s, sweep width = 20 mT; modulation width = 0.4 mT; time constant = 0.3 s.

7.3.3 Fmoc hydrogel preparation and EPR analysis

Fmoc-Tyr (42 mg, 0.104 mmol) was weighed into a sample vial. To this was added water (3 mL) followed by 1 mol dm^{-3} NaOH solution (1 mL). The mixture was then heated to 40 °C for 1 hour with stirring to encourage dissolution, then filtered through glass wool to remove any undissolved material. To modify pH and promote gelation, glucano delta lactone (3 mg, 0.018 mmol) was added, and mixed thoroughly. The observed pH of the resultant solution was approximately pH 5 (by pH paper). The solution was then transferred to a flat cell for EPR analysis, sealed, and left to form a gel slowly overnight. This method produced a 1% (wt.) gel. For 2% gel, Fmoc-Tyr and glucano delta lactone concentrations were doubled. Fmoc-Gly gels were prepared in the same way. Gelation was confirmed by inversion of sample vials containing prepared gel.

EPR analysis was performed by fixing the flat cell with the set gel in the cavity, and irradiating *in situ* with a 100 W Hg lamp. Spectra were recorded before, during and after irradiation. EPR parameters (average of 10 scans, room temperature): Power = 5 mW; Scan Time = 30 s; Sweep Width = 15 mT; Modulation Width = 0.4 mT, Time Constant = 0.1 s.

7.3.4 Preparation of PEG-Tyr gels

PEG_{5000}-Tyr_{15} (20 mg, 0.00259 mmol), PEG_{2000}-Tyr_5 (10 mg, 0.00344 mmol) or PEG_{5000}-Tyr_{10} (20 mg, 0.00293 mmol) was added to water (1 mL). The mixture was sonicated at room temperature for 60 minutes to ensure homogenous dissolution. The mixture was then transferred to either a flat cell or a quartz capillary, and heated to 85 °C for 2 hours (PEG_{5000}-Tyr_{15}), 40 °C for 1 hour (PEG_{2000}-Tyr_5) or 85 °C for 3 hours (PEG_{5000}-Tyr_{10}). After this time, the gel was cooled to room temperature. Gelation was confirmed by inversion of the flat cell.

7.3.5 EPR analysis of PEG-Tyr gel and micelle systems

Samples of 10 mg/mL PEG_{5000}-Tyr_{15} solutions were transferred to a quartz capillary, filled to a height of 2.5 cm – 3.5 cm. Gel samples were prepared by heating the capillary to 85 °C for 2 hours. The capillary was fixed into the EPR cavity and a spectrum was recorded. The sample was then irradiated with a 100 W Hg arc lamp. A spectrum was recorded immediately. EPR parameters (average of 10 scans, room temperature): Power = 10 mW; Scan Time = 90 s; Sweep Width = 8 mT; Modulation Width = 0.4 mT, Time Constant = 0.3 s.

7.4 Chapter 3: Experimental Procedures

7.4.1 DLS analysis of micelle solutions

Solutions of PEG_{2000}-Tyr_5 (1 mg/mL, 0.344 mmol dm^{-3}), PEG_{5000}-Tyr_{10} (1 mg/mL, 0.147 mmol dm^{-3}) and PEG_{5000}-Tyr_{15} (1 mg/mL, 0.130 mmol dm^{-3}) were prepared in milli-Q water. The volume of each sample was 1.1 mL. These were filtered through a 450 nm PTFE micro-mesh filter into a quartz cuvette, then DLS measurements were recorded after 2 minutes temperature equilibration to 25 °C using non-invasive back scatter method at 173°. Size distribution plots were the average of 3 measurements of 12 × 10 second scans, as determined by the instrument.

7.4.2 Measurement of critical micelle concentration by DLS

A series of solutions containing either PEG_{2000}-Tyr_5 or PEG_{5000}-Tyr_{10} were made up in milli-Q water, within the concentration range 0.1 – 0.002 mmol dm^{-3}. Sample volumes were 1.1 mL. Samples were filtered through 450 nm PTFE filters into disposable plastic cuvettes and analysed by DLS, using a non-invasive back scatter technique, angle 173°. The attenuation of the DLS instrument was fixed at 11 to give maximum sensitivity and a comparable count rate between samples. The count rate was analysed and plotted as a function of concentration. The cmc is defined as the point at which count rate starts increasing significantly above baseline.

7.4.3 Testing the stability of micelle structure to UV exposure

1 mg/mL PEG_{5000}-Tyr_{10} solution (1.1 mL) was prepared and analysed by DLS as outlined in Section 7.4.1. The sample was kept sealed in the quartz cuvette after DLS analysis, then irradiated for 2 hours with a 100 W Hg lamp, before another DLS measurement was recorded. This was repeated, with measurements after 2, 4, 6 and 24 hours exposure. Average particle size was calculated from size distribution by intensity, and is based on an average of 3 scans for each measurement.

7.4.4 Spin probing of micelle systems with 12-DOXYL stearic acid

To ethanol (50 mL) was added 12 DOXYL-stearic acid (1.00 mg, 2.60 mmol), to achieve a stock solution with a concentration of 5.2×10^{-5} mol dm^{-3}. 0.5 mL of stock solution was then added to a sample vial, and the ethanol was evaporated. 50 µL of PEG_{5000}-Tyr_{15} sample was then added to the sample vial, it was mixed vigorously for 1 minute, then sonicated for 60 minutes at room temperature to encourage spin probe dissolution and incorporation. The final concentration of spin probe in sample was 5.2×10^{-4} mol. A control sample was prepared using 50 µL of water rather than PEG-Tyr sample.

For studies at pH 3, the PEG-Tyr sample was made up by dissolving into 10^{-3} mol dm^{-3} HCl.

The samples were transferred to a capillary tube, which was sealed, inserted into the EPR cavity and a spectrum recorded. EPR parameters (average of 3 scans, room temperature): Power = 5 mW; Scan Time = 90 s; Sweep Width = 10 mT; Modulation Width = 0.1 mT; Time Constant = 0.1 s.

7.4.5 Synthesis of spin labelled tyrosine methyl ester and non-spin active equivalent

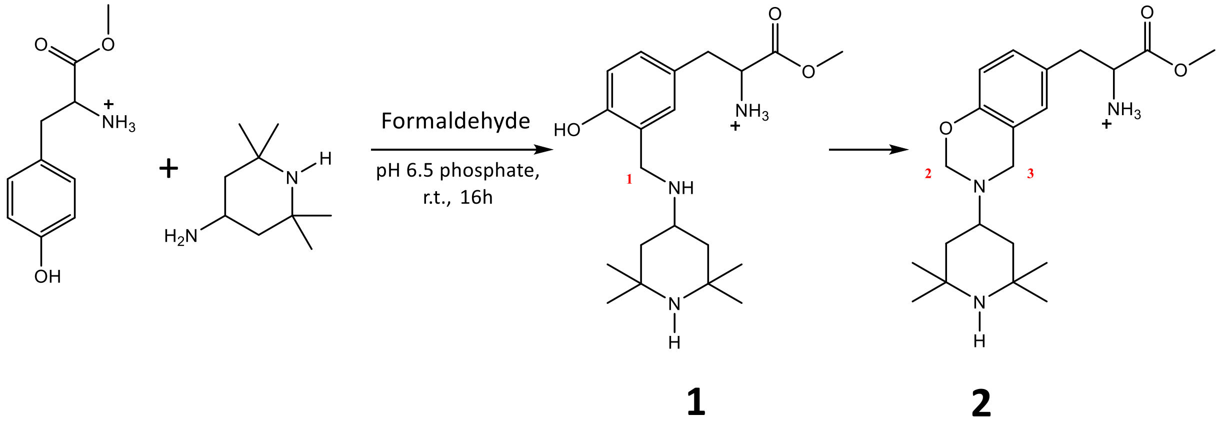

Scheme 7-1: Mannich coupling reaction of tyrosine methyl ester and 4-amino-TEMP with formaldehyde

Tyrosine methyl ester hydrochloride (23.17 mg) was dissolved in 869 µL 10 mmol dm^{-3} pH 6.5 phosphate buffer. 50 µL of 2 mol dm^{-3} solution of amino-TEMP in 1:1 (v/v) acetonitrile: pH 6.5 phosphate buffer was added to the tyrosine solution, followed by 80 µL 12.321 mol dm^{-3} formaldehyde solution (in water, with 10-15% methanol stabiliser). The sample was shaken in air at room temperature for 16 hours. After reaction, the solvent was removed and the resulting yellow oil was washed with chloroform and dried to leave a pale-yellow powder (yield: 32.0 mg, 83.6%). This was analysed by ESI-MS and NMR spectroscopy. ESI-MS peaks found (see Appendix 2): m/z 376.2604 ($C_{21}H_{34}N_3O_3$ benzoxazine product: calc. 376.2595), error 2.4 ppm; m/z 364.2600 ($C_{20}H_{34}N_3O_3$ Mannich bridge intermediate: calc. 364.2600), error 0.05 ppm. NMR (MeOD, 400 MHz): δ = 4.75 ppm (s, 0.5H, 1); δ 4.9 ppm (m, 2H, 3); δ = 5.2 ppm (m, 2H, 2).

Tyrosine methyl ester hydrochloride (23.17 mg) was dissolved in 869 µL 10 mmol dm^{-3} pH 6.5 phosphate buffer. 50 µL of 2 mol dm^{-3} solution of amino-TEMPO in 1:1 (v/v) acetonitrile: pH 6.5 phosphate buffer was added to the tyrosine solution, followed by 80 µL 12.321 mol dm^{-3} formaldehyde solution (in water, with 10-15% methanol stabiliser). The sample was shaken in air at room temperature for 16 hours. After reaction, the solvent was removed and the resulting orange oil was washed with chloroform and dried to leave an orange powder (yield: 28.3 mg, 72.5%). This was analysed by ESI-MS. ESI-MS peaks found (see Appendix 3): m/z 390.2372 ($C_{21}H_{32}N_3O_4$ benzoxazine product: calc. 390.2387), error 3.8 ppm.

7.4.6 Spin labelling of PEG-Tyr polymers

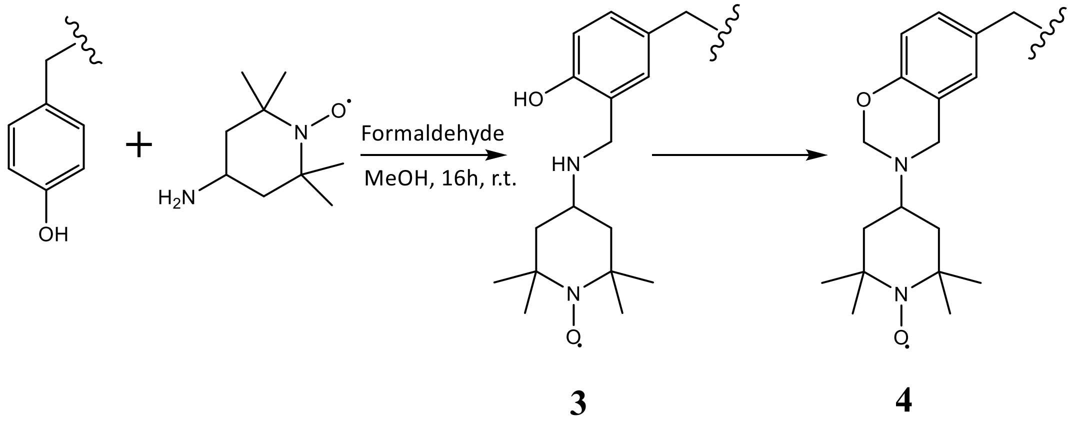

Scheme 7-2: Spin labelling of PEG-Tyr block copolymer tyrosine side chains with 4-amino-TEMPO

PEG_{2000}-Tyr_5 or PEG_{5000}-Tyr_{10} was dissolved in 100 µL methanol to give a concentration of 4.58 mmol dm^{-3}. 50 µL of 58.6 mM amino-TEMPO solution in methanol then added to sample, followed by 8.4 µL formaldehyde 3.5 M solution in methanol. Sample shaken at room temperature for 16 hours, then solvent removed under vacuum. Residue redissolved in 333 µL water, to give an end polymer concentration of 1.38 mmol dm^{-3} and spin concentration 8.79 mmol dm^{-3}. Sample then dialysed in 3 L water to remove any unreacted nitroxide using a 12-14000 Da membrane, with 2 water changes in 24 hours. The yield of labelled Tyr residues was 0.3%. Complete removal of unreacted free nitroxide was confirmed by dialysing the same volume of 8.79 mmol dm^{-3} 4-amino-TEMPO in water with the same water changes, and confirming removal of nitroxide by EPR.

7.4.7 X band EPR analysis of spin labelled system

Spin labelled PEG_{2000}-Tyr_5 samples at a concentration of 5 mg/mL (1.72 mmol dm^{-3}) in Milli-Q water were placed into a quartz flat cell and X-band EPR spectra recorded at room temperature. EPR parameters (average of 5 scans, room temperature): Microwave power = 2 mW, Frequency = 9.128 GHz, Sweep Width = 15 mT, Modulation width = 0.1 mT, Sweep Time = 240 sec, Time constant = 0.1 s.

Spin labelled gel samples were prepared by heating the spin-labelled 5 mg/mL micelle solution within the flat cell in a water bath at 60 °C for 2 hours. Gelation was confirmed by introducing a small (diameter approx. 0.4 mm) lead solder ball to the top of the sample within the flat cell. Following gelation, the increased macroscopic viscosity of the sample prevented the ball sinking through the sample.

7.4.8 Frozen sample Q band EPR measurements

Spin labelled PEG_{2000}-Tyr_5 samples at a concentration of 5 mg/mL (1.72 mmol dm^{-3}) in Milli-Q water were placed into a quartz EPR tube (inner diameter 1.1 mm, Wilmad WG-221T-RB). The sample was then frozen in the EPR cavity using liquid N_2 in an insertion dewar. The minimum temperature reached was 88 K, spectra were recorded at this temperature. EPR parameters (average of 10 scans): Microwave power = 124 µW; Frequency = 34.69 GHz; Sweep Width = 30 mT; Modulation width = 0.1 mT; Sweep Time = 480 sec; Time constant = 0.3 s.

7.4.9 Q band EPR measurements at room temperature

Spin labelled PEG_{2000}-Tyr_5 samples at a concentration of 5 mg/mL (1.72 mmol dm^{-3}) in Milli-Q water were placed into a quartz EPR tube (inner diameter 1.1 mm, Wilmad WG-221T-RB). An EPR spectrum was recorded at room temperature. EPR parameters (average of 10 scans): Microwave power = 124 µW; Frequency = 34.69 GHz; Sweep Width = 30 mT; Modulation width = 0.1 mT; Sweep Time = 480 sec; Time constant = 0.3 s.

7.4.10 Monitoring change in structure upon heating by DLS

1 mg/mL PEG_{5000}-Tyr_{10} solution (1.1 mL) was prepared and analysed by DLS as outlined in Section 7.4.1. The sample was kept sealed in the quartz cuvette after DLS analysis, heated in a water bath at 50 °C for 2 hours, before another DLS measurement was recorded. This was repeated, with measurements after 2, 4, 6 and 24 hours exposure. Average particle size was calculated from size distribution by intensity, and is based on an average of 3 scans for each measurement. A control sample was also prepared in the same way and measured after the same time intervals without heating, to check that micelle structures were stable.

For shorter timescale measurements, 10 mg/mL PEG_{2000}-Tyr_5 solution (1.1 mL) was prepared and analysed by DLS. The sample (in the quartz cuvette) was then immersed in a water bath at 65 °C for 30 seconds, removed, cooled to 25 °C and reanalysed by DLS. The procedure was repeated every 30 seconds up to 4 minutes total heating time. Average particle size was calculated from size distribution by intensity, and is based on an average of 3 scans for each sample.

7.4.11 Monitoring change in structure upon heating by EPR

Spin labelled PEG_{2000}-Tyr_5 solution at a polymer concentration of 10 mg/mL was prepared and placed in a quartz flat cell. A small lead solder ball was added to the flat cell. In the micelle sample, this sank through the sample. An EPR spectrum was recorded at room temperature, then the flat cell was removed from the cavity and placed in a water bath at 65 °C for 30 seconds. The sample was then cooled to room temperature for 5 minutes, then another spectrum recorded. This process was repeated for 30 – 240 second heating periods up to a total heating time of 20 minutes. EPR parameters (average of 20 scans, room temperature): Microwave power = 5 mW; Frequency = 9.128 GHz; Sweep Width = 15 mT; Modulation width = 0.1 mT; Sweep Time = 60 sec; Time constant = 0.1 s.

7.4.12 UV/vis analysis of micelle solutions and gels

5 mg/mL samples of PEG_{2000}-Tyr_5 in milli-Q water were placed in quartz cuvettes (1 cm pathlength). One cuvette was heated to 65 °C for 2 hours to promote gelation. UV-vis spectra were then recorded of both micelle and gel samples, against a water reference sample.

7.4.13 Adding iron to gel systems

A solution of 50 ppm (0.895 mmol dm^{-3}) iron(III) acetylacetonate was prepared in water. This solution (0.3 µL) was then added to 150 µL prepared 5 mg/mL micelle and gel samples in quartz cuvettes, to give a metal concentration of 0.1 ppm. The samples were left for 1 hour to allow the metal to diffuse before irradiation. Dark control samples were prepared in the same way.

7.4.14 Fluorescence analysis of micelle and gel systems

After irradiation, 150 µL ethanol was added to micelle and gel samples to dissolve aggregates. 200 µL of the resulting solution was taken, and 400 µL each of 0.1 mol dm^{-3} pH 5 acetate buffer and 0.4 mol dm^{-3} pH 8.5 borate buffer was added. This decreases the ethanol concentration sufficiently for micelle structures to form, as tested by DLS. Fluorescence emission and excitation spectra were recorded, an average of 3 scans was taken for each sample. Excitation parameters: Emission wavelength = 303 nm, excitation scan 240-300 nm. Emission parameters: Excitation wavelength = 276 nm, emission scan 270-500 nm. Dityrosine fluorescence was also monitored – Excitation parameters: Emission wavelength = 405 nm, excitation scan 240-400 nm. Emission parameters: Excitation wavelength = 320 nm, emission scan 325-550 nm. The extent of Tyr degradation was measured as a percentage decrease in Tyr emission maximum intensity at 310 nm relative to the dark control for each sample.

7.5 Chapter 4: Experimental Procedures

7.5.1 EPR kinetic measurements

0.5 mL samples of 10 mg/mL (1.30 mmol dm^{-3}) PEG$_{5000}$-Tyr$_{15}$ polymer concentration were prepared in 0.1 mol dm^{-3} pH 5 acetate buffer. Iron(III) was introduced by adding 5 µL of FeCl$_3$ (0.181 mol dm^{-3}) stock solution in water, giving a final metal concentration of 100 ppm (1.79 mmol dm^{-3}). Samples were loaded into either a quartz capillary or a flat cell and placed into the EPR cavity. A single EPR scan was then recorded upon irradiation with a 100 W Hg lamp. The magnetic field of the spectrometer was set at the maximum of the observed peak, and programmed to record the change of signal intensity at this point over time. The change was monitored for 5 minutes after the lamp was switched on, and 20 minutes after it was switched off. Kinetics curves are the average of 3-4 measurements. EPR parameters (fixed field, room temperature): Power = 10 mW; Scan Time = 300 s (for growth), 1200 s (for decay); Sweep Width = ± 0 mT; Modulation Width = 0.4 mT, Time Constant = 0.3 s.

7.5.2 Measuring tyrosine fluorescence

140 µL of 2 mg/mL PEG$_{5000}$-Tyr$_{10}$ solution in water was taken, and diluted to a total volume of 290 µL with 0.194 mol dm^{-3} NaOH solution. The solution was then filtered through a 450 nm PTFE micro-filter. 200 µL of the filtrate was taken, and 400 µL each of 0.1 mol dm^{-3} pH 5 acetate buffer and 0.4 mol dm^{-3} pH 8.5 borate buffer was added. Fluorescence excitation and emission spectra were then recorded. Measurement parameters as section 7.4.14.

7.5.3 2D fluorescence and analysis of dityrosine formation

A stock solution of 0.5 mmol dm^{-3} tyrosine methyl ester was made up in water. Two 200 µL samples of this were taken, one was kept in the dark and the other irradiated with a 100 W Hg arc lamp for 24 hours. After irradiation, samples were diluted through the addition of 400 µL each of 0.1 mol dm^{-3} pH 5 acetate buffer and 0.4 mol dm^{-3} pH 8.5 borate buffer, and then analysed by 2D fluorometry. Scan ranges: excitation = 240 – 400 nm; emission 270 – 500 nm. Slit widths 5 nm for both excitation and emission.

Another set of samples was prepared: after irradiation, the solvent was removed and the resulting white powder (dark control) or light brown waxy paste (exposed sample) was analysed by ESI-MS.

7.5.4 Prolonged exposure EPR measurements

0.5 mL samples of 10 mg/mL PEG_{5000}-Tyr_{15} solutions in water were prepared. Iron(III) was introduced to some samples by adding 5 µL of $FeCl_3$ (0.181 mol dm^{-3}) stock solution in water, giving a final metal concentration of 100 ppm (1.79 mmol dm^{-3}). Samples were transferred to a quartz capillary, filled to a height of 2.5 cm – 3.5 cm. The capillary was fixed into the EPR cavity and a background spectrum was recorded. The sample was then irradiated a 100 W Hg arc lamp. An EPR spectrum was recorded immediately. Further spectra were recorded at 20-minute intervals up to 160 minutes with continued irradiation. EPR parameters (average of 10 scans, room temperature): Power = 10 mW; Scan Time = 90 s; Sweep Width = ± 4 mT; Modulation Width = 0.4 mT, Time Constant = 0.3 s.

7.5.5 Prolonged exposure fluorescence measurements

140 µL samples of tyrosine ester (0.5 mmol dm^{-3}), PEG_{5000}-Tyr_{10} (2 mg/mL, 0.294 mmol dm^{-3}) or PEG_{2000}-Tyr_5 (2 mg/mL, 0.688 mmol dm^{-3}) were prepared in 0.1 mol dm^{-3} acetate buffer at pH 5. Stock metal solution was added for metal containing systems to give a final metal concentration of 100 ppm (1.79 mmol dm^{-3} for Fe, 1.57 mmol dm^{-3} for Cu). Samples were then irradiated for the specified time (usually 24 hours, with a sample removed after 3 hours in some cases). A dark control sample was prepared for every measurement.

For samples irradiated in an inert atmosphere, special cuvettes fitted with Young's taps were used. The sample was loaded, then argon was bubbled through the sample within the cuvette for 2 minutes, before the cuvette was sealed.

Samples were treated after irradiation to remove metals before fluorescence measurements. Iron could be removed from samples by precipitation as $Fe(OH)_3$ at high pH. To 140 µL samples was added 150 µL dilute NaOH solution (194 mmol dm^{-3}). Samples were shaken and left for 10 minutes for precipitate to form, then filtered through 450 nm PTFE filters. 200 µL of the resulting solution was taken, 400 µL each of 0.1 mol dm^{-3} pH 5 acetate and 0.4 mol dm^{-3} pH 8.5 borate buffers were added, and the fluorescence emission and excitation spectra recorded (average of 3 scans). Parameters as described in section 7.4.14. The extent of Tyr degradation was measured as a percentage decrease in Tyr emission maximum intensity at 310 nm relative to the dark control for each sample.

Copper was removed from samples by ion exchange. Chelex-100 ion exchange micro-columns were prepared in glass tubes (internal diameter = 2 mm). One end of the tube was thinned but not sealed and plugged with glass wool. The resin was soaked in 0.1 mol dm^{-3} pH 5 acetate buffer overnight, the resulting slurry was pipetted into the column to achieve a bed height of 4-5 cm. Glass wool was added at the top of the bed to prevent disturbance to resin beads upon sample addition (see Figure 7-2). Several bed volumes of buffer were passed through the column to ensure settling before adding sample. During this time the average flow rate of the column was measured by measuring the mass of solvent eluted in five 10 s periods and averaging. The bed volume of columns was estimated as 14.3 µL / cm by measuring the time taken for a coloured solution of 2-nitrophenol to pass through the column. Based on this and the flow rate for each column, the time taken for a sample to pass through each column was estimated.

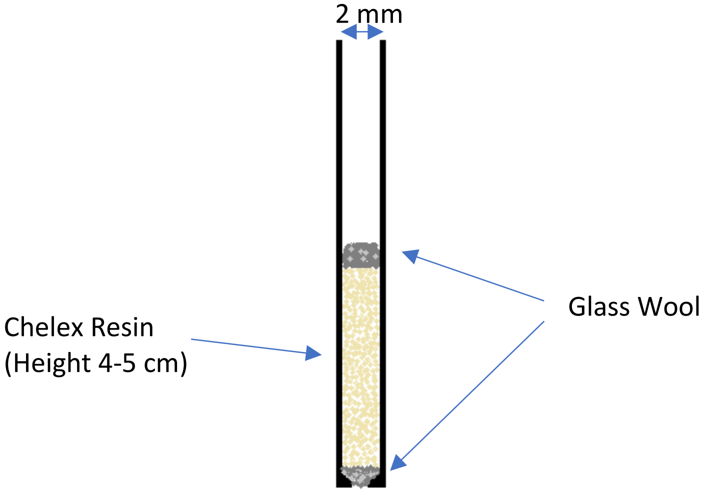

Figure 7-2: Chelex ion exchange micro-column

Copper samples were typically passed through the column twice, to ensure complete metal removal. 140 µL samples were added to the top of the column by syringe, passed through the column and collected. The sample was washed through with approximately 2 bed volumes of acetate buffer, which was also collected. The total volume of sample collected was measured by weighing collected eluent. This process was then repeated and the sample passed through the column a second time. The collected sample was then diluted up to a total volume of 600 µL with 0.1 mol dm^{-3} pH 5 acetate buffer. A further 400 µL 0.4 mol dm^{-3} pH 8.5 borate buffer was added, and fluorescence measurements taken as described in section 7.4.14.

Metal removal was confirmed by ICP-MS analysis. Samples of copper and iron-containing PEG-Tyr were taken before (200 µL) and after (700 µL) treatment, diluted up to 10 mL with deionised water and analysed by ICP-MS in high matrix introduction mode.

7.5.6 Measuring peptide breakdown: Fluorescamine assay

90 µL samples of tyrosine ester (0.5 mmol dm^{-3}) or PEG$_{5000}$-Tyr$_{10}$ (2 mg/mL, 0.294 mmol dm^{-3}) were prepared in 0.1 mol dm^{-3} acetate buffer at pH 5. Stock metal solution was added where required to give a final metal concentration of 100 ppm (1.79 mmol dm^{-3} for Fe, 1.57 mmol dm^{-3} for Cu). Samples were irradiated for 4 hours or 24 hours, with some samples kept as dark controls.

After irradiation, 180 µL of 0.4 mol dm^{-3} borate buffer at pH 8.5 was added to each sample, followed by 90 µL of fluorescamine solution (0.03% w/v in acetone). A further 810 µL of water was added, and the fluorescence emission and excitation spectra recorded (Average of 3 scans). Excitation parameters: Emission wavelength = 490 nm, excitation scan 300-500 nm. Emission parameters: Excitation wavelength = 390 nm, emission scan 400-600 nm.

7.5.7 Partitioning hydrophobic Fe(III) in micelles

Stock iron (III) stearate solution in ethanol at a metal concentration of 50 ppm was prepared. Specific volumes of the stock solution were transferred into sample vials to give the desired metal concentration when diluted by a factor of 100. The ethanol was then removed under vacuum, and PEG$_{2000}$-Tyr$_5$ polymer solutions (0.5 – 5 mg/mL, 0.074 – 0.735 mmol dm^{-3}) were prepared in 0.1 M pH5 acetate buffer, and added to dried Fe stearate residue. Resulting solutions were shaken for 1 hour, sonicated for 1 hour and then shaken for a further hour to ensure partitioning of the hydrophobic metal salt into the colloidal system. Solutions were split into two, one sample kept as a dark control. The other was exposed to a 100 W Hg arc lamp for 24 hours, both samples were then analysed as described in section 7.5.5.

7.5.8 UV vis analysis of iron(III) acetate and tyrosine solutions

10 µL of 0.181mol dm^{-3} FeCl$_3$ stock solution was added to 1 mL 0.1 mol dm^{-3} pH 5 acetate buffer, to produce a solution containing Fe(III) acetate complexes, with metal concentration of 100 ppm (1.79 mmol dm^{-3}). A 0.5 mmol dm^{-3} tyrosine ester solution was also prepared in 0.1 mol dm^{-3} pH 5 acetate buffer. A UV vis absorbance spectrum was recorded of both solutions, with 0.1 mol dm^{-3} pH 5 acetate buffer as a reference.

7.5.9 Spin trapping

2 mg/mL (0.688 mmol dm^{-3}) solutions of PEG$_{2000}$-Tyr$_5$ in 0.1 mol dm^{-3} pH 5 acetate buffer were prepared. A stock solution of DMPO spin trap (1 mol dm^{-3}) was also prepared in the same buffer solution and kept in the freezer. 10 µL of the spin trap solution was transferred into 90 µL of the PEG-Tyr solution, the sample was placed in a quartz capillary and analysed by EPR. Some samples were degassed by bubbling argon through and keeping sealed under a positive argon pressure before transferring to the capillary. The sample was irradiated with a 100 W Hg arc lamp for 5 minutes, the lamp was shut off and another spectrum recorded. The experimental spectrum was deconvoluted by fitting a simple simulation based upon literature hyperfine splitting values using PEST WINSIM software.[238]

7.5.10 Adding antioxidants

Stock BHT solution in ethanol at a concentration of 1.5 mM was prepared. Specific volumes of the stock solution were transferred into sample vials to give the desired BHT concentration when diluted by a factor of 100. The ethanol was then removed under vacuum, and PEG$_{2000}$-Tyr$_5$ polymer solutions (0.5 – 5 mg/mL, 0.074 – 0.735 mmol dm^{-3}) were prepared in 0.1 M pH 5 acetate buffer, and added to dried BHT residue. Resulting solutions were shaken for 1 hour, sonicated for 1 hour and then shaken for a further hour to ensure partitioning of the hydrophobic antioxidant into the colloidal system. Solutions were split into two, one sample kept as a dark control. The other was exposed to a 100 W Hg arc lamp for 24 hours, both samples were then analysed as described in section 7.5.5.

7.6 Chapter 5: Experimental Procedures

7.6.1 EPR of hair samples

Samples of “natural white” hair and “Mid brown virgin” hair were obtained from P&G. These were cut into 4 cm lengths, and placed into a Suprasil® quartz EPR tube with an outer diameter of 5 mm. The mass of hair sample loaded was measured, and was 130 ± 3 mg for each sample. The hair samples were then loaded into the spectrometer and spectra were recorded. EPR parameters (average of 5 scans, room temperature): Power = 2 mW; Scan Time = 480 s; Sweep Width = ± 10 mT; Modulation Width = 0.1 mT, Time Constant = 0.3 s.

7.6.2 EPR analysis of hair samples upon exposure to UV light

Hair samples were prepared as described in section 7.6.1, then placed in the EPR cavity. Sequential scans were run on hair samples at an interval of 48 s (30 s scan time, plus 18 s for the machine to reset) upon exposure to a 100 W Hg lamp. The lamp shutter was opened after the first scan. 150 scans were carried out over a 2-hour period. EPR parameters (150 sequential scans, room temperature): Power = 10 mW; Scan Time = 30 s; Sweep Width = ± 10 mT; Modulation Width = 0.1 mT, Time Constant = 0.03 s.

Following this prolonged exposure period, the lamp was shut off, and subsequent EPR spectra were recorded every 30 minutes over a 24-hour period. These scans used a slower scan time, improving s/n ratio. EPR parameters (48 sequential scans (1 every 30 min), room temperature): Power = 10 mW; Scan Time = 300 s; Sweep Width = ± 10 mT; Modulation Width = 0.1 mT, Time Constant = 0.3 s.

7.6.3 Kinetic analysis of radical formation and decay by EPR

Hair samples were prepared and an EPR spectrum recorded as described in section 7.6.1. The magnetic field of the spectrometer was set at the maximum of the observed peak, and programmed to record the change of signal intensity at this point over time. The change was monitored for 10 minutes after the lamp was switched on, and 10 minutes after it was switched off. EPR parameters (fixed field, room temperature): Power = 10 mW; Scan Time = 600 s; Sweep Width = ± 0 mT; Modulation Width = 0.1 mT, Time Constant = 0.03 s.

7.6.4 Controlling humidity of hair samples

A surprising range of different humidity levels were achievable by utilising the daily variation of ambient humidity levels within the laboratory, which typically ranged from 50-70% depending on weather conditions. For experiments outside this range, artificially controlled humidity environments were created by using a polyethylene glove bag (Aldrich AtmosBag). Hair samples were placed in an open EPR tube in the bag, and equilibrated to a controlled humidity level. This was achieved by using a combination of dry compressed air blown into the bag, warm water reservoirs placed within the bag, and bubbling inlet gas through a solution of saturated salt solutions (see Table 7-1).[253] The set-up is outlined in Figure 7-3.

Table 7-1: Methods used to achieve controlled humidity conditions

Humidity	Method used
25%	Saturated CH_3COOK bubbler
50-70%	Daily variation of ambient humidity
80%	Saturated $(NH_4)_2SO_4$ bubbler
100%	Hot water

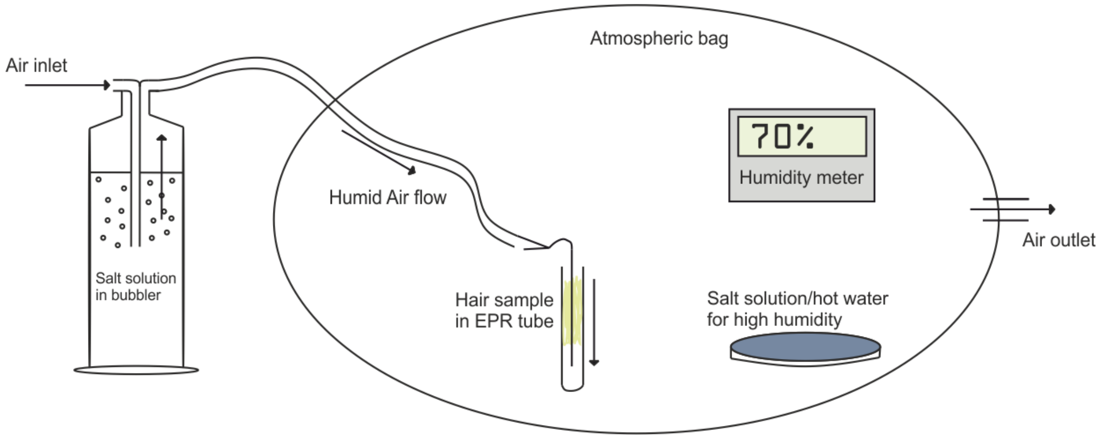

Figure 7-3: Diagram showing bag setup used to achieve controlled humidity. Sample sealed inside bag after equilibration

Dry air samples were prepared by blowing dry air directly into the bag from the lab compressed air supply. Samples in an inert atmosphere were prepared by placing them in the bag, alternately evacuating the bag under vacuum and refilling with N_2 gas 3 times before sealing the sample. Hair samples were equilibrated for 2 hours at all humidity levels, before sealing into the EPR tube within the glove bag. The sealed tubes were then removed and analysed by EPR as described in section 7.6.2.

7.6.5 Treating hair with antioxidants

A saturated solution of sorbic acid (14.27 mmol dm^{-3}) was prepared in water. The pH of the solution was calculated at 3.31. A sample of white hair was treated by soaking in antioxidant solution for 2 hours, before drying for 2 hours in a drying oven at 60 °C and equilibrating to 70% RH as outlined in section 7.6.4 for a further 2 hours. A control sample was prepared in the same way by soaking in dilute HCl at pH 3.3. Samples were sealed after equilibration, and analysed by EPR as outlined in section 7.6.2.

Appendices

Appendix 1

Comparison of experimental and simulated EPR spectra for prolonged exposure EPR measurements (section 4.3.1).

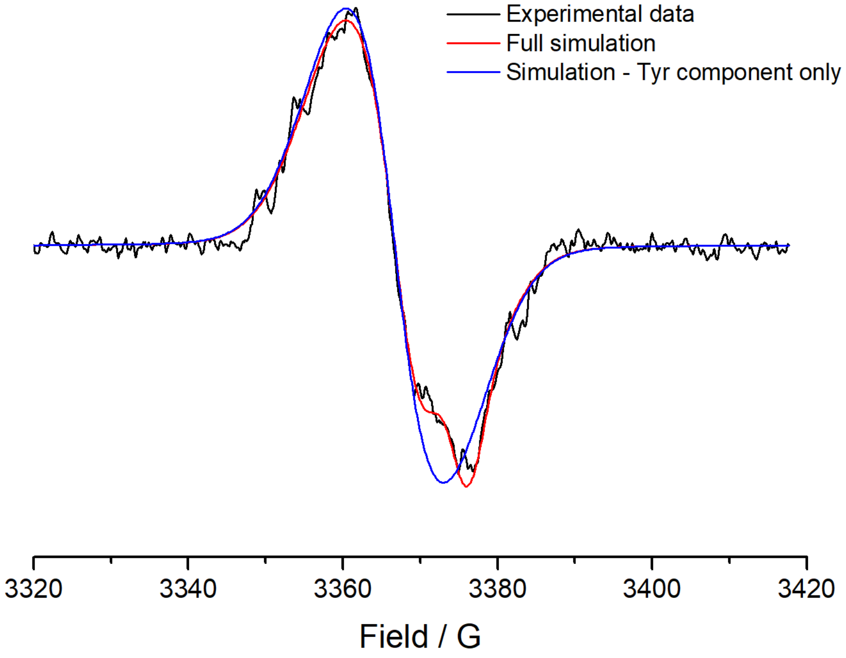

Appendix 2

ESI-MS spectrum of tyrosine ester labelled with amino-TEMP (sections 3.4.3, 7.4.5).

08-01-16-12-ms01

York - Chemistry - Mass Spectrometry Service Report

Analysis Information

Acquisition Date 11/01/2016 13:48:21

Analysis Filename	vc56544pg_P1-A-3_01_63188.d
Method	600p_meoh1260_2c1s.m
Submission Name	vc56544pg
Instrument	micrOTOF
ESI	Positive

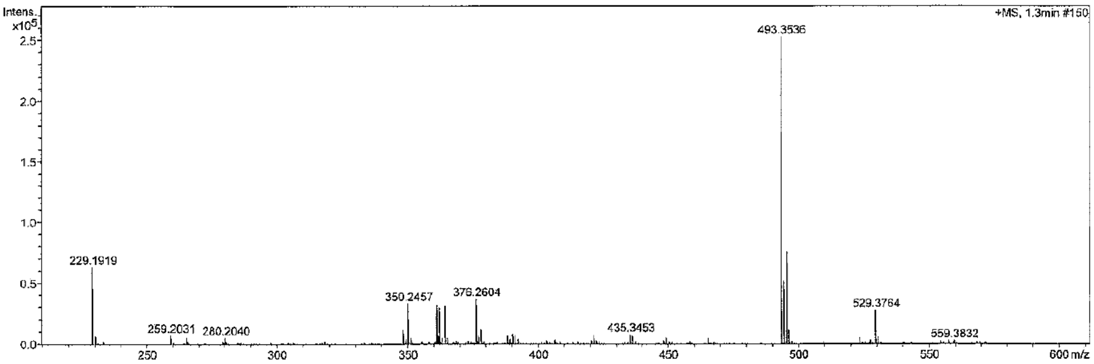

Meas. m/z	#	Formula	m/z	err [ppm]	err [mDa]	mSigma	Mean err [ppm]
376.2604	1	C 21 H 34 N 3 O 3	376.2595	-2.4	-0.9	180.7	6.9

Appendix 3

ESI-MS spectrum of tyrosine ester spin labelled with amino-TEMPO (sections 3.4.3, 7.4.5).

08-01-16-13-ms01

York - Chemistry - Mass Spectrometry Service Report

Analysis Information Acquisition Date 11/01/2016 13:51:17

Analysis Filename	vc56545pg_P1-A-4_01_63189.d
Method	600p_meoh1260_2c1s.m
Submission Name	vc56545pg
Instrument	micrOTOF
ESI	Positive

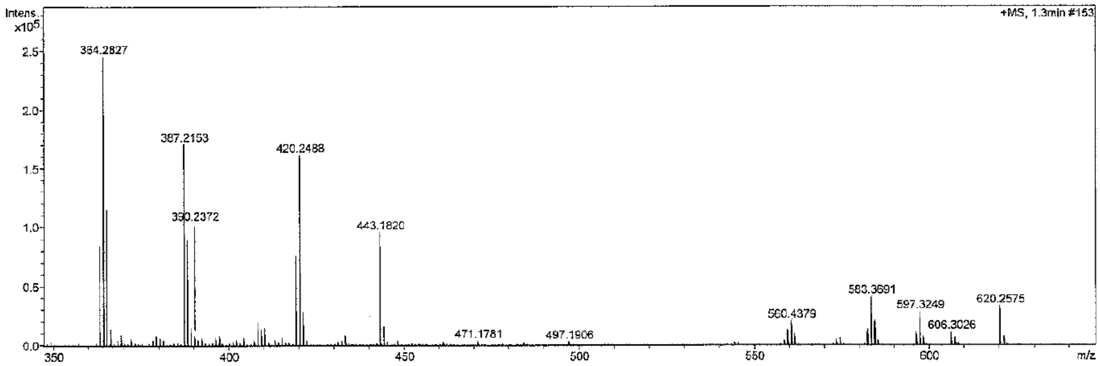

Meas. m/z	#	Formula	m/z	err [ppm]	err [mDa]	mSigma	Mean err [ppm]
390.2372	1	C 21 H 32 N 3 O 4	390.2387	4.0	1.6	447.9	-3.6

Appendix 4

Breakdown of 100 W Hg arc lamp (Oriel 6281 / Ushio USH-102DH) spectral irradiance. Data provided by Newport Corporation, Stratford CT, USA.

	UVC		**UVB**	**UVA**		**VIS**						**IR**
λ / nm	<250	250-280	280-320	320-350	350-400	400-450	450-500	500-550	550-600	600-650	650-700	>700
% of total irradi.	2.4	0.6	9.2	3.0	10.7	12.6	2.5	7.1	7.9	1.4	1.4	41.2

Abbreviations

Å	Ångström (10-10 m)
acac	Acetylacetonate
Ala	Alanine
Arg	Arginine
Asp	Aspartic acid
BHT	Butylated hydroxytoluene
BOP	Broad outer peaks
CD	Cysteinyldopa
cmc	Critical micelle concentration
Cys	Cysteine
DHI	5,6-dihydroxyindole
DHICA	5,6-dihydroxyindole carboxylic acid
DLS	Dynamic light scattering
DMF	Dimethylformamide
DMPO	5,5-dimethyl-1-pyrroline N-oxide
DOPA	3,4-dihydroxyphenylalanine
DOXYL	4,4-dimethyl-3-oxazolidinyloxy, free radical
DPPH	2,2-diphenyl-1-picrylhydrazyl
EA	Electron acceptor
EPR	Electron Paramagnetic Resonance
ESI-MS	Electrospray ionisation mass spectrometry
Fmoc	Fluorenylmethyloxycarbonyl
G	Gauss
Gly	Glycine
His	Histidine
HOMO	Highest occupied molecular orbital
ICP-MS	Inductively coupled plasma mass spectrometry
KAP	Keratin Associated Protein

LMWG	Low molecular weight gelator
LUMO	Lowest unnocupied molecular orbital
Lys	Lysine
MEA	Methyl eicosanoic acid
Met	Methionine
mT	millitesla
NMR	Nuclear magnetic resonance
P&G	Procter & Gamble Co.
PA	Peak area
PEG	Polyethylene glycol
PEO	Polyethylene oxide
Phe	Phenylalanine
ppm	parts per million
PTFE	Polytetrafluoroethylene
RH	Relative humidity
ROS	Reactive oxygen species
Ser	Serine
TEM	Transmission electron microscopy
TEMP	2,2,6,6-tetramethylpiperidine
TEMPO	(2,2,6,6-tetramethylpiperidin-1-yl)oxyl
Trp	Tryptophan
Tyr	Tyrosine
UV	Ultraviolet

References

1. D. R. Graham, K. W. Statham, *J. Soc. Dyers Colour.*, 1956, **72**, 434-438
2. P. A. Duffield, D. M. Lewis, *Rev. Prog. Coloration*, 1985, **15**, 38-51
3. E. Hoting, M. Zimmermann, S. Hilterhaus-Bong, *J. Soc. Cosmet. Chem.*, 1995, **46**, 85-99
4. Haircare: Global Industry Guide, Marketline, 2013
5. K. R. Millington, L. J. Kirschenbaum, *Color. Technol.*, 2002, **118**, 6-14
6. F. Noser, *Ärztl. Kosmetol.*, 1983, **13**, 415-422
7. T. Clausen, A. Schwan-Jonczyk, G. Lang, W. Schuh, K. D. Liebscher, C. Springob, M. Franzke, W. Balzer, S. Imhoff, G. Maresch, R. Bimczok, *Hair Preparations, in Ullman's Encyclopedia of Industrial Chemistry*, 2006
8. B. C. Powell, G. E. Rogers, *in Formation and Structure of Human Hair,* ed. P. Jolles, H. Zahn, Birkhäuser Verlag, Basel, 1997, 59-148
9. R. E. Chapman, *in Biology of the Integument, Vol. 2*, Springer Verlag, Berlin, 1986, 293-317
10. A. G. Matolsty, *Adv. Biol. Skin*, 1967, **9**, 559-569
11. N. Saito, T. Morishima, *Arch. Dermatol. Res.*, 1991, **283**, 7-9
12. A. C. S. Nogueira, I. Joekes, *J. Cosmet. Sci.*, 2007, **58**, 385-391
13. A. Bertazzo, C. Costa, M. Biasiolo, G. Allegri, G. Cirrincione, G. Presti, *Biol. Trace Element Res.*, 1996, **52**, 37-53
14. V. Trunova, N. Parshina, V. Kondratyev, *J. Synchrotron Rad.*, 2003, **10**, 371-375
15. W. G. Crewther, L. M. Dowling, P. M. Steinert, D. A. D. Parry, *Int. J. Macromol.*, 1983, **5**, 267-274
16. C. H. Lee, M. S. Kim, B. M. Chung, D. J. Leahy, P. A. Coulombe, *Nat. Struct. Mol. Biol.*, 2012, **19**, 707-715
17. C. G. Bunick, L. M. Milstone, *J. Invest. Dermatol.*, 2017, **137**, 142-150
18. M. H. Lynch, W. M. O'Guin, C. Hardy, L. Mak, T. T. Sun, *J. Cell Biol.*, 1986, **103**, 2593-2606
19. M. A. Rogers, L. Langbein, S. Praetzel-Wunder, H. Winter, J. Schweizer, *Int. Rev. Cytol.*, 2006, **251**, 209-263
20. The UniProt Consortium; UniProt: the universal protein knowledgebase, *Nucleic Acids Res.*, 2017, **45**, D158-D169

21. L. Langbein, J. Schweizer, *Int. Rev. Cytol.*, 2005, **243**, 1-78

22. C. R. Robbins, C. H. Kelly, *Text. Res. J.*, 1970, **40**, 891-896

23. W. H. Ward, H. P. Lundgren, *Adv. Prot. Chem.*, 1954, **9**, 243-297

24. D. J. Peet, R. E. H. Wettenhall, D. E. Rivett, A. K. Allen, *Comp. Biochem. Physiol.*, 1992, **102B**, 363-366

25. C. R. Robbins, *Chemical and Physical Behavior of Human Hair, 5th Ed.*, Springer, New York, 2012

26. J. D. Simon, D. N. Peles, *Acc. Chem. Res.*, 2010, **43**, 1452-1460

27. S. Ito, K. Wakamatsu, *Photochem. Photobiol.*, 2008, **84**, 582-592

28. G. Agrup, C. Hansson, H. Rorsman, E. Rosengren, *Arch. Dermatol. Res.*, 1982, **272**, 103-115

29. F. W. Ward, *Biochem. J.*, 1923, **17**, 898-902

30. ASTM G173-03(2012), *Standard Tables for Reference Solar Spectral Irradiances: Direct Normal and Hemispherical on 37° Tilted Surface*, ASTM International, West Conshohocken, PA, 2012

31. S. Madronich, R. L. McKenzie, L. O. Björn, M. M. Caldwell, *J. Photochem. Photobiol. B*, 1998, **46**, 5-19

32. M. Blumthaler, W. Ambach, *Science*, 1990, **248**, 206-208

33. S. Solomon, D. J. Ivy, D. Kinnison, M. J. Mills, R. R. Neely, A. Schmidt, *Science*, 2016, **353**, 269-274

34. D. Voet, J. G. Voet, *Biochemistry*, 4th Ed., Wiley, 2011

35. D. Creed, *Photochem. Photobiol.*, 1984, **39**, 563-575

36. E. G. Bendit, *J. Text. I. Trans.*, 1960, **51**, T544-T561

37. D. B. Wetlaufer, J. T. Edsall, B. R. Hollingworth, *J. Biol. Chem.*, 1958, **233**, 1421-1428

38. B. Kierdaszuk, I. Gryczynski, A. Modrak-Wojcik, A. Bzowska, D. Shugar, J. R. Lakowicz, *Photochem. Photobiol.*, 1995, **61**, 319-324

39. R. V. Benasson, E. J. Land, T. G. Truscott, *Excited States and Free Radicals in Biology and Medicine*, Oxford University Press, Oxford, 1993

40. J. W. Longworth, in *Excited States of Proteins and Nucleic Acids*, ed. R. F. Steiner, I. Weinryb, Plenum Press, New York, 1971, 319-484

41. Y. Saito, H. Tachibana, H. Hayashi, A. Wada, *Photochem. Photobiol.*, 1981, **33**, 289-295

42. D. V. Bent, E. Hayon, *J. Am. Chem. Soc.*, 1975, **97**, 2599-2606
43. M. Z. Hoffman, E. Hayon, *J. Am. Chem. Soc.*, 1972, **94**, 7950-7957
44. J. Feitelson, E. Hayon, A. Treinin, *J. Am. Chem. Soc.*, 1973, **95**, 1025-1029
45. M. J. Davies, *Biochem. Biophys. Res. Commun.*, 2003, **305**, 761-770
46. R. W. Redmond, J. N. Gamlin, *Photochem. Photobiol.*, 1999, **70**, 391-475
47. C. Giulivi, N. J. Traaseth, K. J. A. Davies, *Amino Acids*, 2003, **25**, 227-232
48. C. Hasselmann, G. Laustriat, *Photochem. Photobiol.*, 1973, **17**, 275-294
49. H. Østdal, M. J. Davies, H. J. Andersen, *Free Rad. Biol. Med.*, 2002, **33**, 201-209
50. G. B. Strambini, E. Gabellieri, M. Gonnelli, S. Rahuel-Clermont, G. Branlant, *Biophys. J.*, 1998, **74**, 3165-3172
51. Y. Chen, M. D. Barkley, *Biochemistry*, 1998, **37**, 9976-9982
52. C. R. Cantor, P. Pechukas, *Proc. Nat. Acad. Sci. USA*, 1971, **68**, 2099-2101
53. C. A. Ghiron, J. W. Longworth, N. Ramachandran, *Proc. Nat. Acad. Sci. USA*, 1973, **70**, 3703-3706
54. A. B. T. Ghisaidoobe, S. J. Chung, *Int. J. Mol. Sci.*, 2014, **15**, 22518-22538
55. D. Creed, *Photochem. Photobiol.*, 1984, **39**, 537-562
56. S. V. Jovanovic, S. Steenken, M. G. Simic, *J. Phys. Chem.*, 1991, **95**, 684-687
57. W. A. Prütz, E. J. Land, R. W. Sloper, *J. Am. Chem. Soc., Faraday Trans. 1*, 1981, **77**, 281-292
58. D. I. Pattison, A. S. Rahmanto, M. J. Davies, *Photochem. Photobiol. Sci.*, 2012, **11**, 38-53
59. D. Creed, *Photochem. Photobiol.*, 1984, **39**, 577-583
60. N. S. Kosower, E. M. Kosower, *Free Rad. Biol.*, 1976, **2**, 55-84
61. K. R. Millington, J. S. Church, *J. Photochem. Photobiol. B*, 1997, **39**, 204-212
62. O. Mozziconacci, B. A. Kerwin, C. Schöneich, *J. Phys. Chem. B*, 2010, **114**, 3668-3688
63. T. Nauser, G. Casi, W. H. Koppenol, C. Schöneich, *J. Phys. Chem. B*, 2008, **112**, 15034-15044
64. B. S. Berlett, E. R. Stadtman, *J. Biol. Chem.*, 1997, **272**, 20313-20316
65. M. Takahashi, T. Fujita, S. Watanabe, M. Sakamoto, *J. Chem. Soc., Perkin Trans. 2*, 1998, **0**, 487-492
66. R. Kon, A. Nakamura, N. Hirabayashi, K. Takeuchi, *J. Cosmet. Sci.*, 1998, **49**, 13-22
67. C. R. Robbins, M. K. Bahl, *J. Cosmet. Sci.*, 1984, **35**, 379-390

68. E. Hoting, M. Zimmermann, *J. Cosmet. Sci.*, 1996, **47**, 201-211

69. E. Fernández, C. Barba, C. Alonso, M. Martí, J. L. Parra, L. Coderch, *J. Photochem. Photobiol. B*, 2012, **106**, 101-106

70. M. I. Savenkova, D. M. Mueller, J. W. Heinecke, *J. Biol. Chem.*, 1994, **269**, 20394-20400

71. H. Yin, L. Xu, N. A. Porter, *Chem. Rev.*, 2011, **111**, 5944-5972

72. F. Solano, *Polym. Int.*, 2016, **65**, 1276-1287

73. M. L. Tran, B. J. Powell, P. Meredith, *Biophys. J.*, 2006, **90**, 743-752

74. A. Corani, A. Huijser, T. Gustavsson, D. Markovitsi, P.-Å. Malmqvist, A. Pezzella, M. d'Ischia, V. Sundström, *J. Am. Chem. Soc.*, 2014, **136**, 11626-11635

75. N. Maddodi, V. Setaluri, *Photochem. Photobiol.*, 2008, **84**, 528-536

76. M. Gauden, A. Pezzella, L. Panzella, M. T. Neves-Petersen, E. Skovsen, S. B. Petersen, K. M. Mullen, A. Napolitano, M. d'Ischia, V. Sundström, *J. Am. Chem. Soc.*, 2008, **130**, 17038-17043

77. J. B. Nofsinger, Y. Liu, J. D. Simon, *Free Rad. Biol. Med.*, 2002, **32**, 720-730

78. P. Meredith, J. Riesz, *Photochem. Photobiol.*, 2004, **79**, 211-216

79. M. R. Chedekel, *Photochem. Photobiol.*, 1982, **35**, 881-885

80. T. Sarna, P. M. Plonka, in *Biomedical EPR, Part A: Free Radicals, Metals, Medicine, and Physiology*, Springer US, 2005, 125-146

81. R. Bibang, R. Arnaud, J. Lemaire, A. Deflandre, G. Lang, *Pigment Cell Res.*, 1989, **2**, 395-400

82. E. Kim, L. Panzella, R. Micillo, W. E. Bentley, A. Napolitano, G. F. Payne, *Sci. Rep.*, 2015, **5**, 18447

83. J. D. Simon, D. Peles, K. Wakamatsu, S. Ito, *Pigment Cell Melanoma Res.*, 2009, **22**, 563-579

84. K. Wakamatsu, N. Miyazaki, L. Kolbe, S. Ito, *Pigment Cell Melanoma Res.*, 2012, **25**, 434-445

85. I. Nagy, R. A. Floyd, *Biochim. Biphys. Acta, Protein Struct. Mol. Enzymol.*, 1984, **790**, 238-250

86. J. G. Kiselar, M. R. Chance, *J. Mass Spectrom.*, 2010, **45**, 1373-1382

87. B. H. Bielski, G. G. Shiue, *Ciba Found. Symp.*, 1978, **65**, 43-56

88. G. Cohen, R. E. Heikkila, *J. Biol. Chem.*, 1974, **249**, 2447-2452

89. J. Moan, *J. Photochem. Photobiol. B: Biol.*, 1990, **6**, 343-347

90. I. B. C. Matheson, R. D. Etheridge, N. R. Kratowich, J. Lee, *Photochem. Photobiol.*, 1975, **21**, 165-171

91. F. Wilkinson, W. P. Helman, A. B. Ross, *J. Phys. Chem. Ref. Data*, 1995, **24**, 663-1021

92. M. J. Davies, *Photochem. Photobiol. Sci.*, 2004, **3**, 17-25

93. M. Gracanin, C. L. Hawkins, D. I. Pattison, M. J. Davies, *Free Radical Biol. Med.*, 2009, **47**, 92-102

94. J. M. Dyer, S. D. Bringans, W. G. Bryson, *Photochem. Photobiol. Sci.*, 2006, **5**, 698-706

95. W. M. Garrison, *Chem. Rev.*, 1987, **87**, 381-398

96. M. Bonifačić, K.-D. Asmus, *J. Phys. Chem.*, 1976, **80**, 2426-2429

97. C. C. Lawrence, M. Bennati, H. V. Obias, G. Bar, R. G. Griffin, J. Stubbe, *Proc. Natl. Acad. Sci. USA*, 1999, **96**, 8979-8984

98. G. Lassmann, M. Kolberg, G. Bleifuss, A. Gräslund, B.-M. Sjöberg, W. Lubitz, *Phys. Chem. Chem. Phys.*, 2003, **5**, 2442-2453

99. S. Lacombe, H. Cardy, M. Simon, A. Khoukh, J. Ph. Soumillion, M. Ayadim, *Photochem. Photobiol. Sci.*, 2002, **1**, 347-354

100. S. Oae, *Organic Sulfur Chemistry: Structure and Mechanism*, CRC Press, Boca Raton FL, 1991, p222-225

101. I. M. Kempson, W. M. Skinner, K. P. Kirkbride, *Environ. Sci. Technol.*, 2006, **40**, 3423-3428

102. P. Djurdjević, R. Jelić, *Transition Met. Chem.*, 1997, **22**, 284-293

103. H. T. Nyberg, M. Cefola, D. Sabine, *Arch. Biochem. Biophys.*, 1959, **85**, 82-88

104. N. Worasith, B. A. Goodman, *Int. J. Cosmet. Sci.*, 2013, **35**, 424-429

105. C. Sahin, C. Pala, L. Kayner, Y. A. Torun, A. Cetin, F. Kurnaz, S. Sivgin, F. S. Sahin, *Biomed. Rep.*, 2015, **3**, 383-387

106. S. Croft, B. C. Gilbert, J. R. L. Smith, J. K. Stell, W. R. Sanderson, *J. Chem. Soc. Perkin Trans. 2*, 1992, 153-160

107. J. F. Perez-Benito, *J. Inorg. Biochem.*, 2004, **98**, 430-438

108. P. Chábera, Y. Liu, O. Prakash, K. Wärnmark et. al., *Nature*, 2017, **543**, 695-699

109. M. Imanishi, K. Hashimoto, H. Kominami, *App. Catal. B,* 2010, **97**, 213-219

110. M. R. Ermácora, D. W. Ledman, H. W. Hellinga, G. W. Hsu, R. O. Fox, *Biochemistry*, 1994, **33**, 13625-13641
111. M. R. Eftink, C. A. Ghiron, *Anal. Biochem*., 1981, **114**, 199-227
112. K. Kobayashi, Y. Morioka, Y. Isaka, T. Tozawa, *Biol. Pharm. Bull.*, 1998, **21**, 398-400
113. M. J. Davies, *Biochim. Biophys. Acta, Proteins Proteom.*, 2005, **1703**, 93-109
114. L. Hong, Y. Liu, J. D. Simon, *Photochem. Photobiol.*, 2004, **80**, 477-481
115. H. Du, R. A. Fuh, J. Li, L. A. Corkan, J. S. Lindsey, *Photochem. Photobiol.*, 1998, **68**, 141-142
116. H. Edelhoch, *Biochemistry*, 1967, **6**, 1948-1954
117. M. A. Rogers, L. Langbein, H. Winter, C. Ehmann, S. Praetzel, B. Korn, J. Schweizer, *J. Biol. Chem.*, 2001, **276**, 19440-19451
118. C. Pommié, S. Levadoux, R. Sabatier, G. Lefranc, M.-P. Lefranc, *J. Mol. Recognit.*, 2004, **17**, 17-32
119. X. M. Zhou, W. W. Idler, A. C. Steven, D. R. Roop, P. M. Steinert, *J. Biol. Chem.*, 1988, **263**, 15584-15589
120. H. H. Bragulla, D. G. Homberger, *J. Anat.*, 2009, **214**, 516-559
121. M. T. Neves-Petersen, G. P. Gajula, S. B. Petersen, in *Molecular Photochemistry – Various Aspects*, S. Saha (Ed.), InTech, 2012
122. H. I. Joschek, S. I. Miller, *J. Am. Chem. Soc.*, 1966, **88**, 3273-3281
123. P. G. Gordon, W. A. Jerram, R. B. Johns, *Biochem. Biophys. Res. Commun.*, 1966, **23**, 269-272
124. D. Hitchcock, *J. Gen. Physiol.*, 1924, **6**, 747-757
125. E. P. L. Hunter, M. F. Desrosiers, M. G. Simic, *Free Radicals Biol. Med*, 1989, **6**, 581-585
126. D.R. Lide, *Handbook of Chemistry and Physics, 72nd Edition*, CRC Press, Boca Raton, FL, 1991.
127. P. Caregnato, P. M. D. Gara, G. N. Bosio, M. C. Gonzalez, N. Russo, M. del Carmen Michelini, D. O. Mártire, *J. Phys. Chem. A*, 2008, **112**, 1188-1194
128. M. Tomkiewicz, R. McAlpine, M. Cocivera, *Can. J. Chem.*, 1972, **50**, 3849-3856
129. M. L. McCormick, J. P. Gaut, T.-S. Lin, B. E. Britigan, G. R. Buettner, J. W. Heinecke, *J. Biol. Chem.*, 1998, **273**, 32030-32037
130. J. H. Freed, G. K. Fraenkel, *J. Chem. Phys.*, 1963, **39**, 326-348

131. M. F. R. Gavazzoni Dias, A. M. de Almeida, P. M. R. Cecato, A. R. Adriano, J. Pilcher, *Int. J. Trichology*, 2014, **6**, 95-99

132. S. Un, P. Dorlet, A. W. Rutherford, *Appl. Magn. Reson.*, 2001, **21**, 341-361

133. A. Ivancich, P. Dorlet, D. B. Goodin, S. Un, *J. Am. Chem. Soc.*, 2001, **123**, 5050-5058

134. H. B. Gray, J. R. Winkler, *Chem. Phys. Lett.*, 2009, **483**, 1-9

135. E. E. Smissman, J. R. J. Sorenson, J. Org. Chem., 1965, **30**, 4008-4010

136. B. L. Bales, M. Meyer, S. Smith, M. Peric, *J. Phys. Chem. A*, 2009, **113**, 4930-4940

137. M. de Loos, B. L. Feringa, J. H. van Esch, *Eur. J. Org. Chem.*, 2005, **2005**, 3615-3631

138. S. Kiyonaka, K. Sugiyasu, S. Shinkai, I. Hamachi, *J. Am. Chem. Soc.*, 2002, **124**, 10954-10955

139. A. Shome, S. Debnath, P. K. Das, *Langmuir*, 2008, **24**, 4280-4288

140. S. Sutton, N. L. Campbell, A. I. Cooper, M. Kirkland, W. J. Frith, D. J. Adams, *Langmuir*, 2009, **25**, 10285-10291

141. E. A. Appel, J. del Barrio, X. J. Loh, O. A. Scherman, *Chem. Soc. Rev.*, 2012, **41**, 6195-6214

142. L. A. Estroff, A. D. Hamilton, *Chem. Rev.*, 2004, **104**, 1201-1217

143. J. Huang, C. L. Hastings, G. P. Duffy, H. M. Kelly, J. Raeburn, D. J. Adams, A. Heise, *Biomacromolecules*, 2013, **14**, 200-206

144. T. L. Cheng, K. H. Chuang, B. M. Chen, S. R. Roffler, *Bioconjugate Chem.*, 2012, **23**, 881-899

145. R. H. Ruby, I. D. Kuntz, M. D. Calvin, *Proc. Natl. Acad. Sci.*, 1964, **51**, 515-520

146. G. J. M. Habraken, M. Peeters, C. H. J. T. Dietz, C. E. Koning, A. Heise, *Polym. Chem.*, 2010, **1**, 514-524

147. N. Hadjichristidis, H. Iatrou, M. Pitsikalis, G. Sakellariou, *Chem. Rev.*, 2009, **109**, 5528-5578

148. C. S. Thomas, L. Xu, B. D. Olsen, *Biomacromolecules*, 2012, **13**, 2781-2792

149. E. G. Kelley, R. P. Murphy, J. E. Seppala, T. P. Smart, S. D. Hann, M. O. Sullivan, T. H. Epps, *Nat. Commun.*, 2014, 5, 3599

150. G. H. Van Domeselaar, G. S. Kwon, L. C. Andrew, D. S. Wishart, *Colloids Surf. B: Biointerfaces*, 2003, **30**, 323-334

151. J. M. Kim, Y. Sakamoto, Y. K. Hwang, Y. Kwon, O. Terasaki, S. Park, G. D. Stucky, *J. Phys. Chem. B*, 2002, **106**, 2552-2558
152. P. R. Cullis, M. J. Hope, C. P. S. Tilcock, *Chem. Phys. Lipids*, 1986, **40**, 127-144
153. T. Gädt, N. S. Ieong, G. Cambridge, M. A. Winnik, I. Manners, *Nat. Mater.*, 2009, **8**, 144-150
154. D. E. Owens, N. A. Peppas, *Int. J. Pharm.*, 2006, **307**, 93-102
155. Ö. Topel, B. Çakir, L. Budama, N. Hoda, *J. Mol. Liq.*, 2013, **177**, 40-43
156. T. Chakraborty, I. Chakraborty, S. Ghosh, *Arabian J. Chem.*, 2011, **4**, 265-270
157. S. C. Owen, D. P. Y. Chan, M. S. Shoichet, *Nano Today*, 2012, **7**, 53-65
158. I. K. McDonald, J. M. Thornton, *J. Mol. Biol.*, 1994, **238**, 777-793
159. E. N. Baker, R. E. Hubbard, *Prog. Biophys. Mol. Biol.*, 1984, **44**, 97-179
160. T. K. Harris, G. J. Turner, *IUBMB Life*, 2002, **53**, 85-98
161. A. Caragheorgheopol, H. Caldararu, *Electron Paramagn. Reson.*, 2000, **17**, 205-245
162. M. J. N. Junk, *Assessing the Functional Structure of Molecular Transporters by EPR Spectroscopy* (Doctoral thesis), Johannes Gutenberg-Universität Mainz, 2012
163. V. Chechik, A. Caragheorgheopol, *Electron Paramagn. Reson.*, 2007, **20**, 96-130
164. M. A. Rahman, A. K. Ghosh, R. N. Bose, 1979, **29**, 158-162
165. A. Caragheorgheopol, H. Caldararu, I. Dragutan, H. Joela, W. Brown, *Langmuir*, 1997, **13**, 6912-6921
166. Y. Tkachev, V. Timofeev, *in "Nitroxides – Theory, Experiment and Applications"*, A. Kokorin (Ed.), InTech, 2012
167. G. T. Hermanson, *Bioconjugate Techniques*, *3rd Ed.*, 2013, p131
168. J. M. McFarland, N. S. Joshi, M. B. Francis, *J. Am. Chem. Soc.*, 2008, **130**, 7639-7644
169. M. Lorenzi, C. Puppo, R. Lebrun, S. Lignon, V. Roubaud, M. Martinho, E. Mileo, P. Tordo, S. R. A. Marque, B. Gontero, B. Guigliarelli, V. Belle, *Angew. Chemie Int. Ed.*, 2011, **50**, 9108-9111
170. E. Mileo, E. Etienne, M. Martinho, R. Lebrun, V. Roubaud, P. Tordo, B. Gontero, B. Guigliarelli, S. R. A. Marque, V. Belle, *Bioconjug. Chem.*, 2013, **24**, 1110-1117
171. P. K. Witting, D. J. Douglas, A. G. Mauk, *J. Biol. Chem.*, 2000, **275**, 20391-20398
172. A. Caragheorgheopol, W. Edwards, J. G. Hardy, D. K. Smith, V. Chechik, *Langmuir*, 2014, **30**, 9210-9218

173. Y. Tkachev, V. Timofeev, *Uniform EPR Spectra Analysis of Spin-Labeled Macromolecules by Temperature and Viscosity Dependences*, in *Nitroxides - Theory, Experiment and Applications*, Chp.10, In Tech, 2012

174. C. P. Poole, H. A. Farach, *Bull. Magn. Reson.*, 1979, **1**, 162-194

175. C. F. Polnaszek, J. H. Freed, *J. Phys. Chem.*, 1975, **79**, 2283-2306

176. J. H. Freed, *J. Chem. Phys.*, 1977, **66**, 4183-4199

177. S. Stoll, A. Schweiger, *J. Magn. Reson.*, 2006, **178**, 42-55

178. D. Marsh, L. I. Horváth, *in "Advanced EPR: Applications in Biology and Biochemistry"*, A. J. Hoff (Ed.), Elsevier, 2012

179. F. Gardebien, R. R. Thangudu, B. Gontero, B. Offmann, *J. Mol. Graphics Modell.*, 2006, **25**, 186-195

180. P. M. Steinert, *Biochem. J.*, 1975, **149**, 39-48

181. S. Mehboob, B.-H. Luo, W. Fu, M. E. Johnson, L. W.-M. Fung, *Biochemistry*, 2005, **44**, 15898-15905

182. T. Haliloğlu, I. Bahar, B. Erman, W. L. Mattice, *Macromolecules*, 1996, **29**, 4764-4771

183. J. Jansson, K. Schillen, M. Nilsson, O. Soderman, G. Fritz, A. Bergmann, O. Glatter, *J. Phys. Chem. B*, 2005, **109**, 7073-7083

184. M. Correia, M. T. Neves-Petersen, P. B. Jeppesen, S. Gregersen, S. B. Petersen, *PLOS ONE*, 2012, **7**, e50733

185. I. A. Vladimirov, N. I. Perrase, *Biofizika*, 1966, **11**, 578-583

186. D. J. Edge, B. C. Gilbert, R. O. C. Norman, P. R. West, *J. Chem. Soc. (B): Phys. Org.*, 1971, 189-196

187. D. C. McCain, W. E. Palke, *J. Magn. Reson.*, 1975, **20**, 52-66

188. J. Lind, X. Shen, T. E. Eriksen, G. Merényi, *J. Am. Chem. Soc.*, 1990, **112**, 479-482

189. Y. R. Luo, *Comprehensive Handbook of Chemical Bond Energies*, CRC Press, Boca Raton FL, 2007

190. C. J. Fischer, A. Gafni, D. G. Steel, J. A. Schauerte, *J. Am. Chem. Soc.*, 2002, **124**, 10359-10366

191. Z. Maskos, J. D. Rush, W. H. Koppenol, *Arch. Biochem. Biophys.*, 1992, **296**, 521-529

192. J. R. Lakowicz, *Principles of Fluorescence Spectroscopy, 3rd Edition*, Springer US, 2006

193. J. Chen, H. D. Kim, K. C. Kim, *Microfluid. Nanofluid.*, 2013, **14**, 541-550

194. C. R. Wilke, P. Chang, *A. I. Ch. E. Journal*, 1955, **1**, 264-270

195. D. Nohara, T. Kajiura, K. Takeda, *J. Mass Spectrom.*, 2005, **40**, 489-493

196. S. Udenfriend, S. Stein, P. Böhlen, W. Dairman, *Science*, 1972, **178**, 871-872

197. J. V. Castell, M. Cervera, R. Marco, *Anal. Biochem.*, 1979, **99**, 379-391

198. G. Ruppert, R. Bauer, G. Heisler, *J. Photochem. Photobiol. A: Chem.*, 1993, **73**, 75-78

199. S. R. Logan, *J. Chem. Soc. Perkin Trans. 2*, 1989, **0**, 751-754

200. A. Bencini, D. Gatteschi, *EPR of Exchange Coupled Systems*, Courier Dover Publications, 2012, p200

201. S. K. Dogra, H. S. Randhawa, *Molecular Spectroscopy, Chapter 8: Electron Spin Resonance Spectroscopy*, Pearson, 2015

202. B. L. Bales, M. Peric, *J. Phys. Chem. B*, 1997, **101**, 8707-8716

203. S. J. Dixon, B. R. Stockwell, *Nat. Chem. Biol.*, 2014, **10**, 9-17

204. A. Machulek, F. H. Quina, F. Gozzi, V. O. Silva, L. C. Friedrich, J. E. F. Moraes, in *Organic Pollutants Ten Years After the Stockholm Convention – Environmental and Analytical Update*, ed. T. Puzyn, A. Mostrag-Szlichtyng, InTech, 2012, p271-292

205. I. P. Pozdnyakov, E. M. Glebov, V. F. Plyusnin, V. P. Grivin, Y. V. Ivanov, D. Y. Vorobyev, N. M. Bazhin, *Pure Appl. Chem.*, 2000, **72**, 2187-2197

206. H. Żegota, K. Kołodziejczyk, M. Król, B. Król, *Radiat. Phys. Chem.*, 2005, **72**, 25-33

207. W. J. Rutter, *Acta. Chem. Scand.*, 1958, **12**, 438-446

208. G. J. Smith, *Color. Technol.*, 1999, **115**, 346-349

209. Bio-Rad Laboratories Inc, Chelex 100 and Chelex 20 product information

210. I. Puigdomenech, *Medusa, Chemical Equilibrium Diagrams*, 2010, Stockholm

211. D. van der Helm, C. E. Tatsch, *Acta Cryst.*, 1972, **B28**, 2307-2312

212. D. A. Doughty, *Science*, 1996, **271**, 163-168

213. W. A. Pryor, *Ann. Rev. Physiol.*, 1986, **48**, 657-667

214. R. B. Mikkelsen, P. Wardman, *Oncogene*, 2003, **22**, 5734-5754

215. J. A. Sweileh, *Ana. Bioanal. Chem*, 2003, **375**, 450-455

216. G. J. Smith, R. F. C. Claridge, C. J. Smith, *Photochem. Photobiol.*, 1979, **29**, 777-779

217. W. Reiss, J. F. Hazel, W. M. McNabb, *Anal. Chem.*, 1952, **24**, 1646-1648

218. J. J. Pignatello, E. Oliveros, A. MacKay, *Crit. Rev. Env. Sci. Tec.*, 2006, **36**, 1-84

219. S. Ozeki, S. Ikeda, *J. Colloid. Int. Sci.*, 1982, **87**, 424-435

220. T. Nicolai, O. Colombani, C. Chassenieux, *Soft Matter*, 2010, **6**, 3111-3118
221. K. Inaba, *Langmuir*, 1997, **13**, 1501-1509
222. R. B. Simpson, J. D. Ashbrook, E. C. Santos, A. A. Spector, *J. Lipid Res.*, 1974, **15**, 415-422
223. M. G. Simic, M. Karel, *Autoxidation in Food and Biological Systems*, Springer, 2013
224. M. Brewer, *Compr. Rev. Food Sci. Food Saf.*, 2011, **10**, 221-247
225. S. J. Stohs, D. Bagchi, *Free Radic. Biol. Med.*, 1995, **18**, 321-336
226. E. Finkelstein, G. M. Rosen, E. J. Rauckman, *J. Am. Chem. Soc.*, 1980, **102**, 4994-4999
227. B. Kalyanaraman, C. C. Felix, R. C. Sealy, *J. Am. Chem. Soc.*, 1984, **106**, 7327-7330
228. M. M. Mossoba, K. Makino, P. Riesz, R. C. Perkins, *J. Phys. Chem.*, 1984, **88**, 4717-4723
229. M. M. Mossoba, P. L. Gutierrez, *Biochem. Biophys. Res. Commun.*, 1985, **132**, 445-452
230. S. Baluja, K. Bhesaniya, R. Bhalodia, S. Chanda, *Int. Lett. Chem. Phys. Astron.*, 2014, **9**, 48-58
231. W. A. Yehye, N. A. Rahman, A. Ariffin, S. B. A. Hamid, A. A. Alhadi, F. A. Kadir, M. Yaeghoobi, *Eur. J. Med. Chem.*, 2015, **101**, 295-312
232. M. Lucarini, V. Mugnaini, G. F. Pedulli, *J. Org. Chem.*, 2002, **67**, 928-931
233. J. P. Adjimani, P. Asare, *Toxicol. Rep.*, 2015, **2**, 721-728
234. H. Geckil, B. Ates, G. Durmaz, S. Erdogan, I. Yilmaz, *Am. J. Biochem. Biotechnol.*, 2005, **1**, 27-31
235. J. R. Herman*, J. Geophys. Res.*, 2010, **115**, D04203
236. M. S. Jahan, T. R. Drouin, R. M. Sayre, *Photochem. Photobiol.*, 1987, **45**, 543-546
237. L. J. Kirschenbaum, X. Qu, E. T. Borish, *J. Cosmet. Sci.*, 2000, **51**, 169-182
238. D. R. Duling, *J. Magn. Reson., Ser. B*, 1994, **104**, 105-110
239. S. Un, *Magn. Reson. Chem.*, 2005, **43**, S229-S236
240. W. Chamulitrat, R. P. Mason, *J. Biol. Chem.*, 1989, **264**, 20968-20973
241. T. Sarna, H. A. Swartz and Swartz, H. A., in *The Pigmentary System: Physiology and Pathophysiology, Second Edition* (eds J. J. Nordlund, R. E. Boissy, V. J. Hearing, R. A. King, W. S. Oetting and J.-P. Ortonne), Blackwell Publishing Ltd, 2006, Oxford, UK.
242. C. G. Bunick, T. A. Steitz, *Crystal structure of the heterocomplex between coil 2B domains of human intermediate filament proteins keratin 1 (KRT1) and keratin 10 (KRT10*), 2016, DOI: 10.2210/pdb4zry/pdb
243. X. Qu, L. J. Kirschenbaum, E. T. Borish, *Photochem. Photobiol.*, 2000, **71**, 307-313

244. C. C. Felix, J. S. Hyde, R. C. Sealy, *Biochem. Biophys. Res. Commun.*, 1979, **88**, 456-461

245. A. J. Elliot, J. K. S. Wan, *J. Phys. Chem.*, 1978, **82**, 444-452

246. L. R. G. Treloar, *Trans. Faraday Soc.*, 1952, **48**, 567-576

247. Y. K. Kamath, S. B. Ruetsch, *IFSCC Mag.*, 2006, **9**, 325-333

248. A. W. Girotti, W. Korytowski, *Methods in Enzymology*, 2000, **319**, 85-100

249. D. R. Weinberg, C. J. Gagliardi, J. F. Hull, C. F. Murphy, C. A. Kent, B. C. Westlake, A. Paul, D. H. Ess, D. G. McCafferty, T. J. Meyer, *Chem. Rev.*, 2012, **112**, 4016-4093

250. S. Ratnapandian, S. B. Warner, Y. K. Kamath, *J. Cosmet. Sci.*, 1998, **49**, 309-320

251. C. Dubief, *Cosmetics & Toiletries*, 1992, **107**, 95-102

252. C. C. Trowbridge, *Science*, 1896, **4**, 62-65

253. L. Greenspan, *J. Res. Natl. Stand., Sec. A*, 1977, **81A**, 89-96

254. C. N. Pace, F. Vajdos, L. Fee, G. Grimsley, T. Gray, *Protein Science*, 1995, **4**, 2411-2423

255. O. Chiarelli-Neto, C. Pavani, A. S. Ferreira, A. F. Uchoa, D. Severino, M. S. Baptista, *Free Rad. Biol. Med.*, 2011, **51**, 1195-1202

256. S. B. Nimse, D. Pal, *RSC Adv.*, 2015, **5**, 27986-28006

257. L. Camont, C.-H. Cottart, Y. Rhayem, V. Nimet-Antoine, R. Djelidi, F. Collin, J.-L. Beaudeux, D. Bonnefort-Rousselot, *Analy. Chim. Acta*, 2009, **634**, 121-128

258. A. O. Evans, J. M. Marsh, R. R. Wickett, *J. Cosmet. Sci.*, 2011, **62**, 383-391

259. J. E. Grebel, J. J. Pignatello, W. A. Mitch, *Water Res.*, 2011, **45**, 6535-6544

260. C. Winkler, B. Frick, K. Schroecksnadel, H. Schennach, D. Fuchs, *Food Chem. Toxicol.*, 2006, **44**, 2003-2007

261. M. Montalti, A. Credi, L. Prodi, M. D. Gandolfi, in *Handbook of Photochemistry, 3rd Ed.*, CRC Press, 2006, Boca Raton FL, USA

262. C. C. Akoh, D. B. Min, in *Food Lipids: Chemistry, Nutrition, and Biotechnology, 3rd Ed.*, CRC Press, 2008, Boca Raton FL, USA

263. J. Yanez, C. L. Sevilla, D. Becker, M. D. Sevilla, *J. Phys. Chem.*, 1987, **91**, 487-491

264. S. G. Reddy, K. K. Wong, C. V. Parast, J. Peisach, R. S. Magliozzo, J. W. Kozarich, *Biochemistry*, 1998, **37**, 558-563

265. M. D. Sevilla, M. Yan, D. Becker, *Biochem. Biophys. Res. Commun.*, 1988, **155**, 405-410